JOINT DOCTORATE PROGRAMME

COMPREHENSIVE SYSTEM AND NUMERICAL ANALYSIS OF A SMALL-SCALE EJECTOR-BASED NATURAL REFRIGERATION SYSTEM

Doctoral dissertation of:
Rafał Fingas

Supervisor:
Prof. Giorgio Besagni

Supervisor:
Prof. Jacek Smołka

Co-supervisor:
Dr Michał Haida

Gliwice, Poland - Milan, Italy, 2025

Acknowledgments

I would like to express my deepest gratitude to my supervisors, Prof. Jacek Smołka from the Silesian University of Technology and Prof. Giorgio Besagni from Politecnico di Milano, for their time, effort, support, and guidance throughout my PhD studies. Their expertise, dedication, and constructive feedback have been fundamental to the completion of this thesis.

My sincere thanks also go to my co-supervisor, Dr Michał Haida from Silesian University of Technology, for introducing me to academia, guiding me through my first research steps, and for his constant support and readiness to help whenever needed.

I would like to express my gratitude to Marani Sp. z o.o. and Mikołaj Mastrowski for sharing the valuable data and allowing me to use it in my analyses. Their contribution has significantly enhanced the quality and applicability of my research.

My sincere thanks also go to Prof. Fabio Inzoli and Prof. Giorgio Besagni from Politecnico di Milano for giving me the opportunity to pursue my PhD as a joint degree between the Silesian University of Technology and Politecnico di Milano, and for sharing their knowledge, experience, and scientific insight. I am equally grateful to all my friends and colleagues at the CFDLab group of Politecnico di Milano for the inspiring discussions and great moments we shared together during the academic journey.

I would like to extend my appreciation to the entire ejectorPL team at the Silesian University of Technology - Michał Palacz, Jakub Bodys, Michał Stebel, Andrzej Nowak, Edyta Piechnik, Jakub Chrobak, and Tufan Özyıldız, for their research collaboration, continuous support, and many memorable experiences we shared along the way.

Finally, I would like to express my warmest gratitude to my beloved wife

Paulina and my entire family, especially my grandmother Róża, for their unconditional love, patience, and constant encouragement. Your support has been my greatest source of strength and motivation throughout this journey. Without you, this achievement would not have been possible.

Preface

This dissertation has been prepared within the framework of a joint doctoral programme regulated by the cotutelle agreement established between the Silesian University of Technology (Gliwice, Poland) and the Politecnico di Milano (Milan, Italy). The cotutelle agreement was signed with the purpose of strengthening scientific collaboration and promoting international mobility by ensuring joint supervision of doctoral research.

The doctoral candidate was admitted to the PhD programme at the Silesian University of Technology in October 2020 and subsequently to the doctoral programme in Energy and Nuclear Science and Technology at the Politecnico di Milano in November 2021 (XXXVII Cycle). The doctoral training and research activities were carried out alternately at both institutions, in line with the provisions of the joint programme, thereby ensuring exposure to the academic and research environments of two European universities.

The dissertation has been developed under the supervision of Prof. Jacek Smolka and Dr Michal Haida (Silesian University of Technology) and Prof. Giorgio Besagni (Politecnico di Milano). The joint academic guidance provided by the supervisors from both institutions has played a decisive role in shaping the research and in ensuring compliance with the scientific and academic standards of the two doctoral programmes.

This work represents not only a scientific contribution in the field of ejector-based heat pump systems, but also the result of close cooperation between two academic institutions committed to advancing knowledge through joint doctoral education.

Abstract

The growing need to improve energy efficiency and reduce greenhouse gas emissions has intensified interest in technologies capable of utilizing low temperature waste heat sources. Thermally driven refrigeration systems represent a promising alternative to conventional electrically powered units, as they can provide cooling with minimal primary energy consumption. Within this group, the ejector refrigeration systems (ERS) offer particular advantages due to their simple mechanical design and compatibility with natural refrigerants. However, the performance of conventional fixed-geometry ejectors is highly sensitive to varying operating conditions, which limits their application in waste heat recovery systems characterized by variable heat source and ambient temperatures. This thesis presents a numerical investigation of an ultra-low-grade waste heat-driven ERS equipped with a variable geometry ejector (VGE) using the natural refrigerant propane (R290). The work addresses the limitations of fixed-geometry ejectors by studying a controllable spindle-based ejector capable of adapting to fluctuating ambient temperatures and load conditions. An experimental campaign confirmed that the R290 VGE can provide reliable mass entrainment ratio control by changing the effective motive nozzle throat area. The Computational Fluid Dynamics-based (CFD) performance maps were used as a basis for two Reduced Order Models (ROM): a baseline pressure-specific enthalpy model, and a generalized pressure-ratio and inlet temperature model. Both approaches were able to reproduce the CFD results with an error below 1% and were implemented in Dymola for dynamic ERS simulations. System-level simulations using weather data from three climatic zones and three industrial waste heat profiles showed consistent VGE performance gains compared to a system utilizing fixed ejectors, with daily-averaged coefficient of performance (COP) improvements of up to 52% and cooling capacity

increases of up to 13%. The VGE-based ERS showed the highest benefits in hot climates with high daily temperature variability, where spindle control provides continuous on-design operation. The generalized ROM was also applied to the analysis of ERS with alternative refrigerants. The ERS with R1270 utilizing R290 VGE delivered up to 21% higher cooling capacity and 10% COP improvement related to the system utilizing R290, while other R290-based blends showed comparable or lower performance, indicating a need to expand the ROM operational envelope or re-design the ejector for other refrigerants. The thesis confirms that a single VGE can replace multiple fixed ejectors, enabling efficient, flexible cooling driven by ultra-low-grade waste heat.

Abstract

La crescente necessità di migliorare l'efficienza energetica e ridurre le emissioni di gas serra ha intensificato l'interesse per le tecnologie in grado di utilizzare fonti di calore residuo a bassa temperatura. I sistemi di refrigerazione a propulsione termica rappresentano un'alternativa promettente alle unità convenzionali alimentate elettricamente, in quanto sono in grado di fornire raffreddamento con un consumo minimo di energia primaria. All'interno di questo gruppo, i sistemi di refrigerazione a eiettore (ERS) offrono particolari vantaggi grazie al loro design meccanico semplice e alla compatibilità con i refrigeranti naturali. Tuttavia, le prestazioni degli eiettori convenzionali a geometria fissa sono altamente sensibili alle variazioni delle condizioni operative, il che ne limita l'applicazione nei sistemi di recupero del calore residuo caratterizzati da fonti di calore e temperature ambientali variabili. Questa tesi presenta uno studio numerico su un ERS alimentato da calore residuo a bassissima temperatura dotato di un eiettore a geometria variabile (VGE) che utilizza il refrigerante naturale propano (R290). Il lavoro affronta i limiti degli eiettori a geometria fissa studiando un eiettore controllabile basato su mandrino in grado di adattarsi alle fluttuazioni della temperatura ambiente e delle condizioni di carico. Una campagna sperimentale ha confermato che il VGE R290 è in grado di fornire un controllo affidabile del rapporto di trascinamento di massa modificando l'area effettiva della gola dell'ugello motore. Le mappe delle prestazioni basate sulla fluidodinamica computazionale (CFD) sono state utilizzate come base per due modelli a ordine ridotto (ROM): un modello di entalpia specifica della pressione di riferimento e un modello generalizzato del rapporto di pressione e della temperatura di ingresso. Entrambi gli approcci sono stati in grado di riprodurre i risultati CFD con un errore inferiore all'1% e sono stati implementati in Dymola per simulazioni dinamiche

ERS. Le simulazioni a livello di sistema che utilizzano dati meteorologici provenienti da tre zone climatiche e tre profili di calore residuo industriale hanno mostrato miglioramenti costanti delle prestazioni del VGE rispetto a un sistema che utilizza eiettori fissi, con miglioramenti del coefficiente di prestazione (COP) medio giornaliero fino al 52% e aumenti della capacità di raffreddamento fino al 13%. L'ERS basato sul VGE ha mostrato i maggiori vantaggi nei climi caldi con elevata variabilità della temperatura giornaliera, dove il controllo del mandrino garantisce un funzionamento continuo secondo il progetto. Il ROM generalizzato è stato applicato anche all'analisi dell'ERS con refrigeranti alternativi. L'ERS con R1270 che utilizza R290 VGE ha fornito una capacità di raffreddamento superiore fino al 21% e un miglioramento del COP del 10% rispetto al sistema che utilizza R290, mentre altre miscele a base di R290 hanno mostrato prestazioni comparabili o inferiori, indicando la necessità di espandere l'involucro operativo del ROM o riprogettare l'eiettore per altri refrigeranti. La tesi conferma che un singolo VGE può sostituire più eiettori fissi, consentendo un raffreddamento efficiente e flessibile alimentato da calore residuo a bassissima temperatura.

Streszczenie

Rosnąca potrzeba poprawy efektywności energetycznej oraz redukcji emisji gazów cieplarnianych zwiększyła zainteresowanie technologiami umożliwiającymi wykorzystanie niskotemperaturowych źródeł ciepła odpadowego. Układy chłodnicze wykorzystujące energie cieplną stanowią obiecującą alternatywę dla konwencjonalnych, elektrycznie zasilanych jednostek, zapewniając chłodzenie przy minimalnym zużyciu energii pierwotnej. Wśród nich na szczególną uwagę zasługują strumienicowe układy chłodnicze (ang. ERS), charakteryzujące się prostą budową oraz kompatybilnością z naturalnymi czynnikami chłodniczymi. Niestety jednak wydajność konwencjonalnych strumienic o stałej geometrii jest wysoce wrażliwa na zmienne warunki pracy, co ogranicza ich zastosowanie w systemach odzysku ciepła odpadowego, dla których typowa jest zmienność temperatur źródła ciepła i otoczenia. Praca doktorska przedstawia analizę numeryczną ERS zasilanego niskotemperaturowym ciepłem odpadowym, wyposażonego w strumienicę o zmiennej geometrii (ang. VGE) z zastosowaniem naturalnego czynnika propanu (R290). Celem badań było oszacowanie potencjału wykorzystania VGE w systemie ERS, który, w odróżnieniu do strumienic o stałej geometrii, jest w stanie dostosować swoją pracę do zmiennych warunków otoczenia oraz zmiennych warunków obciążenia. Kampania pomiarowa potwierdziła możliwość precyzyjnej regulacji współczynnika eżekcji poprzez zmianę efektywnego przekroju gardzieli za pomocą igły regulacyjnej. W oparciu o mapy efektywności strumienicy uzyskane z wyników symulacji obliczeniowej mechaniki płynów (ang. CFD) opracowano dwa modele zredukowane (ang. ROM) strumienicy VGE: bazowy (ciśnienie-entalpia właściwa) oraz uogólniony (stosunek ciśnień i temperatury wlotowe). Oba modele ROM wiernie odwzorowały wyniki względem CFD ze średnim błędem poniżej 1% i zostały zaimplementowane w

środowisku Dymola do dynamicznych symulacji ERS. Symulacje systemowe z wykorzystaniem danych pogodowych z trzech stref klimatycznych i profili ciepła odpadowego z trzech instalacji przemysłowych wykazały wzrost średniodobowego współczynnika wydajności (ang. COP) o maksymalnie 52% oraz mocy chłodniczej o maksymalnie 13% w porównaniu ze strumienicą o stałej geometrii. Układ wykorzystujący strumienice VGE wykazał największe korzyści pracując w gorącym klimacie o z dużą dobową amplitudą temperatury. Uogólniony model ROM zastosowano także do analizy układów ERS z innymi naturalnymi czynnikami chłodniczymi. Dla układu wykorzystującego propylen (R1270) uzyskano do 21% wyższą moc chłodniczą i wzrost COP o 10% w stosunku do układu wykorzystującego R290, podczas gdy mieszaniny R290 wykazały zbliżoną lub niższą efektywność, wskazując potrzebę rozszerzenia zakresu pracy opracowanych modeli ROM lub przeprojektowania strumienicy dla innych czynników. Wyniki pracy doktorskiej potwierdziły, że pojedyncza strumienica o zmiennej geometrii może zastąpić zestaw strumienic o stałej konstrukcji, zapewniając elastyczne i efektywne chłodzenie zasilane niskotemperaturowym ciepłem odpadowym o różnej zmienności temperatury.

Contents

List of symbols

Abbreviations

AR	Motive nozzle area ratio
CFD	Computational Fluid Dynamics
CPU	Central Processing Units
ERS	Ejector Refrigeration System
FGE	Fixed-geometry ejector
GHG	Greenhouse gases
GPU	Graphics Processing Units
GWP	Global Warming Potential
HC	Hydrocarbons
HEM	Homogeneous Equilibrium Model
HFC	Hydrofluorocarbons
HFO	Hydrofluoroolefins
MIL-100	Methal-organic framework
NXP	Nozzle exit position
POD	Proper orthogonal decompositon

R1150	Refrigerant name for ethylene
R1233zd(E)	Refrigerant name for trans-1-chloro-3,3,3-trifluoropropene
R1234yf	Refrigerant name for 2,3,3,3-tetrafluoropropene
R1234ze(E)	Refrigerant name for trans-1,3,3,3-tetrafluoropropene
R134a	Refrigerant name for 1,1,1,2-tetrafluoroethane
R152a	Refrigerant name for 1,1-difluoroethane
R170	Refrigerant name for ethane
R245fa	Refrigerant name for 1,1,1,3,3-pentafluoropropane
R290	Refrigerant name for propane
R32	Refrigerant name for difluoromethane
R41	Refrigerant name for fluromethane
R600	Refrigerant name for butane
R601	Refrigerant name for pentane
R602	Refrigerant name for hexane
RBF	Radial basis function
RE170	Refrigerant name for dimethyl ether
ROM	Reduced Order Model
SP	Spindle position
UDF	User-Defined Function
UDS	User-Defined Scalar
VGE	Variable-geometry ejector

Latin symbols

$\dot{G}$	Mass flux	kg/(m^{2}s)
$\dot{m}$	Mass flow rate	kg/s
$\dot{P}$	Power	W
$\dot{Q}$	Capacity	W

$\dot{S}_\phi$	Scalar source term	1/(m^{3}s)
$\dot{V}$	Volumetric flow rate	m^3/s
$\hat{a}$	Half-gap between plates	m
$\mathbf{B}$	Matrix of unknown coefficients of selected combination	-
$\mathbf{C}$	Positive semi-definite covariance matrix	-
$\mathbf{F}$	Matrix of interpolation functions	-
$\mathbf{f}^{\mathrm{a}}(k)$	Vector of interpolation functions	-
$\mathbf{U}$	Rectangular snapshot matrix	-
$\mathbf{u}^{\mathrm{a}}(k)$	Snapshot calculated for the arbitrary parameter k	-
$\mathbf{u}^{\mathrm{j}}$	Vector of the arbitrary snapshot	-
$\mathbf{U}^{\mathrm{T}}$	Transpose of snapshot matrix	-
$\mathbf{V}$	Modal matrix	-
A	Cross-sectional area	m^2
A_{i}	Area of the plate segment i	m^2
A_{eff}	Effective cross-sectional area of motive nozzle throat	m^2
B_{p}	Plate width	m
c	Specific heat	J/(kgK)
C_{nb}	Nucleate boiling correction factor	-
C_{Ra}	Roughness-effect coefficient	m
c_{ss}	Speed of sound	m/s
c_p	Specific heat at constant pressure	J/(kgK)
D_ω	Cross-diffusion term	m/s
d_{h}	Hydraulic diameter	m
$F(P^*)$	Reduced pressure effect function	-
G_ω	Generation of turbulent dissipation	kg/(ms^3)

G_K	Generation of turbulence kinetic energy due to mean velocity gradients	kg/(ms^3)
h	Specific enthalpy	J/kg
K	Turbulence kinetic energy	m^2/s^2
L	Half-width of a rectangular fin	m
L_p	Plate length	m
M	Half-length of a rectangular fin	m
m	Mass	kg
m_i^v	Mass of vapor in a cell i	kg
p	Pressure	Pa
P^*	Reduced pressure related to the fluid critical point	-
P_l	Horizontal distance between tubes in a tube bundle	m
P_t	Vertical distance between tubes in a tube bundle	m
p_lift	Pressure lift	-
q	Local heat flux	W/m^2
r	Radius	m
R_a	Arithmetic mean roughness of plate surface	m
r_s	Smoothing factor of interpolation functions	-
t	Time	s
V	Volume	m^3
v	Velocity	m/s
w	Mean velocity	m/s
x	Wave number	-
Y	Arbitrary performance parameter	-
Y_ω	Fluctuating dilatation dissipation of ω	kg/(ms^3)
Y_K	Fluctuating dilatation dissipation of K	kg/(ms^3)

AR	Ratio of effective throat area to the exit area of the motive nozzle	-
Bo	Boiling number	-
E	Total enthalpy	J/kg
K	Number of POD modes retained (truncation order)	-
k	Parameter approximated by RBF	-
k^i	Reference parameter for interpolation	-
Nu	Nusselt number	-
Pr	Prandtl number	-
Re	Reynolds number	-
Re_{eq}	Equivalent Reynolds number for two-phase flow	-
X	Vapor quality	-
X_{tt}	Martinelli parameter	-

Greek symbols

α_k^j	Unknown coefficient vector related to the snapshot generating parameters	-
β	Ratio of horizontal and vertical distances between the tubes in inline arrangement	
$\boldsymbol{\upsilon}$	Velocity vector	m/s
$\boldsymbol{\Phi}$	Matrix of orthogonal POD basis vectors	-
χ	Phase correction factor	-
ΔJ_{LV}	Latent heat of vaporisation	J/kg
Δp	Pressure decrease/increase	Pa
Δp_{loss}	Pump power losses	W
δ	Thickness	m
η	Efficiency	-
Γ	Effective diffusion coefficient	m^2/s

ι	Temperature parameter of the fin	-
κ	Polytropic constant	-
Λ	Wavelength	m
λ	Thermal conductivity	W/(mK)
λ_{i}	Eigenvalues vector	-
$\mathbf{\Lambda}$	Diagonal matrix of eigenvalues	-
$\mathbf{C}$	Covariance matrix	-
μ	Dynamic viscosity	kg/(ms)
ω	Turbulent dissipation term	W/kg
$\overline{\alpha}$	Matrix of unknown constant coefficients	-
$\overline{\Phi}^{\mathrm{k}}$	K-th element of the truncated orthogonal basis	-
ϕ	Mass entrainment ratio	-
ϕ^{i}	Orthogonal POD basis vector	-
ϕ_{fin}	Geometrical parameter of the fin	-
ϕ_S	Arbitrary scalar	-
Π	Pressure ratio	-
ψ	Ratio of vertical distances between the tubes in inline arrangement	
ρ	Density	kg/m^3
τ	Stress tensor	-
Θ	Gas volume fraction	-
φ	Plate inclination angle	$^\circ$
Ξ	Surface enlargement factor	-
ξ	Pressure drop (due to friction) coefficient	-
ζ	Friction factor	-
X	Vapor quality	-

Subscripts

$*$	Nozzle throat
0	Reference
cb	Convective boiling
cond	Condensation process
crit	Critical point of the fluid
diff	Diffuser
drive	Drive
eff	Effective
evap	Evaporator
fin	Fin
gap	Plate gap in a plate heat exchanger
gen	Generator
i	Cell index
in	Inlet, inner
L	Liquid phase
m	Mean value
mn	Motive nozzle
nb	Nucleate boiling
opt	optimum
out	Outlet, outer
pump	Pump
r	Refrigerant
rw	Between refrigerant and wall
sc	Subcooled region
sh	Superheated region

shaft	Shaft
sn	Suction nozzle
V	Vapor phase
valve	Expansion valve
w	Wall
wsf	Between wall and secondary fluid

CHAPTER 1

Introduction

1.1 Background

The global cooling demand is rapidly increasing across multiple sectors, driven by technological advancement, urbanization, and climate change. In commercial refrigeration, the transition to natural refrigerants has gained momentum after the introduction of regulations on the use of harmful refrigerants. These policies have been instrumental in accelerating the transition to more sustainable and cleaner refrigeration technologies. The Montreal Protocol [1] and its Kigali Amendment [2] mandated phase-outs of ozone-depleting and high global warming potential (GWP) refrigerants, driving the industry toward natural working fluids and thermally driven systems [3]. Europe's F-gas Regulations [4, 5] imposed leakage checks, maintenance protocols, and efficiency standards, while incentivizing the refrigerants that have the least effect on the environment through bans of harmful refrigerants and performance mandates in certain sectors [6]. The European installations of CO_2-only systems, which are the principal representative among the new-age refrigerants, more than doubled within a few years, reflecting regulatory and market pressures toward lower GWP solutions [7].

Within the sustainable energy transition, the socioeconomic factors em-

phasize the need for sustainable cooling systems. The rapid advancement of artificial intelligence and the overall digitization of society have led to data centers significantly contributing to operational expenditures and greenhouse gas (GHG) emissions [8], establishing a drive for technology improvement, competitive performance, and environmental sustainability [9]. Moreover, the global climate change intensifies cooling requirements, as higher ambient temperatures lead to increased energy use and further emissions. Conventional vapor-compression systems characterized by the drop of performance at ultra-low cooling temperatures and under variable loads, induce the innovations to the currently used technologies, such as the parallel compression [10], [11], cascade systems, and tri-generation architectures [12], [13], and the adoption of alternative refrigerants and their blends [14], [15], characterized by superior thermodynamic properties when applied in the novel refrigeration systems. Therefore, the refrigeration industry requires an integrated approach towards sustainable transition, which, based on current trends, is focused on the following aspects: the adoption of natural refrigerants, improvement of the performance of the vapor compression system, the deployment of thermally driven cycles, and waste heat utilization strategies.

1.2 Thermally driven refrigeration technology

Thermally driven refrigeration technologies represent a viable alternative to conventional electrically driven vapor compression systems, particularly in the context of mitigating GHG emissions and utilizing waste heat sources. Among the various thermally driven refrigeration technologies, the most important ones are absorption, adsorption, and ejector-based refrigeration cycles, which are specifically designed to exploit thermal energy from renewable sources or waste heat, in order to drive the cooling process. This heat harvesting methodology facilitates enhanced energy efficiency and promotes environmental sustainability [9]. In the following sections of this chapter, the review of the aforementioned thermally-driven refrigeration technologies, which are considered to be the most promising solutions according to the literature.

1.2.1 Absorption systems

The absorption refrigeration systems produce a cooling effect by utilizing the thermal energy source instead of the electrical one to drive the refrigeration process. The schematic layout of the simple absorption refrigeration system is presented in Figure 1.1.

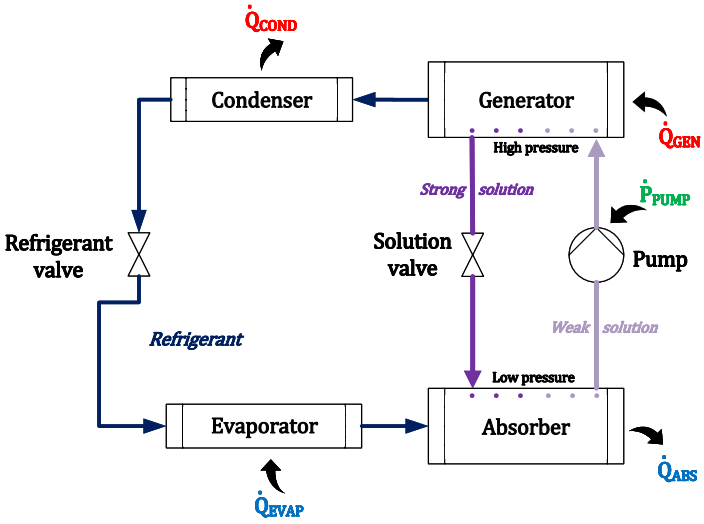

Figure 1.1: *Schematic layout of the single-effect absorption refrigeration system.*

In these systems, a refrigerant-absorbent working pair is utilized, allowing the refrigerant to evaporate at low pressure and absorb heat from the conditioned space, subsequently being absorbed by a liquid absorbent. The resulting weak concentration solution is pumped to a higher pressure and heated in a generator to desorb the refrigerant vapor, which then condenses and returns to the evaporator through an expansion device. The strong absorbent solution leaving the generator is throttled to the low pressure of the absorber, where the absorption of the refrigerant occurs, thereby closing the loop. The most commonly used working pairs include water-lithium bromide and ammonia-water. These systems are particularly advantageous with low-grade heat sources, such as waste heat, solar energy, or geothermal energy. Depending on the system configuration, absorption chillers can be classified into single-effect, double-effect, or triple-effect types. Single-effect chillers use one generator and one absorber, relying on a single-stage heat input to separate the refrigerant from the absorbent. In contrast, double-effect and triple-effect chillers include additional stages—typically with high- and low-temperature generators—that allow for partial recovery and reuse of the input heat. This staged utilization of energy improves thermal efficiency and enables higher coefficients of performance (COP), especially when higher temperature heat sources are available. Srikhirin et al. [16] analyzed different configurations of absorption chillers, and reported that

single-effect lithium bromide/water absorption chillers operating with the generator temperature in the range of 80 and 110°C can deliver the COP from 0.5 to 0.7, while the double-effect systems require the supplied temperature in the range of 120 and 150°C and achieve COP from 0.8 to 1.2. Triple-effect systems can reach COP in the range of 1.4 and 1.5 at the supplied temperature of 200 to 230°C. The authors also stated that the water/ammonia systems are suitable for sub-zero cooling at similar generator temperatures in the range of 120 and 150°C, but with the resulting COP around 0.5.

Nikbakhti et al. [17] in their analysis indicated that modern single-effect lithium bromide/water systems can achieve COP ranged from 0.65 to 0.78 at a relatively low heat source in the range of 75 and 95°C, while double-effect systems reach COP in the range of 1.25 and 1.48 at higher source temperatures, i.e. from 130 to 160°C. Moreover, the authors stated that the nanofluid additives and including direct generator-absorbent heat transfer improve the baseline COP value by 12 to 15%, making absorption systems viable for the low-grade heat recovery. However, the main drawback of the absorption systems is their relatively high conditioning space temperature, which in general ranges from 2 to 15°C, which limits their applicability.

In the experimental analysis of Garma et al. [18], the authors analyzed the diffusion absorption refrigerator using butane (R600) as refrigerant with low GWP, hydrocarbon n-nonane as absorbent, and helium as auxiliary gas. The system reached the maximal COP of 0.18 providing the cooling capacity of 58 W at the generator temperature of 140°C and -10°C at evaporator. The authors highlighted a key drawback of the absorption system, being the generator temperature limit. Beyond the limit, additional heating does not enhance the system cooling capacity but instead lowers the COP, reducing system efficiency.

Liang et al. [19] presented three absorption refrigeration systems designed to recover industrial waste heat from 150°C down to 60°C to provide cooling at -40°C, combining ammonia-water, lithium bromide-water, and absorption heat transformer cycles in different sequences. The systems achieve a maximum COP of 0.14 (ammonia-water first stage), 0.17 (lithium bromide-water second stage), and 0.18 (ammonia-water third stage with modified sequence), with the exergy efficiency of up to 0.19. Their heat source outlet temperatures at each stage are, for the ammonia-water first-stage system: from 136 to 146°C, from 71 to 101°C, and from 83 to 98°C; for the lithium bromide-water second-stage system: from 122 to 127°C, from 71 to 101°C, and from 83 to 98°C; and for the modified ammonia-water system: from 125 to 145°C, 60°C, and from 110 to 126°C. Compared to typical cascade systems, these designs recover 50% more waste heat and deliver higher

cooling capacity, with two configurations reducing the cost of unit cold energy by 8.7% and 15.2%. The study concludes that these approaches enable effective and economical production of very low-temperature cooling from low-grade industrial waste heat.

Su et al. [20] proposed an innovative lithium bromide-water absorption refrigeration system for cooling geothermal tunnels using the high-temperature water of the tunnel as the heat source. In that work, two cycle configurations were analyzed: single-effect absorption and two-stage absorption system. The maximal theoretical COP for the single-effect cycle was around 0.75 at the evaporation temperature of 5°C with the heat source water temperature of 85°C and the condensation temperature of 35°C, while the two-stage cycle achieved COP about 0.4 with the heat source temperature as low as 50°C and the same evaporation and condensation temperatures. In on-site testing under real tunnel conditions (heat source water temperature of 65°C, cooling water temperature of 30°C), the two-stage system delivered 12 kW of cooling capacity at a COP of 0.67, successfully reducing the restroom air temperature from 37°C to 25°C, with an ambient temperature of 36.5°C in 18 minutes. The study concluded that this approach enables effective, low-cost cooling for the tunnel construction by utilizing waste heat resources, significantly lowering the energy use and carbon dioxide emissions compared to the electric compression cooling.

In summary, absorption refrigeration systems provide an effective means to convert low-grade thermal energy into useful cooling, offering a sustainable alternative to conventional vapor-compression systems that rely on electricity. By using suitable refrigerant-absorbent pairs such as lithium bromide-water or ammonia-water, these systems can exploit waste heat, solar energy, or geothermal sources across a wide range of operating temperatures. Although their COP values generally remain lower than those of electric compression systems—especially at very low cooling temperatures, the ongoing improvements including advanced system designs, nanofluid additives, and heat recovery enhancements, continue to increase their efficiency and applicability. Despite challenges such as high generator temperature requirements and limits on achievable cooling temperatures, absorption systems remain a promising technology for sustainable cooling, particularly in the small-scale and low-cost applications.

1.2.2 Adsorption systems

The other type of thermally driven refrigeration system, closely related to the absorption system described above, is the adsorption system. Its schematic

representation is presented in Figure 1.2. As opposed to the previous system, the refrigerant vapor is adsorbed onto the surface of a solid material, such as silica gel, activated carbon, or zeolite, rather than being absorbed into a liquid.

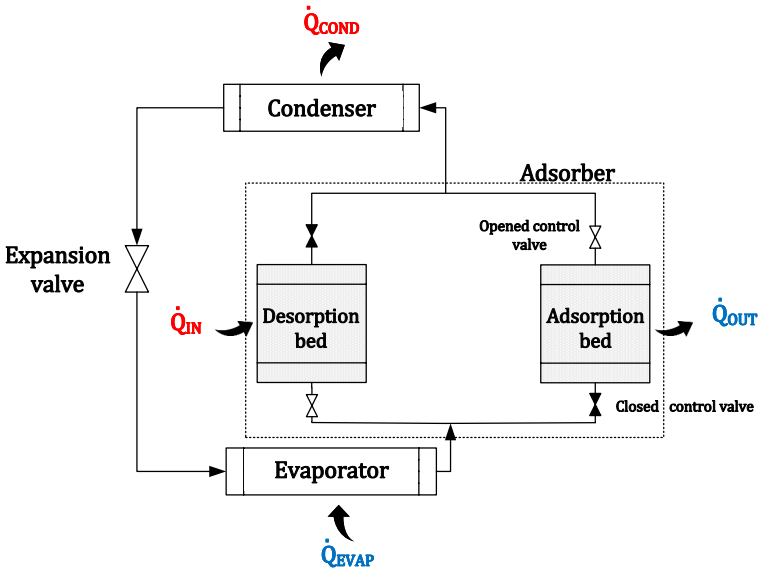

Figure 1.2: *Schematic layout of the two-bed adsorption refrigeration system.*

The cycle operates by alternately heating and cooling adsorber beds. During the desorption phase, heat input causes the adsorbent to release refrigerant vapor, which then condenses in the condenser and releases heat to the environment. The liquid refrigerant passes through an expansion valve into the evaporator, where it evaporates at low pressure, absorbing heat from the cooled space. In the adsorption phase, the vapor is adsorbed back into the cooled adsorbent bed, releasing heat to the environment. In the two-bed adsorption system presented in Figure 1.2, the process repeats cyclically between two beds to enable continuous cooling. This kind of system can operate at lower waste heat temperatures, but often at the expense of system complexity and size [21].

Verde et al. [22] presented the adsorption refrigeration system for automotive applications, in particular, an engine coolant-driven adsorption system utilizing heat at the temperature range of 80 to 90°C using silica gel/water pairs. In that study, the system provided the average cooling power range from 2.0 to 3.0 kW, and achieved the maximal COP of 0.6. The system provided the cooling effect at the chilled water temperature range of 5 to

10°C.

Cai et al. [23] tested numerically and experimentally an adsorption refrigeration system using silica gel-water as the working pair, incorporating different composite adsorbents with improved heat and mass transfer. The best-performing configuration uses a silica gel/MIL-100/copper foam composite. Under optimal conditions, i.e. the generator inlet temperature at 75°C, the condenser inlet temperature at 25°C, and the evaporator inlet temperature at 15°C, it achieved a maximum COP of 0.58 with the cooling capacity of 6.5 kW. The maximum cooling capacity point of 9.7 kW was reached when the evaporator inlet temperature was increased to 23°C, resulting in a COP value of 0.64. The study concludes that for this composite, the relative improvement for both cooling capacity and COP is 22% and 12.8%, respectively, when compared to a conventional silica gel-water system.

Xu et al. [24] tested experimentally a hybrid adsorption refrigeration system with desiccant-coated heat exchangers for ultra-low-grade heat utilization in the range from 50 to 80°C. The system achieved its highest COP of 0.67 under the hot water inlet temperature of 50°C, with the evaporator cooling water at 25°C and the air temperature of 32°C. The corresponding cooling capacity for this operating point was 3.3 kW. On the other hand, the maximum cooling capacity of 4.6 kW was reached with the heat source temperature of 80°C and at the same operating conditions at the evaporator and air heat exchanger, resulting in the COP value of 0.46. The study concludes that the hybrid system demonstrates superior adaptability and efficiency compared to conventional systems, offering a promising solution for recovering low-grade industrial and renewable heat.

Askalany et al. [25] proposed an adsorption desalination system using silica gel/water combined with two ejectors and internal heat recovery. The system working with the low-pressure evaporator at 7°C and the high-pressure evaporator at 25°C (for desalination) and with the regeneration (hot water inlet) temperature at 85°C. Under these conditions, the system without internal heat recovery achieved its highest COP of 1.64. With internal heat recovery, performance improved further, when working at 95°C of regeneration temperature, and the same evaporator temperatures, the system reached a maximum COP of 2.22.

Gado et al. [26] analyzed an adsorption-compression refrigeration system powered by renewable energy for providing the cold storage at -20°C, using a silica gel/water pair in the adsorption cycle and R134a in the compression cycle. The system was modeled for Egyptian climatic conditions using real temperature data. The vapor-compression system was driven by electricity from photovoltaic panels and a wind turbine, whereas the thermal

energy for the adsorption system was provided from photovoltaic panels and biomass gasification. The nominal system cooling capacity was 6 kW for the adsorption unit and 2.5 kW for the compression unit to maintain the cold room temperature. For the nominal conditions, the highest COP of the adsorption system was around 0.15 under the reduced condenser saturation temperature of 14°C, the source temperature of 60°C, and the evaporator temperature of -6°C. The overall cascade COP, which was able to maintain the desired cold room temperature at -20°C, was around 3.5. The study concluded that cascade integration reduces electric consumption by 42% when compared to a typical vapor compression system working at the same conditions, demonstrating technical and economic viability for off-grid cold storage in hot climates.

In summary, adsorption refrigeration systems represent a flexible and sustainable solution for converting low-grade thermal energy into cooling, leveraging solid adsorbents such as silica gel, activated carbon, or advanced composites. Compared to absorption systems, adsorption units can often operate at lower heat source temperatures, making them well-suited for waste heat and renewable energy integration. While their COP values are generally modest, usually between 0.4 and 0.7 for single-stage designs, recent research shows clear gains through new adsorbent materials, hybrid cycle configurations, or implementation of internal heat recovery. Adsorption systems can also be effectively integrated into cascade or hybrid setups with vapor-compression units to achieve low-temperature cooling while reducing electricity demand. The adsorption refrigeration offers promising pathways to enhance energy efficiency, lower emissions, and expand sustainable cooling access in diverse applications ranging from automotive and building air-conditioning to industrial and off-grid cold storage.

1.2.3 Ejector-based refrigeration systems

The next type of alternative refrigeration systems is the ejector refrigeration cycles, which represent another promising class of thermally driven systems. These cycles utilize the momentum of a high-pressure motive fluid, usually using recovered waste heat or renewable heat source, to entrain and compress a secondary fluid, thus achieving refrigeration without the need for mechanical compressors [3]. The performance of ejector systems is highly dependent on the thermophysical properties of the working fluid, as well as the design and control of the ejector itself. The use of natural refrigerants in these systems is particularly attractive due to their low global warming potential and favorable thermodynamic properties [7].

The integration of thermally driven refrigeration with waste heat recovery is especially relevant in industrial and commercial settings, where significant amounts of low-grade heat are often available. Roman and Hernandez [27] performed a theoretical analysis of the Ejector Refrigeration System (ERS) operating with natural refrigerants R290, R600, and R600a, as well as halocarbons R152a and R134a, using the simplified 1-D ejector model. Their simulations were conducted for a system with a unitary cooling capacity of 1 kW. Among the refrigerants analyzed, R290 achieved the best overall performance, reaching the COP value of 0.72 at the generator temperature of 95°C, the evaporator temperature of 10°C, and the condenser temperature of 30°C. The schematic layout of the basic ERS is presented in Figure 1.3. The ERS uses the thermal energy in the generator to produce vapor and drive the gas ejector, where it entrains and compresses vapor coming from the evaporator. The mixed flow is then condensed in the condenser. After condensation, part of the liquid is pumped to the generator pressure level, while the remaining portion is throttled through an expansion valve to the evaporator pressure.

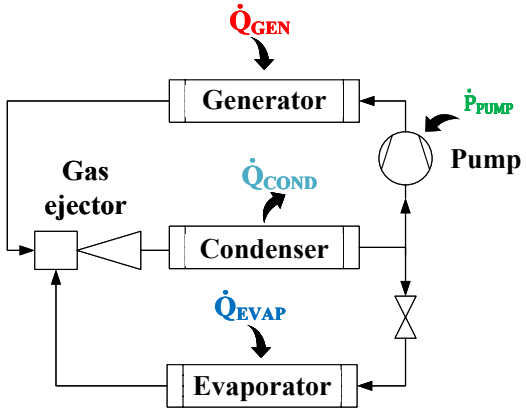

Figure 1.3: *Schematic layout of the Ejector Refrigeration System. Adapted and modified from Besagni et al. [3].*

Besagni et al. [28] performed a wide comparative performance analysis of ERS using four low-GWP refrigerants: R1234yf, R1234ze(E), R152a, and R290. The ERS was evaluated using a 1-D ejector model coupled with thermodynamic cycle simulations under varying operating conditions, specifically the generator temperature ranging from 70°C to 100°C, the

evaporator temperature from 0°C to 15°C, and the condenser temperature from 30°C to 40°C. Among all the analyzed refrigerants, the system running with R290 showed the most effective operation, achieving a high COP of 0.74 at the analyzed operating conditions. In the next work, Besagni et al. [29] proposed an optimized R290 Variable Geometry Ejector (VGE) with a spindle. The variable ejector concept enabled adjustment of the ejector primary nozzle throat area to match varying operating conditions, providing high ejector performance across a broader range of analyzed operating conditions. In this study, the authors reported the maximum COP of 0.85 at the same operating conditions as in the previous study [28], showing a notable performance improvement, and demonstrating an effective application of the R290 VGE. The authors emphasized that using a VGE, the system stability improves across a wide range of operating conditions, reduces the performance drops for the operating conditions away from the design point, and enhances integration with renewable heat sources like solar thermal collectors. The ability to adapt the ejector operation to varying generator temperatures enhances compatibility, thereby indicating the R290 VGE as a promising solution for sustainable cooling systems.

Eames et al. [30] performed experimental analysis of a jet-pump (ejector) refrigeration system with 3 heat exchangers and a layout similar to the ERS. Their system was operating with R245fa, achieving COP values from 0.25 to 0.7 and the evaporator cooling power reaching between 2 and 5 kW. The authors stated that the system performance was highly dependent on the nozzle geometry and operating conditions, and their optimization of nozzle exit position improved COP by up to 40%. These results demonstrate the suitability of R245fa for low-grade thermal-driven air conditioning applications.

Khaldi et al. [31] analyzed numerically a low-grade waste heat-driven ejector refrigeration system, comparing the phased-out R134a refrigerant and the low-GWP refrigerant R1234yf using a numerical model. They showed that for the analyzed system, the COP increases with the evaporator temperature, reaching about 0.72 for R134a and 0.65 for R1234yf at 13°C and 23 bar of the generator pressure. R134a generally showed higher COP at lower generator pressures, between 4.3% and 5.3% of improvement for 25 bar of the generator pressure, up to between 25% and 43% of advantage at the generator pressure equal to 9 bar. The study concludes that R1234yf is a viable, sustainable alternative under specific conditions, emphasizing the need for careful refrigerant selection and operating parameter optimization for efficient, low-GWP cooling.

Gagan et al. [9] conducted the first industrial-scale experimental assess-

ment of an R1233zd(E) ERS system utilizing low-temperature waste heat recovered from industrial air compressors. The system achieved the maximum cooling capacity of 45 kW and COP exceeding 0.22 under optimal conditions, i.e. the motive temperature of 68°C, and the condensation temperature below 28°C. However, the system performance decreased significantly with slight increases in the condenser saturation temperature, indicating a narrow off-design operational range. Compared to other low-GWP refrigerants such as R1234ze(E) or R600a, the studied R1233zd(E) demonstrated lower ejector component efficiency, but it benefits from being non-flammable. These results highlight the trade-offs between safety and efficiency and provide valuable data for model validation and design of ERS using new-generation refrigerants.

In the next work of Gagan et al. [32], the authors presented experimental validation of a bivalent hybrid ejector-compressor refrigeration system designed for chilled water production at 6/12°C using the low-GWP R1234ze(E). Their system combined a waste heat-driven ejector and a conventional compressor, with mode-switching governed by condensation pressure and ambient temperature. The results showed that the ejector mode achieved a COP of up to 0.30, and the cooling capacity ranged from 26 to 29 kW when driven by a thermal source at approximately 65°C. In contrast, the compressor mode achieved a COP of 0.7 under standard operating conditions. The system transitions between modes at a bivalent point corresponding to the condensation temperature of around 25°C, thereby optimizing performance across a wide range of environmental conditions. The study estimated up to 88% annual energy savings with the system mainly operating in the ejector mode, underscoring its applicability in air-conditioning for data centers, hospitals, or industrial facilities with access to a low-grade heat source.

Gil et al. [33] presented a performance analysis of a solar-powered ejector air-conditioning system using R601 and R602 as refrigerants. In their system, the generator was producing refrigerant vapor by absorbing the solar irradiation of around 800 W/m^2. For R601, the maximum overall COP was 0.42 at the evaporator temperature of 12°C, the condenser temperature of 30°C, and the generator temperature around 135°C, and the solar irradiance of 800 W/m^2, with the cooling capacity of about 1 kW. For n-hexane, the maximum COP reached 0.39 under similar evaporator and condenser conditions, but with a slightly higher generator temperature of 165°C. The resulting cooling capacity for the system running with hexane was approximately half of that of pentane. The authors conclude that reducing condenser temperature significantly improves system efficiency and that pentane yields

higher cooling capacity for the same system configuration, making it a better refrigerant choice under the examined conditions.

In summary, the ejector refrigeration systems offer an efficient way to turn low-grade waste heat or renewable thermal energy into cooling without mechanical compression. Their simplicity, low maintenance, and ability to use natural or low-GWP refrigerants make them attractive for sustainable cooling in industrial, commercial, and off-grid settings. While their COP remains moderate and the performance can be sensitive to operating conditions, advances in the ejector design and hybrid configurations are steadily improving efficiency and flexibility, supporting broader adoption for waste heat recovery and climate-friendly cooling applications.

1.2.4 Economic assessment of thermally driven refrigeration technologies

From an economic perspective, the thermally driven refrigeration technologies differ considerably in terms of efficiency expressed in COP, investment cost, and operational expenses. Among the technologies presented in the previous section, the ejector refrigeration systems stand out due to their mechanical simplicity and the ability to utilize a wide range of waste heat temperatures. Reported performance shows typical COP values in the range from 0.4 to 0.8 [9, 31–33], with specific energy costs as low as 0.04 € per kWh of cooling [34]. Their relatively low capital cost, around 1 100 € per kW of installed cooling capacity, combined with minimal maintenance requirements, further strengthens their competitiveness [35].

In contrast, the absorption systems, especially the double-effect lithium bromide-water (LiBr-H_2O) configurations, achieve higher thermodynamic efficiency, with COP values up to 1.5 for the favorable operating conditions [16–20]. However, this performance advantage comes at the expense of a more complex system architecture, requiring multiple heat exchangers and advanced control strategies. As a consequence, absorption units are characterized by higher capital investments, and their specific energy cost is typically in the range of 0.06-0.10€ per kWh of cooling [36]. They are therefore best suited to installations with continuous operation or abundant low-cost waste heat, where the higher upfront cost can be justified by improved long-term efficiency.

Adsorption refrigeration systems represent another alternative, often coupled with solar energy. These systems are characterized by very robust operation and the absence of moving parts, but their performance is comparatively lower, with COP values usually between 0.2 and 0.7 [22–26, 37].

Their specific energy cost is in the range from 0.06 to 0.12€ per kWh of cooling, and the capital costs are generally similar to, or higher than, those of ejector systems. The higher cost is primarily associated with the need for advanced adsorbent materials and extended heat transfer surfaces. These features make adsorption systems suitable for niche applications where durability and low maintenance outweigh efficiency considerations.

A comparative overview of the three technologies is summarized in Table 1.1.

Table 1.1: *Economic and performance benchmark of the thermally driven refrigeration system.*

System Type	COP	Specific energy cost, €/kWh cooling	Capital cost, €/kW cooling
Ejector refrigeration	0.4-0.8 [9, 31–33]	0.04 [34]	1,100 [34]
Absorption	0.1-1.5 [16–20]	0.06-0.10 [36]	Higher than ejector systems [36]
Adsorption [22–26, 37]	0.2-0.7	0.06-0.12 [34]	Similar or higher than ejector [34, 37]

In summary, ejector refrigeration systems emerge as the most economically attractive option for the utilization of low-temperature heat sources, owing to their low capital cost and competitive operating expenses. Absorption systems, while achieving higher efficiency, require substantially higher investment, which restricts their suitability to applications with stable, long-duration operation or abundant waste heat. Adsorption systems, on the other hand, are mainly selected for applications where robustness and low maintenance are prioritized, despite their relatively lower efficiency and higher specific costs.

1.3 Natural refrigerants for refrigeration systems

The effectiveness of ejector-based refrigeration systems is strongly influenced by the choice of working fluid. Moreover, the selection of refrigerants plays a critical role in the environmental sustainability of refrigeration and air-conditioning systems. In response to the significant climate impact of high GWP hydrofluorocarbons (HFCs), international policies and regional regulations have implemented the phase-down actions to reduce their use [5, 6]. These regulatory efforts have accelerated the transition

toward refrigerants with minimal environmental impact. Among the alternatives, hydrofluoroolefins (HFOs) have emerged as synthetic low-GWP solutions offering performance comparable to conventional HFCs. However, ongoing research is investigating their environmental influence, including potential degradation products that may pose ecological risks and their long-term effects are yet to be determined [38]. In contrast, natural refrigerants, including ammonia, carbon dioxide, hydrocarbons (HC), or water, are substances already present in the environment, with negligible or zero GWP and ODP. Their inherent environmental compatibility positions them as highly sustainable choices, aligning with the growing demand for conscious, climate-friendly refrigeration technologies. The main groups of refrigerants and their characteristics are presented in Table 1.2.

Table 1.2: *Main groups of refrigerants and their characteristics. Adapted and modified from [39].*

Name	GWP	ODP	Status
CFCs (e.g., R12)	High (ten thousands)	High (1)	Phased out
HCFCs (e.g., R22)	High (thousands)	Moderate (0.05)	Being phased out
HFCs (e.g., R134a, R404A)	High (hundreds to thousands)	Zero	Phasing down due to GWP concerns
HFOs (e.g., R1234yf)	Low (usually <1)	Zero	Emerging synthetic low-GWP refrigerants
Natural refrigerants (e.g., R717, R744, R290, R600, R600a)	Very low to zero	Zero	Increasing adoption for sustainability

Natural refrigerants have gained increasing attention in recent years as sustainable alternatives to synthetic fluids with high GWP. These naturally occurring substances in the environment include carbon dioxide (R744), ammonia (R717), hydrocarbons such as propane (R290), isobutane (R600a), butane (R600), or propylene (R1270). The appeal of these refrigerants lies primarily in their low or negligible impact on the environment, making them suitable candidates for long-term adoption in the context of increasingly rigorous environmental regulations. Each natural refrigerant comes with a unique set of advantages and challenges.

Ammonia boasts excellent thermodynamic performance and high energy efficiency, especially in industrial systems, but it is toxic and mildly

flammable. Carbon dioxide is non-toxic and non-flammable, yet it operates at significantly higher pressures, requiring more durable, and thus more expensive, components, and has a relatively high triple point temperature of -56.6°C, which can complicate operation in ultra-low-temperature applications [40]. Hydrocarbons in general provide favorable thermophysical properties and high energy efficiency, but their high flammability restricts their use in certain applications due to safety concerns. Water, while non-toxic and abundant, requires vacuum conditions for low-temperature refrigeration, which is not practical for compact or small-scale systems.

The characteristics of the most commonly used natural refrigerants in the refrigeration applications are summarized in Table 1.3.

Table 1.3: *Key characteristics of selected natural refrigerants. Adapted and modified from [41].*

Refrigerant	Class	Critical Point	Notes
R744	A1 (non-toxic, non-flammable)	31.0°C / 73.8 bar	High-pressure operation, transcritical cycles
R717	B2L (toxic, mildly flammable)	132.4°C / 113.6 bar	High efficiency, toxicity concern
R290	A3 (flammable)	96.7°C / 42.5 bar	Good efficiency, safety risk
R600a	A3 (flammable)	134.7°C / 36.3 bar	Used in domestic refrigeration
R600	A3 (flammable)	152.0°C / 38.0 bar	Similar to R600a, slightly different properties
R1270	A3 (flammable)	91.0°C / 45.6 bar	Similar to R290, higher volumetric capacity
RE170	A3 (flammable)	127.3°C / 53.4 bar	R290 replacement, better performance but more expensive

Recent advancements in natural refrigeration research focus on improving system designs to accommodate their specific challenges. For instance, transcritical R744 cycles are now commonly optimized using ejectors, internal heat exchangers, or parallel compression to overcome the efficiency penalty associated with high ambient temperatures [39,42]. Similarly, charge reduction strategies and advanced safety controls are being developed to broaden the application range of flammable hydrocarbons in commercial and industrial settings.

In the following subsections, the most recent technological advancements

for each of the commonly used natural refrigerants will be detailed. This includes a focused discussion of specific cycle modifications, safety strategies, and component innovations tailored to the unique properties and challenges of each refrigerant.

1.3.1 Ammonia

The R717 has been recognized for its favorable thermodynamic properties as a refrigerant, mainly the low molecular weight and high latent heat of vaporization, which contributes to its high COP in vapor compression cycles. This high latent heat allows for significant heat transfer with relatively small mass flow rates, which in turn reduces the required compressor work and enhances overall system efficiency [43]. The critical temperature and pressure of ammonia are well-suited for typical refrigeration applications, enabling efficient condensation and evaporation processes under a wide range of operating conditions.

Thermodynamic analysis of ammonia-based systems reveals that the its low boiling point facilitates efficient evaporation at low temperatures, which is essential for applications requiring deep cooling. On the other hand, the high critical temperature of ammonia (132.4°C) allows for effective heat rejection even at elevated ambient temperatures, minimizing the risk of performance degradation in warm climates [44]. Furthermore, the high volumetric refrigeration capacity of ammonia means that smaller compressors and heat exchangers can be used, reducing both capital and operational costs. From an energy efficiency perspective, ammonia systems often outperform synthetic refrigerants, particularly in large-scale industrial applications. In addition to its intrinsic thermodynamic advantages, ammonia compatibility with thermally driven and ejector-based refrigeration systems further enhances its appeal for sustainable applications. The integration of waste heat utilization, for example, can be effectively realized with ammonia due to its high temperature glide and favorable heat transfer properties. This enables the system designs not only to reduce primary energy consumption but also to capitalize on thermal energy that would otherwise be wasted, thereby improving overall exergy efficiency [43].

Ammonia-based refrigeration systems have found diverse application scenarios, particularly where large-scale, energy-efficient, and environmentally conscious cooling is required. One of the examples is the maritime transport, where ammonia starts to be predominantly utilized for refrigeration on vessels, especially in systems designed for long operational lifespans. The preference for ammonia in this context is driven by its natural origin, zero

ODP, and negligible GWP, making it a long-term solution for sustainable marine refrigeration. The adoption of ammonia in maritime applications is further motivated by the need to comply with increasingly stringent environmental regulations and the desire to future-proof investments in shipboard cooling infrastructure [6].

Hu et al. [45] in their experimental study demonstrated an ammonia-water absorption-compression refrigeration system driven by ocean thermal energy for maritime cold chain applications. The system achieved cooling capacities of 6.8 kW at the evaporation temperature of -24.5°C and 10.2 kW at -18°C. Under operating conditions of 30°C of warm surface seawater and 9°C of cold deep seawater, the highest measured COP reached 6.6, outperforming conventional vapor-compression systems. The optimal COP was observed at lower evaporation pressures, balancing reduced compressor power with effective thermal compression from ocean thermal gradients.

Yu et al. [46] performed an experimental study on absorption refrigeration systems for fishing ships comparing binary ammonia-water and ternary ammonia-water-lithium bromide working fluids under exhaust gas heat recovery conditions. The ternary system achieved a higher cooling capacity ranged from 6.3 to 9.2 kW and COP in the range of 0.18 and 0.24, compared to the cooling capacity range of 5.3 and 7.1 kW and the COP range of 0.14 and 0.23 for the binary system, with exhaust gas inlet temperatures from 245 to 350°C. Notably, the ternary system operated at higher evaporation temperatures, i.e. from -16.7 to -15.0°C, but benefited from a 16% reduction in rectifier heat exchange area and lower operating pressures, enhancing energy conversion efficiency and suitability for shipboard conditions.

In the study of Hu et al. [47], the authors investigated compression-assisted ammonia-water absorption refrigeration cycles for seafood freezing on offshore platforms, using ocean thermal energy with surface warm seawater at 29°C and deep cold seawater at 8°C. Under these design conditions, both high- and low-pressure compression-assisted configurations deliver 5 kW of the cooling capacity at -15°C of the evaporation temperature. The low-pressure cycle achieves a maximum exergy efficiency of 0.28 at an intermediate (absorption) pressure of 0.45 MPa, outperforming the high-pressure cycle 0.25 at 0.35 MPa. The primary energy rate ratio reaches up to 1.4 for the low-pressure configuration, demonstrating superior energy efficiency over conventional vapor compression systems under the given marine operating conditions.

Apart from maritime transport and storage, ammonia-based systems play also a critical role in industrial and commercial refrigeration, where their high thermodynamic efficiency and favorable environmental profile

are advantageous. These systems are particularly suitable for centralized installations, such as cold storage warehouses, food processing plants, and large-scale air conditioning, where the toxicity of ammonia can be managed through robust safety protocols and system design. It requires careful risk assessment and system containment, especially in applications where human exposure is possible. The use of ammonia in these scenarios is often justified by its superior heat transfer properties and the ability to achieve high COP, which results in lower operational costs and reduced primary energy consumption over the system lifetime [43] [44].

The study of Lu et al. [48] demonstrates an ammonia-water absorption refrigeration system with a two-stage evaporation and absorption process designed to better match industrial cooling processes with temperature-distributed heat loads. The system achieves a maximum COP of 0.8, which is 31% higher with comparison to the conventional single-stage system. The analyzed system conditions were -15°C of the evaporation temperature, 160°C of the generation temperature, 35°C of the condensation and absorption temperatures, and 0.7 MPa of intermediate pressure. At these conditions, the cooling capacity reached approximately 11.8 kW for LNG pre-cooling, with significantly improved internal heat recovery, and resulted in the 40% reduction in the exergy destruction during the cooling process.

Amaris et al. [49] analyzed an R717/R744 cascade refrigeration system for retail food applications. The authors stated that the proposed cascade delivers superior performance over R744 booster systems at higher ambient temperatures. For a supermarket application with a total cooling capacity of 145 kW (120 kW for medium temperature of -10°C and 25 kW for low temperature loads of -32°C), the cascade system achieves its highest COP at ambient temperatures above 16°C, outperforming both typical and parallel-compressor R744 booster configurations. The cascade system also maintains subcritical operation, with minimal sensitivity to ambient temperature, unlike the R744 booster systems whose COP declines sharply with temperature.

Chen et al. [50] analyzed ultra-low temperature cascade refrigeration systems using R717 as the high-temperature cycle refrigerant in the two-compression system, and R170, R41, or R1150 in the low-temperature cycle, targeting evaporation temperatures between -80 and -50°C with thee design cooling capacity of 9 kW. At the -60°C of the evaporation temperature and 40°C of the condensation temperature, the optimum COP of the R717/R170 cascade system, presenting the best performance among analyzed pairs, reached 1.15, outperforming the conventional R404A/R23 system by 13.3%. Over the entire studied range, the two-stage R717/R170 cascade refrigeration cycle exhibited COP improvements of up to 18.6% compared to R404A/R23.

Despite the advantages, the implementation of ammonia systems requires careful consideration not only for the safety measures, but also due to the corrosiveness of this refrigerant. Ammonia corrosiveness towards copper and its alloys mandates the exclusive use of resistant materials such as carbon steel or selected aluminum grades, increasing both capital cost and maintenance complexity. To mitigate these hazards, modern systems employ double-walled piping, hermetic components, advanced sensors for trace-level detection, and automated controls for real-time monitoring and shutdown under abnormal conditions [51]. Hybrid configurations, such as ammonia-water absorption cycles or ammonia blends with R744, reduce charge and leak potential, presenting a promising avenue for leveraging the ammonia efficiency and zero-GWP benefits without compromising safety [52]. Nevertheless, the thermodynamic superiority of ammonia remains a driving force behind its continued adoption in sustainable refrigeration, especially as regulatory pressure increases to phase out high-GWP refrigerants. The ongoing development of advanced control strategies and system designs, including the use of ejectors and heat recovery, is expected to further enhance the efficiency and sustainability of ammonia-based refrigeration technologies.

1.3.2 Carbon dioxide

The R744 refrigeration systems are increasingly recognized as a robust and environmentally sustainable alternative to conventional HFC-based technologies due to their ultra-low global warming potential and favorable thermophysical properties [7]. Due to the relatively low critical temperature (around 31°C), the R744 refrigeration system in majority operates in the transcritical parameters. In consequence, in transcritical cycles, heat rejection occurs above the critical pressure in a gas cooler instead of a condenser, requiring precise control of the gas cooler pressure to maintain high efficiency [53]. Recent numerical and experimental studies have shown that optimizing this pressure and integrating advanced components such as ejectors or expanders can significantly enhance system performance by recovering expansion work and reducing throttling losses [7]. However, the high operating pressures impose the demands on material strength and the risk of refrigerant leakage remains a key concern [6].

Design strategies, such as ground coupling or hybrid configurations that blend transcritical and subcritical features, have been explored to mitigate these challenges and adapt system performance to varying ambient conditions [54]. From an operational standpoint, the R744 systems benefit from

high volumetric cooling capacity and excellent heat transfer characteristics, enabling compact and efficient designs well-suited for both commercial and industrial applications. Safety considerations further favor R744 over flammable alternatives like hydrocarbons, expanding its applicability in large-scale or public installations [55].

The potential for waste heat recovery, especially in ejector-enhanced cycles, provides additional opportunities for energy savings and emissions reduction, strengthening the R744 role in sustainable refrigeration solutions. As an example, in a study of Sengupta et al. [56] the heat-driven multi-ejector chiller cycle using R717 was integrated with R744 supermarket refrigeration systems to improve performance via subcooling. The R717 refrigerant was identified as the most suitable natural refrigerant for the chiller due to its high COP (up to 0.5 at the generator-to-condenser pressure ratio from 2.5 to 4.0) and superior waste-heat utilization at the generator temperature up to 120°C. The highest cooling capacity of the combined system was 56.7 kW at 47°C of the ambient temperature with the R744 operating in parallel compression configuration and with multi-ejectors module. The maximum COP improvement for the combined system over a standard parallel compression unit was observed between 28 and 40°C of the ambient temperature, achieving the COP increase from 4.2 to 24%. The authors highlighted the suitability of the proposed combined system for warm and hot climates.

In the work of Boupda et al. [57], the solar-assisted transcritical R744 refrigeration system that integrates an ejector and a Brayton subcycle to improve energy efficiency was analyzed. In the proposed design, solar energy is collected by a parabolic trough concentrator and used to heat a fraction of the circulating R744 working fluid. This vapor generated in the concentrator expands in a turbine, generating mechanical power that reduces the compressor electrical demand. Simulations of the combined refrigeration system with Brayton cycle at the evaporation temperature of -10°C, the gas cooler temperature of 40°C, and with the solar irradiation of 300 W/m^2 demonstrated the cooling capacity of approximately 15 kW and the corresponding COP value of 2.9, marking a 30% improvement over the conventional ejector cycle. Moreover, by increasing the solar irradiation to 1000 W/m^2, the system COP can go beyond 2.9 and achieve energy savings up to 43%, while the cooling capacity remains stable around 15 kW.

The study of Ávila-Gutiérrez et al. [58] presented a transcritical R744 refrigeration system combined with a dedicated ejector subcooling cycle with two hydrocarbon refrigerants analyzed, R290 and R600a. Heat recovery in the system occurs by utilizing the high-temperature discharge of the R744

compressor to drive the ERS running on hydrocarbons. This ERS system provides subcooling at the R744 gas cooler outlet without additional compressor work, and in consequence, improving the overall system COP. Under optimum conditions (the evaporation temperature of -35°C, the ambient temperature in the range of 25 and 35°C and the generator temperature in the range of 60 and 92°C for R290), the combined system achieved COP improvements of on average 20% over the baseline R744 cycle, with maximum cooling capacity up to 6.4 kW in the test facility. The highest subcooling degrees and COP enhancements were achieved for R290 at higher generator temperatures approaching 90°C, due to its lower latent heat enabling greater heat absorption in the dedicated ejector subcooling at the generator.

Despite the remaining challenges in system integration, component standardization, and intelligent control development of the transcritical cycle, the combination of low environmental impact, non-toxicity and non-flammability, and competitive efficiency makes the R744 a leading candidate for next-generation refrigeration systems aligned with global climate targets [7], [6], [54].

1.3.3 Hydrocarbons

As far as the HC refrigerants are concerned, they are increasingly recognized as efficient, environmental friendly alternatives to synthetic refrigerants, offering very low GWP and zero ODP [44]. Their high flammability restricts their applications to small-scale domestic and commercial units due to the charge limits imposed for safety reasons [59]. The favorable thermophysical properties such as high latent heat of vaporization, low viscosity, and strong heat transfer characteristics enable high COP and compact system designs, which are particularly advantageous in small- to medium-capacity refrigeration and air conditioning applications [60].

These attributes reduce not only refrigerant charge requirements but also compressor work and energy consumption, enhancing economic viability and environmental sustainability. However, their flammability poses a critical challenge, necessitating implementation of the risk mitigation strategies and compliance with international safety standards, which define charge limits, safety classifications, and equipment design criteria [61]. Engineering measures like minimizing refrigerant charge, employing high-efficiency heat exchangers, integrating leak detection and enhanced ventilation, and implementing automatic shut-off valves, are crucial to reduce ignition risks [62]. Studies show that site-specific factors, including ambient temperature and humidity, can significantly influence flammability boundaries, emphasizing

the need for dynamic safety assessments and rigorous validation through realistic leak and ignition tests [60]. Procedural safeguards, such as comprehensive training for technicians, routine maintenance, and clear emergency protocols, further strengthen the safety profile of hydrocarbon systems. Regulatory trends driven by environmental frameworks are accelerating the shift towards low-GWP refrigerants, reinforcing the hydrocarbons relevance in sustainable cooling technologies [62].

As far as the hydrocarbon-based refrigeration systems are concerned, in the numerical study of de Carvalho et al. [63] the authors compared the conventional vapor compression cycle and a cycle with a flash tank vapor injection using hydrocarbon refrigerant blends. The latter differs from a conventional cycle by the addition of a second compression stage and a flash tank that allows vapor injection between compression stages. The flash tank vapor injection cycle consistently showed higher COP than the conventional cycle, with improvements ranging from 4 to 36% depending on the mixture. The optimum result was achieved with a R290/R600 mixture (60/40% mass), yielding a COP of 4.9 in the flash tank injection cycle versus 4.5 in the vapor injection cycle, along with lower refrigerant mass flow requirements. These findings suggest that HC-based mixed refrigerants can improve system efficiency and reduce the refrigerant charge, offering advantages over typical single-stage compression systems despite higher system complexity. When carefully engineered and operated, hydrocarbon-based systems can achieve performance comparable to or exceeding those of traditional refrigerants and other natural options, such as R744 or R717, especially when integrated in hybrid or cascade cycles optimized for various temperature levels and load conditions [55].

In the study performed by Lee and Su [64], the authors analyzed the small-scale domestic vapor-compression refrigeration system utilizing R600a. Their system was divided into two cooled compartments, devoted to cold storage and freezing of products. The evaporator temperatures for the cold storage and freezing applications were tested in the ranges of -14°C to -4°C and 0°C to 8°C, respectively. The cooling capacity for both applications reached between 0.3 to 0.8 kW. The authors reported that the system reached the COP between 1.2 and 4.5 in the cold storage application and between 0.8 and 3.5 in the freezing application.

Joudi and Al-Amir [65] tested split-type air-conditioning units with R22 and R290 operating with the relatively high ambient air temperature between 35 and 55°C. The air inside the conditioned compartment was maintained at 25°C dry bulb temperature for all tests. For the analyzed range of ambient temperature, the R290 system cooling capacity reached between 6.3 to 7.8,

whereas the reported system COP was from 2.5 to 3.1. On the other hand, system with R22 reached better cooling capacity, showing values between 2.9 to 3.2, but at the expense of lower COP, reaching between 2.2 and 2.6.

Faruque et al. [66] performed a thermodynamic analysis of a three-stage cascade refrigeration system using hydrocarbon refrigerants for ultra-low-temperature applications. The study employed pure hydrocarbon refrigerants including m-Xylene in the high-temperature circuit, 1-butene in the low-temperature circuit, and Heptane, Toluene, Trans-2-butene, or Cis-2-butene in the mid-temperature circuit. For a nominal fixed 10 kW of cooling load, the system achieved maximum COP values ranging from 0.43 at -120°C of the evaporator temperature to 0.70 at -90°C of the evaporator temperature with exergy efficiency of up to 55.1%. Hydrocarbon refrigerant pairs enabled effective operation at reported very low temperatures without compromising thermodynamic performance compared to conventional single-stage vapor compression systems, which are infeasible at such low temperatures due to excessive pressure ratios. The study demonstrates that hydrocarbons can be viable, environmentally friendly alternatives in multi-stage cascade systems for ultra-low-temperature refrigeration.

In summary, hydrocarbons combine high energy efficiency and environmental advantages with manageable safety challenges, provided that modern design practices, robust engineering controls, and stringent operational protocols are consistently applied.

1.3.4 Hydrocarbon blends

Blends and mixtures of hydrocarbon refrigerants have gained attraction as a flexible strategy to tailor thermophysical properties and operational performance, while addressing safety concerns inherent to pure hydrocarbons [55]. By combining carefully selected components, these mixtures can balance high latent heat, favorable thermal conductivity, and low viscosity with adjusted flammability, allowing designers to optimize efficiency and safety simultaneously. Zeotropic mixtures, particularly those incorporating dimethyl-ether (RE170) with hydrocarbons, have demonstrated promising performance improvements [67, 68].

Calleja-Anta et al. [68] reported that such blends can outperform traditional single-component hydrocarbons in small-capacity refrigeration systems. In their recent study, the authors evaluated binary mixtures of hydrocarbons as alternatives to R600a in a commercial cooler, both theoretically and experimentally. Three blends, namely R1234ze(E)/R600 (8/92% mass), R152a/R600 (8/92% mass), and R32/R600 (2/98% mass)

were tested. The first two mixtures showed clear improvements over pure R600a, achieving reductions in the energy consumption of 2.7 and 5.0%, respectively, while exhibiting the estimated COP increases of 11 and 13%, respectively. By contrast, the R32/R600 blend offered only a marginal COP improvement of around 5%. The study identifies R152a/R600 (8/92% mass) as the best-performing candidate, offering the largest energy savings with comparable operating pressures and acceptable thermodynamic properties for drop-in use in the existing equipment.

Hydrocarbon blends generally maintain the intrinsic benefits of pure HCs high latent heat and superior heat transfer, while offering opportunities to mitigate flammability risks through compositional adjustment [55]. Martinez-Angeles et al. [11] evaluated R744-doped blends with R152a, R1234yf, R1234ze(E), and R1233zd(E) in single-stage refrigeration cycles with internal heat exchangers and parallel compression. Adding small amounts of 5 to 10% mass of these additives generally improves COP over pure R744, especially at higher ambient temperatures above 20°C. The COP improvements in the cycle with internal heat exchanger reached a maximum of 7.7% for R744/R1233zd(E) at the ambient temperature of 31°C, while the parallel compression cycle shows even larger improvements, up to 12% at the same mixture composition and 27°C of the ambient temperature, attributed to the beneficial effects of fractionation. However, these improvements come with a significant reduction of up to 25% in the volumetric cooling capacity, and large effective temperature glides above >10 K, which complicate heat exchanger design. Moreover, the authors stated that R744 doping shifts the cycle from transcritical to subcritical operation at high ambient temperatures, reducing operating pressures and enabling better efficiency in simpler system architectures, although experimental validation remains necessary.

In the study of Sobieraj [69], a novel wet sublimation cascade refrigeration cycle was tested using low-GWP binary mixtures of R744 with R290 and R32 as solvents for dry ice. The tested blends consisted of an R744/R32 mixture with a 67/33 mass ratio and an R744/R290 mixture with a 30/70 ratio. Both blends achieved ultra-low temperatures near -72°C, but the R744/R32 mixture consistently delivered higher heat transfer coefficients (from 1.9 to 3.5 kW/(m^2·K)) comparing to the R744/R290 mixture (from 1.4 to 2.4 kW/(m^2·K)) and lower wall superheat due to its higher partial pressure and better thermophysical properties. The R744/R32 blend emerged as the better candidate for low-temperature applications, offering improved heat transfer and system efficiency over typical hydrocarbon mixtures, while mitigating flammability concerns at appropriate R744 concentrations.

The synergy of hydrocarbons with other natural refrigerants, such as R744, is also being explored to leverage complementary advantages, for example adding R744 can moderate discharge temperatures and alter volumetric heating capacity, which benefits compressor reliability and system lifespan [70]. Nonetheless, trade-offs may arise, including potential reductions in the heating or cooling capacity, which must be balanced through careful blend formulation and advanced system control.

In summary, hydrocarbons and their blends represent an important step forward in sustainable refrigeration technology, combining the thermodynamic strengths of individual components, while mitigating drawbacks through appropriate mixing ratios and robust control. Continued research into mixture behavior, practical validation under real-world conditions, and standardization efforts will be vital for fully realizing their potential in the global shift towards natural refrigerants.

1.4 Waste heat utilization in thermally driven refrigeration systems

Given the significant potential of natural refrigeration application for the thermally-driven systems, it emerges as a promising technology for harnessing the waste heat sources. The waste heat recovery is a key strategy for decarbonization of industrial systems of different kinds, improving their energy efficiency, lowering operational costs, generating savings or other sources of profits. Particularly in refrigeration technology, utilization of waste heat as a driving source enables thermally driven cycles to replace or supplement electrically powered vapor compression systems. Moreover, such an approach reduces primary energy consumption and the refrigeration associated emissions resulting from system operation or leakages [71]. The waste heat is typically referred to a by-product of industrial processes, arising from chemical reactions, fuel combustion, or mechanical work, and is often discharged unused into the environment despite containing valuable thermal energy [72].

1.4.1 Potential of industrial waste heat recovery

The classification of industrial waste heat levels is fundamental for the effective integration of thermally driven refrigeration systems, as the temperature and quality of waste heat directly influence the selection and performance of cooling technologies. Waste heat in industrial processes is typically characterized by its temperature, type of medium, and pressure, with the

most important one being the temperature, which determines the thermodynamical potential and helps with selecting appropriate technology that can be used to recover it. The industrial waste heat in the European Union in terms of temperature is categorized into three main temperature levels: low (<200°C), medium (from 200 to 500°C), and high (>500°C). Approximately one-third of the total technically recoverable waste heat potential (estimated at 300 TWh/year) is available in the low-temperature category below 200°C. Typical sources include exhaust gases, drying, and preheating processes in sectors such as food, paper, chemicals and food industry, and by-product of machines operation that require cooling for safe operation. The medium-temperature waste heat (around 78 TWh/year) comes largely from pulp, paper, iron and steel processes, while high-temperature (>500°C) waste heat (around 124 TWh/year) is mostly from the steel, cement, and chemical industries [73].

In recent years, researchers have extensively investigated waste heat recovery, with a predominant focus on low-temperature sources in the range of 100 to 200°C due to their superior thermal and economic significance. Within the low-grade category, however, an important distinction is often made to isolate a subset of even lower temperature sources, usually referred to as ultra-low grade, which is below <100°C. This distinction highlights significantly different thermodynamic challenges involved in recovering heat at such low temperatures and having small temperature differentials, that reduce the driving force for heat transfer and therefore limits the application of thermally driven technologies [73]. In the study of Luberti et al. [74], the authors performed an estimate of the waste heat available in European Union based on the data for the year 2018. The authors stated that the largest fraction of waste heat in the European Union is available at temperatures between 40 and 60°C coming from the power generation sector, being around 6441.4 $\cdot 10^6$ GJ. It corresponds to the 73% of the waste heat fraction at temperatures below 100°C released by the combined industrial and power generation sectors, and around 97% for power generation only [74]. Moreover, it is predicted that the amount of ultra low-temperature waste heat in transportation, construction and residential sectors, not taken into account in the previous analysis, has also a huge potential [75], and the overall amount of waste heat at this temperature will be identified, and the potential to harvest it will steadily grow in the next years [74].

Despite its modest thermo-economic value, ultra-low grade waste heat is widely available, offering great opportunity for enhancing energy efficiency and reducing environmental impact through integrated waste heat recovery systems [76]. Common sources of ultra-low grade waste heat in industrial

and commercial settings include condensate from steam systems (50-90°C), warm cooling water from chillers or condensers (25-40°C), low-temperature flue gases after primary heat recovery stages (60-100°C), heat, ventilation and air-conditioning systems exhaust air (20-30°C), heat rejected from refrigeration and heat pump condensers (30-50°C), and industrial process by-products such as waste water from food and beverage production (30-60°C) [72].

1.4.2 Refrigeration technology for waste heat recovery

Unlike conventional vapor-compression systems that rely entirely on electrical work input, the waste-heat driven systems harness heat sources such as industrial waste heat, vehicle exhaust gases, district heating networks, or solar thermal energy to drive refrigeration cycles. They are designed to convert stream of industrial processes byproducts, being the thermal energy, into useful cooling potential. Technologies in this category include adsorption, absorption, ejector-based, and hybrid refrigeration systems, each with unique thermodynamic principles, design pros and cons, and suitable temperature ranges. The following review summarizes recent research and experimental studies on thermally driven refrigeration for waste heat recovery, highlighting their operational characteristics, advantages, limitations, and potential applications across stationary and mobile contexts.

Zhang [77] performed experimental tests of intermittent adsorption cooling system to recover diesel engine exhaust heat for vehicle air conditioning, using zeolite 13X-water as the working pair. The system used a finned double-tube adsorber that was heated alternately by exhaust gas of temperature around 310°C and cooled by ambient air of around 25°C, with evaporator and condenser temperatures of 10°C and 45°C, respectively. The maximum measured COP reached under these conditions was 0.4 with the specific cooling power of 25.7 W/kg of adsorbent. The study concluded that while such systems can meet waste-heat utilization requirements, their low SCP makes them inefficient for practical mobile applications without further improvements in adsorbent heat transfer properties.

Chaudhari and Desai [78] performed an experimental study of a single-bed adsorption refrigeration system using an activated charcoal-ammonia working pair driven by waste heat energy. The system features a shell-and-tube adsorption bed heated to 120°C with cooling water at 30°C. The maximum measured cooling capacity was 50.6 W, and the highest COP achieved was 0.10. The ammonia adsorption capacity reached up to 0.22 W/kg of the activated charcoal. Their environmentally friendly system can

effectively use low-grade waste heat for small-scale cold storage. It is a promising, sustainable alternative to conventional refrigeration systems, with potential improvements via multi-bed designs and heat recovery to enhance performance.

Gagan et al. [32] in their experimental study presented the performance of a novel bivalent hybrid ejector-compressor refrigeration system designed for air-conditioning applications using low-grade heat sources such as waste heat or district heating. The system achieved a COP of approximately 0.30 in the ejector-driven mode (with cooling capacity between 23 and 26 kW) and an average COP of 4.70 in the compressor-driven mode, with seamless mode-switching at a condensation temperature of 25°C. The results indicate significant energy savings potential of up to 80% under certain scenarios by substituting compressor work with heat-driven ejector operation for majority of the year, highlighting the hybrid system promise for reducing electricity demand in comparison to conventional vapor-compression refrigeration, especially in moderate climates with district heating infrastructure.

Zadeh and Chung [79] analyzed the adsorption refrigeration systems, in which the system is powered by recovering the engine coolant or exhaust gases heat for the internal combustion engines, and the heat from battery cooling system for the electric vehicles. The authors reported that the adsorption system can provide a cooling power ranged from 0.4 to 3.6 kW and achieve COP values from 0.2 to 1.4, depending on the materials used. The activated carbon/ethanol pairs achieve the maximum specific cooling power of 488 W/kg, among all analyzed material pairs.

Fernandes et al. [80] analyzed the current state of art of solar-powered adsorption refrigeration systems designed for cooling, air-conditioning, and ice-making, especially in remote areas where access to electricity is limited. The analyzed flat-plate solar collectors operating with activated carbon-methanol pairs are relatively simple and cost-effective. However, their performance remains limited, with low COP values typically ranging between 0.1 and 0.3, and relatively low cooling capacities depending on the size of solar collectors that have not significantly improved over recent decades. Scaling up their size to increase their cooling capacity makes them economically unviable. Despite these limitations, solar adsorption systems are great representatives of sustainable refrigeration by utilizing free solar energy without the need for conventional energy inputs, making them an environmentally attractive option in suitable climates.

Huang et al. [81] proposed a compression-assisted absorption refrigeration-heating system designed to recover low-grade waste heat from liquid-cooled data centers, providing simultaneous chilled water for cooling and hot water

for domestic use. The system uses R152a/1-hexyl-3-methylimidazolium bis(trifluoromethylsulfonyl)imide as the working pair, selected for its superior performance in both refrigeration and heating sub-cycles. Under waste heat source at 60°C, cooling water for condenser at 24°C, and the saturation evaporator temperature of 10°C, the system achieved the maximum COP of 0.5 with the cooling capacity of 4.3 kW for air-conditioning and 1.4 kW heating capacity for hot water production at 70°C. The analysis demonstrates that increasing the compression ratio lowers the minimum required generation temperature from 52°C to 27.2°C as compression ratio increases from 1.1 to 2.0. The study concludes that the proposed system can fully meet data center air-conditioning needs while recovering waste heat for domestic hot water supply, offering a promising method for low-grade waste heat utilization despite challenges such as high equipment costs and the price of ionic liquid working pairs.

In summary, adsorption systems demonstrate particular suitability for low-temperature waste heat sources, offering environmental benefits through the use of natural refrigerant pairs, although their performance is often limited by low specific cooling powers and COP values. Absorption systems can deliver higher cooling capacities and are commercially mature in some applications, but their efficiency and feasibility depend on careful selection of working fluids and source temperatures. Ejector-based and hybrid ejector-compressor systems offer an effective means to integrate waste heat recovery with conventional refrigeration, enabling flexible operation and substantial electricity savings. Despite technical challenges such as low COP, limited heat transfer rates, and system costs, advances in materials science, system integration, and hybrid configurations continue to expand the potential of these technologies. Overall, thermally driven refrigeration offers an environmentally sustainable strategy to enhance energy efficiency, reduce fossil fuel dependence, and support the decarbonization of cooling demand in both stationary and mobile applications.

1.5 Fundamentals of thermally driven ejector refrigeration system for waste heat recovery

Thermally driven refrigeration technologies represent a key opportunity for the effective recovery and utilization of industrial waste heat, particularly low- and medium-grade sources that are challenging to exploit for power generation. As highlighted in the preceding literature review, significant technical potential for converting waste heat into useful cooling is available across diverse industrial contexts, supported by a range of mature and

emerging technologies. Absorption and adsorption systems, for example, are well-established for low-grade heat recovery but often involve specific working pairs, complex designs, and higher capital costs, limiting their scalability in certain applications.

Among the available options, ejector-based refrigeration cycles have emerged as especially promising solutions for waste heat recovery [30, 33, 56]. They leverage well-understood ejector technology without requiring new working mediums or fundamentally novel components, making them comparatively easy to integrate with existing systems. Their simplicity, absence of moving parts in the expansion stage, and suitability for a wide range of conventional refrigerants enable straightforward scaling from small to medium capacities [3]. In the following sections, the principles of ejector operation and recent advancements in the ejector technology will be discussed to provide a comprehensive understanding of their suitability for waste heat-driven refrigeration applications. Next, a schematic layout of the ejector refrigeration system, along with the derivation and presentation of the main equations used to evaluate key system performance parameters.

1.5.1 Ejector fundamentals

An ejector is a fluid dynamics device that utilizes the momentum transfer between a high-pressure primary fluid and a lower-pressure secondary fluid to achieve fluid entrainment, mixing, and subsequent pressure recovery [82]. Its fundamental operation is based on converting the pressure energy of the motive or driving flow into kinetic energy through a converging-diverging nozzle, creating a suction effect at the nozzle exit that entrains the secondary fluid. In the case of a supersonic ejector, the high-temperature primary fluid is accelerated to supersonic conditions in the motive converging-diverging nozzle and then expanded in the mixing chamber, where it entrains the low-pressure secondary flow coming from the suction nozzle. The two streams are mixed in the mixing section and subsequently compressed in the diffuser to an intermediate pressure, enabling effective energy transfer and pressure recovery in a relatively simple, compact device. The geometry of a typical ejector can be divided into the motive nozzle, suction chamber, mixing chamber, and diffuser as schematically presented in Figure 1.4. Moreover, the geometry and relative positioning of these components are critical, as they directly influence the entrainment ratio, pressure recovery, and overall efficiency of the ejector [83].

Ejectors can be categorized according to both the type of working fluid and the method of capacity modulation. In terms of working medium, ejec-

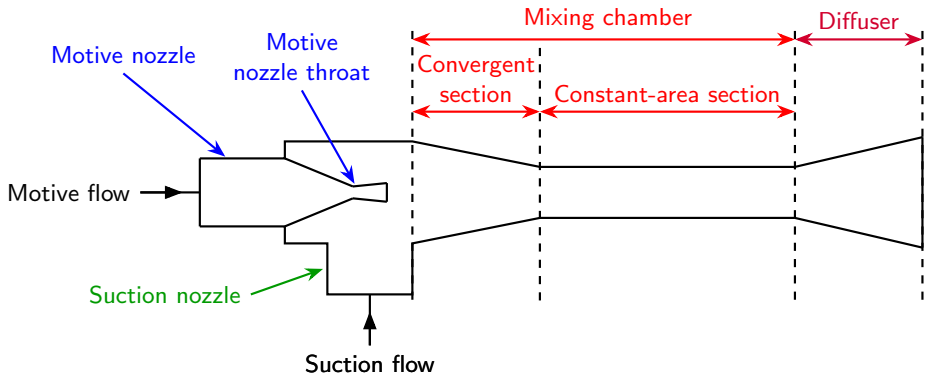

Figure 1.4: *Schematic layout of the fixed-geometry ejector with representation of its main sections.*

tors are typically classified as gas ejectors (commonly used in refrigeration and heating, cooling, and air-conditioning applications), liquid ejectors (utilized in fluid transport and mixing), and two-phase ejectors (employed in processes involving phase change, such as transcritical refrigeration cycles) [84]. Another fundamental classification distinguishes between the geometry of ejectors, so the fixed-type ejectors and variable-geometry ejectors [85]. The first group of ejectors have a constant internal geometry, as illustrated in Figure 1.5 (a), which makes them robust and simple, but limits their efficiency under varying operating conditions. In contrast, variable-type ejector schematically presented in Figure 1.5 (b), employs the mechanical adjustments to modify the ejector geometry, mainly by introducing a spindle (needle) to the motive nozzle and thereby changing the nozzle area ratio, so the ratio of nozzle outlet area to the nozzle throat area. It allows the real-time adaptation to changing load and boundary conditions. This capability of control is particularly advantageous in refrigeration systems subject to dynamic variations of system operating conditions, providing enhanced control over the entrainment ratio and overall system performance.

The operation of the ejector throughout the literature is expressed using a several performance parameters, with the most important one being the mass entrainment ratio, describing the ratio of the entrained (suction nozzle) mass flow rate to the motive nozzle mass flow rate:

$$\phi = \frac{\dot{m}_{\text{sn,in}}}{\dot{m}_{\text{mn,in}}} \tag{1.1}$$

where ϕ is the mass entrainment ratio, $\dot{m}$ is the mass flow rate, and the

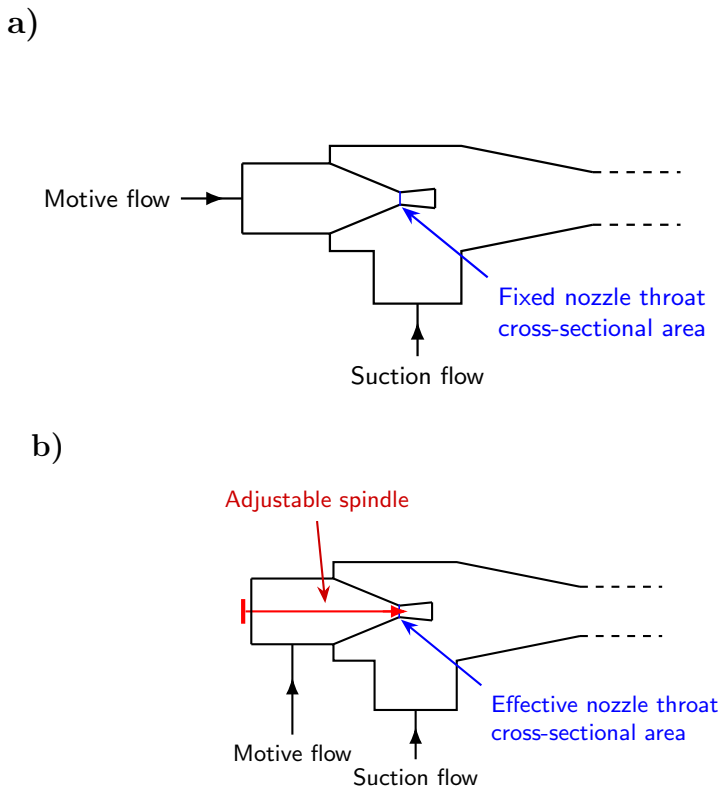

Figure 1.5: *Schematic representation of: a) fixed- and b) variable-geometry ejector.*

subscripts mn, sn and in denote the ejector motive nozzle, the ejector suction nozzle and the inlet, respectively.

To better characterize the operational regime of the ejector under specific conditions, the pressure difference of between the ejector (diffuser) outlet and suction nozzle inlet is utilized. It is helpful for determining the mode of operation when plotted against the mass entrainment ratio:

$$p_{\text{lift}} = p_{\text{diff,out}} - p_{\text{sn,in}} \tag{1.2}$$

where p_{lift} is the pressure lift, p is the pressure, and the subscripts diff and out denote the ejector diffuser and the outlet, respectively.

Another parameter defining the pressure conditions at which the ejector operates is the pressure ratio, being the ratio of the diffuser outlet pressure to the suction nozzle inlet pressure:

$$\Pi = \frac{p_{\text{diff,out}}}{p_{\text{sn,in}}} \tag{1.3}$$

where Π is the pressure ratio.

The ejector operation depends on the fluid dynamics phenomena that occur within the device and have an impact on its performance. The schematic representation of the ejector operation with local pressure and velocity profiles is presented in Figure 1.6 (a).

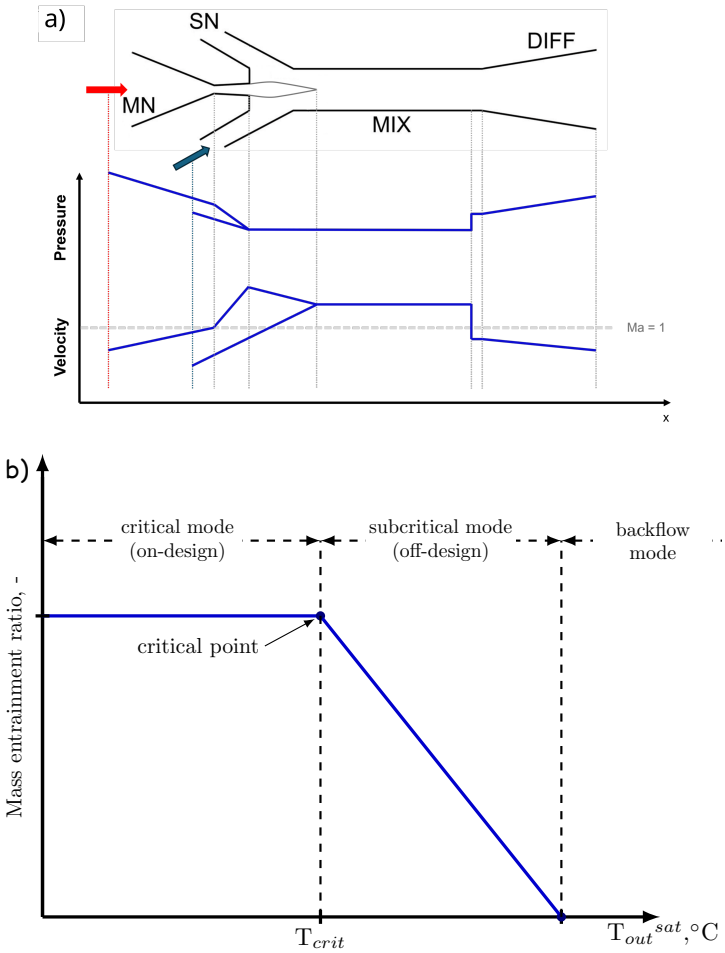

Figure 1.6: *Schematic representation of the supersonic ejector: a) local pressure and velocity profiles across the ejector components and b) ejector efficiency curve representing the mass entrainment ratio as a function of saturation temperature at the ejector outlet. Adapted and modified from Fingas et al. [86].*

Three modes of ejector operation can be distinguished, of which the

most desired is the critical mode, so the on-design ejector conditions are characterized by the highest mass entrainment ratio. The optimal point of ejector operation in given operating conditions is called the critical point, i.e. the point of maximum outlet pressure for which the mass entrainment ratio parameter still reaches its maximum. With a further increase of the ejector outlet pressure, it enters a subcritical, off-design mode, in which the mass entrainment ratio decreases with the increase of outlet pressure, up to a level above which the suction stream is no longer entrained, indicating the ejector entering into a backflow mode. In case of the gas ejectors working in vapor compression refrigeration systems, the critical point is often expressed in terms of temperature, being a saturation temperature for an outlet pressure (or back pressure) at the ejector critical point, since it is closely related with the ambient temperature at which operates the condenser. The representation of the ejector efficiency curve with all modes of operation is presented in Figure 1.6 (b).

1.5.2 Ejector design and shape optimization

For the efficient design and optimization of ejector systems, diverse modeling techniques have been used in literature. Zero-dimensional (0-D) models present a streamlined and effective method for predicting ejector performance and output parameters with low computational expense, rendering them ideal for system-level optimization under varied operating conditions [87]. More advanced models, including those based on computational fluid dynamics (CFD), provide detailed insights into the flow dynamics and allow for the exploration of complex geometrical and operational influences on ejector behavior [88] [89]. Performance maps, derived from experimental data or empirical correlations, are also widely used to predict ejector characteristics under varying conditions, supporting both design and control strategies [53].

1.5.3 Ejector control

The use of thermally driven ejectors is constrained by the need for access to a low-grade heat source and by their sensitivity to operating conditions, as their efficiency drops significantly under off-design conditions. As a result, introducing capacity control to allow the ejector to adapt to varying conditions emerges as a promising strategy for improving its performance even under less favorable conditions.

One approach for controlling ejector operation is the multi-ejector module first introduced by Hafner et al. [90]. In this concept, multiple ejectors

of different sizes operate in parallel, and capacity is modulated by switching individual ejectors on or off, enabling the module to match the system capacity requirements. Banasiak et al. [91] developed a performance map for an R744 multi-ejector module, demonstrating that it can span a wide operational range in refrigeration systems while maintaining efficiencies exceeding 30% across a broad range of conditions. Haida et al. [92] conducted an experimental study on a transcritical R744 refrigeration system equipped with such a module, showing a COP of up to 3.18, which represents a 7% COP improvement over a conventional vapor compression system, and an exergy efficiency of up to 13.6%, marking a 13.7% increase compared to the parallel compression system.

Another method for achieving variable ejector control was investigated by Ge et al. [93], who examined the impact of nozzle exit position for two different ejector geometries, i.e., a cylindrical mixer and a conical-cylindrical mixer, using water as the working fluid. Their findings revealed that the conical-cylindrical mixer achieved a higher entrainment ratio under all tested conditions. Furthermore, the conical shape of the mixer inlet stabilized the flow at both nozzles, as it effectively directed the expansion shockwave train produced by the motive fluid after nozzle expansion.

Another promising approach for the ejector control is the use of a VGE, which can dynamically adapt to changing boundary conditions, thus improving performance and broadening its application range relative to fixed-geometry ejectors, as described by Chen et al. [94]. The initial concept proposed by Elbel and Hrnjak [95] demonstrated that a needle-driven ejector can enhance the performance of a transcritical R744 system by regulating high-side pressure conditions similarly to an expansion valve in a conventional direct-expansion system, but with increases in cooling capacity and COP of up to 8% and 7%, respectively, compared to the valve-based system. Chandran et al. [96] reported that an R744 VGE featuring forward spindle movement can maintain the ejector pressure ratio by keeping the motive flow choked even as the mass flow rate decreases up to a certain spindle position. As the spindle advances, the motive flow gradually declines while the suction flow initially increases to a maximum before dropping sharply as the spindle moves deeper into the nozzle throat.

Another method for modulating ejector performance called a vortex-based control was introduced by Zhu and Elbel [97]. The schematic representation of this mechanism is presented in Figure 1.7. This technique enables the adjustment of ejector mass flow rate and capacity without changing the nozzle geometry but by generating a controllable vortex at the inlet of the motive nozzle. By splitting the refrigerant flow entering the motive

nozzle, a portion is directed into the motive nozzle tangentially, creating the vortex inside motive nozzle chamber, while the remainder enters the motive nozzle chamber axially. A valve at the tangential inlet regulates the flow ratio, thereby adjusting the vortex intensity. This dynamic vortex is able to modify the motive nozzle mass flow rate.

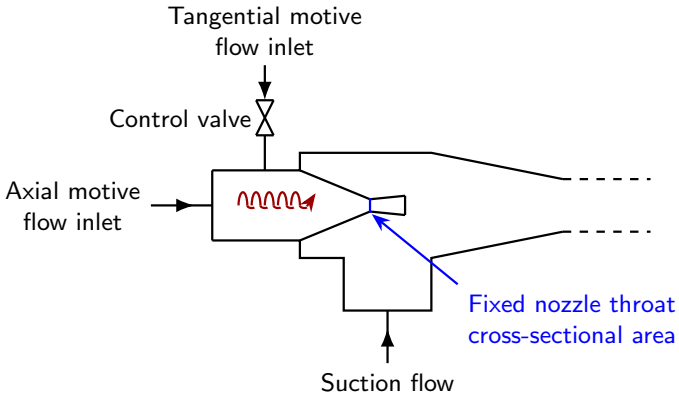

Figure 1.7: *Schematic representation of the vortex control mechanism for the ejector capacity control. Adapted and modified from Zhu and Elbel [97].*

The authors reported that the presence of a stronger inlet vortex was found to significantly reduce the flow through the motive nozzle up to 36% under constant inlet and outlet conditions. Moreover, in the next work, the authors demonstrated that this vortex-based capacity control strategy employed in the ejector-based transcritical R744 systems operating under off-design conditions, the implementation of vortex control increased cooling capacity by up to 11% and the COP by approximately 8.1% [98]. These improvements make the vortex ejector concept a promising candidate for efficient and adaptable vapor compression systems, especially where variable load conditions are common.

The novel approach for controlling the ejector capacity was proposed by Gullo et al. [99], in which the ejector was controlled using a pulse-width modulation strategy, where a solenoid valve installed upstream of the motive nozzle was switched periodically on and off within a defined cycle time. The ratio of the valve opening time to the cycle period determined the refrigerant mass flow rate. A pressure-width period of 2 s was identified as optimal, ensuring stable operation and minimizing valve delay effects. By varying the valve opening time, the high-side pressure could be adjusted between 87 and 112 bar, enabling effective ejector control. The method was then tested experimentally by Gullo et al. [100] in the small-scale

transcritical R744 system, in which the pulse-width modulation of ejector provided energy savings in the range from 7.0 to 11.1% without evaporator overfeeding and from 11.5 to 16.3% with overfeeding, corresponding to COP improvements of up to 15.1% at optimal conditions, when compared to a conventional R744 system with a vapor bypass valve. This novel capacity control approach, being simpler and less prone to clogging than needle- or vortex-based mechanisms, thus represents an effective and robust solution for controlling ejector capacity in small-capacity transcritical R744 systems.

In a CFD comparison of fixed and variable geometry R744 ejectors, Smolka et al. [101] demonstrated that introducing a spindle into the motive nozzle of a VGE can boost efficiency by up to 35% compared to a fixed-geometry ejector. However, further reductions in the effective area ratio can lead to declines in both the motive nozzle mass flow rate and the ejector efficiency. Their study also observed a similar pattern in the suction nozzle mass flow rate, with a peak value occurring after inserting the spindle a few millimeters into the nozzle.

Li et al. [102] carried out an experimental analysis of a transcritical R744 refrigeration cycle equipped with three VGEs, comparing its performance to a standard single-stage compression cycle with an expansion valve. By applying an effective operation strategy to the controllable multi-ejector setup, they achieved a cooling COP ranging from 2.6 to 4.0, reflecting improvements of 12.4% to 30.7% over the single-stage system under the tested conditions.

Varga et al. [103] presented a CFD analysis of a novel steam ejector design incorporating a spindle that can move axially in the primary nozzle to vary the nozzle area ratio. Their results indicated that for constant evaporator and generator pressures, increasing the area ratio enhanced the mass entrainment ratio while simultaneously lowering the ejector critical point temperature. By adjusting the spindle position (SP), they were able to improve ejector performance through control of the area ratio.

In a separate study, Besagni and Cristiani [28] performed a multiscale CFD investigation of VGEs for an R290 refrigeration system, assessing the impact of spindle-controlled ejectors on propane-based ejector refrigeration systems. Their findings showed that increasing the primary nozzle area ratio, defined as the outlet-to-throat cross-sectional area ratio, could reduce the system thermal input and raise average COP, although it also lowered the critical discharge temperature, limiting the highest feasible condenser temperature. For instance, a 33% increase in the nozzle area ratio led to an average COP improvement of 57%, while decreasing the average critical temperature by 6.7 K.

An experimental test of an ERS operating with R600a and a controllable ejector was conducted by Pereira et al. [104] using a small-scale facility with the cooling capacity of 1.6 kW. The authors noted that adjusting the spindle position allowed the ejector to reduce the primary mass flow rate while maintaining a generator saturation temperature of 83.0°C. They also identified the optimal spindle position for maximizing the system COP, which ranged between 0.45 and 0.88 for the ejector outlet pressures of 2.8 bar and 3.8 bar, corresponding to the condensation temperatures of 17°C and 21°C, respectively.

Finally, Nguyen et al. [105] found that in an R600a refrigeration system assisted by solar energy, the use of a VGE design instead of fixed geometry yielded COP improvements of up to 24%, with the maximum COP of 0.29 at the cooling capacity of 1.6 kW, thanks to the spindle responsiveness to varying operating conditions in a real-world scenario.

1.5.4 Ejector Refrigeration System

The refrigeration system used in this study is an ERS designed to utilize the low-temperature waste heat to drive the ejector which, due to the pumping effect, is able to recirculate the secondary flow through the evaporator. The schematic diagram of a simple thermally driven ERS is presented in Figure 1.8. The system comprises a gas ejector and three heat exchangers: the generator to provide the high-pressure and high-temperature gas to drive the ejector, the evaporator to generate the necessary cooling power, and the condenser to convert the gas phase from the ejector outlet nozzle into liquid. Part of this liquid is then directed to the pump, where its pressure is increased to the level required by the generator. The remaining portion, the value of which is the result of the operation of the ejector, is the flow involved in the cooling process in the evaporator, after its throttling to the evaporating pressure in a throttling valve.

The ejector-based cycle performance can be expressed as COP, which in case of the ERS utilizing waste heat takes into account the rate of cooling capacity in the evaporator to the sum of the waste heat recovered in the generator and the shaft power for driving the pump. The capacity of each heat exchanger, the pump power input and the COP are calculated based on the thermodynamic properties in the points presented in Figure 1.8:

$$\dot{Q}_{\text{evap}} = \dot{m}_{\text{sn,in}} \left(h_2 - h_5 \right) \tag{1.4}$$

where $\dot{Q}$ is the capacity, h is specific enthalpy, and the subscript evap denotes the evaporator.

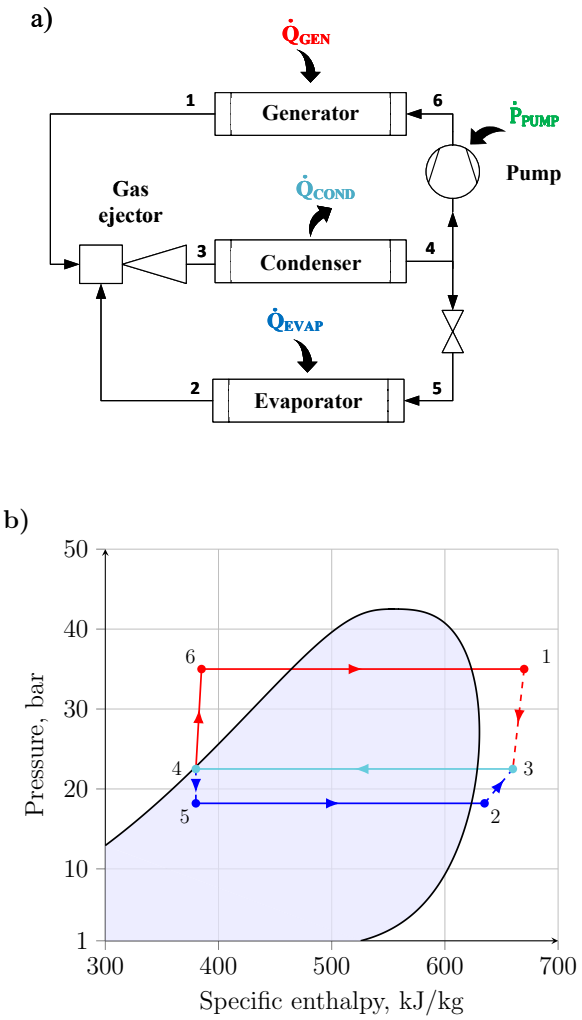

Figure 1.8: *Schematic representation of the ejector refrigeration system for low-grade heat utilization: a) diagram of the system, and b) its representation on the pressure-specific enthalpy diagram of the R290. Adapted and modified from Besagni et al. [3].*

$$\dot{Q}_{\text{gen}} = \dot{m}_{\text{mn,in}} \left(h_1 - h_6 \right) \tag{1.5}$$

where the subscript gen denotes the generator.

$$\dot{P}_{\text{pump}} = \dot{m}_{\text{mn,in}} \left(h_6 - h_4 \right) \tag{1.6}$$

where $\dot{P}$ is power, and the subscript pump denotes the pump.

$$\text{COP} = \frac{\dot{Q}_{\text{evap}}}{\dot{Q}_{\text{gen}} + \dot{P}_{\text{pump}}} = \phi \frac{h_2 - h_5}{h_1 - h_4} \tag{1.7}$$

1.6 Motivation and objectives

The growing global demand for cooling, driven by urbanization, digitization, and climate change, is amplifying the urgency to adopt sustainable refrigeration technologies. Among these, thermally driven refrigeration systems offer a compelling pathway for decarbonizing the cooling sector by utilizing low-grade waste heat, yet disregarded but possessing huge energy potential and being available in many industrial and commercial contexts. Recent regulatory actions intensify the push towards natural refrigerants with negligible environmental impact. However, while ERS represent a promising option due to their simplicity, low maintenance, and compatibility with waste heat sources, their practical deployment faces significant challenges.

The biggest challenge lies in the performance sensitivity of ejector systems to varying boundary conditions, particularly in waste heat-driven applications where heat source temperatures and ambient conditions are fluctuating. Fixed-geometry ejectors often operate far from their design point under these real-world variations, leading to suboptimal entrainment ratios and reduced COP. Recent advances in the VGE designs have shown strong potential to mitigate this limitation, enabling dynamic adaptation to changing operating conditions through real-time adjustment of their nozzle area ratios. However, there remains a scientific gap in accurately assessing the VGE performance under these varying conditions in different climatic conditions, and a need to develop an optimal control system for the spindle is necessary to maximize the VGE-based ERS potential and gain industry attention.

Existing studies on ERS rely on steady-state simulations with idealized boundary conditions, neglecting the dynamic nature of real characteristics of waste heat and ambient temperatures in different climatic zones. Such simplifications limit the practical understanding of the system characteristics and challenges. Similarly, while most ERS designs focus on single-component natural refrigerants, there is a growing interest in exploring blends of natural refrigerants to optimize their thermodynamic properties, balance flammability risks, and expand applicability across a wider range of operating conditions.

This study aims to address these gaps by performing a dynamic simulations of the R290 ERS equipped with VGE using real source and weather temperature data. The research employs advanced CFD modeling to charac-

terize the ejector behavior across varying operating regimes and by means of reduced-order models (ROM) suitable for integration into dynamic system-level simulations will enable to develop a proper control system of the VGE. By implementing real-world waste heat profiles and temperature data from different climatic zones, the study will enable a realistic assessment of the ERS potential for waste heat recovery and its operational flexibility. Moreover, the investigation will evaluate the feasibility of repurposing ejector designs developed for a single hydrocarbon refrigerant to other natural refrigerant and their blends, highlighting performance trade-offs and design considerations.

Based on the aforementioned scientific gaps, the following partial goals are defined to address the identified research needs:

- development of an R290 ERS equipped with a VGE utilizing real low-temperature waste heat source and weather temperature data to perform analyses of the VGE-based system under realistic operating conditions,
- development of the two different VGE ROMs based on the CFD results, including a novel approach for the ejector reduced order modeling to improve the flexibility and transferability of the ROM across different refrigerants or their blends with similar thermophysical properties,
- assessment of the waste heat recovery potential of the ERS using real-world waste heat temperature profiles and analyzing the system operation in different climatic zones under varying environmental and load conditions,
- investigation of the feasibility of adapting the VGE design developed for R290 to other natural refrigerant blends, identifying the performance trade-offs and key design considerations for multi-refrigerant ejector.

These objectives reflect the key innovations and methodological contributions of the study, and collectively form the foundation for achieving the overall aim of this PhD thesis.

1.7 Scope

The thesis consists of the following chapters:

Chapter 1 is this chapter.

Chapter 2 describes the design of the controllable R290 VGE, the spindle mechanism with geometrical parameters of selected for this analysis spindle

positions, and the manufactured ejector, with practical insights about its integration into the R290 test loop.

Chapter 3 describes the experimental setup and methodology for the experimental tests of the R290 VGE. It outlines the measurement system, testing procedures, and the operational range during the experiments. Additionally, it presents the findings of the ejector capacity control and the analysis of the static pressure profile.

Chapter 4 describes the development of two VGE ROM based on the typical specific-enthalpy and mass flow rates approach and the generalized approach using the pressure ratios and temperature to evaluate the mass entrainment ratio of ejector. It discusses the mathematical model formulation, sensitivity analysis for the resolution of the grid of points used for building of the model, the resulting operational envelope of the developed ROMs and their implementation to the dynamic system analysis.

Chapter 5 describes the comprehensive analysis of the R290 ERS model equipped with VGE under varying ambient temperature conditions from historical data. It presents the system layout built in Dymola software, describes the mathematical formulation of all system components, selected solver and its settings, the ejector control logic and simulated ERS conditions, representing representing its operation in three different climatic zones. The results of the analysis comprise the direct comparison of the ERS equipped with controllable VGE with the typically used fixed geometry ejectors.

Chapter 6 analyzes the R290 ERS performance under variable ambient temperature and temperature waste heat sources. It presents the characteristics of the realistic industrial waste heat temperature data obtained from the company, depicts the simulated cases. The results give insights of the system operating in different environmental and industrial scenarios, focusing on the evaluation of the best application of the proposed R290 ERS system.

Chapter 7 evaluates the application of the ERS system for alternative natural refrigerants and selected blends using the generalized approach for ROM. It describes the screening of other refrigerants similar to R290 for a selected reference operating condition, and presents the simulation results for the

Chapter 8 summarizes the essential findings and conclusions, highlighting the potential of application of the ERS with spindle-based VGE as the efficient way for utilization of the low-temperature waste heat. It describes the model and system limitations and provides the potential future steps and directions for the development of the system being the main subject of this thesis.

CHAPTER 2

Design of Variable Geometry Ejector

The gas ejector used in this study is a VGE with a centrally aligned spindle that enables flexible control of its internal motive nozzle geometry by changing the effective throat cross-sectional area. The ejector geometry and control mechanism were originally analyzed in detail in CFD by Besagni and Cristiani [29], whose work provides the concept foundation for this study. The authors applied a finite volume approach using the ANSYS Fluent software to solve the steady-state Reynolds-Averaged Navier-Stokes equations, modeling the turbulent, compressible, single-phase flow of a Newtonian fluid through a supersonic gas ejector. Their simulations offered valuable insight into the behavior of gas ejectors under various geometric and boundary condition settings, serving as a validated reference for the geometry adopted in this work.

The CFD analysis conducted by Besagni et al. [106] involved a systematic comparison of different solver setups, turbulence models, and mesh topologies to determine the most accurate and computationally efficient configuration for predicting single-phase ejector performance. Particular focus was put on capturing shock structures, expansion behavior, and recirculation zones that are critical to accurately representing supersonic ejector operation. Their results demonstrated the ability of the VGE design to adapt to varying

operating conditions by altering the throat area of the motive nozzle through a spindle displacement, making it suitable for dynamic energy systems such as waste heat recovery or variable load refrigeration cycles.

The choice of R290 as a working fluid was supported by the screening study by Besagni et al. [28], in which the thermodynamic performance of several commonly used refrigerants was evaluated under typical conditions of the ejector refrigeration cycle. The R290 emerged as a highly promising fluid, offering a favorable combination of high entrainment performance directly influencing the efficiency of the ERS cycle, and low GWP, which aligns with the current trend toward natural refrigerants and the development of environmentally friendly working fluids. Their analysis reported COP values ranging from 0.5 to 1.0 under varying conditions, placing R290 among the most efficient natural refrigerants studied. However, the relatively low fixed-ejector critical temperature range (20.7-25.0°C) imposes a need for expanding the design constraints of the ejector geometry, particularly in terms of introducing an approach for a precise and adaptable ejector solution such as the VGE.

In this context, the spindle-based VGE design offers a key advantage. By allowing direct adjustment of the motive nozzle throat area, the ejector can maintain near-optimal entrainment ratios for a wider range of operating conditions. Therefore, the VGE improves the operational flexibility and allows the system to track transient operating conditions more effectively, reducing the risk of ejector operation in inefficient regimes and helping to avoid its operation in the backflow conditions. The subsequent sections describe the geometry characteristics, physical construction of the device, and presents the control mechanism of the spindle-based VGE.

2.1 Ejector geometry

The ejector used in this study is designed with a convergent-divergent motive nozzle, a mixing chamber with a conical entrance followed by a short constant cross-sectional area section, and a conical diffuser. The internal design parameters of the ejector are presented in Figure 2.1. The motive nozzle throat diameter is equal to 2 mm, and its exit diameter is 3 mm. The motive nozzle cone half-angle in the divergent section is 1.4°. This configuration enables the nozzle to accelerate the primary flow to supersonic velocities at the exit, ensuring effective entrainment of the secondary flow. Downstream of the nozzle, the mixing chamber is designed with a 40 mm long and 0.6° half-angle conical entrance followed by a 3.2 mm long constant-area section and having a diameter of 4 mm. The use of the conical

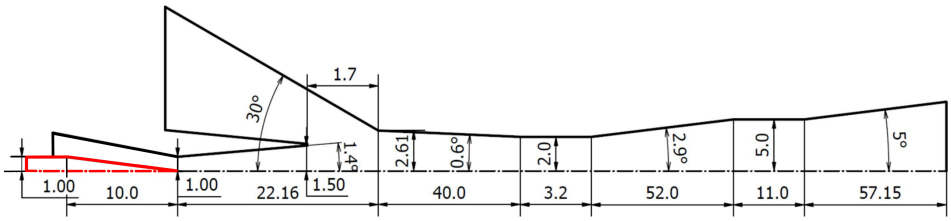

Figure 2.1: *Geometrical parameters of the R290 VGE with spindle (red). Adapted from Besagni and Cristiani [29].*

entrance promotes supersonic compression within the convergent region of the chamber, minimizing the formation of strong shock waves in the constant-area section. This design approach has been reported to improve ejector performance by reducing shock-induced losses [107]. Finally, the flow is decelerated in a conical diffuser with a 52 mm of length and a 2.9° half-angle, which recovers the static pressure and facilitates efficient mixing of the primary and secondary streams. The ejector geometry is then finished with another 11 mm constant-area cross-section with a diameter of 10 mm followed by divergent section that is 57.15 mm long with a half-angle of 5°.

The spindle (highlighted in red) is able to move along the ejector axis, which reduces the effective cross-sectional area of the motive nozzle throat. Its diameter in the constant-area cross-section is 2 mm, and the length of the converging part is 10 mm, with a half-angle of 5.71°. The neutral position in which the spindle tip is placed right in the nozzle throat is called the spindle position (SP) 0. Moving the spindle towards the nozzle exit, the nozzle throat cross-sectional area is reduced and, since the nozzle exit area is unchanged, the motive nozzle area ratio (AR) is increased. In this study, the effects of SP are analyzed in the range from 0 to 7 mm, with 1 mm step. Spindle positions with their geometry code names, their cross-sectional area of the nozzle, and the AR are presented in the next section.

2.2 Spindle control

The control of the spindle position represents the core mechanism for real-time modulation of the ejector capacity. The spindle, located concentrically inside the axisymmetric motive nozzle, is designed to translate along the longitudinal axis of the ejector body. This axial movement allows the spindle to change the effective cross-sectional area of the nozzle, thereby changing the choked flow characteristics and consequently the motive nozzle mass flow rate. This variation enables the ejector to regulate its entrainment capacity

and adapt to fluctuating boundary conditions in the realistic operation of the ERS. This design feature enables the creation of a series of eight discrete internal geometries, denoted SP0 to SP7, where each SP corresponds to a unique cross-sectional configuration of the motive nozzle. At SP0, the spindle tip is retracted and aligned with the MN throat, maintaining the maximum effective diameter of the motive nozzle. As the spindle moves forward in 1 mm increments up to SP7, the effective flow area decreases due to the intrusion of the spindle into the nozzle throat. This results in a progressive increase in AR, a critical parameter of the geometry of the ejector that influences the expansion behavior, shock formation, and entrainment characteristics of the ejector. The SP7 is the last analyzed spindle position, since this is the last one for which the ejector can entrain the secondary stream. The AR of the motive nozzle is defined as the ratio between the effective throat area and the constant exit area of the nozzle:

$$AR = \frac{A_{\text{eff}}}{A_{\text{MN,out}}} \tag{2.1}$$

where A_{eff} is the effective cross-sectional area of the motive nozzle throat, and A is the cross-sectional area. The effective cross-sectional area of the throat is determined as the difference between the fixed-geometry throat cross-sectional area and the cross-sectional area of the spindle at the throat, that changes with the SP:

$$A_{\text{eff}}(SP) = \pi \left[\left(\frac{d_{\text{throat}}}{2} \right)^2 - \left(\frac{d_{\text{spindle,eff}}(SP)}{2} \right)^2 \right] \tag{2.2}$$

where d_{throat} is diameter of the motive nozzle throat, and $d_{\text{spindle,eff}}$ is diameter of the spindle cross-section at the throat line at particular spindle position.

Since the half-angle of the converging part of spindle is known, the effective spindle diameter at the throat can be defined as:

$$d_{\text{spindle,eff}}(SP) = 2 \cdot (SP \cdot \tan(\alpha_{\text{spindle}})) \tag{2.3}$$

where α_{spindle} is the half-angle of the conical section of the spindle.

The representation of the effective throat area and the AR of the VGE as functions of the SP is presented in Figure 2.2.

As the SP increases, the effective throat area of VGE decreases due to the increasing obstruction of the throat cross-section by the spindle. As opposite, the AR exhibits a progressive increase with the increase of SP. At SP0, the effective throat area is equal to the fixed-geometry throat and has a value of approximately 3.14 mm^2, while the AR is 2.25. As the

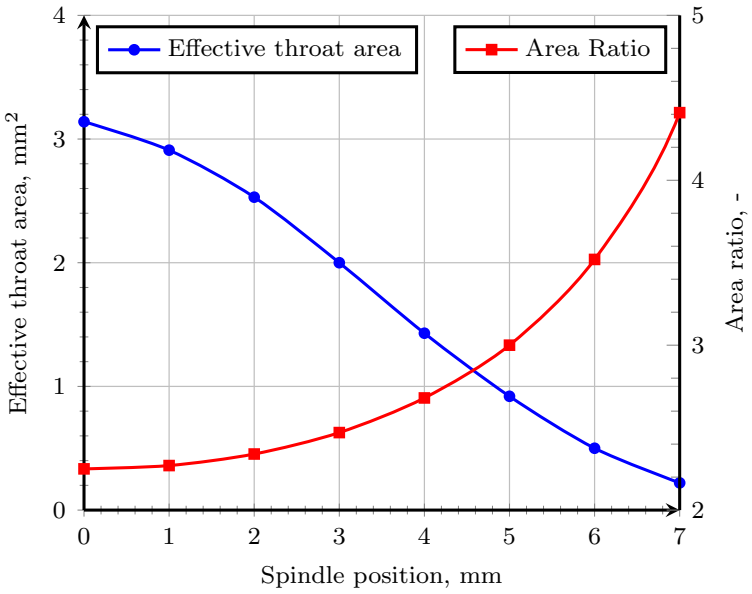

Figure 2.2: *Representation of VGE geometrical parameters of effective cross-sectional area of motive nozzle throat and motive nozzle AR.*

spindle advances to SP7, the effective throat area decreases to approximately 0.22 mm^2, corresponding to a reduction of nearly 90% relative to its initial value, whereas the AR increases to around 4.5, representing an increase of approximately 105%. This relationship between the ejector effective throat area and the AR demonstrates the geometric modulation mechanism of the VGE, in which spindle displacement enables continuous adjustment of the nozzle geometry.

To support visual understanding, Figure 2.3 provides side-by-side images of each spindle position from fully open at Figure 2.3 a) to almost fully closed at Figure 2.3 h). These demonstrate the gradual reduction in throat cross-sectional area and the resulting increase in AR, offering insight into how the following SPs directly influence the geometrical parameters of the motive nozzle.

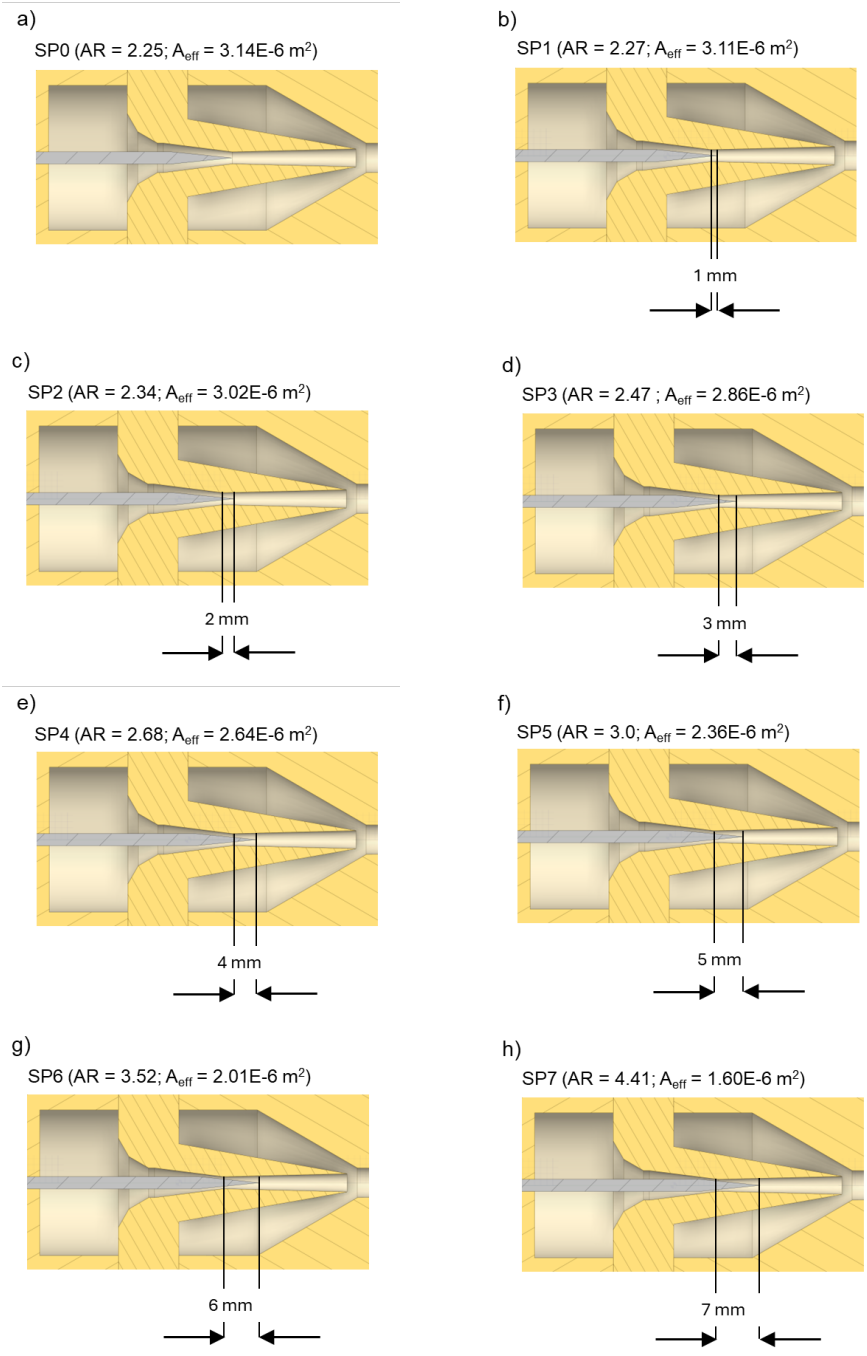

Figure 2.3: *Spindle positions of the VGE with their code names, motive nozzle AR and effective throat area. Adapted and modified from Besagni et al. [29].*

2.3 Manufactured ejector

The ejector assembly with all components is presented in Figure 2.4. The body of the ejector consists of 6 brass parts prepared by mechanical turning and drilling, which are assembled together with bolts and screws. The modular structure of the VGE and the replaceable spindle unit provides a practical advantage for laboratory and industrial testing purposes. For pipe connections, three 10 mm internal diameter straight connectors were used for the ejector inlets and outlet ports. In addition, six additional connectors were used to measure pressure drop with an internal diameter of 6 mm.

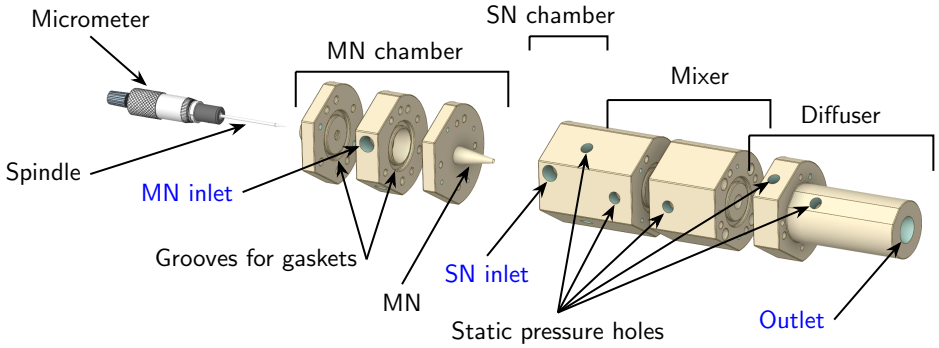

Figure 2.4: *Assembly drawing of the R290 VGE parts.*

The precision manufacturing of the ejector components plays a crucial role in ensuring reliable performance and repeatable control of the spindle position. The geometric tolerance achieved by the manufacturer was below ± 0.01 mm for the longitudinal and $\pm 0.1\%$ for the angular dimensions. Another important aspect is the roughness of the internal surfaces in the ejector passages and the surface of the needle, since any small deviations on the material surfaces may disturb the boundary layer and shock stability within the motive stream, influencing the critical mass flow rate through the motive nozzle and consequently affecting the entrainment performance. The roughness of the internal passages was maintained at a maximum level of Ra = 1.25.

To change the effective cross-section of the throat, the controllable spindle with micrometric knob for precise mechanical control was used, enabling satisfactory resolution in controlling the spindle position. Although the current prototype design allows for more refined positioning, the analyzed spindle step was 1 mm in order to see notable changes in the device operation. In the manufactured ejector, the spindle positions were set manually.

For industrial applications, the spindle may be connected to an electric actuator, which would allow implementation of the precise control system with a proper control algorithm.

To ensure proper sealing of the internal channels, the nitrile butadiene rubber gaskets were placed between the brass elements in specially prepared grooves. Before running the tests, the fully assembled device undergone pressure tests using nitrogen at 60 bar to check the leak tightness. The photo showing the fully assembled VGE with the spindle control mechanism and straight connectors is presented in Figure 2.5.

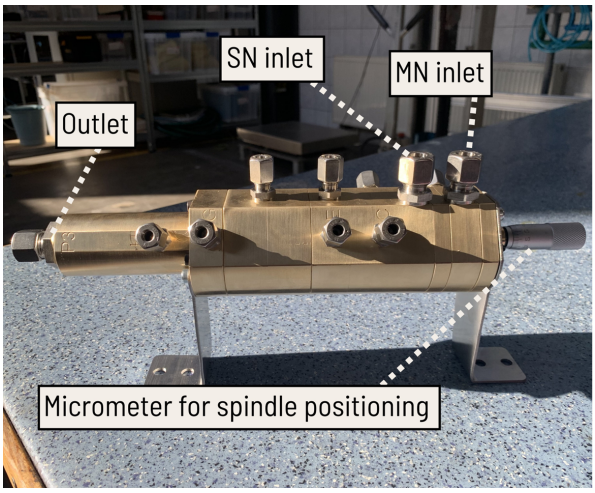

Figure 2.5: *Overview of the assembled R290 VGE with a spindle featuring the micrometric knob and mounting brackets.*

CHAPTER 3

Experimental analysis of the R290 Variable Geometry Ejector with a spindle

This chapter presents the results of an experimental investigation conducted to evaluate the performance of VGE utilizing R290 as a working fluid. The primary objective of this study was to assess the influence of spindle positioning on mass entrainment characteristics and the internal flow behavior of the manufactured VGE under varying boundary conditions.

The experimental campaign was carried out on a dedicated test rig designed for high-pressure natural refrigerant applications. The test setup enabled the measurement of mass flow rates, temperatures, and static pressure profiles across the ejector body. The ejector was tested at eight spindle positions (from SP0 to SP7), and under various pressure lift conditions to simulate different ejector operating conditions.

First, a detailed description of the test rig, instrumentation, and measurement methodology is provided, including the description of operating conditions and their deviations from the nominal design values. Next, the experimental procedures and uncertainty analysis used to ensure the reliability and accuracy of the collected data are presented.

In the the latter section of the chapter, the experimental results are dis-

cussed. First, the analysis of the ejector's capacity control capability, with a detailed investigation of the experimentally determined ejector performance curves and the spindle control line, which visualizes the potential for the ejector capacity control in real conditions, is presented. The final section focuses on pressure profile analysis, offering insights into internal flow dynamics and shockwave behavior across multiple spindle settings.

3.1 Test rig for the study of Variable Geometry Ejector

A schematic diagram of the experimental setup is presented in Figure 3.1.

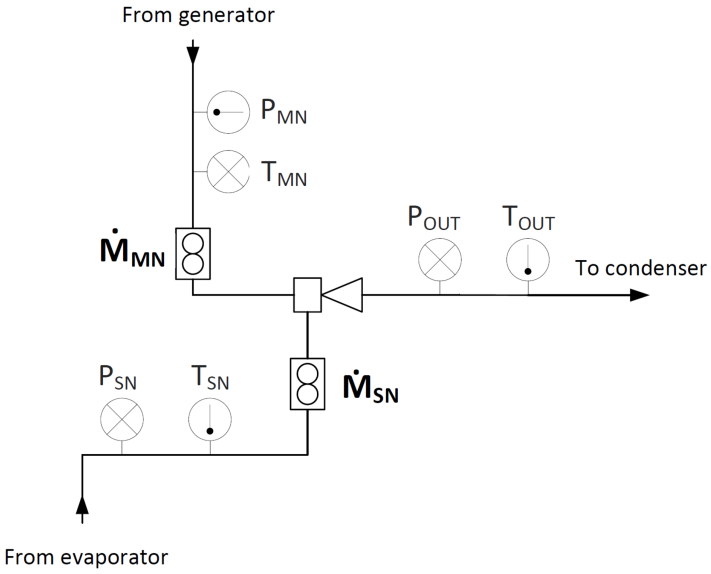

Figure 3.1: *Schematic diagram of the test rig for the R290 VGE campaign.*

The ejector was examined on a separate test rig connected to the heat pump system, which allowed the maintenance of the operating conditions for gas ejector operation. The Frascold A1-6AXH compressor designed to operate with R290 with a displacement of 5.47 m^3/h was used to produce the high pressure gas to the ejector motive nozzle inlet. However, the operating conditions were limited by the operating range of the compressor used, and therefore VGE was tested in a different range of operating conditions than those for which it was originally designed. As a consequence, the resulting mass entrainment ratios obtained by the VGE are lower than the originally reported in the CFD analysis of Besagni et al. [29]. The pressure of the motive nozzle was kept between 15.8 and 20.2 bar with a motive

nozzle temperature between 80 and 105°C. The pressure at the outlet was maintained between 2.3 and 6.0 bar, with a resulting temperature of 48°C up to 78°C. The pressure in the suction nozzle was regulated by the expansion valve, which throttled from the condensation pressure to the evaporating pressure, and varied between 2.2 and 5.4 bar depending on the operating point. The suction nozzle temperature varied in the range between 22 to 36°C.

The motive and suction mass flow rates were measured using the Endress-Hauser Coriolis flow meters installed on the inlet lines right next to the VGE. The absolute pressure sensors were connected to both inlet and outlet ports to measure the refrigerant pressure at the ejector ports. The temperature was measured using T-type thermocouples attached to the copper pipe walls. Moreover, the thermally conductive paste was used to ensure proper contact of the sensors with the pipe surface. All the pipes were insulated using a thick layer of 20 mm of polyethylene foam with a thermal conductivity of 0.040 W/(m·K). This kind of insulation withstands high operating temperatures and ensure high accuracy of the measurements.

One of the objectives of the tests was to analyze the pressure profile along the device, which can be later processed for the validation of the numerical tools used for the design and optimization process of the ejectors. Therefore, five differential pressure sensors were installed to measure the pressure profile along the ejector. The sensors were installed on a board presented in Figure 3.2 and connected to the ejector ports using 6 mm copper pipes. The first of these sensors was used to measure the pressure drop inside the motive nozzle. Therefore, the measurement range of that pressure transducer was from 0.0 to 25.0 bar. The measurement range of the rest of pressure sensors was lower, being able to measure the differential pressure in the range from 0.0 to 2.0 bar. The VGE ejector was prepared with holes drilled at the positions A-H presented in Figure 3.3. The differential pressure sensors were arranged in three angular positions, as presented in the diagram, to facilitate their proper tightening to the assembled device. Since only 5 differential pressure sensors were used for the testing, holes B and G were not used in this investigation. The pressure profile was defined for SP0, SP2, SP4, and SP7 for two different ejector pressure ratios for each SP analyzed, in order to show the influence of the boundary conditions and the position of the spindle on the internal flow behavior. Each successive differential pressure sensor measured the pressure drop in the port relative to the previous one. Therefore, by having the motive nozzle absolute pressure measured, the static pressure profile along the ejector was defined.

The types and precision of the measuring devices used in the experimental

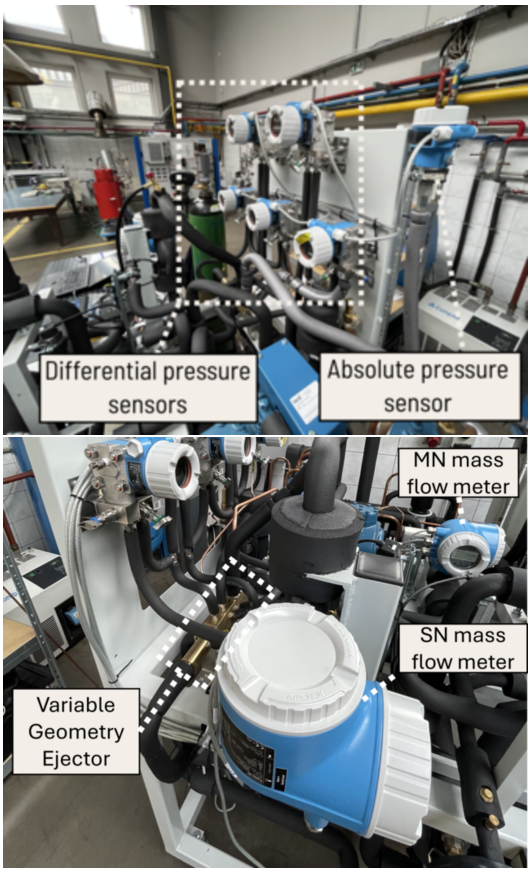

Figure 3.2: *Experimental test rig for the R290 VGE tests with the differential pressure (top) and mass flow rate sensors (bottom).*

campaign are collected in Table 3.1.

Table 3.1: *Description of the measurement instruments installed at the test rig.*

Parameter	Sensor type	Model	Range and accuracy
Pressure	Ratiometric transmitter	Danfoss AKS32R	-1.0 - 32.0 bar, 0.8% · x
	Differential pressure	E+H Deltabar PMD55	0.0 - 25.0 bar (DP1), 0.8% · x
		E+H Deltabar PMD55	0.0 - 2.0 bar (DP2-DP6), 0.8% · x
Temperature	T-type thermocouple	Termoaparatura TTP	-40.0 - 350.0°C, ±0.5°C
Mass flow rate	Coriolis type	E+H Cubemass C300	0 - 90 kg h^{-1}, 0.1% · x

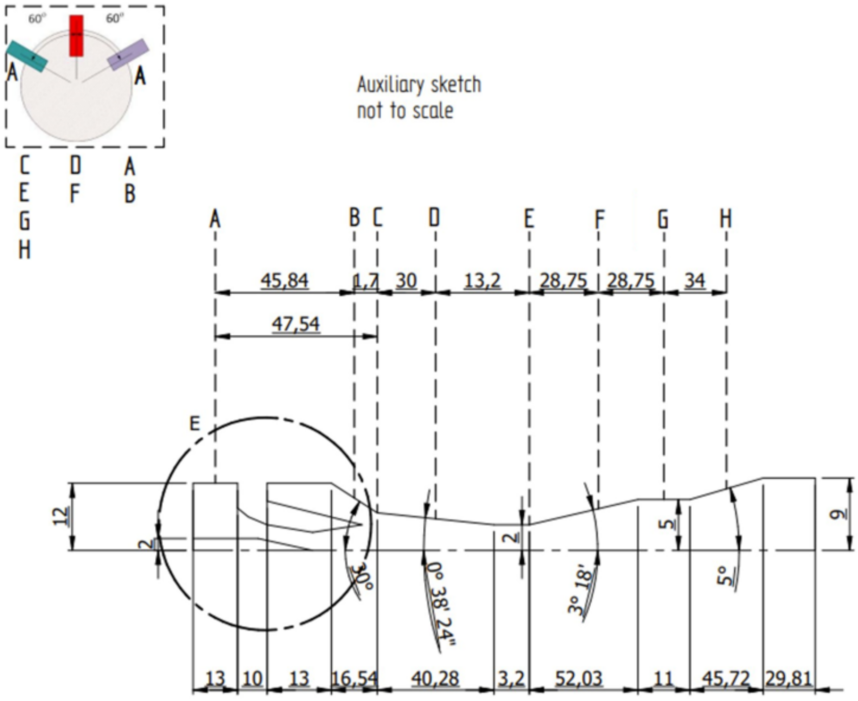

Figure 3.3: *Positioning of ports for the local static pressure measurements of the R290 VGE presented on an axisymmetric view of the ejector.*

3.2 Experimental procedure

The experimental campaign was structured in two parts, each devoted to investigate different aspects of the VGE performance. In the first phase, a comprehensive series of tests was performed across all eight spindle positions (from SP0 to SP7) under consistent boundary conditions. The pressure levels at the motive, suction, and outlet nozzles were kept approximately constant to focus solely on the evaluation of the capacity control capability of the ejector, specifically assessing how changes in spindle displacement affect mass flow rates through the motive and suction nozzles, as well as the resulting entrainment ratio.

In the second phase of the campaign, a more detailed analysis of the static pressure profiles was conducted for four representative spindle configurations: SP0, SP2, SP4, and SP7. These positions were selected to cover the full range of geometries, from fully open SP0, to the point at which the ejector operated with the most restricted throat area at SP7. In this part of

the study, the system was tested under varying suction pressure to adjust the pressure lift across the ejector. The outlet pressure was kept within a controlled range of 5 to 6 bar to replicate typical condenser-side conditions in real systems.

For each operating point, the data acquisition process began only after the system reached steady state and measurements were recorded continuously for a period of five minutes to ensure the accuracy of the measurement.

It is important to note that the operating conditions during the experimental campaign differed from the original on-design parameters proposed in the numerical work of Besagni and Cristiani [29]. These deviations were primarily due to the constraints imposed by the laboratory-scale test facility, which was not tailored as an ERS but rather configured as a flexible platform for standalone ejector testing. In particular, the compressor employed in the test rig had a limited discharge temperature range and was unable to reach higher saturation temperatures.

Additional constraints were imposed by the selection of the expansion valve used to control the suction nozzle pressure. The relatively large nominal capacity of the valve led to imprecise pressure level control, limiting the ability to accurately maintain low suction nozzle pressure and accurately control the pressure lift across the ejector. This in turn affected the stability and range of entrainment operation. Consequently, these hardware-related constraints forced the ejector operation outside of its design conditions, at a lower pressure ratio and with reduced flexibility in defining the full operating envelope. Despite these limitations, the experimental results provide valuable insights into the behavior of the VGE under realistic operating conditions.

3.2.1 Operating conditions

To illustrate a full range of operating conditions under which the VGE was tested, Figure 3.4 presents the inlet and outlet nozzles parameters on the pressure-specific enthalpy (Figure 3.4 a)) and the temperature-specific entropy (Figure 3.4 b)) diagrams for the R290 working fluid. These plots provide a comprehensive thermodynamic representation of the fluid states at the motive, suction, and outlet ports for all the tests carried out in the experimental campaign. Analyzing both graphs, it can be observed that the motive nozzle inlet conditions during the tests were in the high-pressure, superheated vapor region between approximately 15 and 20 bar. The motive nozzle temperatures during the tests ranged from 80°C to 105°C. The suction nozzle conditions present a lower pressure range from 2.2 to 5.4 bar and

are located closer to the saturation line. This indicates that the suction flow was slightly superheated vapor with temperatures ranging between 20°C and 35°C. Eventually, the outlet nozzle pressure conditions were between the values at the suction and the motive nozzle, mostly within the range of 2.3 and 6.0 bar, depending on the operational conditions, as an effect of intensive mixing of inlet streams and indicating effective pressure recovery in the throttling process.

3.2.2 Uncertainty analysis

Measurement uncertainties arising from statistical and instrumental inaccuracies were calculated for each of the variables, using Type A analysis for test series and Type B analysis for instrumentation precision. For the error analysis of parameters affected by multiple independent variables, the uncertainty propagation approach was used, which is the methodology that is in accordance with the NIST guidelines [108].

For the parameters that were measured during the tests, i.e. the measurements of temperature, pressure, and mass flow rate, the standard uncertainty was calculated using Equation (3.1):

$$u_{\mathrm{i}}(X_{\mathrm{i}}) = \sqrt{u_{\mathrm{A}}^2(X_{\mathrm{i}}) + u_{\mathrm{B}}^2(X_{\mathrm{i}})} \tag{3.1}$$

where $u_{\mathrm{A}}(X_{\mathrm{i}})$ is the standard uncertainty of parameter X, $u_{\mathrm{B}}(X_{\mathrm{i}})$ is the measurement device uncertainty, and X_{i} is a single observation of the parameter X.

The parameter $u_{\mathrm{A}}(X_{\mathrm{i}})$ being a standard deviation of the measured test series, was calculated using Equation (3.2):

$$u_{\mathrm{A}}(X_{\mathrm{i}}) = \sqrt{\frac{1}{N-1}\sum_{\mathrm{i=1}}^{N}(X_{\mathrm{i}} - \overline{X_{\mathrm{i}}})^2} \tag{3.2}$$

where the $\overline{X_{\mathrm{i}}}$ is the mean average of measured parameter X, and N is the number of samples.

To calculate the measurement device uncertainty parameter, the following equation was used:

$$u_{\mathrm{B}}(X_{\mathrm{i}}) = \frac{a}{\sqrt{3}} \tag{3.3}$$

where a is an absolute limit error, calculated individually for each measuring instrument, using the precision provided by the manufacturer, which is listed in Table 3.1.

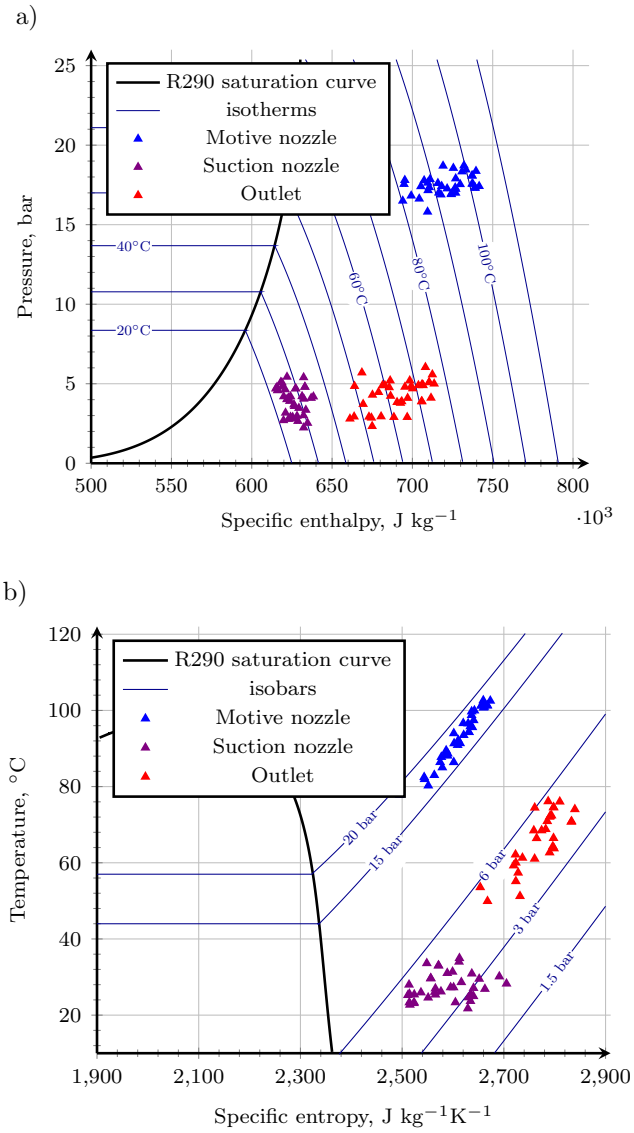

Figure 3.4: *The inlet and outlet conditions of the R290 VGE presented in: a) pressure-specific enthalpy diagram, and b) temperature-specific entropy diagram.*

For the mass entrainment ratio and the pressure lift parameters, the uncertainty of each parameter was calculated using the uncertainty propagation formula (combined standard uncertainty or Type C) expressed by the foollowing equation (3.4):

$$u_{\mathrm{C}}(X_{\mathrm{i}}) = \sqrt{\sum_{\mathrm{i=1}}^{\mathrm{n}} \left(\frac{\delta F_{\mathrm{i}}}{\delta f_{\mathrm{i}}} u(X_{\mathrm{i}}) \right)^2} \tag{3.4}$$

where n is the number of partial derivatives and $\frac{\delta F_{\mathrm{i}}}{\delta f_{\mathrm{i}}}$ is the partial derivative of the function F_{i} over a variable f.

The uncertainty calculations were performed in the Matlab software [109] and their outcomes were introduced to the graphs and tables representing the results presented in the next section.

3.3 Results and discussion

3.3.1 Capacity control analysis

The relationship between spindle position and mass flow rates through the motive and suction nozzles was evaluated to assess the potential of the ejector capacity control. The results are presented in Figure 3.5, which illustrates the mass flow rate changes throughout the entire range of SP, i.e. from SP0 to SP7. For the mass flow rate measurement, the Type A uncertainties are below 1%, therefore only averaged values are described on the graphs. The motive nozzle mass flow rate presented a clear decreasing trend with increasing the SP value. At SP0, corresponding to the fully open position, the motive nozzle mass flow rate was approximately 36 kg/h. As the spindle moved forward towards SP7, thereby progressively reducing the effective throat cross-sectional area at the motive nozzle, the mass flow rate steadily decreased, reaching a minimum of 12 kg/h.

Interestingly, the rate of change varied across the SP range. From SP0 to SP4, so the reduction of the effective cross-sectional area of the throat by 14%, the reduction in the motive nozzle mass flow rate was relatively low, approximately 5%, indicating that the early stages of spindle movement had a limited effect on the choked mass flow rate. However, beyond SP4 the reduction became more visible, with a total drop of approximately 65% observed between SP4 and SP7, with the latter being a reduction of effective cross-sectional area of the throat by 49% relative to the throat at SP0. This behavior reflects the nonlinear sensitivity of the effective area to the spindle intrusion, particularly once the motive nozzle throat begins to significantly restrict flow, which is a behavior that has been already observed in the literature [101].

A similar trend was observed in the suction nozzle mass flow rate. Initially, as the spindle moved from SP0 to SP3, the suction flow increased,

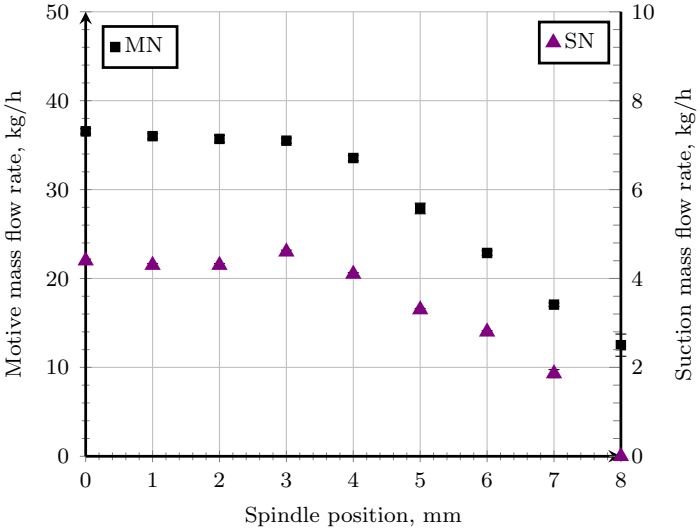

Figure 3.5: *R290 VGE mass flow rate as a function of the varying spindle position for* p_{MN} *= 17.5 bar.*

reaching a peak at SP3 of about 4.4 kg/h. This result is consistent with observations in the literature that report that a slight restriction in the motive nozzle can enhance entrainment by improving pressure conditions in the mixing chamber. However, beyond SP3, the suction mass flow rate decreased sharply with further spindle advancement. At SP7, no measurable suction flow was observed, indicating a complete backflow or breakdown of entrainment, particularly under the relatively low motive nozzle pressure conditions at the test rig.

It is important to note that the absolute values of the suction nozzle mass flow rate obtained during the experimental campaign were substantially lower than those predicted in the CFD simulations presented by Besagni et al. [29]. Several factors may contribute to this discrepancy. First, the pressure of the motive nozzle in the experimental setup was significantly lower than the one used in the referenced numerical analysis, which directly affects the potential for entrainment. Second, the presence of additional pressure ports along the mixing chamber may have introduced local disturbances to the suction stream, especially in the region near the wall, thereby affecting the annular development of the flow and reducing the overall entrainment efficiency. These practical considerations highlight the challenges in translating idealized CFD predictions into real-world performance, especially when working with small-scale ejector prototypes for natural refrigeration

systems of small cooling requirements.

Next, the evaluation of ejector performance curves by analyzing the relationship between the mass entrainment ratio and outlet the pressure increase was performed for selected spindle positions. This approach allows for the definition of the ejector efficiency in a wide range of operating conditions and helps to define the influence of internal geometry on the behavior of the entrainment of the secondary flow.

For SP0 presented in Figure 3.6 a), the ejector demonstrated an on-design mass entrainment ratio ranging from 0.29 to 0.31. The critical operating point was experimentally identified at a pressure lift of approximately 0.32 bar. Beyond this point, the mass entrainment ratio declined under off-design conditions from 0.21 to 0.08, with the highest recorded pressure lift reaching 0.82 bar. During the tests of SP0, a distinct measurement gap was observed between pressure lift values of 0.39 and 0.60 bar, attributed to an unstable interaction between the suction and outlet pressures. Small fluctuations in the suction pressure resulted in equivalent shifts in outlet pressure, making it difficult to define stable operating points in that region. This instability appears to be specific to the SP0 configuration and was not encountered in tests with other spindle positions, suggesting that for the baseline ejector design, with no throat constriction, the ejector is characterized by less stable operation.

At SP2, shown in Figure 3.6 b), the ejector exhibited improved stability and higher performance. The mass entrainment ratio for on-design operation increased to between 0.33 and 0.37, and the critical point was experimentally defined at a pressure lift of 0.29 bar. Under off-design conditions, the mass entrainment ratio decreased from 0.30 to 0.08, while the maximum pressure lift reached 0.81 bar. Compared to SP0, the performance curve for SP2 was easier to define as it covered a few points in terms of the pressure lift along the off-design curve, indicating that a slight constriction of the motive nozzle enhances system responsiveness and control range.

Ejector operation at SP4, presented in Figure 3.6 c), showed the best results in terms of both operational stability and an extended operating window. The on-design mass entrainment ratio reached values between 0.38 and 0.39. The critical point for SP4 was identified at a pressure lift of approximately 0.25 bar. In the off-design region, the mass entrainment ratio gradually decreased from 0.34 to 0.12, with the maximum achievable pressure lift recorded at 0.88 bar. Unlike SP0 and SP2, SP4 provided a more gradual performance decline under off-design conditions and the best visualization of the ejector performance curve. This suggests that this configuration provides an effective balance between the entrainment

performance and stable operation.

Finally, the performance curve for SP7, corresponding to the most restricted throat among analyzed SPs, is shown in Figure 3.6 d). This configuration yielded the highest on-design mass entrainment ratio observed in the study, with values between 0.40 and 0.45. However, the slope of the performance curve was visibly steeper compared to other SPs, indicating a more rapid deterioration in performance when moving away from the optimal point. Under off-design conditions, the mass entrainment ratio dropped from 0.35 to 0.17, with the maximum pressure lift limited to 0.38 bar. This narrow operating range suggests that while SP7 is capable of best performance in optimal conditions, its sensitivity to system changes is higher, making it less suitable for fluctuating operating environments without an active control intervention.

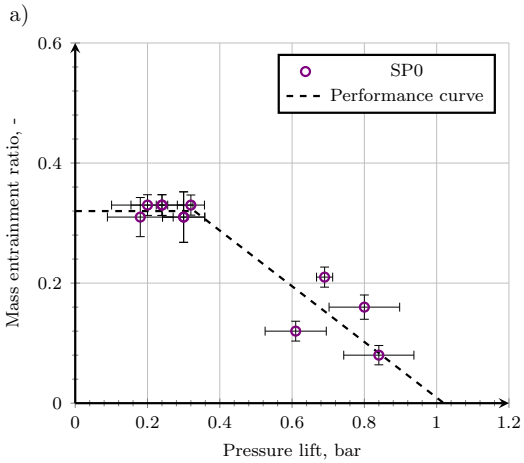
a)
SP0
Performance curve
Mass entrainment ratio, -
Pressure lift, bar
0
0.2
0.4
0.6
0.8
1
1.2

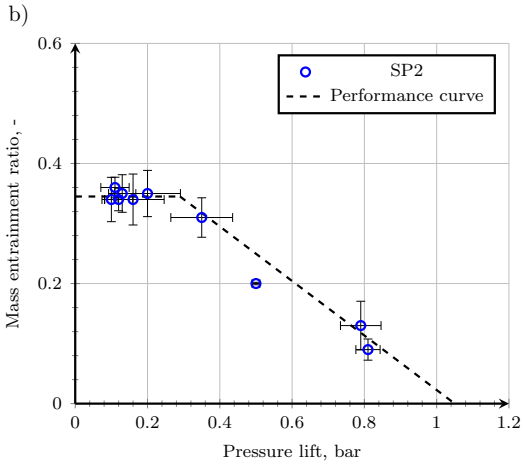
b)
SP2
Performance curve
Mass entrainment ratio, -
Pressure lift, bar
0
0.2
0.4
0.6
0.8
1
1.2

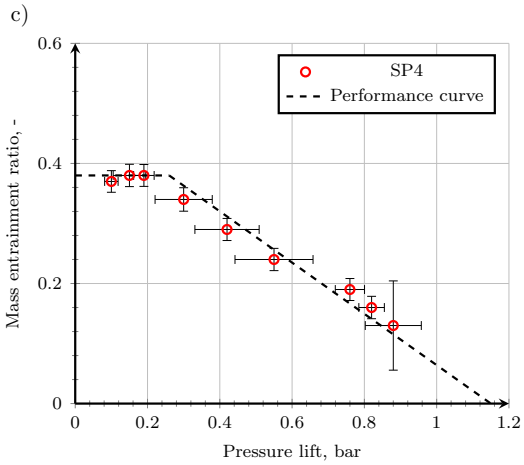
c)
SP4
Performance curve
Mass entrainment ratio, -
Pressure lift, bar
0
0.2
0.4
0.6
0.8
1
1.2

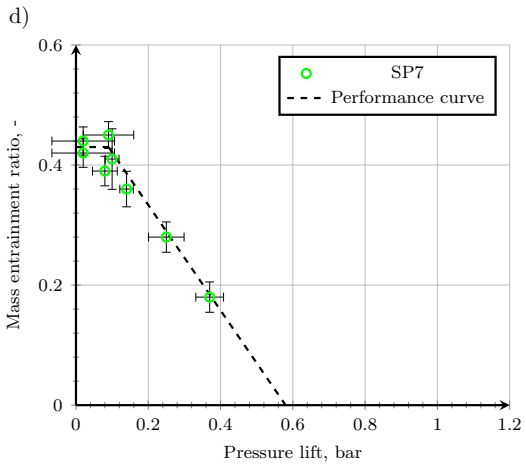

Figure 3.6: *Ejector performance curves presenting the mass entertainment ratio as a function of the pressure lift determined experimentally for four spindle positions (SP).*

To better illustrate the characteristics of the manufactured ejector and its modulation capability, Figure 3.7 overlays all the individual efficiency curves previously presented in Figure 3.6 a)-d) for selected spindle positions. By connecting the experimentally determined critical points, a spindle control line is formed. This curve effectively captures the relationship between the SP and the peak of efficiency of the ejector, offering a visual representation of the modulation range of entrainment enabled by the variable geometry design.

Contrary to the linear spindle control trends reported in the literature for ejectors operating under ideal or design-point conditions, the control line obtained in this study exhibits a distinctly curved shape. This deviation may again be attributed to the significantly lower pressure of the motive nozzle used in the present experimental setup compared to the nominal design conditions of the ejector. Under these suboptimal conditions, only SP7 appears to operate within the double-choking regime, a supersonic flow condition in which the mixed streams reach critical flow. In contrast, for positions SP0 through SP4, the ejector is likely operating in a single-choking regime, where only the motive nozzle is choked and the suction flow remains subcritical. This has implications not only for the device efficiency but also for the stability and control sensitivity of the ejector.

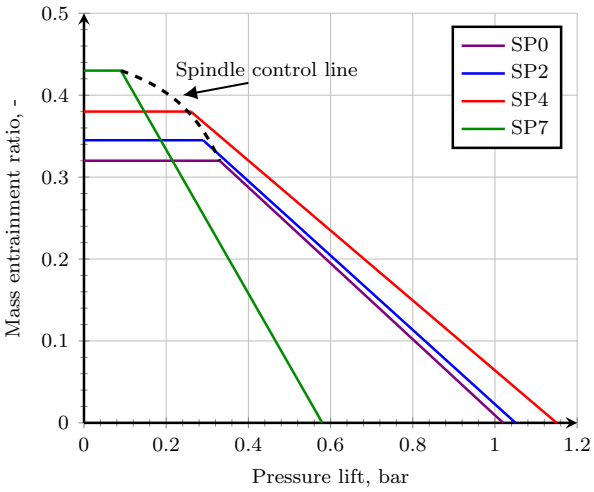

Figure 3.7: *The R290 VGE efficiency curves for four SP and the representation of potential ejector capacity control as a spindle control line.*

3.3.2 Pressure profile analysis

The second part of the experimental campaign was focused on the analysis of the static pressure distribution along the ejector measured by differential pressure sensors installed at multiple locations along the ejector body, that were previously presented in Figure 3.3. This approach aimed to provide deeper insight into the flow behavior, including the mixing process, shock wave propagation, and pressure recovery, particularly in relation to the influence of the spindle position.

First, the pressure profile was defined for the spindle position SP0. Two operating points with the motive nozzle inlet pressures of 17.49 bar and 17.90 bar were selected for a comparison. The resulting pressure distributions are presented in Figure 3.8. In the Figure 3.8 a), the ejector operated with a pressure ratio of 1.061. The pressure profile shows a visible pressure drop across the motive nozzle to the premixer pressure, lower than that of the suction nozzle, allowing for entrainment of the suction nozzle stream. As the supersonic flow progressed into the converging section of the mixing chamber, the pressure increased up to 6 bar. Then, in the constant area section of the mixing chamber, a local pressure drop occurred, falling below the upstream premixer pressure. This behavior indicates a shockwave train forming within the mixer, a phenomenon commonly associated with unsteady flow and underexpanded supersonic jets. Downstream of the mixer,

the pressure rose steadily in the diffuser, reaching 6.40 bar at the outlet.

For the second operating point (Figure 3.8 b)), where the motive nozzle pressure was slightly higher, i.e. 17.90 bar, the pressure ratio increased to 1.268. Despite this change, the pressure drop across the motive nozzle up to the premixer remained nearly identical compared to the previous case, suggesting that the premixer flow conditions were relatively insensitive to small increases in the motive inlet pressure at SP0. However, in the converging section of the mixing chamber, a more pronounced pressure increase of almost 1 bar was observed. This phenomenon indicates a stronger mixing or a more developed shock structure under the higher pressure ratio. The pressure again decreased slightly in the constant-area section of the mixer, likely due to the same shock-induced mechanisms, before recovering in the diffuser. The outlet pressure in this case stabilized at 5.20 bar, significantly lower than in the first scenario.

As far as the results for SP2 are concerned, the motive nozzle inlet pressure for the analyzed points presented in Figures 3.9 a) and 3.9 b) were 17.61 bar and 17.54 bar, respectively. In the Figure 3.9 a), the ejector operated with the diffuser outlet pressure of 5.73 bar, and the pressure ratio equal to 1.177. The pronounced pressure drop immediately downstream of the motive nozzle indicates a potential for effective suction flow entrainment in the premixer. This sharp decline suggests the presence of strong local expansion effects or shock-wave interactions that begin within the mixing section. In the constant-area section of the mixer, a further pressure drop is observed, going lower than the suction nozzle pressure. In the diffuser section, the expected pressure recovery occurs, with a steady increase in static pressure up to the outlet, confirming the efficient momentum exchange and flow deceleration.

The second pressure profile for SP2 (Figure 3.9 (b)) was determined at an outlet pressure of 5.25 bar, yielding an overall pressure ratio of 1.253. The general shape of the profile closely resembles that of the Figure 3.9 a), and is similar to the SP0 case presented in Figure 3.8 b). Small differences in the profile are visible in the mixer and diffuser sections. In particular, the pressure variations within the mixer are more pronounced in the SP2 configuration, suggesting a more complex shockwave structure. Additionally, the diffuser exhibits a more effective pressure recovery, with the outlet pressure surpassing that of SP0 at a similar pressure ratio (Figure 3.8 b)). These observations highlight the impact of the operating conditions on both flow behavior and the efficiency of pressure recovery in the ejector.

Figure 3.10 a) presents the static pressure profile of the ejector at the spindle position SP4, characterized by the motive nozzle inlet pressure

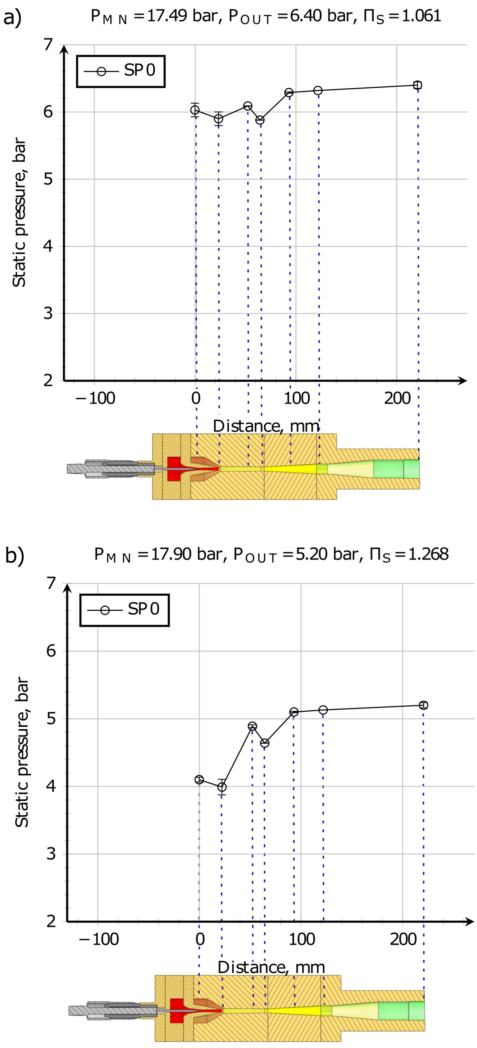

Figure 3.8: *Static pressure profile of the R290 VGE operating with a spindle at SP0.*

of 17.35 bar and the diffuser outlet pressure of 4.60 bar, resulting in a pressure ratio of 1.095. The profile starts with a substantial pressure drop immediately downstream of the motive nozzle. In the mixing chamber, the pressure continues to decline, accompanied by pronounced oscillations within the constant-area section. These oscillations indicate complex flow structures, reflected shock waves and turbulent mixing layers. Subsequently, the diffuser exhibits the anticipated gradual pressure recovery, ultimately achieving the measured outlet pressure.

In comparison, Figure 3.10 b) illustrates the pressure distribution at the

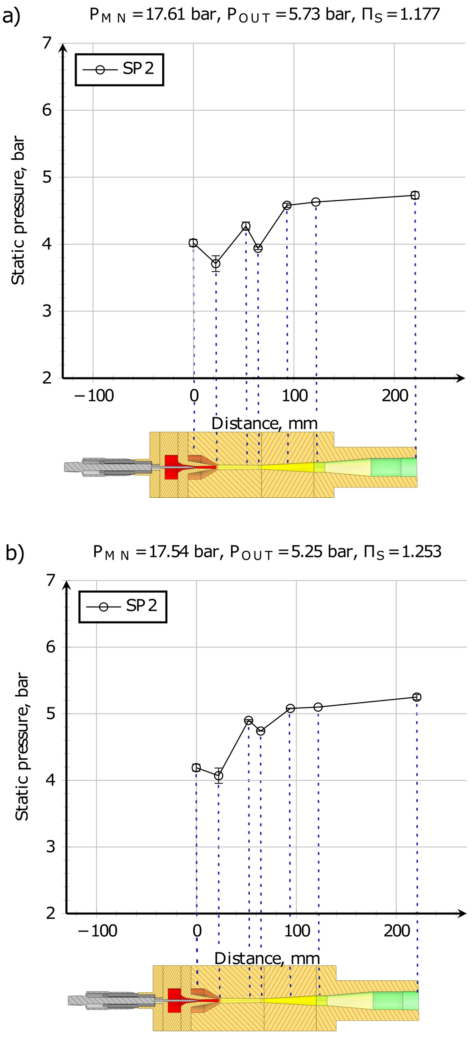

Figure 3.9: *Static pressure profile of the R290 VGE operating with a spindle at SP2.*

second operating point characterized by the motive nozzle inlet pressure of 17.33 bar and the diffuser outlet pressure of 4.14 bar, yielding the pressure ratio of 1.375. The profile exhibits a similar initial trend, characterized by the pressure drop following the motive nozzle and at the onset of the mixer section. However, in this case, the pressure within the mixer section presents fewer and smaller oscillations, indicating a more stable internal flow behavior. Although the diffuser section still facilitates a smooth pressure increase towards the outlet, the overall recovery is less pronounced than in the previous scenario, as indicated by the lower final outlet pressure.

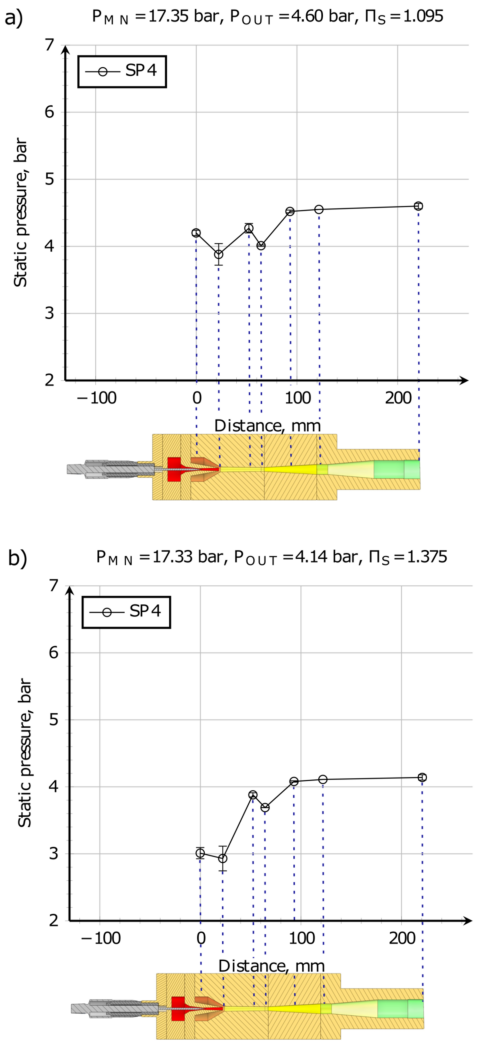

Figure 3.10: *Static pressure profile of the R290 VGE operating with a spindle at SP4.*

In the last SP position examined, namely the SP7, the motive nozzle inlet pressure for both cases is below 17 bar. Starting with Figure 3.11 a), with the motive nozzle inlet pressure of 16.63 bar, the outlet diffuser pressure of 3.11 bar, and the pressure ratio of 1.119, the pressure profile exhibits a sharp decrease immediately after the motive nozzle outlet. In the downstream region, pressure fluctuations are minimal relative to the previous cases, indicating an enhanced pressure stability attributed to the reduced discharge pressure, which implies a significant expansion within the ejector at the reduced throat cross-sectional area at this SP. The mixing

chamber exhibits a pressure recovery after a slight drop in pressure in the constant cross-sectional part of the mixing chamber. Finally, the pressure rise in the diffuser is almost negligible when compared to all the pressure profiles presented in the previous figures.

Lastly, Figure 3.11 b) shows the VGE operation with the motive nozzle inlet pressure of 16.95 bar and the diffuser outlet pressure of 3.20 bar. In this case, the pressure ratio is slightly higher than in the case presented in Figure 3.11 a) and is equal to 1.265. The pressure drop downstream the motive nozzle is relatively small compared to all other pressure profiles. In the mixer section, the pressure shows a moderate increase followed by a slight decrease, indicating a different flow dynamics relative to the SP4 profiles (Figure 3.10 a) and Figure 3.10 b)). The diffuser exhibits a more pronounced pressure recovery, resulting in the diffuser outlet pressure marginally higher than that in Figure 3.11 a), yet still lower than in the SP4 cases due to the low outlet pressure.

In conclusion, the pressure profiles recorded for the SP2 and SP4 configurations exhibit highly dynamic behavior within the mixing chamber, characterized by significant pressure fluctuations and oscillations. These patterns indicate complex internal shockwave interactions and unsteady flow structures. In contrast, the SP7 profiles demonstrate a more stable pressure distribution within the mixer. However, this stability corresponds to a reduced pressure recovery in the diffuser, as evidenced by the relatively lower outlet pressures. The observed differences across spindle positions underscore the influence of ejector capacity control on local flow regimes and wave propagation within the ejector.

3.4 Conclusions

The experimental results presented in this chapter confirm that the SP significantly influences the mass entrainment characteristics of the ejector. Higher SP values presented increased the mass entrainment ratios under identical motive pressure conditions, demonstrating effective capacity control through changes in the AR of the motive nozzle. The ability to adjust the effective throat area using the spindle enables performance optimization under varying pressure lift conditions, allowing the ejector to maintain operation closer to its design point. This confirms the potential of the VGE as a dynamic and efficient component within refrigeration systems operating under variable thermal loads.

The analysis of relationship between mass entrainment ratio and the outlet pressure increase for the selected SPs demonstrated that ejector operation at

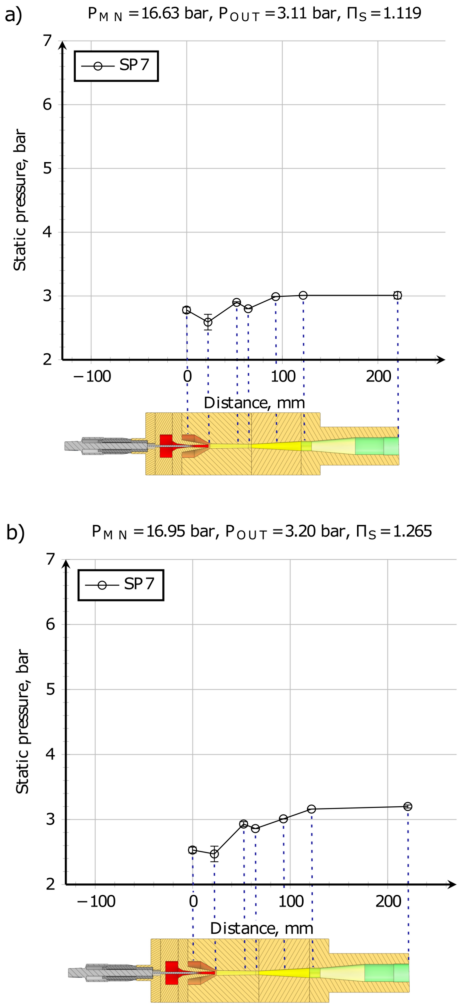

Figure 3.11: *Static pressure profile of the R290 VGE operating with a spindle at SP7.*

SP4 shows the most favorable performance, combining operational stability with an extended operatinf range. This configuration provided a smoother performance transition under off-design conditions compared to SP0 and SP2, presenting the closest visualization of the ejector performance curve to the theoretical one. These characteristics indicate that SP4 achieves an effective balance between entrainment performance and stable operation.

As the ejector operated under conditions that deviate from those for which it was originally intended, particularly with respect to the motive nozzle pressure, the observed behavior of the ejector control line was nonlinear, unlike the one presented in the literature. Nonetheless, the experimental

results validate the efficacy of the spindle mechanism in enabling capacity control of the ejector, even in non-ideal operating scenarios.

The determined local pressure profiles highlighted differences in the internal flow behavior under similar operating conditions but different spindle positions. The experimentally observed trends offer valuable insights for validation of future CFD models, particularly for refining the detailed interaction between shock structures and mixing efficiency in VGE.

CHAPTER 4

Reduced Order Model of Variable Geometry Ejector

The growing demand for energy-efficient refrigeration systems has driven the development of advanced modeling techniques for ejector components. Therefore, this chapter presents the different ejector ROM approaches used for preparing the VGE models based on CFD simulations, which were implemented in the dynamic model of the ERS utilizing a waste heat recovery. The ROM data source is a set of CFD simulation results obtained using an advanced and versatile homogeneous equilibrium model (HEM) that enables simulation of supersonic flow in single-phase and two-phase ejectors. This approach offers a computationally efficient yet accurate method for the ejector characterization across a wide operational envelope, which may be implemented in any kind of system equipped with the gas ejector, i.e. the ERS.

4.1 Data collection for the Reduced Order Model

4.1.1 Selection of a data source

The methodology of reduced order modeling of ejectors used in this study was initially prepared and thoroughly validated by Haida et al. [110]. This modeling approach was designed to provide fast and accurate simulations suitable for dynamic analysis of the transcritical R744 refrigeration systems. The first ROM of the two-phase R744 ejector was formulated using the Proper Orthogonal Decomposition (POD) technique combined with the Radial Basis Function (RBF) interpolation approach and trained exclusively on the data obtained with CFD simulations using HEM. This model demonstrated prediction accuracy within $\pm 10\%$ for both mass flow rates when compared to experimental measurements, and achieved computational times below 0.05 seconds per case, making it well-suited for real-time applications. To enhance the model accuracy and extend its applicability to a wider range of operating conditions, including subcritical regimes, an approach of hybrid ROM [111] was introduced. This variant comprised input data from both CFD and experimental results, i.e. a dataset of approximately 5 380 CFD and 200 experimental points. Validation against independent experimental data revealed that the hybrid ROM predicted the mass flow rates of the motive and the suction nozzle within $\pm 5\%$ and $\pm 10\%$, respectively. The hybrid ROM also demonstrated excellent agreement in the mass entrainment ratio prediction, achieving relative errors within $\pm 1\%$ when compared with the experimental system measurements. These results highlight the suitability of the hybrid ROM approach for integration into system-level simulation environments, offering a reliable and computationally efficient alternative to high-fidelity CFD in transient simulations of ejector-based refrigeration systems.

In this study, the input data used to develop the ROM of the R290 VGE was generated only by means of the CFD simulations similar to [110]. The choice of not using the experimental data for preparing the input dataset to create ROM was due to the limitations of the available experimental facility previously described in Chapter 3. Its operational range is not in the desired range of operating conditions for the dynamic analyses of the R290 VGE application in the ERS, which is the target system for the considered ROM application. Therefore, the pure numerical approach based on the advanced HEM modeling of VGE was adopted for the reduced order modeling. This ensured a consistent, well-controlled ejector operation in the desired ejector operating range.

4.1.2 CFD model formulation

The CFD model used in this study employed the enthalpy-based energy equation on the basis of the homogeneous equilibrium flow assumptions initially developed and tested by Smolka et al. [88]. This model is suitable for simulating single-phase, two-phase, and supercritical fluid flows. The model has been thoroughly tested for different ejector geometries and a variety of operating conditions of the two-phase ejector working in the transcritical R744 refrigeration system in the work of Palacz et al. [112]. It is characterized by high mass flow rate accuracy with relative errors below 10% for the the motive nozzle conditions in area close to and above the critical point. In the single-phase region, Haida et al. [113] reported in their validation of the liquid R744 ejector that the HEM achieved accuracy below 11% for the motive nozzle mass flow rate and below 10% for the suction nozzle mass flow rate for two analyzed liquid ejector geometries. Moreover, it was successfully applied for the R744 supercritical operation of the R744 ejector-based Brayton cycle [114]. Besides the R744, the CFD model used in this thesis was also applied in the ejector designing process for other refrigerants, like butane, liquified natural gas or the HFOs.

To solve the governing equations, Ansys Fluent software with a pressure-based solver was selected. Since the model was developed for simulating the two-phase flow, where it presented high accuracy, it can be succesfully applied for the single-phase flow analysis. Thanks to its absolute pressure-specific enthalpy definition, it is also capable of predicting the transition to the two-phase flow and its characteristics, which is not possible with a standard single-phase model employing a temperature-based energy equation. Moreover, it has already been configured with the reduced order modelling of the ejector, where it demonstrated high accuracy of the mass flow rates prediciton and was characterized by quick and robust operation when implemented to the dynamic modeling [115]. However, in this work, the ROM was completed with a novel, more universal framework based on a ejector performance parameters, with different sets of inputs and output, described in more details in the following sections of this chapter.

Homogeneous Equilibrium Model

The energy equation based on enthalpy [88] was used instead of the default temperature-based energy equation to simulate supersonic flow inside the R290 VGE. The model, suitable also for simulating two-phase flows, assumes that both phases are in thermodynamic and mechanical equilibrium, which means that the pressure, temperature, velocity, turbulence kinetic en-

ergy, and turbulence dissipation rate are the same for both phases. Hence, all the thermodynamic properties for the vapor and liquid phases are determined as a function of pressure and specific enthalpy:

$$f(p,h) = \rho, \mu, \lambda, c_p \tag{4.1}$$

where ρ is the density, μ is the dynamic viscosity, λ is the thermal conductivity, and c_p is the specific heat capacity.

The governing equations for a steady-state compressible fluid flow used in this study, presenting the conservation of mass and momentum, are described in Equations (4.2) and (4.3).

$$\nabla \cdot (\overline{\rho}\widetilde{\boldsymbol{\upsilon}}) = 0 \tag{4.2}$$

where symbols $\overline{(\cdot)}$ and $\widetilde{(\cdot)}$ denote the Reynolds- and Favre-averaged quantities, respectively, and $\boldsymbol{\upsilon}$ is the velocity vector.

$$\nabla \cdot (\overline{\rho}\widetilde{\boldsymbol{\upsilon}}\widetilde{\boldsymbol{\upsilon}}) = -\nabla p + \nabla \cdot \widetilde{\tau} \tag{4.3}$$

where τ is the stress tensor.

To simulate the supersonic flow inside the ejector, the SST turbulence model was used, being characterized by a high level of reproduction of flow characteristics and accuracy of predicting mass flow rates [106,112,116,117]. Therefore, the additional governing equations for the turbulence kinetic energy and the turbulence dissipation rate are as follows:

$$\nabla \cdot (\overline{\rho}\widetilde{\boldsymbol{\upsilon}}K) = \nabla \cdot \left[\Gamma_K \nabla K\right] + \widetilde{G_K} - Y_K \tag{4.4}$$

$$\nabla \cdot (\overline{\rho}\widetilde{\boldsymbol{\upsilon}}\omega) = \nabla \cdot \left[\Gamma_K \nabla \omega\right] + G_\omega + Y_\omega + D_\omega \tag{4.5}$$

where K is the turbulence kinetic energy, G_K is the generation of the turbulence kinetic energy due to the mean velocity gradients, G_ω is the generation of turbulent dissipation, Y_K and Y_ω is the dissipation of K and ω due to the turbulence, ω is the turbulent dissipation rate and D_ω is the cross-diffusion term.

The set of equations described above must be completed with the temperature or the specific enthalpy as an independent variable by the energy equation:

$$\nabla \cdot (\overline{\rho}\widetilde{\boldsymbol{u}}E) = \nabla \cdot (\lambda \nabla \widetilde{T} + \widetilde{\tau} \cdot \widetilde{\boldsymbol{u}}) \tag{4.6}$$

where E is the total enthalpy.

The total enthalpy defined in the energy equation is the sum of mixture-specific enthalpy and kinetic energy:

$$E = \widetilde{h} + \frac{\widetilde{\boldsymbol{u}}^2}{2} \tag{4.7}$$

Because the energy transfer in this work is modeled using an enthalpy formulation, the diffusive term is transformed to:

$$\nabla \cdot (\lambda \nabla \widetilde{T}) = \nabla \cdot (\Gamma \nabla h) - \nabla \cdot \left[\Gamma \left(\frac{\partial h}{\partial p} \right)_T \nabla p \right] \tag{4.8}$$

where Γ is the effective diffusion coefficient defined using Equation (4.9).

$$\Gamma = \left(\frac{\lambda}{\frac{\partial h}{\partial T}} \right)_p \tag{4.9}$$

The diffusive heat transfer for the simulated transonic flow is not significant, and the enthalpy dependence on the pressure is not as strong as its dependence on the temperature. Therefore, the last term in Equation (4.8) is neglected in this analysis.

Instead of solving a classical temperature-based energy equation implemented in the software, the user-defined transport equation is derived and implemented into the solver. The Fluent software allows for implementation of an additional scalar equation, called User-Defined Scalar (UDS), of which the steady-state Favre averaged equation has the following form:

$$\nabla \cdot (\rho \tilde{\boldsymbol{u}} \tilde{\phi_S}) = \nabla \cdot \left(\Gamma_{\text{eff}} \nabla \tilde{\phi_S} \right) + \dot{S}_\phi \tag{4.10}$$

where ϕ is an arbitrary scalar, Γ_{eff} is the effective diffusion coefficient of this scalar and $\dot{S}_\phi$ is the scalar source term. The Reynolds averaged form of the energy equation (Equation (4.8)) can be written as follows:

$$\begin{aligned} \nabla \cdot \left\{ \overline{\rho(\tilde{\boldsymbol{u}} + u'') \left[(\tilde{h} + h'') + \frac{(\tilde{u}_i + u_i'')^2}{2} \right]} \right\} \\ = \nabla \cdot \left[\Gamma \nabla \overline{(\tilde{h} + h'')} \right] + \nabla \cdot \left[\overline{(\tilde{\boldsymbol{\tau}} + \boldsymbol{\tau}'') \cdot (\tilde{\boldsymbol{u}} + \boldsymbol{u}'')} \right], \quad i = 1, 2, 3 \end{aligned} \tag{4.11}$$

Employing the properties of fluctuations (e.g. the term $\overline{\rho y'} = 0$ for any quantity y), and neglecting the term with $\overline{h'}$, Equation (4.11) can be rewritten in the following form:

$$\begin{aligned}\nabla \cdot \Bigg(& \rho\tilde{\boldsymbol{u}}\tilde{h} + \overline{\rho \boldsymbol{u}'' h''} + \overline{\rho\tilde{u}\frac{\tilde{u}_i\tilde{\boldsymbol{u}}_i}{2}} + \overline{\rho\tilde{\boldsymbol{u}}\frac{u_i'' u_i''}{2}} \\ & + \overline{\rho u'' u_i'' \tilde{u}_i} + \overline{\rho \boldsymbol{u}''\frac{u_i'' u_i''}{2}} \Bigg) \\ & = \nabla \cdot (\Gamma \nabla \tilde{h}) + \nabla \cdot (\overline{\tilde{\boldsymbol{\tau}} \cdot \tilde{\boldsymbol{u}}}) + \nabla \cdot (\overline{\tilde{\boldsymbol{\tau}} \cdot u''})\end{aligned} \tag{4.12}$$

The considered terms of Equation (4.12) are modeled in the following manner using the SST turbulence model:

$$-\overline{\rho u'' h''} = \Gamma_T \nabla \tilde{h} \tag{4.13}$$

$$\frac{1}{2}\overline{\mu_i'' \mu_i''} = K \tag{4.14}$$

$$-\overline{\rho u'' u_i''}\tilde{u}_i = \boldsymbol{\tau}_T \cdot \tilde{\boldsymbol{u}} \tag{4.15}$$

$$\overline{\rho \boldsymbol{u}''\frac{u_i'' u_i''}{2}} - \overline{\tilde{\boldsymbol{\tau}} \cdot \boldsymbol{u}''} = -\left(\mu + \frac{\mu_T}{\sigma_K}\right)\nabla K \tag{4.16}$$

where σ_K is the turbulent Prandtl number for the kinetic energy.

$$\Gamma_T = \frac{\mu_t}{\sigma_T} \tag{4.17}$$

The two fluctuation-related terms on the left-hand side of Equation (4.16), are assumed to have a negligible contribution compared to the modeled turbulent diffusion term and are therefore omitted from the analysis. Therefore, to obtain the mechanical energy equation, the terms presented in Equations (4.13)-(4.15) are substituted into the energy equation (Equation (4.12)), and by separating the kinetic energy contribution from the total energy balance, the mechanical energy equation for the mean flow can be expressed as:

$$\nabla \cdot \left(\rho\tilde{\boldsymbol{u}}\frac{\tilde{u}^2}{2}\right) = -\nabla\overline{p} \cdot \tilde{\boldsymbol{u}} + \nabla\tilde{\boldsymbol{\tau}} \cdot \tilde{\boldsymbol{u}} \tag{4.18}$$

The thermal energy equation in the form of scalar equation for implementation in the Ansys Fluent software, by replacing the scalar ϕ_S by the specific enthalpy, is eventually taking the following form:

$$\nabla \cdot (\rho \tilde{\boldsymbol{u}} \tilde{h}) = \nabla \cdot \left(\Gamma_{h,\text{eff}} \nabla \tilde{h} \right) + \dot{S}_{h1} + \dot{S}_{h2} + \dot{S}_{h3} \tag{4.19}$$

where the effective diffusion coefficient $\Gamma_{h,\text{eff}}$ is the sum of the effective diffusion coefficient (Equation (4.9)) and the turbulent diffusion coefficient (Equation (4.17)). The source terms $\dot{S}_{h1}$, $\dot{S}_{h2}$ and $\dot{S}_{h3}$ describe the mechanical energy, the irreversible dissipation of the kinetic energy variations and the dissipation of the turbulent kinetic energy, respectively. These sources have the following forms:

$$\dot{S}_{h1} = \tilde{\boldsymbol{u}} \cdot \nabla \overline{p} \tag{4.20}$$

$$\begin{aligned} \dot{S}_{h2} = (\mu + \mu_T) \Bigg\{ & 2 \left[\left(\frac{\partial \tilde{u}}{\partial x} \right)^2 + \left(\frac{\partial \tilde{v}}{\partial y} \right)^2 + \left(\frac{\partial \tilde{w}}{\partial z} \right)^2 \right] \\ & + \left(\frac{\partial \tilde{u}}{\partial y} + \frac{\partial \tilde{v}}{\partial x} \right)^2 + \left(\frac{\partial \tilde{u}}{\partial z} + \frac{\partial \tilde{w}}{\partial x} \right)^2 \\ & + \left(\frac{\partial \tilde{v}}{\partial z} + \frac{\partial \tilde{w}}{\partial y} \right)^2 - \frac{2}{3} (\nabla \cdot \tilde{\mathbf{u}})^2 \Bigg\} \\ & - \frac{2}{3} \overline{\rho} K \nabla \cdot \tilde{\mathbf{u}} \end{aligned} \tag{4.21}$$

$$\dot{S}_{h3} = -\overline{\rho} \tilde{\boldsymbol{u}} \cdot \nabla K \tag{4.22}$$

The source terms are implemented to the Ansys Fluent by means of the User-Defined Functions (UDF), which are the custom C-language functions that extend the capabilities of the standard software.

Boundary conditions

For the CFD model used in this study, the pressure-based boundary conditions at both inlets and the pressure-outlet at the diffuser (ejector) outlet were selected. At the inlet boundaries, the pressure and specific enthalpy were prescribed with the values defined for the considered operating points, creating the set of inputs for the ROM to ensure an accurate representation of the expected operating conditions. The range of specific enthalpy at the ejector inlets was widened in order to create an operational envelope of VGE, taking into account various levels of superheating parameters, ensuring that the ROM is capable of handling the fluctuating operating conditions of the ERS during dynamic system simulations. For the pressure-outlet

boundary condition, the fixed value of the pressure was prescribed, with a user-defined function (UDF) calculating the specific enthalpy profile from the neighboring cell row, which resulted from the enthalpy scalar equation being updated at each simulation iteration. All simulations assumed adiabatic conditions, with all ejector walls having prescribed zero heat flux at wall-type boundaries.

The global range of operating conditions considered for the VGE, specified to cover the operational envelope necessary for the application of the ejector in ERS, is presented in Table 4.1.

Table 4.1: *Global ranges of the boundary conditions at the motive and suction nozzle inlets and the diffuser outlet used for the numerical simulations of R290 VGE.*

Ejector port	Pressure, bar	Spec. enth., kJ/kg	Sat. temp., °C	Superheating, -
Motive nozzle	25.9 - 41.2	595.8 - 660.9	70 - 103	0 - 8
Suction nozzle	5.0 - 7.3	577.1 - 606.0	2 - 15	0 - 8
Diffuser	5 - 15	–	–	–

4.1.3 Numerical mesh

The numerical meshes for all the analyzed SP positions from Besagni et al. [29] were used to perform the CFD simulations of the VGE operation. The numerical grid of VGE at SP0 presented in Figure 4.1 was prepared as a structured 2-D axisymmetric grid using Ansys Mesher software.

Following a similar approach presented in other ejector studies [28, 118, 119], special care was taken to ensure proper mesh cell sizes in areas with expected strong gradients of flow parameters, particularly in the zone near the motive nozzle exit and at the beginning of the mixing section. For this study, eight individual numerical meshes were prepared, each corresponding to one of the spindle positions shown in Figure 2.3. The meshes consist of approximately 145k elements, with 110 cells in the longitudinal direction, and a maximum aspect ratio of 3 to maintain element quality and solver stability. The value of y^+ was maintained in the range of 30-200 to properly resolve the boundary layer with wall-function-based turbulence modeling. Additionally, two cycles of mesh refinement were applied in the Ansys Fluent on the basis of the Mach number gradient criterion, using a threshold of 0.1. This local mesh refinement allowed for the capture of the shock structures and local compressibility effects with higher accuracy. The meshing strategy selected for this study ensures both numerical stability and physical accuracy for simulations of supersonic flow in the ejector domain. The convergence criterion for the simulations was set for both mass flow

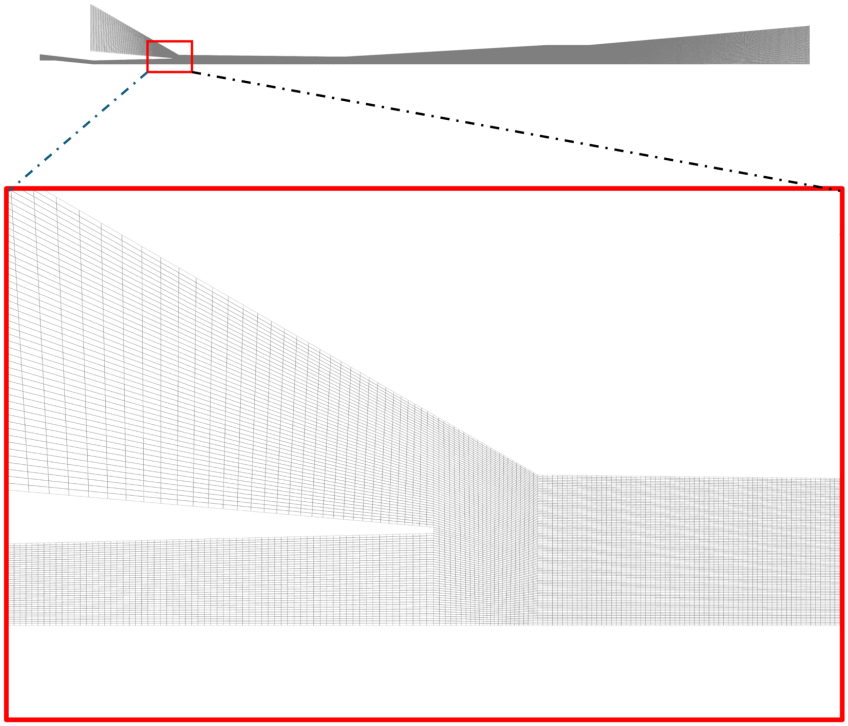

Figure 4.1: *Visual representation of the numerical mesh of the R290 VGE at SP0 from Besagni et al. [29] with a zoomed-in view at the motive and suction nozzle outlets and beginning of the mixing section. Adapted and modified from Besagni et al. [29].*

rates to be below 0.001 kg/s of change within 50 iterations. Each simulation required approximately 30-45 minutes of computation time, depending on the operating condition.

4.1.4 Numerical modeling of ejector

The numerical model presented in the previous sections was executed 275 968 times for simulations of the R290 VGE using the boundary conditions presented in Table 4.1 and considering all the analyzed 8 SPs. In this section, its performance is analyzed for a single operating condition and four representative spindle positions, namely SP0, SP2, SP4, and SP7. The selected operating condition of the ejector for the visualization of its operation at different SPs correspond to a typical air-conditioning application utilizing the low-temperature waste heat for generating the gas for the ejector

motive nozzle, where the motive nozzle saturation temperature $T_{MN,sat}$ is equal to 84°C and the motive nozzle inlet temperature is 89°C. The suction nozzle saturation temperature $T_{SN,sat}$ was set to 5°C, with the nozzle inlet temperature of 9°. The outlet saturation temperature $T_{outlet,sat}$ was set at 20°C, representing the ERS operation at that level of ambient temperature. These conditions were chosen as representative for the ejector operation in a typical operation of the R290 ERS, ensuring a realistic assessment of the ejector flow regimes under different spindle displacements.

Starting with the analysis of mass flow rates for the considered SPs presented in Table 4.2, the results shows the influence of the ejector control using spindle on the mass flow rates and resulting mass entrainment ratio. At SP0, the ejector operates in the highly-efficient on-design mode with the highest motive nozzle mass flow rate of 0.304 kg/s and the highest mass entrainment ratio of 0.29 for this set of motive and suction nozzle operating conditions. Moving the spindle to SP2 and SP4, the ejector still maintains the efficient on-design operation, but the motive nozzle mass flow rate decreases to 0.0291 and 0.0254 kg/s, respectively. The spindle movement toward the motive nozzle throat increases the mass entrainment ratio, which reaches 0.32 for SP2 and 0.39 for SP4. For the most closed spindle position of SP7, the ejector operates in the malfunction regime, in which the ejector no longer entrains the secondary flow, or even works as a secondary outlet, which is indicated by the negative value of the suction nozzle mass flow rate. These results demonstrate that ejector performance is highly sensitive to the SP. While moderate spindle adjustments (SP2-SP4) allow efficient operation with improved entrainment characteristics, excessive closure (SP7) leads to flow reversal and ejector malfunction. Therefore, precise spindle control is essential to maintain stable and efficient ejector operation.

Table 4.2: *Motive and suction nozzle mass flow rates and the corresponding mass entrainment ratio values for selected operating point of R290 VGE for SP0, SP2, SP4 and SP7.*

SP	$\dot{m}_{\text{MN}}$, kg/s	$\dot{m}_{\text{SN}}$, kg/s	MER, -
SP0	0.0304	0.0088	0.29
SP2	0.0291	0.0092	0.32
SP4	0.0254	0.0099	0.39
SP7	0.0152	-0.0063	-0.41

Moving to the contour results, looking at the contours of absolute pressure presented in Figure 4.2, it can be observed that the variation in SP strongly influences the expansion process in the motive nozzle and the subsequent pressure distribution inside the ejector. The cases SP0, SP2, and SP4 represent the on-design operating conditions, while the SP7 corresponds to

the malfunction regime, also referred to as the backflow condition, in which the ejector ceases to entrain the secondary flow. In the cases of SP0-SP4, the supersonic flow is over-expanded due to the relatively low outlet pressure, with a visible normal shock in the entrance to the diffuser.

For the most open configuration presented in Figure 4.2 a), the fully developed expansion through the motive nozzle results in a pronounced pressure drop downstream of the throat and the formation of a low-pressure core that propagates deep into the mixing section. The pressure drop in the premixer drives the effective entrainment of the secondary stream, and the gradual pressure recovery is observed along the diffuser. At the intermediate spindle positions (Figure 4.2 b) and c)), the partial closure of the motive nozzle modifies the expansion behavior and increases the local back pressure, resulting in a more visible expansion downstream the motive nozzle in the premixer. The pressure fields show the occurrence of multiple oblique shock structures downstream of the nozzle exit and an oblique shock in the diffuser. The observed distribution is characteristic of moderate throttling, where the motive flow still entrains the secondary stream, although with reduced intensity and less uniform mixing.

For the most closed spindle position of SP7 presented in Figure 4.2 d), the strong throttling effect in the motive nozzle together with a relatively high outlet pressure result in suppression of the supersonic expansion. The low-pressure core is no longer sustained along the mixer section, and the flow in the mixing section becomes entirely subsonic. The pressure contours reveal the presence of a slightly higher value of pressure in the secondary chamber of the ejector suction nozzle, associated with the occurrence of backflow from the mixing section into the suction chamber. This condition marks the malfunction regime, in which the ejector ceases to entrain the secondary flow.

Overall, the pressure fields confirm that as the spindle advances from SP0 to SP7, the ejector transitions from the stable supersonic on-design operation towards the malfunction regime. This progression is associated with the gradual disappearance of the low-pressure region, intensification of local shock structures, and eventual establishment of backflow in the mixing section, which prevents further suction flow entrainment.

Next, the velocity contour plots are presented in Figure 4.3. The analyzed cases present different throttling characteristics at various SPs, which is reflected in the extent of expansion in the ejector mixing section and the corresponding velocity magnitudes inside the mixer.

For the most open configuration of SP0 presented in Figure 4.3 a), the flow expands through the motive nozzle reaching the highest velocities

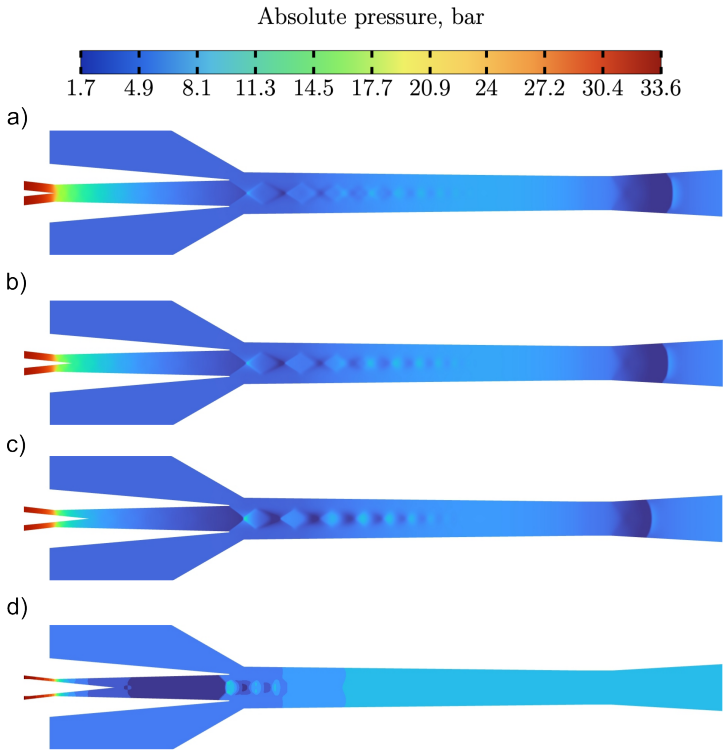

Figure 4.2: *Pressure contours in bar of the R290 VGE operating at: a) SP0, b) SP2, c) SP4, and d) SP7.*

exceeding 430 m/s, corresponding to the Mach = 2. The supersonic core extends far downstream into the mixing section, and the weak shock structures formed in the core region indicate a smooth pressure recovery process. At intermediate spindle positions SP2 and SP4 presented in Figures 4.3 b) and c), respectively, the partial closure of the motive nozzle increases the local back pressure, resulting in a more pronounced normal shocks downstream of the nozzle throat. These shock structures are clearly visible in the mixing section, where the interaction between the high-momentum motive flow and the entrained suction flow generate alternating regions of the flow acceleration and deceleration. Stronger reflections and shock patterns observed in these cases are associated with increased mixing intensity and energy dissipation, corresponding to moderate entrainment ratios.

For the most closed configuration of SP7 representing the ejector operation in malfunction regime, the reduction of the motive nozzle exit area leads to earlier termination of the supersonic jet and the formation of a compact subsonic region at the beginning of the mixer. The velocity in the

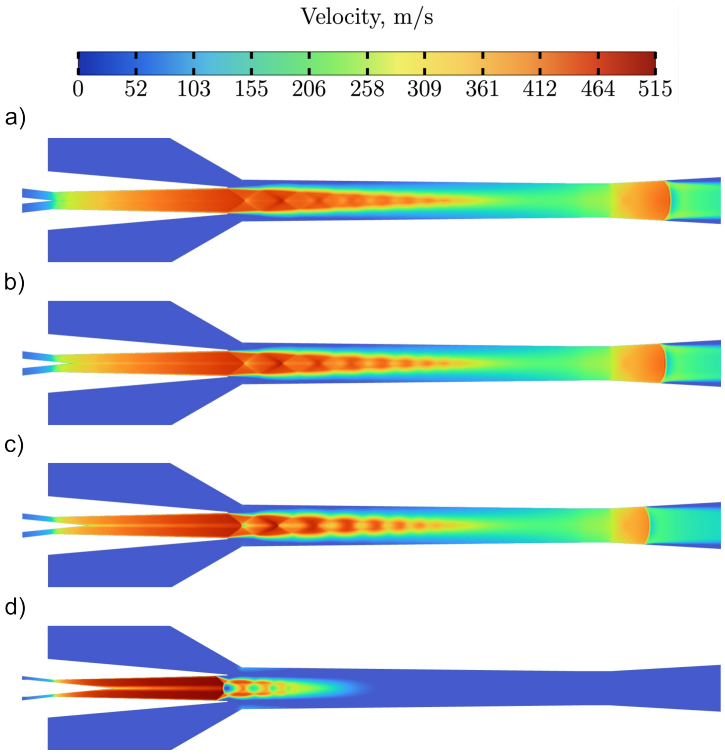

Figure 4.3: *Velocity contours in m/s of the R290 VGE operating at: a) SP0, b) SP2, c) SP4, and d) SP7.*

motive nozzle exceeds the 500 m/s, corresponding to the Mach = 2.5. The velocity field shows a rapid drop of the jet momentum and the appearance of a low-velocity zone in the premixer. The shortened supersonic core indicate excessive throttling and inefficient momentum exchange, which reduces the overall ejector performance and pressure recovery in the diffuser.

Looking at the fields representing the specific enthalpy for the R290 VGE presented in Figure 4.4, it can be observed that for cases of SP0, SP2 and SP4 presented in Figures 4.4 a)-c), the motive nozzle flow entrains the suction stream, which is then dragged along the mixing section and gradually mixed with the high-speed motive flow. The distribution of specific enthalpy illustrates the energy exchange between the two streams and the thermal homogenization along the ejector length indicating the thorough mixing.

For the first three cases of SP0, SP2 and SP4, the high specific-enthalpy motive flow expands efficiently, producing a distinct low-enthalpy core downstream the nozzle throat. The mixing process is gradual, with the specific enthalpy increasing smoothly along the mixing section until a uni-

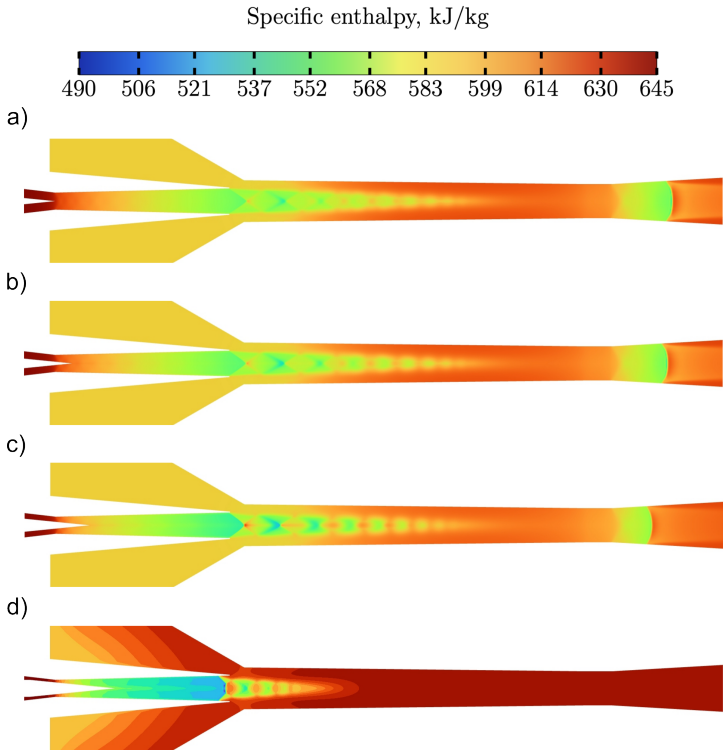

Figure 4.4: *Specific enthalpy contours in kJ/kg of the R290 VGE operating at: a) SP0, b) SP2, c) SP4, and d) SP7.*

form field is achieved at the diffuser outlet. This indicates a highly-efficient on-design ejector operation, in which the entrained secondary stream is effectively accelerated and mixed without strong local discontinuities. In the shock wave, the alternating local values of lower and higher specific enthalpy fields are visible, corresponding to the local pressure variation in the shock waves. These features confirm the presence of an intense mixing process.

At the SP7, the strong throttling at the motive nozzle exit results in a reduced expansion and the relatively high value of absolute pressure in the pre-mixer section does not allow the entrained flow to be introduced. The supersonic core vanishes rapidly, and the entire mixing section is filled with the higher enthalpy values, indicating the ejector malfunction and backflow conditions, in which the ejector is not entraining the secondary nozzle flow to the mixer and the ejector operates as a typical throttling device. Therefore, the suction chamber is filled with the high specific enthalpy fluid, of values closer to those observed at the ejector outlet.

Overall, it can be concluded that as the spindle advances towards the closed position, the specific enthalpy field transitions from a smooth and continuous mixing regime to the operation at ejector backflow for the analyzed operating conditions. This confirms that excessive throttling deteriorates the ejector performance by reducing the expansion work potential and weakening the entrainment of the secondary stream, and that the spindle position should be appropriately selected for the given operating conditions of the ejector.

4.2 Reduced Order Model formulation

The ROM is developed using the POD technique combined with RBF interpolation based on the data generated by the CFD model presented in the Section 4.1. This POD-RBF application for modeling ejectors was prepared and thoroughly validated by Haida et al. [111] for the R744 two-phase eject1ors. This approach allows the ROM to approximate the fluid dynamics behavior of complex devices such as supersonic ejectors under operating conditions not covered by the input dataset with high accuracy. Moreover, this method, implemented in an object-oriented environment such as Modelica, enables the fast execution of system simulations, allowing studies of dynamic behavior and creation of in-house control systems, with ROM computation times typically in a fraction of a second [115].

4.2.1 Mathematical approach

The POD technique creates an optimal approximation base from the set of N sampled values of the ejector flow parameters, which are stored in vectors referred to as snapshots [120]. Collecting M of such snapshot vectors, each corresponding to a specific set of operating conditions, produces the rectangular snapshot matrix U. These snapshots are functions of input parameters. Therefore, the main aim of POD is to determine the orthogonal matrix F that reconstructs the matrix $\mathbf{U}$ through a linear combination of the snapshots:

$$\mathbf{\Phi} = \mathbf{U} \cdot \mathbf{V} \tag{4.23}$$

where $\mathbf{V}$ is the modal matrix, which is obtained by solving the eigenvalue problem:

$$\mathbf{C} \cdot \mathbf{V} = \mathbf{\Lambda} \cdot \mathbf{V} \tag{4.24}$$

with $\mathbf{\Lambda}$ being a diagonal matrix of eigenvalues, and $\mathbf{C}$ the positive semi-definite covariance matrix defined as:

$$\mathbf{C} = \mathbf{U}^{\mathrm{T}} \cdot \mathbf{U} \tag{4.25}$$

where $\mathbf{U}^{\mathrm{T}}$ is the transpose of the snapshots matrix. Solving this eigenvalue problem yields the POD basis vectors:

$$\mathbf{C} \cdot \phi^{\mathrm{i}} = \lambda_{\mathrm{i}} \cdot \phi^{\mathrm{i}} \tag{4.26}$$

where ϕ^{i} is the orthogonal POD basis vector and λ_{i} are the eigenvalues stored by the diagonal matrix $\mathbf{\Lambda}$.

The truncated POD model $\overline{\Phi}$ considers K $<$ N elements for M operating points, reducing the size of the orthogonal basis:

$$\overline{\Phi} = \mathbf{U} \cdot \overline{\mathbf{V}} \tag{4.27}$$

where $\overline{\mathbf{V}}$ is the truncated modal matrix with first K eigenvectors of covariance matrix $\mathbf{C}$. This reduced POD basis remains orthogonal and preserves optimal approximation properties. Reconstruction of a given snapshot using this truncated approximation depends on the parameters used to generate the snapshot. An arbitrary snapshot can defined as as:

$$\mathbf{u}^{\mathrm{j}} \approx \sum_{\mathrm{k=1}}^{\mathrm{K}} \overline{\Phi}^{\mathrm{k}} \alpha_{\mathrm{k}}^{\mathrm{j}} \tag{4.28}$$

where $\mathbf{u}^{\mathrm{j}}$ is the vector of the arbitrary snapshot, $\overline{\Phi}^{\mathrm{k}}$ is the k-th element of the truncated orthogonal basis, and $\alpha_{\mathrm{k}}^{\mathrm{j}}$ the unknown coefficient vector related to the snapshot generating parameters. This approximation is valid only for the training snapshots. To predict ejector performance at new operating conditions, an interpolation step is necessary. From Equation (4.28), the snapshot matrix $\mathbf{U}$ can be written as a linear combination of the truncated POD vectors basis:

$$\mathbf{U} = \overline{\Phi} \cdot \overline{\alpha} \tag{4.29}$$

where $\overline{\alpha}$ is the matrix of unknown constant coefficients, which can be calculated by transposing the matrix of orthogonal truncated POD basis multiplied by the snapshot matrix:

$$\overline{\alpha} = \overline{\Phi}^{\mathrm{T}} \cdot \mathbf{U} \tag{4.30}$$

In this ROM approach, the unknown coefficient matrix $\overline{\alpha}$ is defined as a nonlinear function of the input parameters. This functional dependence can be written as:

$$\overline{\alpha} = \mathbf{B} \cdot \mathbf{F} \tag{4.31}$$

where $\mathbf{B}$ is the matrix of the unknown coefficients of selected combination, and $\mathbf{F}$ is the matrix of interpolation functions $f_{\mathrm{i}}(k - k^{\mathrm{i}})$ built from the k parameter distances used in generating the snapshots. In this work, the RBF interpolation, specifically the thin-plate spline radial function with a smoothing parameter, is chosen given its suitability for multidimensional approximation. The spline radial function is as follows:

$$f_{\mathrm{i}}\left(\left|k - k^{\mathrm{i}}\right|\right) = \left(\frac{\left|k - k^{\mathrm{i}}\right|}{r_s}\right)^2 \cdot \ln\left(\frac{\left|k - k^{\mathrm{i}}\right|}{r_s}\right) \tag{4.32}$$

where $\left|k - k^{\mathrm{i}}\right|$ denotes the distance between the current parameter set k and the reference parameters k^{i}, and r is the smoothing factor. Using this definition, the matrix $\mathbf{F}$ is structured as:

$$\mathbf{F} = \begin{bmatrix} f_1\left(|k^1 - k^1|\right) & \cdots & f_1\left(|k^{\mathrm{M}} - k^1|\right) \\ \vdots & \ddots & \vdots \\ f_{\mathrm{i}}\left(\left|k^1 - k^{\mathrm{i}}\right|\right) & \cdots & f_{\mathrm{i}}\left(\left|k^{\mathrm{M}} - k^{\mathrm{i}}\right|\right) \\ \vdots & \ddots & \vdots \\ f_{\mathrm{M}}\left(|k^1 - k^{\mathrm{M}}|\right) & \cdots & f_{\mathrm{M}}\left(|k^{\mathrm{M}} - k^{\mathrm{M}}|\right) \end{bmatrix} \tag{4.33}$$

After the generation of matrix $\mathbf{F}$, the matrix $\mathbf{B}$ in Equation (4.31) can be determined using the singular value decomposition technique [120]. The final prediction of a snapshot at any new parameter set k is then given by:

$$\mathbf{u}^{\mathrm{a}}(k) \approx \overline{\Phi}\, \mathbf{B}\, \mathbf{f}^{\mathrm{a}}(k) \tag{4.34}$$

where $\mathbf{u}^{\mathrm{a}}(k)$ is the snapshot calculated for the arbitrary parameters k, and $\mathbf{f}^{\mathrm{a}}(k)$ is the vector of interpolation functions as defined in Equation (4.32). Implementation of RBF into the POD model reduces the dimensionality of the ROM to the number of unknown parameters k.

4.2.2 Different approaches for building Reduced Order Model of Variable Geometry Ejector

In this thesis, two distinct approaches for reduced order modeling differing in the sets of input and output parameters were analyzed. The first model

utilizes a conventional approach concerning the typical thermodynamic variables as inputs, so the pressure and specific enthalpy at the ejector inlet nozzles, and the pressure at the diffuser outlet. As an output, the ROM predicts the motive and suction mass flow rates for the given operating point within the operational range of the ejector. This pressure-specific enthalpy-based ROM formulation is directly tied to the thermophysical properties of the selected refrigerant for which the ejector was designed, and offers a reliable method for the ejector modeling.

The baseline formulation, referred to as VGE ROM, enables detailed prediction of the mass flow rate for a given operating point within the range of the design refrigerant. The set of input and output parameters of the VGE ROM is as follows:

VGE ROM inputs

- Inlet pressure of the motive nozzle,
- Inlet specific enthalpy of the motive nozzle,
- Inlet pressure of the suction nozzle,
- Inlet specific enthalpy of the suction nozzle,
- Outlet pressure of the diffuser,

with the following parameters being the model outputs:

VGE ROM outputs

- Mass flow rate of the motive nozzle,
- Mass flow rate of the suction nozzle.

In the second approach, the Universal Low-Pressure Fluids VGE ROM (ULF-VGE ROM) is based on a general concept designed to improve the flexibility and transferability of the ejector modeling across different refrigerants with similar thermophysical properties, mainly in terms of their pressure-wise operation in the subcritical refrigeration system. Instead of relying on the aforementioned pressure-specific enthalpy set of inputs that are tied to the ejector operation for a particular fluid, this new approach utilizes two pressure ratios and fluid temperature at inlet nozzles as the model inputs, with the mass entrainment ratio being the single output of the

model. The pressure ratio defining the motive nozzle conditions is a ratio of motive nozzle inlet pressure to the pressure at the diffuser outlet:

$$\Pi_{\mathrm{M}} = \frac{p_{\mathrm{MN}}}{p_{\mathrm{OUT}}} \tag{4.35}$$

where the subscript M denotes the relation of the pressure at the motive nozzle to the one at the diffuser outlet. The secondary pressure ratio is the ratio of diffuser outlet to the suction nozzle inlet pressure:

$$\Pi_{\mathrm{S}} = \frac{p_{\mathrm{OUT}}}{p_{\mathrm{SN}}} \tag{4.36}$$

where the subscript S denotes the relation of secondary nozzle pressure to the diffuser outlet pressure.

This methodology ensures maintaining the characteristics of ejector operation for a wide range of conditions, while enabling the device to be utilized with other refrigerants. Moreover, the mass entrainment ratio as an output can be further combined with different robust modeling methods for the motive nozzle mass flow rate prediction. This structure enables the model to capture the physics of fluid dynamics governing the ejector performance and opens up the possibility to combine it with different methods of ejector modeling. In this thesis, this novel ROM approach was used for analysis of the ERS equipped with an optimized ejector geometry for the R290, but simulating the system with other low-pressure working fluids and their blends, remarkably broadening the scope of study. The set of input parameters and a snapshot of the ULF-VGE ROM are as follows:

ULF-VGE-ROM inputs

- Pressure ratio of the motive nozzle inlet to the diffuser outlet,
- Inlet temperature at the motive nozzle,
- Pressure ratio of the diffuser outlet to the suction nozzle inlet,
- Inlet temperature of the suction nozzle,

with the single output being:

ULF-VGE-ROM output

- Mass entrainment ratio.

Both the presented approaches are based on the same set of CFD input data, but using a different way of defining the operating point of the ejector, which is used to call the ROM. The visual representation of the mechanisms of calling the ROM, aiming exactly at the same operational point for VGE ROM, and ULF-VGE ROM for R290, is presented in Figure 4.5.

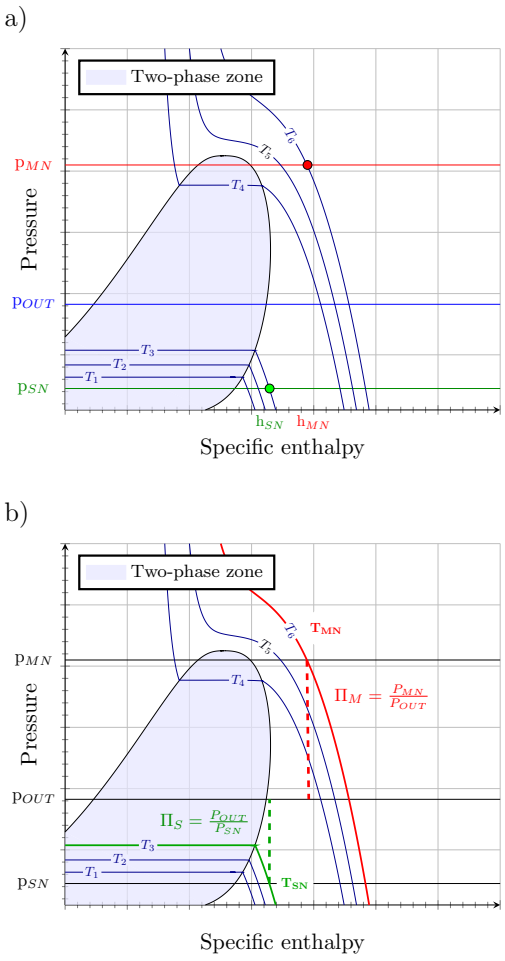

Figure 4.5: *The visual representation of the mechanisms of calling the ROM, aiming exactly at the same operational point for: a) pressure-specific enthalpy approach of VGE ROM, and b) generalized formulation of ULF-VGE ROM.*

4.2.3 Resolution of input data

To provide high accuracy of the ROM based on CFD results, a model calibration was conducted to determine the required resolution of the map of CFD points for the specified operating envelopes at each ejector port. As a result, the ROM is able to reproduce the ejector performance between the CFD results points. This analysis assesses the impact of reducing the number of CFD cases on ROM accuracy, particularly in predicting the mass flow rate at the motive and suction nozzles for various operating conditions.

Three discretization levels for the CFD operating envelope were evaluated to analyze their effect on ROM accuracy. Maps of CFD points were constructed for boundary conditions at the motive and suction nozzles, and the diffuse outlet, varying key thermodynamic parameters: the absolute pressure at all ejector ports, and the temperature with different values of superheat at the inlets of the motive and suction nozzles. For each discretization level, a ROM of single SP was built using a set of CFD simulation results and subsequently validated against an additional CFD simulation performed at an intermediate operating condition, not included in the set of data used to build the ROM. For the model calibration, the SP3 was selected, being the intermediate representative of average ejector operation. The procedure allowed for assessing the minimum required resolution of the CFD map needed to accurately reproduce motive and suction mass flow rates, as well as the mass entrainment ratio across the operating envelope. Three refinement levels were analyzed, and their characteristics are presented in Table 4.3, while the resulting map of points presented in the pressure-specific enthalpy diagram of R290 is presented in Figure 4.6.

Table 4.3: *Definition of CFD envelope refinement levels for model calibration.*

Resolution level	Points for eight SPs	ΔT_{sat}, °C	ΔSH, K	ΔP at p_{out}, bar
Coarse	945	10	4	1.5
Medium	9900	5	2	1.0
Fine	275 968	2	1	0.5

The coarse resolution represents a low-resolution discretization with 945 points per SP, resulting from a saturation temperature interval of 10°C, a superheat step of 4 K, and outlet pressure steps of 1.5 bar. The medium resolution increases the density to 9 900 points per SP, resulting from saturation temperature intervals of 5°C, superheat steps of 2 K, and outlet pressure steps of 1.0 bar. Finally, the fine resolution provides the highest resolution with 275 968 points per SP, resulting from 2°C intervals in saturation temperature, 1 K superheat steps, and 0.5 bar of pressure steps at the outlet

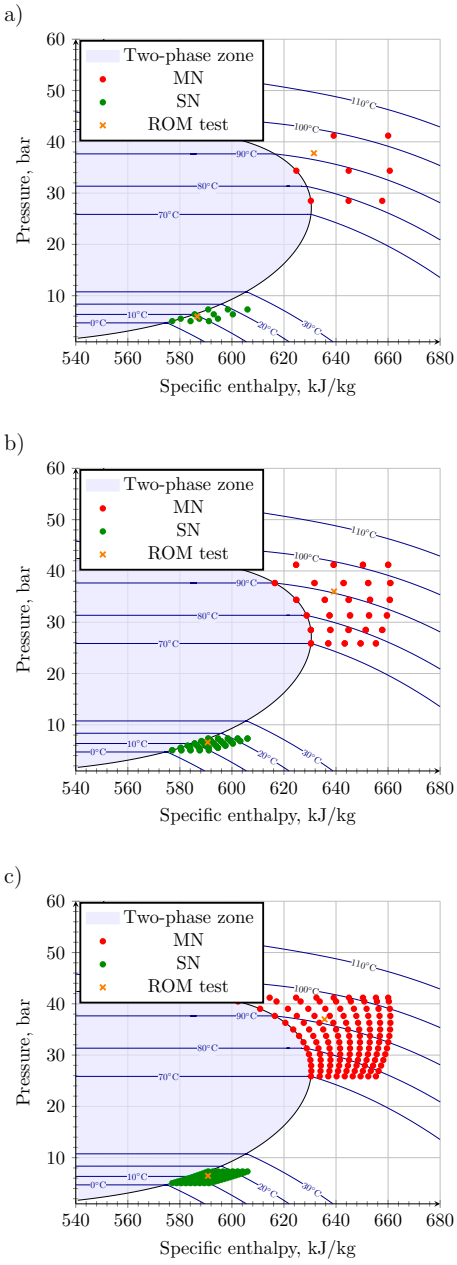

Figure 4.6: *Discretization of the map of CFD results used for input points for the ROM of VGE at SP3: a) coarse resolution, b) medium resolution, and c) fine resolution with highlighted point for ROM testing.*

nozzle. These progressively refined levels allowed systematic evaluation of the minimum required CFD map resolution to achieve accurate ROM prediction of ejector performance across the operating envelope.

For each refinement level, a test point for the direct analysis of ROM results with the CFD simulation result for the determined operating condition was created. The test points were determined as midpoints between the CFD input data in terms of the pressure and superheat value embodied in the specific enthalpy. The selection of this specific methodology of defining test points comes from the fact that, at that location, being at the furthest distance from the other points surrounding that location, is having the lowest accuracy within the operational envelope of the ejector.

The model calibration was performed for the baseline VGE ROM with the inputs specified as the absolute pressure and the specific enthalpy at the motive and suction nozzles, and the pressure at the diffuser outlet. The outputs of the motive and suction mass flow rates, together with the mass entrainment ratio, were compared with the CFD results for the three discretization levels and are presented in Table 4.4. Starting with the coarse resolution, the ROM comparison with CFD results presents poor agreement with CFD results across the entire analyzed outlet pressure operating range.

Table 4.4: *Model calibration results for coarse resolution: comparison of CFD and ROM predictions of the motive and suction nozzle mass flow rates with relative errors.*

P_{out}, bar	Motive nozzle			Suction nozzle		
	$\dot{m}_{MN}^{CFD}$, kg/s	$\dot{m}_{MN}^{ROM}$, kg/s	$\Delta\dot{m}_{MN}$	$\dot{m}_{SN}^{CFD}$, kg/s	$\dot{m}_{SN}^{ROM}$, kg/s	$\Delta\dot{m}_{SN}$
6.0	$3.18{\cdot}10^{-2}$	$3.19{\cdot}10^{-2}$	0.3%	$1.05{\cdot}10^{-2}$	$1.01{\cdot}10^{-2}$	-4.0%
7.5	$3.18{\cdot}10^{-2}$	$3.19{\cdot}10^{-2}$	0.3%	$1.02{\cdot}10^{-2}$	$9.97{\cdot}10^{-3}$	-2.4%
9.0	$3.18{\cdot}10^{-2}$	$3.20{\cdot}10^{-2}$	0.4%	$9.91{\cdot}10^{-3}$	$9.81{\cdot}10^{-3}$	-1.0%
10.5	$3.18{\cdot}10^{-2}$	$3.20{\cdot}10^{-2}$	0.4%	$7.95{\cdot}10^{-3}$	$8.95{\cdot}10^{-3}$	12.5%
12.0	$3.18{\cdot}10^{-2}$	$3.20{\cdot}10^{-2}$	0.5%	$-2.10{\cdot}10^{-3}$	$5.04{\cdot}10^{-5}$	-102.4%
13.5	$3.18{\cdot}10^{-2}$	$3.20{\cdot}10^{-2}$	0.4%	$-1.38{\cdot}10^{-2}$	$-1.43{\cdot}10^{-2}$	3.6%
15.0	$3.18{\cdot}10^{-2}$	$3.20{\cdot}10^{-2}$	0.4%	$-2.55{\cdot}10^{-2}$	$-2.46{\cdot}10^{-2}$	-3.4%

Looking at the mass flow rates, the suction nozzle mass flow rate error reached a value of -102.4%, similar to the ones of the mass entrainment ratio, while the motive nozzle errors remained relatively low within 0.45%. This highlights the fact that despite good reproduction of the motive nozzle mass flow rate, the coarse discretization is insufficient to capture the sensitivity of the suction nozzle mass flow rate, and as a result, also the mass entrainment ratio. This discrepancy is also reflected in the ejector efficiency curve presented in Figure 4.7, so the mass entrainment ratio is presented as a function of outlet pressure. The ROM-based curve fails to

reproduce the characteristic drop in value after reaching the ejector critical point, with relative errors peaking at over -100% near the critical point, so the switching point from on-design to off-design operation. The large relative error variability ranges from approximately +20% down to below -100%.

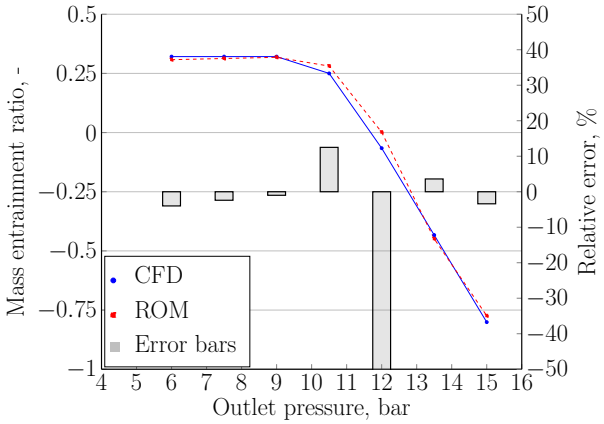

Figure 4.7: *Model calibration of the mass entrainment ratio and the relative error of ROM model to CFD results for coarse resolution (Figure 4.6 a)).*

For the medium resolution results, the ROM provides a significantly improved reproduction of the ejector characteristics, which in this case is very similar to the CFD model results. The obtained suction nozzle mass flow rate errors presented in Table 4.5 are between -3% and +3%, with the motive nozzle errors around $\pm 0.1\%$, and the mass entrainment ratio deviations within $\pm 3\%$, except for a few outliers in the vicinity of the ejector critical point. This level of refinement offers acceptable accuracy for many engineering analyses but may miss local details near critical operating conditions.

Looking at the overall shape of the efficiency curve presented in Figure 4.8, the curve is captured with the visible switch from the flat on-design part to the off-design operation of the ejector. The majority of the mass entrainment relative errors remain within $\pm 5\%$, although the region around the critical point still shows local peaks exceeding +20%.

Finally, the analysis of the fine resolution and the corresponding errors are presented in Table 4.6. The fine resolution demonstrates the best agreement with CFD data across the analyzed range of outlet pressure conditions. The individual values of the suction nozzle mass flow rate errors are generally below 0.3%, with one error value of -4.5%, whereas the errors for the motive

Table 4.5: *Model calibration results for medium resolution: comparison of CFD and ROM predictions of motive and suction nozzle mass flow rates with relative errors.*

P_{out}, bar	Motive nozzle			Suction nozzle		
	$\dot{m}_{MN}^{CFD}$, kg/s	$\dot{m}_{MN}^{ROM}$, kg/s	$\Delta\dot{m}_{MN}$	$\dot{m}_{SN}^{CFD}$, kg/s	$\dot{m}_{SN}^{ROM}$, kg/s	$\Delta\dot{m}_{SN}$
5.0	$2.99{\cdot}10^{-2}$	$2.99{\cdot}10^{-2}$	0.1%	$1.19{\cdot}10^{-2}$	$1.22{\cdot}10^{-2}$	2.7%
6.0	$2.99{\cdot}10^{-2}$	$2.99{\cdot}10^{-2}$	-0.1%	$1.19{\cdot}10^{-2}$	$1.17{\cdot}10^{-2}$	-1.5%
7.0	$2.99{\cdot}10^{-2}$	$2.98{\cdot}10^{-2}$	-0.1%	$1.20{\cdot}10^{-2}$	$1.20{\cdot}10^{-2}$	-0.1%
8.0	$2.99{\cdot}10^{-2}$	$2.98{\cdot}10^{-2}$	-0.1%	$1.23{\cdot}10^{-2}$	$1.24{\cdot}10^{-2}$	0.7%
9.0	$2.99{\cdot}10^{-2}$	$2.99{\cdot}10^{-2}$	0.1%	$1.25{\cdot}10^{-2}$	$1.27{\cdot}10^{-2}$	1.7%
10.0	$2.99{\cdot}10^{-2}$	$2.99{\cdot}10^{-2}$	0.1%	$1.17{\cdot}10^{-2}$	$1.20{\cdot}10^{-2}$	3.1%
11.0	$2.99{\cdot}10^{-2}$	$2.99{\cdot}10^{-2}$	0.0%	$8.29{\cdot}10^{-3}$	$1.02{\cdot}10^{-2}$	23.0%
12.0	$2.99{\cdot}10^{-2}$	$2.99{\cdot}10^{-2}$	0.0%	$1.36{\cdot}10^{-3}$	$1.36{\cdot}10^{-3}$	0.1%
13.0	$2.99{\cdot}10^{-2}$	$2.99{\cdot}10^{-2}$	0.0%	$-7.96{\cdot}10^{-3}$	$-7.88{\cdot}10^{-3}$	-1.0%
14.0	$2.99{\cdot}10^{-2}$	$2.98{\cdot}10^{-2}$	-0.1%	$-1.75{\cdot}10^{-2}$	$-1.70{\cdot}10^{-2}$	-3.0%
15.0	$2.99{\cdot}10^{-2}$	$2.99{\cdot}10^{-2}$	0.2%	$-2.63{\cdot}10^{-2}$	$-2.66{\cdot}10^{-2}$	1.0%

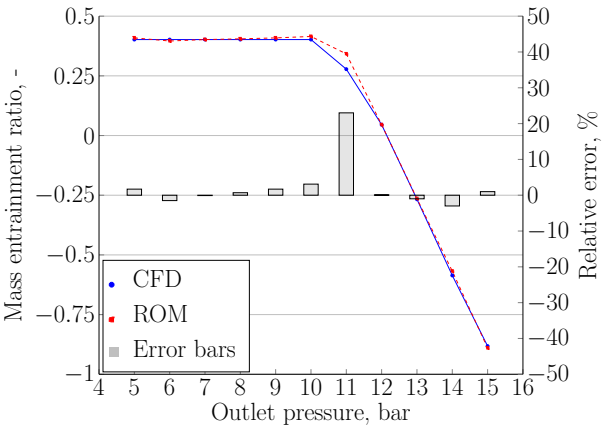

Figure 4.8: *Model calibration of the mass entrainment ratio and the relative error of ROM model to CFD results for medium resolution (Figure 4.6 b)).*

nozzle for this refinement level are negligible (mostly from 0 to 0.1%).

The ROM almost perfectly reproduces the ejector efficiency curve presented in Figure 4.9, including the critical point transition from on-design to off-design operation. The relative errors of the mass entrainment ratio are consistently below 1%, with small peaks visible near the critical point region; however, at an acceptable level of errors below 5%.

This study demonstrates that sufficient resolution in the CFD-derived map of points was achieved by the fine resolution. Therefore, this approach was selected as the optimal discretization, providing robust and accurate reproduction of the ejector efficiency curve, while maintaining low relative

Table 4.6: *Model calibration results for fine resolution: comparison of CFD and ROM predictions of motive and suction nozzle mass flow rates with relative errors.*

P_{out}, bar	Motive nozzle			Suction nozzle		
	$\dot{m}_{MN}^{CFD}$, kg/s	$\dot{m}_{MN}^{ROM}$, kg/s	$\Delta\dot{m}_{MN}$	$\dot{m}_{SN}^{CFD}$, kg/s	$\dot{m}_{SN}^{ROM}$, kg/s	$\Delta\dot{m}_{SN}$
5.0	$3.09{\cdot}10^{-2}$	$3.10{\cdot}10^{-2}$	0.1%	$1.16{\cdot}10^{-2}$	$1.16{\cdot}10^{-2}$	0.0%
5.5	$3.09{\cdot}10^{-2}$	$3.10{\cdot}10^{-2}$	0.1%	$1.16{\cdot}10^{-2}$	$1.16{\cdot}10^{-2}$	0.0%
6.0	$3.09{\cdot}10^{-2}$	$3.09{\cdot}10^{-2}$	0.0%	$1.16{\cdot}10^{-2}$	$1.16{\cdot}10^{-2}$	0.0%
6.5	$3.09{\cdot}10^{-2}$	$3.09{\cdot}10^{-2}$	0.0%	$1.17{\cdot}10^{-2}$	$1.17{\cdot}10^{-2}$	0.0%
7.0	$3.09{\cdot}10^{-2}$	$3.09{\cdot}10^{-2}$	0.0%	$1.17{\cdot}10^{-2}$	$1.17{\cdot}10^{-2}$	0.0%
7.5	$3.09{\cdot}10^{-2}$	$3.09{\cdot}10^{-2}$	0.0%	$1.18{\cdot}10^{-2}$	$1.18{\cdot}10^{-2}$	0.0%
8.0	$3.09{\cdot}10^{-2}$	$3.09{\cdot}10^{-2}$	0.0%	$1.19{\cdot}10^{-2}$	$1.19{\cdot}10^{-2}$	0.1%
8.5	$3.09{\cdot}10^{-2}$	$3.09{\cdot}10^{-2}$	0.0%	$1.20{\cdot}10^{-2}$	$1.20{\cdot}10^{-2}$	0.0%
9.0	$3.09{\cdot}10^{-2}$	$3.09{\cdot}10^{-2}$	0.0%	$1.20{\cdot}10^{-2}$	$1.20{\cdot}10^{-2}$	0.0%
9.5	$3.09{\cdot}10^{-2}$	$3.09{\cdot}10^{-2}$	0.0%	$1.18{\cdot}10^{-2}$	$1.18{\cdot}10^{-2}$	0.0%
10.0	$3.09{\cdot}10^{-2}$	$3.09{\cdot}10^{-2}$	0.0%	$1.13{\cdot}10^{-2}$	$1.13{\cdot}10^{-2}$	0.0%
10.5	$3.09{\cdot}10^{-2}$	$3.09{\cdot}10^{-2}$	0.0%	$1.02{\cdot}10^{-2}$	$1.03{\cdot}10^{-2}$	1.0%
11.0	$3.09{\cdot}10^{-2}$	$3.09{\cdot}10^{-2}$	0.0%	$8.44{\cdot}10^{-3}$	$8.06{\cdot}10^{-3}$	-4.5%
11.5	$3.09{\cdot}10^{-2}$	$3.09{\cdot}10^{-2}$	0.0%	$5.72{\cdot}10^{-3}$	$5.80{\cdot}10^{-3}$	1.3%
12.0	$3.09{\cdot}10^{-2}$	$3.09{\cdot}10^{-2}$	0.0%	$2.10{\cdot}10^{-3}$	$2.11{\cdot}10^{-3}$	0.3%
12.5	$3.09{\cdot}10^{-2}$	$3.09{\cdot}10^{-2}$	0.0%	$-2.21{\cdot}10^{-3}$	$-2.21{\cdot}10^{-3}$	0.2%
13.0	$3.09{\cdot}10^{-2}$	$3.09{\cdot}10^{-2}$	0.0%	$-6.88{\cdot}10^{-3}$	$-6.90{\cdot}10^{-3}$	0.3%
13.5	$3.09{\cdot}10^{-2}$	$3.09{\cdot}10^{-2}$	0.0%	$-1.16{\cdot}10^{-2}$	$-1.16{\cdot}10^{-2}$	0.3%
14.0	$3.09{\cdot}10^{-2}$	$3.09{\cdot}10^{-2}$	0.0%	$-1.62{\cdot}10^{-2}$	$-1.62{\cdot}10^{-2}$	0.1%
14.5	$3.09{\cdot}10^{-2}$	$3.09{\cdot}10^{-2}$	0.0%	$-2.07{\cdot}10^{-2}$	$-2.07{\cdot}10^{-2}$	0.2%
15.0	$3.09{\cdot}10^{-2}$	$3.09{\cdot}10^{-2}$	0.0%	$-2.50{\cdot}10^{-2}$	$-2.50{\cdot}10^{-2}$	0.1%

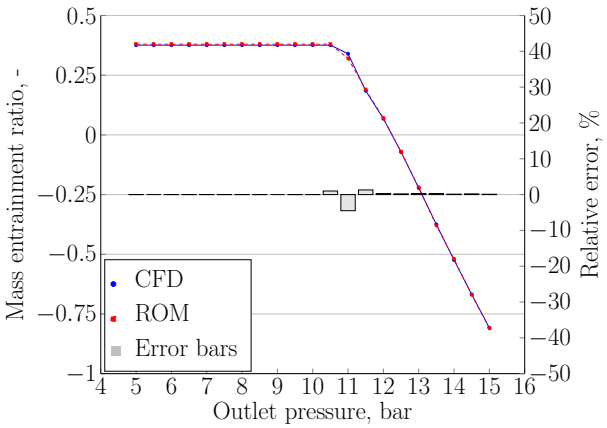

Figure 4.9: *Model calibration of the mass entrainment ratio and the relative error of ROM model to CFD results for fine resolution (Figure 4.6 c)).*

errors for both motive and suction nozzle mass flow rates, as well as good reproduction of the mass entrainment ratio curve.

4.3 Ejector operating envelopes

Each of the ROM of VGE and its resulting operating envelopes were created for an extended operating regime of the ejector to investigate the ejector performance in the dynamic simulations of the R290 ERS system. The operating envelope for the motive and suction nozzles was prepared in a manner that during the simulation of the refrigeration system, the ROM does not exceed its operating range, which could cause the unrealistic behavior of the ejector, and thus lead to instabilities in the simulations of the whole system. Thanks to the HEM model used for generation of the CFD results, the operating conditions of the VGE cover the vapor phase region from the saturation line up to the superheated vapor of 8 K for both inlet nozzles, which ensure the simulation convergence, even at the events of rapid changes in the input parameters, which cause variations in the thermodynamic parameters of the system.

The representation of operating envelopes of the ROM of R290 VGE represented on a pressure-specific enthalpy diagram for the motive and suction nozzle inlets, and the diffuser outlet is presented in Figure 4.10. The range of motive nozzle pressure spans from 27 to 40.7 bar, allowing for an analysis of ejector performance in both the subcritical and the near-critical area.

The range of the motive nozzle temperature was defined from approximately 70 to 106°C, which ensures that the VGE can handle the system operation under varying conditions of the low-temperature heat source. The suction nozzle operating conditions were defined to evaluate the VGE performance for the saturation temperatures between 2.5 and 15°C, representative for operating conditions typical for refrigeration system applications. The resulting operating range of the suction nozzle pressure ranges from 5.25 to 7.2 bar. As far as the diffuser outlet conditions are concerned, the considered pressure range from 5 to 15 bar was specified for all the SPs to cover the entire operating range of the condenser installed in ERS. However, the actual on- and off-design ranges for each SP are strongly dependent on the VGE conditions at the inlet nozzles, so the single SP outlet pressure ranges are limited to the narrower bands. Nonetheless, the broader approach for the definition of this outlet pressure operational envelope also committed to the reliability of simulations and helped with avoiding non-physical ejector behavior arising from operating outside of the ROM operating area, which is crucial for the fluctuating behavior of dynamic simulations.

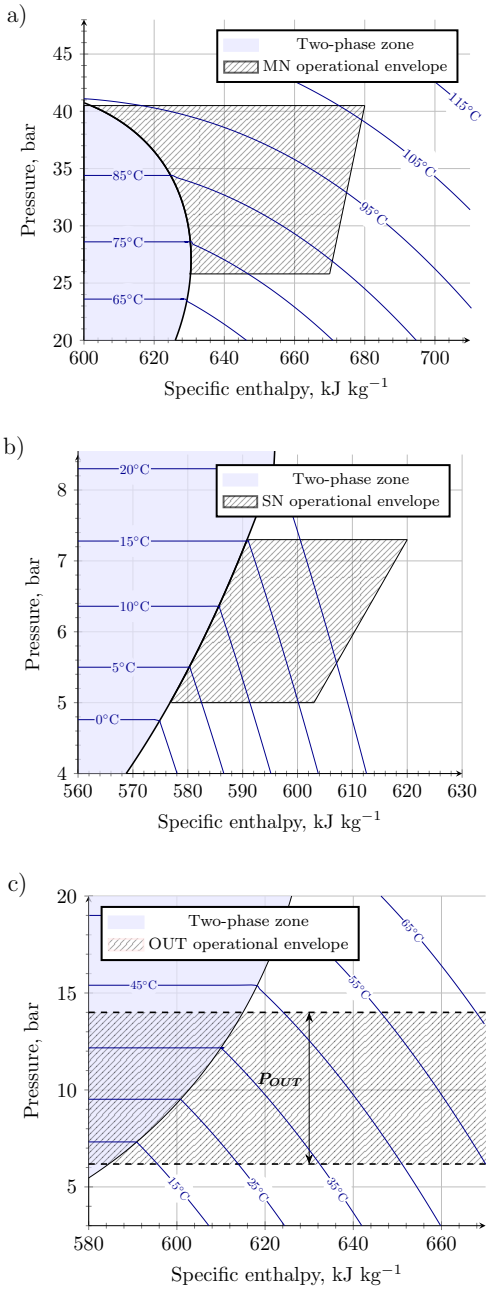

Figure 4.10: *Operating envelope of the R290 VGE presented on a pressure-specific enthalpy diagram for: a) motive nozzle, b) suction nozzle, and c) diffuser outlet.*

4.4 Ejector performance in the Ejector Refrigeration System application

To get to know the characteristic of the VGE before introducing it into the system-level models, the performance maps presenting the motive and suction nozzle mass flow rates were generated using the VGE-ROM with varying motive nozzle conditions. The suction nozzle inlet conditions were fixed at saturation temperature of 10°C with the superheat of 4 K, and the diffuser outlet pressure was fixed at value corresponding to the saturation temperature of 20°C. These performance color maps present the ejector performance in terms of the mass flow rate when operating within the operational area range of the VGE implemented to the R290 ERS operating in the subcritical and near-critical region. The heat maps were prepared for the R290 pressure-enthalpy diagrams for selected representative spindle positions of SP0, SP2, SP4, and SP7. This approach allows for visualization of the VGE behavior distinguishing the difference of its operation in the different cross-sectional areas of the motive nozzle throat.

First, the analysis of the motive nozzle mass flow rate under fixed suction nozzle inlet conditions and the diffuser outlet conditions is presented in Figure 4.11. The gray-shaded region denotes the two-phase zone of R290, limited by the saturation curve in between.

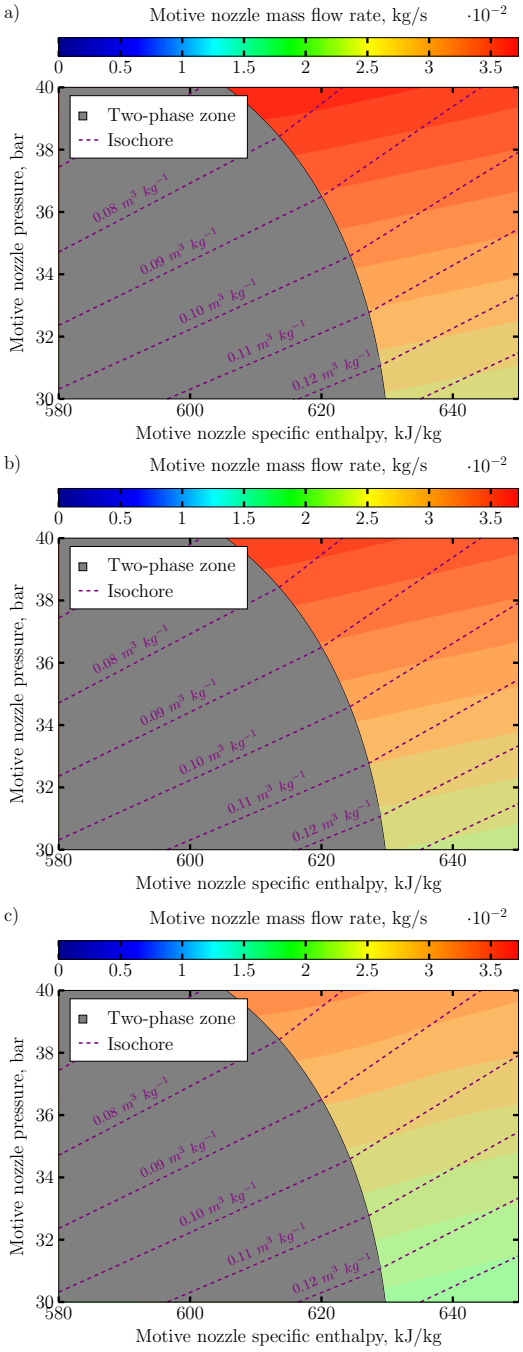
a)
Motive nozzle mass flow rate, kg/s
$\cdot 10^{-2}$
0
0.5
1
1.5
2
2.5
3
3.5
Two-phase zone
Isochore
0.08 m^3 kg^{-1}
0.09 m^3 kg^{-1}
0.10 m^3 kg^{-1}
0.11 m^3 kg^{-1}
0.12 m^3 kg^{-1}
Motive nozzle pressure, bar
Motive nozzle specific enthalpy, kJ/kg
b)
Motive nozzle mass flow rate, kg/s
$\cdot 10^{-2}$
Two-phase zone
Isochore
Motive nozzle pressure, bar
Motive nozzle specific enthalpy, kJ/kg
c)
Motive nozzle mass flow rate, kg/s
$\cdot 10^{-2}$
Two-phase zone
Isochore
Motive nozzle pressure, bar
Motive nozzle specific enthalpy, kJ/kg

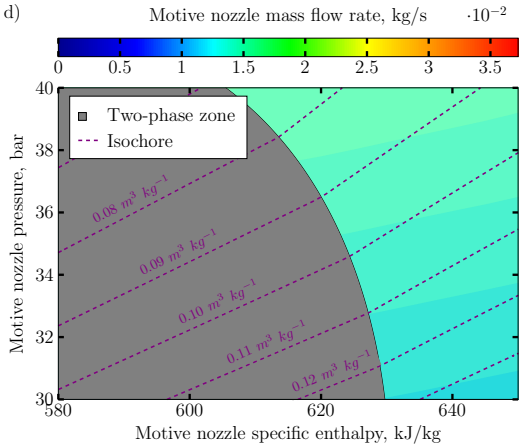

Figure 4.11: *R290 VGE performance maps of the motive nozzle mass flow rate with fixed $T_{SN,sat}$ = 10°C, T_{SN} = 14°C, and $T_{OUT,sat}$ = 20°C, for: a) SP0, b) SP2, c) SP4, and d) SP7.*

Looking at the color maps, the consistent trend of the motive nozzle mass flow rate increase with the increase of the motive nozzle inlet pressure is observed. Moreover, the lower motive nozzle specific enthalpy contributes to higher motive nozzle mass flow rates, indicating that the mass flow rate is the highest for the low values of superheat. This behavior is attributed to the higher density closer to the two-phase region, enhancing the choked flow conditions through the nozzle. The maximum values of the mass flow rates for each SP are observed in the top-left corners of each map, with approximate peak values of $3.6 \cdot 10^{-2}$ kg/s for SP0 and SP2, $3.0 \cdot 10^{-2}$ kg/s for SP4, and a notably reduced value of $1.4 \cdot 10^{-2}$ kg/s for SP7. Conversely, the minimum values of the motive nozzle mass flow rates in each color map are located at low pressure and specific enthalpy furthest from the saturated curve, with the values of $2.4 \cdot 10^{-2}$ kg/s to $1.0 \cdot 10^{-2}$ kg/s for the SP0 and SP7, respectively. When comparing the charts of Figure 4.11 a)-d) with each other, a clear reduction in the overall mass flow rate is observed as the SP advances from SP0 to SP7, which reflects the decrease of the cross-sectional area of the motive nozzle throat. The gradient of the mass flow rate within the single-phase region becomes progressively flatter from SP0 to SP7, suggesting a reduction in flow sensitivity to thermodynamic changes at the motive nozzle.

Next, the contour color map of the suction nozzle mass flow rate is presented in Figure 4.12. The charts of this figure correspond again to the ejector operation at SP0, SP2, SP4, and SP7, respectively, under the fixed

suction nozzle inlet and diffuser outlet conditions.

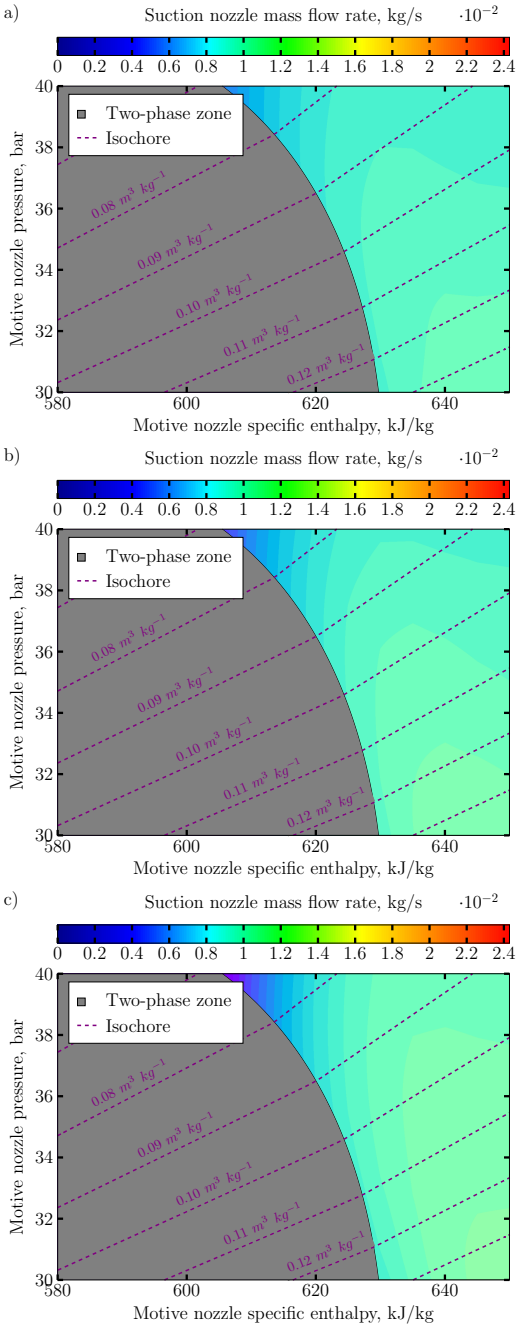

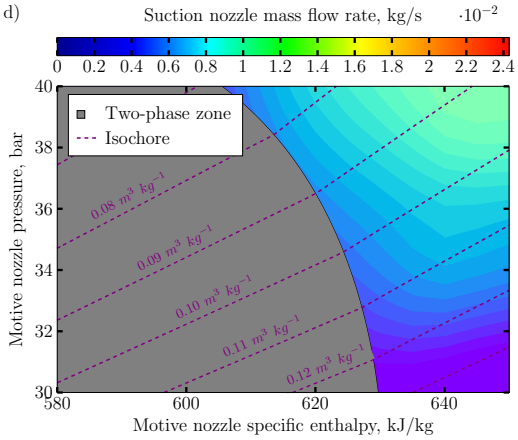

Figure 4.12: *R290 VGE performance maps of the suction nozzle mass flow rate with fixed $T_{SN,sat}$ = 10°C, T_{SN} = 14°C, and $T_{OUT,sat}$ = 20°C and varying motive nozzle inlet conditions presented on a pressure-specific enthalpy diagram for: a) SP0, b) SP2, c) SP4, and d) SP7.*

When analyzing the suction mass flow rate color maps, it can be observed that the suction nozzle mass flow rate increases with the motive nozzle inlet specific enthalpy, with visible optimum values for each of the color map values at some distance from the saturation curve. Moreover, for the charts in Figure 4.12 a) - c), the minimum values of the mass flow rate are close to the critical point of R290, indicating that the ejector experiences a performance drop, which may be a numerical error of the approximation when the model operates close to the limits of the operational envelope. Analyzing the charts of Figure 4.12 a) and b), it can be concluded that the suction nozzle mass flow rate increases with the decrease of the motive nozzle pressure for SP0 and SP2, whereas in Figure 4.12 c) representing SP4, the suction nozzle mass flow rate is independent on the pressure in the analyzed range of the motive nozzle inlet conditions. Finally, when analyzing the contour map of SP7 presented in Figure 4.12 d), it can be observed that for the smallest tested cross-sectional area of VGE motive nozzle, the ejector requires higher motive nozzle inlet pressure values to provide the ejector suction, and indicates that the ejector does not entrain secondary fluid below 32 bar of the motive nozzle inlet pressure.

The maximum value of the suction nozzle mass flow rate for SP0 is $1.0 \cdot 10^{-2}$ kg/s, with the minimum observed value of $0.7 \cdot 10^{-2}$ kg/s. For SP2, the observed maximum flow rate is $1.5 \cdot 10^{-2}$ kg/s , and the minimum value is $0.6 \cdot 10^{-2}$ kg/s. For the SP4, the maximum suction mass flow rate is $1.5 \cdot 10^{-2}$ kg/s, but the ejector is not entraining the secondary flow when

operating in the vicinity of the critical point for the given suction and outlet operating conditions. Finally, for the SP7, the maximum suction nozzle mass flow rate was reached $1.5 \cdot 10^{-2}$ kg/s, and the ejector does not entrain the secondary flow when the motive nozzle operates below 32 bar and in the vicinity of critical point. This may indicate the ejector operating in the choked conditions, which limit the ejector performance and do not allow the device to entrain higher value of the secondary mass flow.

Moreover, the visualization of the VGE performance for the SP ranging from SP0 to SP7 by means of the generated ejector performance curves, so the mass entrainment ratio curves, is presented as a function of outlet pressure. Their analysis for four different operating conditions is illustrated in Figure 4.13.

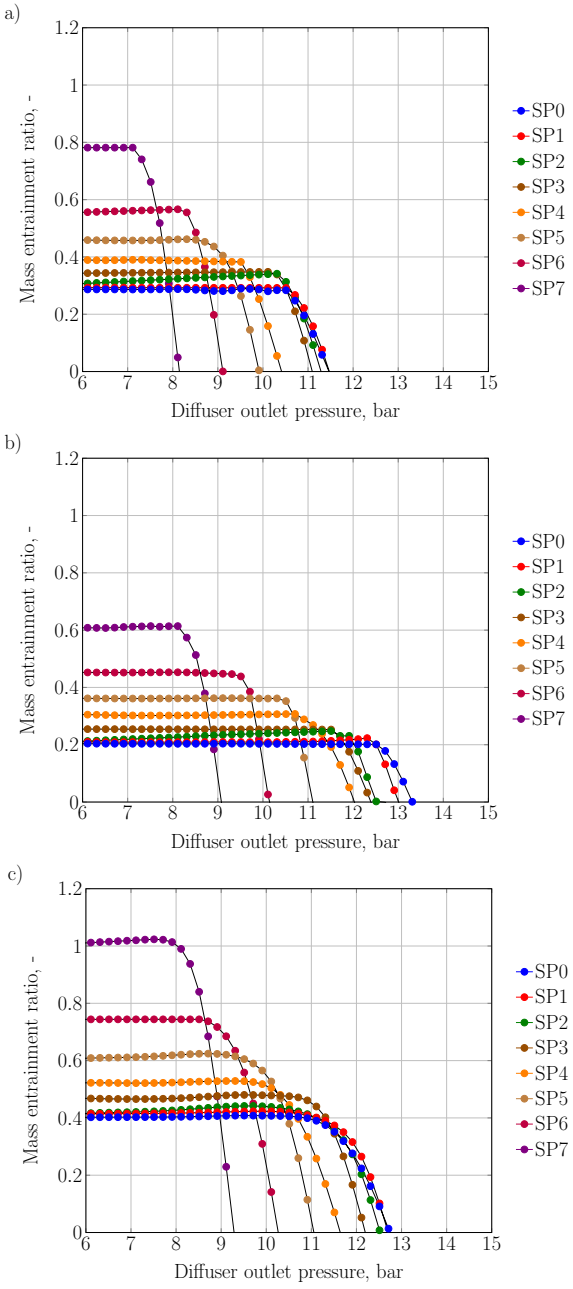
a)
Mass entrainment ratio, -
Diffuser outlet pressure, bar
SP0
SP1
SP2
SP3
SP4
SP5
SP6
SP7
b)
Mass entrainment ratio, -
Diffuser outlet pressure, bar
SP0
SP1
SP2
SP3
SP4
SP5
SP6
SP7
c)
Mass entrainment ratio, -
Diffuser outlet pressure, bar
SP0
SP1
SP2
SP3
SP4
SP5
SP6
SP7

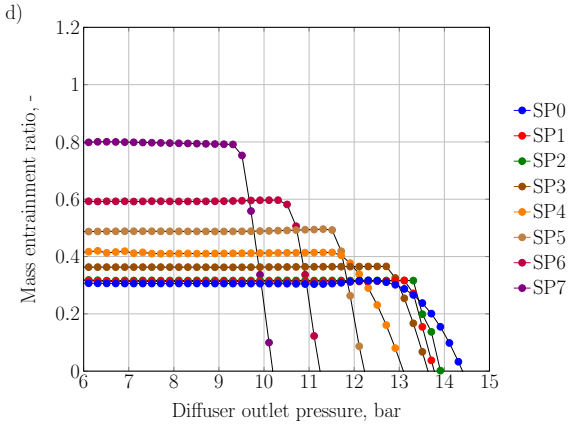

Figure 4.13: *The ejector performance curves of the R290 VGE for SP0-SP7 with varying pressure at the diffuser outlet for: a) $T_{MN,sat}$ = 84°C, $T_{SN,sat}$ = 5°C, b) $T_{MN,sat}$ = 94°C, $T_{SN,sat}$ = 5°C, c) $T_{MN,sat}$ = 84°C, $T_{SN,sat}$ = 15°C, and d) $T_{MN,sat}$ = 94°C, $T_{SN,sat}$ = 15°C.*

The data for these graphs were generated using pairs of constant motive and suction nozzle operating conditions, i.e., two motive nozzle inlet pressure levels corresponding to the saturation temperature of 84°C and 94°C, and similarly, two suction nozzle inlet pressure levels of the saturation temperature of 5°C and 15°C were analyzed. The curves were generated by altering the diffuser outlet pressure by 0.5 bar for the range of 6 to 14 bar.

For each SP, the ejector performance curve presents the typical ejector operation with visible distinction of on- and off-design modes. In the on-design zone observed at the lower outlet pressure values, the device operates at its optimum with constant and the highest possible mass entrainment ratio, thanks to the choked motive flow. The off-design mode of ejector operation is the zone in which the mass entrainment ratio decreases with an increment in outlet pressure. The point at which the ejector transitions from the plateau on-design to a declining trend of the off-design mode is called the critical point, and the pressure value at which it occurs is called the critical pressure of the ejector.

Figure 4.13 a) presents the ejector operation at the motive nozzle saturation temperature of 84°C and the suction nozzle saturation temperature of 5°. The ejector working at these operating conditions achieves its maximum mass entrainment ratio of around 0.8 for SP7 with a relatively low critical pressure of 7.2 bar. The effective VGE operation, thanks to the adjustable spindle, can be broadened up to the critical point of SP0-SP3 at the outlet pressure of 10.5 bar, in which the VGE is able to work at the mass entrainment ratio of approximately 0.3.

When looking at Figure 4.13 b), which corresponds to the motive nozzle saturation temperature of 94°C and the same suction nozzle saturation temperature of 5°C as in 4.13 a), the effect of higher motive nozzle saturation temperature extending the range of the ejector operation in terms of the diffuser outlet pressure can be observed. However, this occurs at the cost of lower mass entrainment ratio. The SP7 reaches the mass entrainment ratio of 0.6 with its critical point shifted to approximately 8.1 bar. At the same time, the SP0-SP2 operate at the mass entrainment ratio of 0.22 with the critical point of approximately 12.5 bar, showing a difference of the critical point pressure of 2 bar related to the ejector operation at 10 K lower saturation temperature of the motive nozzle presented in Figure 4.13 a).

Figure 4.13 c) presents the ejector operation at the motive nozzle saturation temperature of 84°C and the suction nozzle saturation temperature of 15°C. It can be observed that the higher saturation temperature at the suction nozzle leads to an increase of the entrainment performance, due to the lower pressure ratio of the ejector. For these conditions, the maximum mass entrainment ratio for SP7 exceeds the value of 1, with the critical point outlet pressure at 7.2 bar, i.e., a slightly lower value than in the case of the operating condition presented in Figure 4.13 a). These operating conditions are characterized by the wider range of the on-design modes of the analyzed SP, ranging from 0.4 to 1.0. At the same time, the critical point range is extended in terms of outlet pressure, reaching up to 11 bar for the critical points of SP0-SP3.

Finally, Figure 4.13 d) presents the VGE operation at the motive nozzle saturation temperature of 94°C and the suction nozzle saturation temperature of 15°C. In this figure, it can be observed that with the increase of both motive and saturation nozzle pressure, the VGE is able to cover the widest range of outlet pressures, maintaining relatively high entrainment performance. The highest value of the mass entrainment ratio reached at SP7 is 0.8, with the critical point pressure of around 9.3 bar, i.e., the highest for SP7 among analyzed cases. The effective on-design operation of VGE at SP0-SP3 is distinguished by the mass entrainment ratio of around 0.35 at the critical pressures of around 13.2 bar.

Across the analyzed operating conditions, the above-described plots clearly illustrate the typical on-design and off-design behavior of the VGE. Thanks to the adjustable spindle, the operating range of VGE is able to replace several fixed-geometry ejectors, which, with appropriate spindle control, allows for the optimal operation of the device in the single SP on-design modes for a wide range of operating conditions. The overall shift of the on-design region towards higher outlet pressures with the increased

motive nozzle inlet temperature indicates that a greater pressure head is favorable for extending the operational range of the ejector in terms of the diffuser outlet conditions. On the other hand, the increase of the suction nozzle temperature results in a higher mass entrainment ratio, which in the case of ERS operation translates into the increased cooling capacity. Thus, it can be concluded that the use of the VGE ejector is the most suitable for applications in ERS with a high temperature difference between source and ambient temperatures, and that with an increase in the temperature of the cooled space, the cooling capacity increases, which is consistent with classical vapor-compression refrigeration systems [3].

4.5 Implementation of the ejector Reduced Order Model in system analysis

All the VGE ROMs used in the study have been implemented in the Dymola software using a Python code with a mathematical procedure that creates an input file with a set of input data taken at each time step from the Dymola model, and executing a binary file with the ROM that searches for the ejector characteristic outputs for the given operating point. Then, the ROM creates an output snapshot saved in the text file, which at the end of the execution loop is imported back into Dymola.

To implement all the considered models, three separate external ROM call structures were prepared. Each ROM variant is deployed as a compiled binary file accessed using the Python interface that handles file-based communication with the Dymola environment. Figure 4.14 illustrates two approaches: a) the standard pressure-specific enthalpy based VGE ROM returning the motive and suction mass flow rates of the VGE for the given operating conditions, and b) the ULF-VGE ROM using the pressure ratios and temperatures as inputs and providing the output ejector characteristic in a form of the mass entrainment ratio, that can be used to determine the ejector operation for different fluids and their blends. All of the models combine a highly accurate approach to numerical ejector modeling with a highly responsive and robust solution that can be used for a variety of dynamic ejector-based systems analyses.

The Dymola software enables the implementation of add-on utilities via the external functions approach. For this reason, the ejector model in the system was built and derived from the TLK partial ejector model, in which the suction nozzle mass flow rate was introduced directly from the VGE ROM inputs, rather than calculated from the fixed ejector efficiency. The motive nozzle mass flow rates for the VGE ROM were passed to the ejector

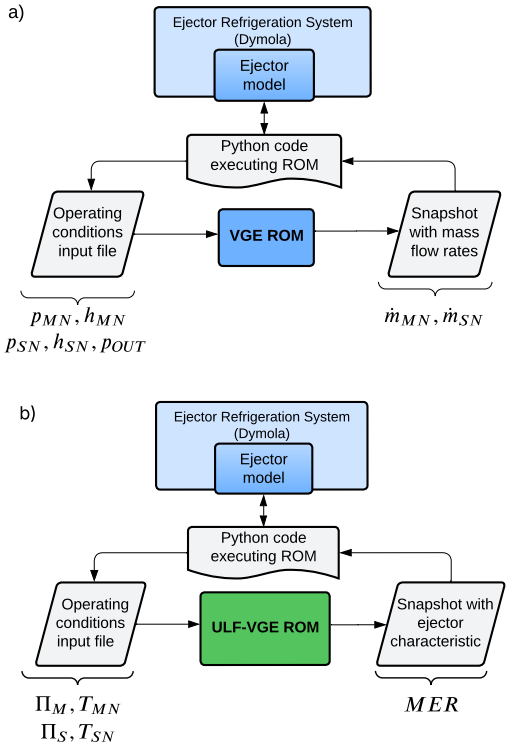

Figure 4.14: *Flowcharts of the implementation of the R290: a) standard VGE ROM, and b) ULF-VGE ROM into the Ejector Refrigeration System in Dymola.*

model by creating a new nozzle model that just passed the value of the mass flow rate from ROM to Dymola.

For the ULF-VGE ROM, which has only a single output of the mass entrainment ratio parameter, the reduced modeling approach was combined with a simple mathematical model for calculating the motive nozzle mass flow rate. The built-in Dymola nozzle model of Brennen correlation for the refrigerant flow through a nozzle (Brennen et al. [121]) was used, with the variable input of the effective nozzle throat cross-sectional area of VGE (see Figure 2.3) that are stored in an array element and load at each simulation time step based on the currently used SP setting. The suction nozzle mass flow rate was calculated in the Dymola function using the mass entrainment ratio equation (Equation (1.1)).

The selected communication approach for the implementation of all the ROMs to the Dymola software allowed to obtain a very fast model for dynamic simulations, which was able to load the ROM outputs to the simulation software within fractions of a second, which did not slow down

the simulation of the considered ERS systems.

4.6 Conclusions

In this chapter, the development of the CFD-based ROM of the R290 VGE was presented. The ROMs were created using a POD-RBF technique, enabling fast and accurate reproduction of ejector behavior while drastically reducing the computational demand in dynamic system simulations. Three ROM variants were introduced: a standard approach of pressure-specific enthalpy-based VGE ROM, and a generalized model based on pressure ratios and temperatures for application with alternative refrigerants, denoted as the ULF-VGE ROM.

A model calibration confirmed that the high-resolution CFD input data is essential for accurate ROM performance, especially in capturing the suction mass flow and the entrainment behavior. The fine resolution approach yielded the relative errors below 1%, ensuring its reliability in dynamic simulations. Moreover, the performance maps and determined characteristic curves highlighted the VGE's flexibility and adaptability to varying thermal and pressure conditions. The ROMs were successfully implemented in Dymola, ensuring a quick response of highly accurate ejector modeling for dynamic system simulations.

CHAPTER 5

Dynamic analysis of R290 ejector-based refrigeration system using varying ambient conditions

This chapter presents the development of the dynamic numerical model of the R290 ERS equipped with the reduced order model of VGE, which, using a highly accurate ejector modeling approach, enables the evaluation of system performance under realistic operating conditions. The objective of this model is to evaluate the transient behavior of the system components, assess the interaction between the VGE and system dynamics, and to implement real-time control strategies. The model was developed in an object-oriented equation-based modeling environment based on the Modelica language [122], which enables simulation of multi-domain thermodynamic systems under dynamic ambient conditions.

The numerical framework is built around the integration of predefined customizable components from the existing ThermoSystems library created by TLK-Thermo GmbH [123], including heat exchangers, pumps, expansion valve, controllers, etc. Each component is configured to reflect physical constraints, geometrical specifications, and its operating principles are based on empirical data and the literature. The dynamic simulation environment

integrates the commonly used literature correlations for heat transfer and pressure drop, and a control logic to ensure realistic thermal and flow behaviors.

The ejector model implementation to Dymola was previously described in Chapter 4.5. This setup allows an accurate simulation of ejector performance, thereby enhancing the model robustness and applicability to real-world operating scenarios. This methodology forms the foundation for simulating various scenarios evaluated in the subsequent Chapters, including different model assumptions, a sensitivity analysis of critical parameters, and the incorporation of additional time-dependent variables.

5.1 System analysis assumptions

In the first stage of the system analysis in this thesis, the performance of the R290 ERS was evaluated for a simplified set of operating conditions, where only the ambient temperature varied over time. This configuration was devoted to isolate the influence of condenser-side waste heat thermal fluctuations on system performance, while maintaining fixed operating conditions at both inlet nozzles of VGE. The motive nozzle inlet conditions representing the generator-side pressure and temperature were held constant throughout each simulation, mimicking a steady waste heat source with a fixed temperature of 90°C and a superheat level of 5 K. Similarly, the conditions at the evaporator outlet (suction nozzle of the VGE) were also held constant, with an evaporation temperature of 10°C and a superheat value of 5 K. The only time-varying input parameter was the ambient temperature, which influenced the condenser and ejector outlet pressures. These ambient profiles were based on historical weather data for three distinct climate zones and were introduced into the model as a 24-hour dataset with hourly values, which were then interpolated for the system time steps using linear interpolation. This setup allowed for a controlled evaluation of how external environmental variations affect the operation of the ERS and provided a baseline for assessing the benefits of incorporating dynamic capacity control of VGE using the spindle. By limiting variability to the ejector outlet side, this phase of the study focused on understanding the ejector system sensitivity to ambient conditions, while maintaining stable conditions at the generator and evaporator. The resulting analysis served as a reference point for later stages, where greater complexity was introduced through variable waste heat temperature data.

5.2 Dynamic model formulation

To evaluate the performance of the proposed VGE-based refrigeration system under varying ambient conditions, a dynamic object-oriented model of the ERS was developed using Dymola simulation software [124]. It is based on the Modelica language, an equation-based, high-level, declarative modeling language that is suitable for the simulation of complex engineering systems. Moreover, it supports both steady-state and dynamic simulation of multi-domain physical systems, and its modular, object-oriented structure makes it highly flexible for applications in the thermal-fluid, mechanical, electrical, and control domains [90, 125–128].

The system model was composed using the TLK ThermoSystem Libraries, specifically TILMedia and TILSuite [123]. The TILMedia provides critical thermophysical properties for various working fluids, including air, water, refrigerants, and commonly utilized heat transfer fluids, while the TILSuite is a validated component library for thermal systems, featuring a range of ready-to-use and customizable elements, such as heat exchangers, compressors, valves, and ejectors. Both TILMedia and TILSuite have been widely applied in the literature for modeling and analysis of thermal systems, and their open structure allows for straightforward modification and integration into user-defined subsystems. In this study, the selected system component parameters and dimensions were adapted to meet the specific thermodynamic requirements of the ejector-based refrigeration cycle investigated.

5.2.1 System layout

The ERS used in this analysis was designed as a vapor-compression ejector-based system equipped with a controllable ejector. The system, of which the layout is presented in Figure 5.1, consists of three heat exchangers: a brazed-plate heat exchanger working as a generator for the waste heat utilization, a fin-and-tube evaporator for cooling, and another fin-and-tube condenser for heat rejection from the system to ambient environment. Furthermore, the system includes a pump, a variable-geometry expansion valve, and a VGE with a spindle.

The auxiliary side of the generator is a loop simulating a waste heat source, with the inlet temperature held constant during the analytical phase. A proportional-integral (PI) controller is utilized on the auxiliary side of the generator to maintain the temperature difference between the inlet and outlet of the auxiliary loop at 4 K, thereby ensuring stable heat transfer without significant energy losses. Ambient temperature conditions for the

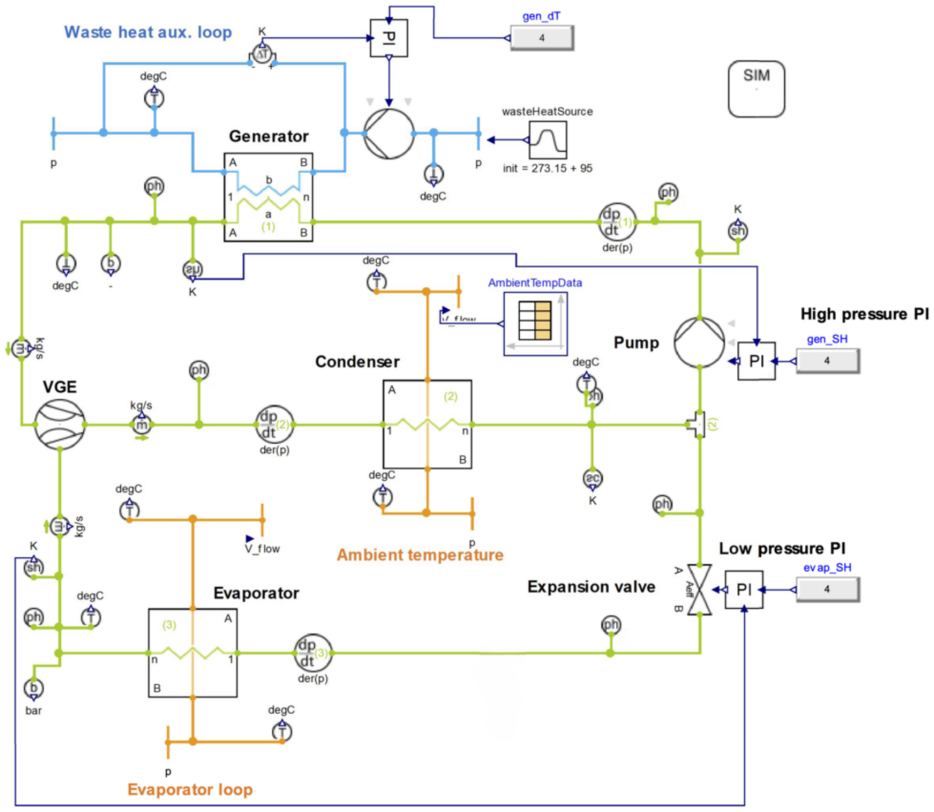

Figure 5.1: *PID diagram of the R290 Ejector Refrigeration Cycle equipped with VGE built in the Dymola software.*

condenser are introduced through a 24-hour temperature table, enabling the simulation of realistic variable ambient conditions specific for different climate zones. In the refrigeration loop, two PI controllers are used to regulate the superheating parameters. First one controls the refrigerant pump to maintain a fixed superheating at the outlet of the generator, while the second one adjusts the opening of the expansion valve to ensure stable superheating at the evaporator outlet. The evaporator air loop is maintained at a fixed inlet temperature to reflect constant cooling demand conditions.

The critical component of the system, the VGE, is implemented in order to enhance system performance by entraining the high-pressure motive flow from the generator and mixing it with the low-pressure refrigerant stream from the evaporator. Therefore, the motive nozzle of the VGE is connected downstream of the generator, the suction nozzle receives the superheated refrigerant coming from the evaporator, and the throttled and thoroughly

mixed fluid flow at the ejector outlet is directed to the condenser inlet. Thanks to such configuration, the ejector utilizes the pumping effect, which in overall significantly improves the efficiency of the refrigeration cycle.

The model incorporates detailed thermodynamic measurements, including pressure and specific enthalpy at key state points, and the mass flow rate measurements on each of the pressure line. These diagnostics allow for the precise characterization of transient behavior and validation of control responses across varying operating conditions.

5.2.2 System components

Each component of the ERS is adapted from the TLK libraries and configured for the operation with the R290 refrigerant. The components characteristics, geometries and materials are selected to match commercially available equipment, while the selection of heat transfer and pressure drop correlations are taken from the literature based on their high accuracy and experimental validation at similar applications.

The following subsections describe each component's governing equations and selected parameters.

Brazed plate heat exchanger

The generator of the ERS was modeled as a brazed-plate heat exchanger using a predefined component available in the TLK ThermalSystems library for Modelica. It uses a 1-D modeling approach based on the finite volume elements, and relies on the equations of mass and energy balance. The brazed plate heat exchangers are commonly used heat exchangers, due to its ease of tailoring for a desired application, compactness, and high efficiency. The geometrical parameters of the plate heat exchanger, based on which the heat transfer area was calculated, are listed in Table 5.1. The schematic drawing of the brazed-plate heat exchanger is presented in Figure 5.2.

These dimensions were selected to mimic the commercially available plate heat exchangers designed for similar applications and thermal duties, ensuring a realistic representation of physical system behavior and pressure drop characteristics. The heat transfer rate and pressure drop on the refrigerant side was modeled using empirical correlations provided in the VDI Heat Atlas [129], specifically those developed for Chevron-type plate geometries, which are widely adopted in calculations of commercial brazed plate heat exchangers. These correlations incorporate the influence of plate geometry, flow regime, and thermophysical fluid properties, providing high accuracy

Table 5.1: *Geometrical parameters defined for the generator modeled as a brazed-plate heat exchanger.*

Geometrical parameter		Value	Unit
Plate geometry	Number of plates	30	-
	Length (L_p)	0.526	m
	Width (B_p)	0.119	m
	Inclination angle (φ)	35	°
Plate characteristic parameters	Wall thickness	$7.5 \cdot 10^{-4}$	m
	Pattern amplitude ($2\hat{a}$)	$2.0 \cdot 10^{-3}$	m
	Pattern wavelength (Λ)	$1.3 \cdot 10^{-2}$	m

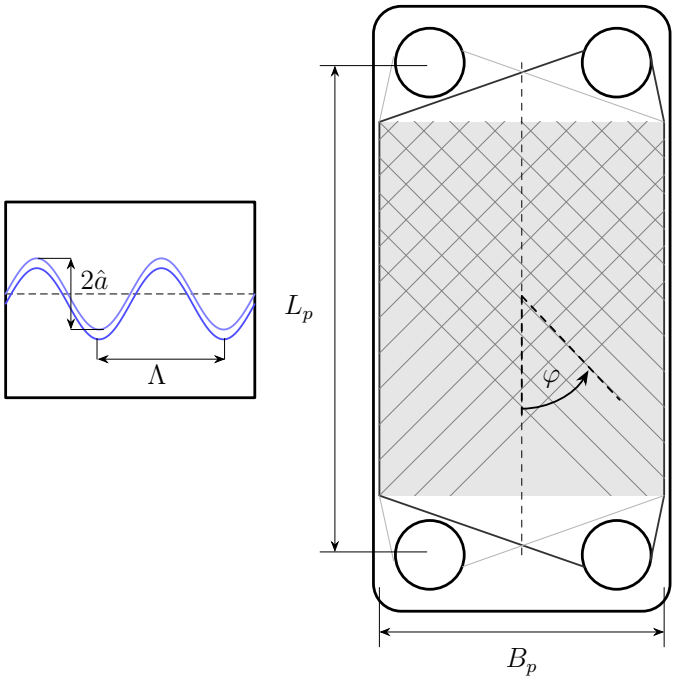

Figure 5.2: *Schematic layout of brazed plate heat exchanger. Adapted from VDI atlas [129].*

for both single- and two-phase flows under the operating conditions analyzed in this study.

In the parallel-flow brazed plate heat exchanger, each of the n discretized cells along the refrigerant and auxiliary fluid domains obeys transient mass and energy balance equations. Conservation of mass in the refrigerant side (denoted with subscript r) in cell i, is calculated using the following mass

balance:

$$\frac{dm_{\text{r,i}}}{dt} = \dot{m}_{\text{r,i-1}} - \dot{m}_{\text{r,i}} \tag{5.1}$$

where m is the mass of refrigerant in cell i, t is the time, the subscript r is for the refrigerant side and subscript i denotes the single cell of the discretized heat exchanger.

The conservation of energy in each refrigerant side cell combines convective enthalpy transport with heat transfer between the refrigerant and the solid plate wall. The energy balance for the refrigerant side is as follows:

$$\frac{d\left(m_{\text{r,i}} h_{\text{r,i}}\right)}{dt} = \dot{m}_{\text{r,i-1}} h_{\text{r,i-1}} - \dot{m}_{\text{r,i}} h_{\text{r,i}} + \dot{Q}_{\text{rw, i}} \tag{5.2}$$

where $\dot{Q}_{\text{rw,i}}$ is the heat transfer rate between refrigerant and a plate wall as denoted by the subscript rw.

The brazed-plate wall in each discretized segment i stores the thermal energy according to its material properties and volume of the cell. It gains heat from the refrigerant side and transfers heat to the secondary fluid via a plate wall, which can be expressed by the following equation:

$$\rho_{\text{w}}\, V_{\text{w}}\, c_{\text{w}}\, \frac{dT_{\text{w,i}}}{dt} = \dot{Q}_{\text{rw,i}} - \dot{Q}_{\text{wsf,i}} \tag{5.3}$$

where V is the volume of the discretized part i, the subscript w is for a plate wall, and $\dot{Q}_{\text{wsf,i}}$ is the heat transfer rate from a plate wall to a secondary fluid as denoted by the subscript wsf.

The secondary fluid side (sf) is modeled as an incompressible liquid. The transient mass behavior of the fluid is neglected due to the relatively high mass flow rate in relation to the heat exchanger geometry. The flow rate of the pump is controlled by the PI controlling the temperature difference between the generator inlet and outlet temperatures. The temperature changes due to the convective enthalpy transport and heat gain from the plate wall at cell i is calculated from the following energy balance:

$$\rho_{\text{sf}}\, V_{\text{sf,i}}\, c_{p,\text{sf}}\, \frac{dT_{\text{sf,i}}}{dt} = \dot{m}_{\text{sf,i-1}}\, c_{\text{p,sf}}\, T_{\text{sf,i-1}} - \dot{m}_{\text{sf,i}}\, c_{\text{p,sf}}\, T_{\text{sf,i}} + \dot{Q}_{\text{wsf,i}} \tag{5.4}$$

where the subscript sf denotes the secondary fluid and c_p is the specific heat at constant pressure.

The local heat transfer rates for the refrigerant and secondary fluid sides at single cell are calculated from Newton's law of cooling:

$$\dot{Q}_{\mathrm{rw,i}} = A_{\mathrm{i}}\, \alpha_{\mathrm{r,i}}\, (T_{\mathrm{r,i}} - T_{\mathrm{w,i}}) \tag{5.5}$$

$$\dot{Q}_{\mathrm{wsf,i}} = A_{\mathrm{i}}\, \alpha_{\mathrm{sf,i}}\, (T_{\mathrm{w,i}} - T_{\mathrm{sf,i}}) \tag{5.6}$$

where A_{i} the plate area of cell i, $\alpha_{\mathrm{r,i}}$ and $\alpha_{\mathrm{sf,i}}$ are the heat transfer coefficients on the refrigerant and secondary fluid sides.

The heat transfer coefficients $\alpha_{\mathrm{r,i}}$ and $\alpha_{\mathrm{sf,i}}$ are computed at each time step using the appropriate single-phase or two-phase correlations, according to the procedure that selects a proper correlation depending on the heat transfer mode. For the brazed plate heat exchanger operating as a generator, four different correlations are employed, each corresponding to specific heat exchanger operating zones: two address the single-phase heat transfer in single-phase subcooled and superheated zones, and two others cover the two-phase heat transfer, subdivided into evaporation and condensation regions.

The model defines the refrigerant thermodynamic state in the cell zone i based on the vapor quality, which in turn denotes a selection of a proper correlation. The vapor quality is controlled along the discretized plate heat exchanger using the following balance equation:

$$\frac{dX_{\mathrm{r},i}}{dt} = \frac{(m_{\mathrm{rV},\,i-1} - m_{\mathrm{rV},\,i})}{m_{\mathrm{r},i}} \tag{5.7}$$

where $X_{\mathrm{r,i}}$ and $m_{\mathrm{rV,i}}$ are the vapor quality and the vapor mass of the refrigerant of cell i, respectively.

For each cell in the single-phase superheated vapor region, the heat transfer coefficient is calculated using the equation presented by Longo and Gasparella [130]:

$$\alpha_{\mathrm{sh}} = 0.277\, \frac{\lambda}{d_{\mathrm{h}}}\, \mathrm{Re}^{0.766}\, \mathrm{Pr}^{\frac{1}{3}} \tag{5.8}$$

where the subscript sh is the superheated single-phase region, d_{h} is the hydraulic diameter, Re is the Reynolds number, and Pr is the Prandtl number.

The dimensionless numbers are defined as follows:

$$\mathrm{Re} = \frac{w\, d_{\mathrm{h}}\, \rho}{\mu} \tag{5.9}$$

$$\mathrm{Pr} = \frac{\mu\, c_p}{\lambda} \tag{5.10}$$

where w is the mean velocity and μ is the dynamic viscosity.

The mean velocity can be calculated from the volumetric flow rate through the gap between two plates, divided by the average cross-section of the gap:

$$w = \frac{\dot{V}_{\text{gap}}}{2\hat{a}B_{\text{p}}} \tag{5.11}$$

where $\dot{V}_{\text{gap}}$ is the volumetric flow rate through the plate gap, $\hat{a}$ is the half-gap between plates, and B_{p} is the plate width.

The hydraulic diameter for the refrigerant side of the brazed plate heat exchanger can be calculated from:

$$d_{\text{h}} = \frac{4\,\hat{a}}{\Xi} \tag{5.12}$$

where Ξ is the surface enlargement factor, so the ratio of the wavy plate surface to its plane projection.

The surface enlargement factor for the sinusoidal corrugation can be approximately calculated from the following formula:

$$\Xi(x) \approx \frac{1}{6}\left(1 + \sqrt{1+x^2} + 4\sqrt{1+\frac{x^2}{2}}\right) \tag{5.13}$$

where x is the wave number, so the ratio of amplitude to the wavelength. The wave number is calculated as follows:

$$x = \frac{2\pi\hat{a}}{\Lambda} \tag{5.14}$$

where Λ is the wavelength.

The heat transfer coefficient for a subcooled liquid refrigerant (α_{sc}) is calculated using the equation proposed by Thonon et al. [131]:

$$\alpha_{\text{sc}} = 0.2267\,\frac{\lambda}{d_{\text{h}}}\,\text{Re}^{0.631}\,\text{Pr}^{\frac{1}{3}} \tag{5.15}$$

where the subscript sc is for the subcooled liquid refrigerant.

For the cells in which the evaporation process takes place, Longo et al. [132] formulated highly accurate empirical correlations separately for convective and nucleate boiling mechanisms. The heat transfer coefficient based on the convective boiling (α_{cb}) is computed as follows:

$$\alpha_{cb} = 0.122\,\Xi\,\frac{\lambda}{d_h}\,{\text{Re}_{\text{eq}}}^{0.8}\,\text{Pr}^{\frac{1}{3}} \tag{5.16}$$

where the subscript cb is for the convective boiling of the refrigerant, $\mathrm{Re}_{\mathrm{eq}}$ is the equivalent Reynolds number calculated using the mean vapor quality between the inlet and the outlet from the following equation:

$$\mathrm{Re}_{\mathrm{eq}} = G\left[(1 - X_{\mathrm{m}}) + X_{\mathrm{m}}\left(\rho_{\mathrm{L}}/\rho_{\mathrm{V}}\right)^{\frac{1}{2}}\right]\frac{d_{\mathrm{h}}}{\mu_{\mathrm{L}}} \tag{5.17}$$

where $\dot{G}$ is the mass flux, X is the vapor quality, subscript m is for the mean value, and the subscripts V and L are for the saturated vapor and saturated liquid phase, respectively.

The mass flux is calculated using the following formula:

$$\dot{G} = \frac{\dot{m}}{2\hat{a} \cdot B_p} \tag{5.18}$$

The heat transfer coefficient based on the nucleate boiling (α_{nb}) is evaluated as:

$$\alpha_{\mathrm{nb}} = C_{\mathrm{nb}}\,\Xi\,\alpha_0\,C_{\mathrm{Ra}}\,F(P^*)\,\left(\frac{q}{q_0}\right)^{0.467} \tag{5.19}$$

where the subscript nb is for the nucleate boiling of the refrigerant, C_{nb} is a correction factor equal to 0.58, α_0 is a reference heat transfer coefficient determined based on the refrigerant $\alpha_0 = 4.12$ kW/(m^2·K) for R290 [129]), C_{Ra} is a coefficient that accounts for the effect of the arithmetic mean roughness and equals to 0.4 m for corrugated stainless steel plates [132], q is heat flux, q_0 is reference heat flux ($q_0 = 20$ kW/m^2), and $F(P^*)$ is a function that accounts for the effect of reduced pressure P^*.

The roughness coefficient can be calculated using the following equation:

$$C_{\mathrm{Ra}} = \left(\frac{R_{\mathrm{a}}}{0.4}\right)^{0.1333} \tag{5.20}$$

where R_{a} is the arithmetic mean roughness of the plate surface.

The equation accounting for the reduced pressure of the fluid is:

$$F(P^*) = 1.2\,P^{*\,0.27} + \left(2.5 + \frac{1}{1 - P^*}\right) \tag{5.21}$$

where P^* is the locally reduced pressure, so the ratio of actual pressure to the critical pressure of the fluid:

$$P^* = \frac{p}{p_{crit}} \tag{5.22}$$

where subscript $crit$ stands for the critical point of the fluid.

The criterion based on which the model selects the proper correlation for the specific boiling mechanism is the product of the boiling number (Bo) and the Martinelli parameter (X_{tt}). The boiling number is calculated using the following formula:

$$\mathrm{Bo} = \frac{q}{(G \Delta J_{\mathrm{LV}})} \tag{5.23}$$

where ΔJ_{LV} is the latent heat of vaporization.

The Martinelli parameter is defined using the mean vapor quality, calculated as the arithmetic mean between the inlet and outlet of the heat exchanger:

$$X_{\mathrm{tt}} = \left[(1 - X_{\mathrm{m}})\, X_{\mathrm{m}} \right]^{0.9} \left(\frac{\rho_{\mathrm{V}}}{\rho_{\mathrm{L}}} \right)^{0.5} \left(\frac{\mu_{\mathrm{L}}}{\mu_{\mathrm{V}}} \right)^{0.1} \tag{5.24}$$

where X_{tt} is the Martinelli constant.

The selection of the boiling mechanism is based on the following criteria:

- if $\mathrm{Bo} \cdot \mathrm{X_{tt}} < 0.00015$, then the convective boiling mechanism is selected,
- if $\mathrm{Bo} \cdot \mathrm{X_{tt}} > 0.00015$, then the nucleate boiling mechanism is selected.

For vertical flow through a plate gap, the pressure drop is defined as:

$$\Delta p = \xi \, \frac{\rho \, w^2 \, L_{\mathrm{p}}}{2 \, d_{\mathrm{h}}} \, , \tag{5.25}$$

where Δp is the pressure drop and ξ is the pressure-drop coefficient.

The pressure drop coefficient can be calculated from:

$$\xi = \frac{2 \, \Delta p \, d_{\mathrm{h}}}{\rho \, w^2 \, L_{\mathrm{p}}} \, , \tag{5.26}$$

The correlation applied for the secondary fluid side of the brazed plate heat exchanger incorporates the geometric design to determine the friction parameters essential for calculating the heat transfer coefficient. The friction factor is integrated into the pressure drop coefficient. The geometric parameters utilized in these calculations are depicted in Figure 5.2.

$$\mathrm{Nu} \; = 0.122 \; \mathrm{Pr}^{\frac{1}{3}} \left(\frac{\eta_{\mathrm{sf}}}{\eta_{\mathrm{wall}}} \right)^{\frac{1}{6}} \left(\xi \; \mathrm{Re}^2 \sin\left(2\varphi\right) \right)^{0.374} \tag{5.27}$$

where Nu is the Nusselt number, η_{wall} is the dynamic viscosity at wall boundary layer.

The local heat transfer coefficients for the secondary fluid side of the heat exchanger is calculated from the general equation:

$$\alpha_{\mathrm{sf}} = \frac{\mathrm{Nu}\,\lambda_{\mathrm{sf}}}{d_{\mathrm{h}}} \tag{5.28}$$

All the specific empirical correlations used in the model are summarized in Table 5.2.

Table 5.2: *Empirical correlations used for modeling of the generator as a brazed-plate heat exchanger.*

Applied Region	**Parameter**	**Correlation**
Secondary fluid side	Heat transfer model	VDI Plate Alpha [129]
	Pressure drop	Assumed no pressure drop
Refrigerant side	Heat transfer model	Longo [132]
	Pressure drop	VDI Plate pressure drop [129]
Wall modeling	Material	Stainless steel
	Heat conduction model	Geometry based conduction

To identify an optimal discretization of the heat exchangers that balances numerical precision with computational robustness, a short analysis was performed. From this study, a discretization level n equal to 15 was adopted uniformly across all heat-exchangers, as it delivered both high accuracy and stability of simulations under changing the operation conditions and rapid model execution.

For the auxiliary loop of the generator, the Therminol 59 [133] was chosen from among the candidate heat transfer fluids provided by the TIL suite, owing to its good thermophysical properties in the targeted waste-heat temperature range [134, 135]. It is a synthetic heat transfer fluid that can be applied for the heat transfer in the temperature range of -39 °C to 315 °C. The Therminol mass flow rate was regulated via a proportional-integral controller to maintain a fixed temperature differential of 15 K between the generator's inlet and outlet.

To provide a reliable start-up of the model, the initial specific enthalpy distribution of the refrigerant for the brazed plate heat exchanger was set by linearly interpolating between prescribed inlet and outlet specific enthalpy values. This initialization method enhanced numerical stability while preserving the accuracy of the steady-state solution.

Simultaneously, the auxiliary loop was initialized under the assumption of a uniform liquid Therminol temperature, thus approximating the pre-modulation thermal condition of the fluid.

Fin-and-tube heat exchangers

The condenser and evaporator components were modeled as TLK Thermal-Systems fin-and-tube heat exchangers with specified geometrical dimensions, optimized to achieve the nominal cooling capacity under the analyzed operating conditions. Their geometrical parameters are presented in Table 5.3.

Table 5.3: *Geometrical parameters defined for the evaporator and condenser modeled as a fin-and-tube heat exchanger.*

Heat exchanger	Geometrical parameter	Value	Unit
Evaporator	Tube length	4	m
	Distance between serial tubes	$2.0 \cdot 10^{-2}$	m
	Number of serial tubes	4	-
	Distance between parallel tubes	$2.5 \cdot 10^{-2}$	
	Number of parallel tubes	16	-
Condenser	Tube length	0.6	m
	Distance between serial tubes	$2.0 \cdot 10^{-3}$	m
	Number of serial tubes	8	-
	Distance between parallel tubes	$2.5 \cdot 10^{-3}$	m
	Number of parallel tubes	14	-

In the cross-flow heat exchanger model, similarly to the previously described brazed plate heat exchanger, the geometry of the heat exchangers is discretized into the n number of sections, and its operation is governed by transient mass and energy balance equations, coupled by the interfacial heat transfer.

For the tube side, the refrigerant in cell i satisfies the mass and energy balance similar to these presented in the section of brazed plate heat exchanger in Equations (5.1) and (5.2). Similarly to the previous component, the model uses different correlations for different modes of heat transfer. Starting with the single-phase correlations, different equations for the Nu number are distinguished depending on the Re number, denoting the flow regime:

- If Re < 2300, then the Nusselt number for laminar flow is equal to:

$$\mathrm{Nu} = 3.6568 \tag{5.29}$$

- If Re > 2300 and Re < 10e^5, then the correlation for transition and turbulent from Gnielinski [136] is selected.

$$\mathrm{Nu} = \frac{\left(\frac{\zeta}{8}\right)(\mathrm{Re} - 1000)\,\mathrm{Pr}}{1 + 12.7\sqrt{\frac{\zeta}{8}}\left(\mathrm{Pr}^{\frac{2}{3}} - 1\right)} \tag{5.30}$$

  It takes into account the friction factor, which is calculated from the equation below:

$$\zeta = (0.79\,\ln(\max(\mathrm{Re}, 10^{-12})) - 1.64)^{-2} \tag{5.31}$$

  where ζ is friction factor.

- If Re > 10^5, then the turbulent flow correlation from Dittus and Boelter [137] is selected.

$$\mathrm{Nu} = 0.023\max(\mathrm{Re}, 10^{-12})^{\frac{4}{5}}\,\mathrm{Pr}^{\frac{1}{3}} \tag{5.32}$$

In case of the two-phase correlations for the fin-and-tube heat exchangers, the correlations are divided depending on whether the heat exchanger works as the evaporator or condenser. The model guesses the use of the component based on the direction of the heat flow. For the evaporator, the correlation by Steiner et al. [138] for horizontal tubes is used. The authors proposed a correlation that uses the two-phase correction factor and calculates the two-phase flow correlation based on the correlations for liquid and vapor phases separately, using the equations for the Nusselt number presented in Equations (5.29)-(5.32) to calculate the heat transfer coefficient.

$$\begin{aligned}\chi = (1-X)^{0.01}&\left((1-X)^{1.5} + 1.9X^{0.6}\left(\frac{\rho_\mathrm{L}}{\rho_\mathrm{V}}\right)^{0.35}\right)^{-2.2} \\ &+ X^{0.01}\left[\left(\frac{\alpha_\mathrm{V}}{\alpha_\mathrm{L}}\right)\left(1 + 8(1-X)^{0.7}\left(\frac{\rho_\mathrm{L}}{\rho_\mathrm{V}}\right)^{0.67}\right)\right]^{-2}\end{aligned} \tag{5.33}$$

where χ is the phase correction factor.

$$\alpha_L = f\left(\mathrm{Re_L}, \mathrm{Pr_L}\right) \tag{5.34}$$

$$\alpha_V = f\left(\mathrm{Re_V}, \mathrm{Pr_V}\right) \tag{5.35}$$

On the other hand, to calculate the heat transfer coefficient for the condensation process, the correlation from Shah [139] employing the heat transfer coefficient from Equation (5.34) is applied:

$$\alpha_{cond} = \alpha_L \left((1-X)^{0.8} + \frac{3.8\, X^{0.76}(1-X)^{0.04}}{(P^*)^{0.38}} \right) \tag{5.36}$$

$$\alpha_{\mathrm{L}} = \frac{0.023\, \mathrm{Re}^{0.8}\, \mathrm{Pr}^{0.4}\, \lambda_{\mathrm{L}}}{d_{\mathrm{h}}} \tag{5.37}$$

The conduction of the component's wall is calculated according to the properties of the material and the heat exchanger geometry. For the material of the heat exchanger walls, copper was selected. The heat transfer from the refrigerant to the fin wall is governed by the following equation:

$$\rho_{\mathrm{w}}\, V_{\mathrm{w}}\, c_{\mathrm{w}} \frac{dT_{\mathrm{w,\,i}}}{dt} = \dot{Q}_{\mathrm{rw,i}} - \dot{Q}_{\mathrm{wsf,\,i}} \tag{5.38}$$

In order to determine the heat transfer between the secondary fluid (air) and fins, the correlation for finned inline bundled tubes proposed by Haaf et al. [140] was used. To simplify the calculations of fin efficiency, the approach of Schmidt [141] using the simplified fin efficiency was applied.

The mass balance of the moist air side is as follows:

$$\frac{d}{dt}\left(m_{\mathrm{sf,\,i}}\right) = \dot{m}_{\mathrm{sf,\,i\text{-}1}} - \dot{m}_{\mathrm{sf,\,i}} \tag{5.39}$$

The energy balance of the secondary fluid (air) side is governed by the following equation:

$$\frac{d}{dt}\left(m_{\mathrm{sf,\,i}} h_{\mathrm{sf,\,i}}\right) = \dot{m}_{\mathrm{sf,\,i\text{-}1}} h_{\mathrm{sf,\,i\text{-}1}} - \dot{m}_{\mathrm{sf,\,i}} h_{sf,i} + \dot{Q}_{\mathrm{wsf,\,i}} \tag{5.40}$$

The local heat transfer between fin and air in cell i is governed by the following equation:

$$\dot{Q}_{\mathrm{wsf,i}} = \eta_{\mathrm{fin}}\, A_{\mathrm{i}}\, \alpha_{\mathrm{sf,i}} (T_{\mathrm{w,i}} - T_{\mathrm{sf,i}}) \tag{5.41}$$

where η_{fin} is the fin efficiency which is evaluated by approximating the actual fin geometry through a discretization of the heat exchanger fin pack into a

series of smaller elements. Then, for the simplification, each rectangular segment is represented by an equivalent circular fin outer radius of a given fin size, so that the circular and rectangular geometries exhibit the same thermal performance.

For the heat exchanger with rectangular fin, Schmidt [141] has formulated the following set of equations for calculating the efficiency. First, the equivalent circular fin outer radius is calculated from:

$$\frac{r_{\text{fin,out,e}}}{r_{\text{fin,in}}} = 1.28\,\psi\,(\beta - 0.2)^{1/2} \tag{5.42}$$

$$\psi = \frac{P_t}{r_{\text{fin,in}}} \tag{5.43}$$

$$\beta = \frac{P_l}{P_t} \tag{5.44}$$

where P_l and P_t are the horizontal and vertical distances between the inline tubes in the tube bundle presented in Figure 5.3, ψ is the ratio of vertical distance between tubes in inline tubes arrangement and the tube diameter, and β is the ratio of the horizontal and vertical distances between the inline tube arrangement.

Next, the fin efficiency is calculated using the expression for a uniform circular fin:

$$\eta_{\text{fin}} = \frac{\tanh(\phi_{\text{fin}}\,\iota\,r_{\text{fin,in}}\,)}{\phi_\text{f}\,\iota\,r_{\text{fin,in}}} \tag{5.45}$$

where the parameters ι and ϕ_{fin} are defined as:

$$\iota = \left(\frac{2\alpha}{\delta_{\text{fin}}\lambda_{\text{fin}}}\right)^{1/2} \tag{5.46}$$

$$\phi_{\text{fin}} = \left(\frac{r_{\text{fin,out,e}}}{r_{\text{fin,in}}} - 1\right)\left[1 + 0.35\ln\left(\frac{r_{\text{fin,out,e}}}{r_{\text{fin,in}}}\right)\right] \tag{5.47}$$

where $r_{\text{fin,in}}$ is the inner radius of the fin, $r_{\text{fin,out,e}}$ is the equivalent outer radius of the circular fin, and δ_{fin} is the fin thickness.

The heat transfer correlation for the air flowing through the inline bundled fin tubes is taken from Haaf et al. [140]. As presented in Equation (5.48), it takes into account the ratio of the internal radius of the tube and the horizontal distance between them:

$$\text{Nu} = 0.31\,\text{Re}^{0.625}\;\text{Pr}^{\frac{1}{3}}\left(\frac{r_{\text{fin,in}}}{P_\text{l}}\right)^{1/3} \tag{5.48}$$

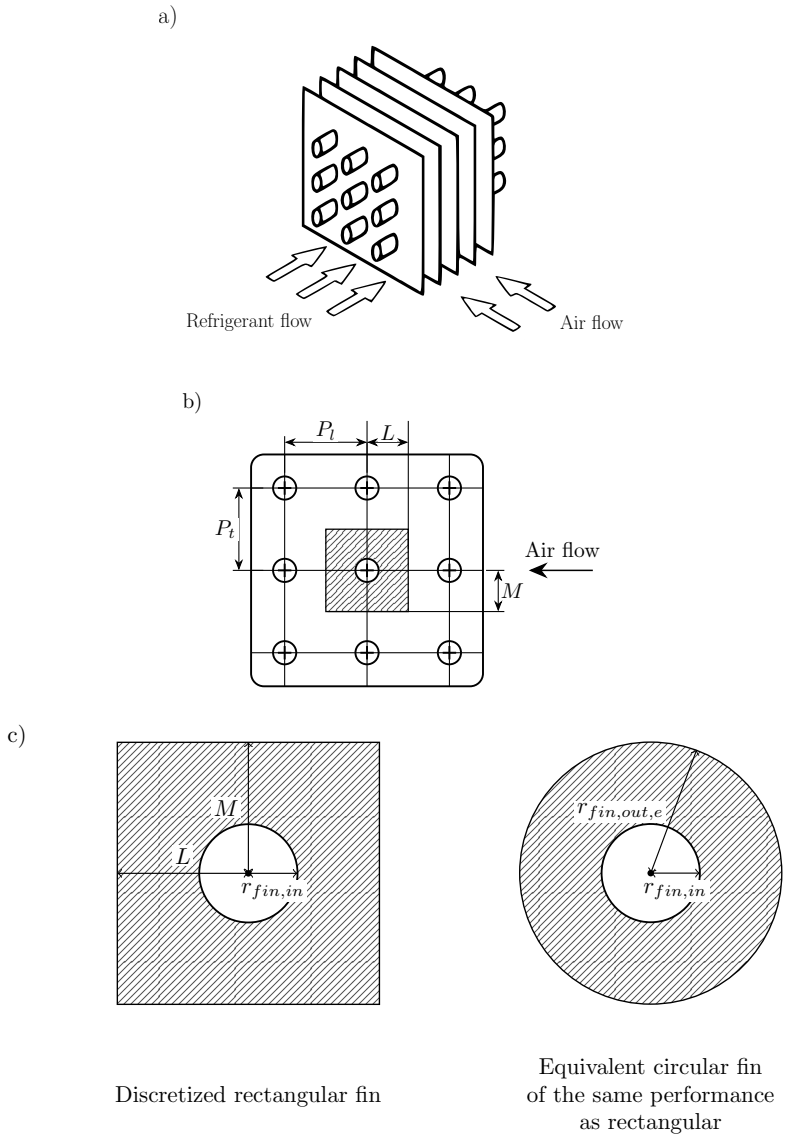

Figure 5.3: *Schematic layout of the fin and tube heat exchanger: a) general representation of its operation, and b) geometrical parameters, and c) the schematic representation of the equivalent circular fin. Adapted and modified from [129, 141].*

The built-in TLK heat transfer and pressure drop correlations used for the component calculations are summarized in Table 5.4.

A dry air stream was supplied to both the evaporator and condenser com-

Table 5.4: *The empirical correlations used for modeling of the fin-and-tube heat exchanger.*

Applied region	Parameter	Correlation
Air side	Heat transfer coefficient	Haaf [140]
	Pressure drop	Zero pressure drop
Refrigerant side	Heat transfer coefficient	Steiner [138], Shah [139], Gnielinski [136], Dittus-Boelter [137]
Tube	Pressure drop	Zero pressure drop
	Material	Copper
Fin	Fin efficiency model	Geometry based conduction
	Efficiency	Schmidt [141]

ponents. For the evaporator, the inlet air temperature was set as a constant boundary condition. Both heat exchangers operated under a uniform volumetric airflow of 7 m^3/s across all scenarios to ensure that the temperature difference of the air was less than 5 K.

The refrigerant side of each exchanger was initialized by linearly interpolating the specific enthalpy between the specified inlet and outlet values, thereby expediting convergence during start-up transients. In the condenser, the initial wall state was treated as isothermal at 35°C. In the evaporator, the initial wall temperature was set equal to the prescribed inlet air temperature. The superheat at the evaporator outlet was maintained by a proportional-integral control loop that adjusted the effective flow area of the expansion valve to sustain the target superheating.

Pump

A TLK ThermalSystems simple pump component with a variable mass flow rate was selected for modeling for both the refrigerant circulation pump and secondary fluid pump implemented in the ERS. The mass and energy balance of the pump are presented in Equations (5.49) and (5.50):

$$\dot{m}_{\text{pump,out}} = \dot{m}_{\text{pump,in}} \tag{5.49}$$

The energy balance takes into account the hydraulic work of the pump influenced by the pump efficiency:

$$h_{\text{pump,out}} = h_{\text{pump,in}} + \frac{\Delta p_{\text{pump}}}{\rho\,\eta} \tag{5.50}$$

where Δp is the pressure increase, and η is efficiency. The pressure increase is defined as:

$$\Delta p_{\text{pump}} = p_{\text{pump,out}} - p_{\text{pump,in}} \tag{5.51}$$

The volumetric flow rate of the pump is calculated as:

$$\dot{V}_{\text{pump}} = \frac{\dot{m}_{\text{pump}}}{\rho_{\text{r}}} \tag{5.52}$$

For the refrigerant circulation pump, the power consumption of the pump was necessary to calculate the system COP. In order to do that, first the hydraulic power delivered to the fluid was determined as:

$$\dot{P}_{\text{hyd}} = \Delta p_{\text{pump}} \dot{V}_{\text{pump}} \tag{5.53}$$

where subscript hyd denotes the hydraulic power.

The shaft and drive power of the pump are calculated with the following equations

$$\dot{P}_{\text{shaft}} = \frac{\dot{P}_{\text{hyd}}}{\eta} \tag{5.54}$$

where subscript shaft denotes the pump shaft.

$$\dot{P}_{\text{drive}} = \frac{\dot{P}_{\text{shaft}}}{\eta_{\text{drive}}} \tag{5.55}$$

where subscript $drive$ denotes the pump drive.

Finally, the internal loss of power is calculated using the pump efficiency:

$$\Delta \dot{P}_{\text{loss}} = \dot{P}_{\text{drive}} \left(1 - \eta\right) \eta_{\text{drive}} \tag{5.56}$$

where $\Delta \dot{P}_{\text{loss}}$ is the pump power loss.

The pump components were connected to the proportional integral component that controlled the generator superheat parameter by adjusting the mass flow rate in case of refrigerant pump, and the temperature difference by adjusting the secondary fluid mass flow rate in the secondary fluid loop. Therefore, the pressure values at the inlet and outlet necessary to calculate the pressure increase are determined by the components upstream and downstream of the pump. The pump and drive efficiencies were fixed and equal to 0.75 and 0.85, respectively, defined as typical values for the rotary refrigerant pumps in ERS [142, 143]. The limits of the mass flow of the pump, set as the PI limits, were set between 0.01 and 0.04 kg/s for the

refrigerant pump, and between 0.0001 and 0.01 kg/s for the secondary fluid pump.

Expansion valve

The expansion valve model was introduced to maintain the desired superheat level at the evaporator by adjusting the evaporating pressure to the air temperature flowing through the heat exchanger. It was carried out by controlling the evaporation pressure using a predefined orifice-type valve model with an effective flow area that was controlled by the proportional integral controller. The expansion process was assumed as isenthalpic, and the resulting pressure drop across the valve was calculated from the Bernoulli equation:

$$\dot{m}_{\text{valve}} = A_{\text{eff}} \sqrt{\frac{p_{\text{valve,in}} - p_{\text{valve,out}}}{2\,\rho_{\text{valve,in}}}} \tag{5.57}$$

where A_{eff} is the effective flow area.

The effective flow area was controlled by the PI within the specified minimum and maximum limits of $1{\cdot}10^{-10}$ and $4{\cdot}10^{-4}$ to maintain a superheat of 4 K at the evaporator outlet.

Ejector

The numerical model of the ejector implemented in this study is a simple model using two steady-state mass and energy balances, taking the parameters at the inlet motive and suction nozzles and the outlet diffuser into consideration:

$$\dot{m}_{\text{mn,in}} + \dot{m}_{\text{sn,in}} = \dot{m}_{\text{diff,out}} \tag{5.58}$$

$$\dot{m}_{\text{mn,in}}\, h_{\text{mn,in}} + \dot{m}_{\text{sn,in}}\, h_{\text{sn,in}} = \dot{m}_{\text{diff,out}}\, h_{\text{diff,out}} \tag{5.59}$$

The pressure and specific enthalpy values at the motive and suction nozzle inlets are obtained directly from the upstream heat exchanger outlets. For the VGE ROM model, the values of the motive and suction mass flow rates are retrieved from the reduced order model of the VGE. Namely, the reduced order model of the specific SP is called by the ejector model using the current step boundary conditions, namely pressure and specific enthalpy at the motive nozzle and suction nozzles, and outlet pressure, as previously described in Section 4.5. These serve as input parameters, along with the selected SP provided by the ejector control logic. Then the reduced order

model returns the predicted motive and suction nozzle mass flow rates corresponding to those conditions. Therefore, the balance equations are used to determine the mass flow rate at the ejector outlet and the specific enthalpy of the mixed stream at that outlet.

As far as the ULF-VGE ROM is concerned, this model provides as an output a single parameter of the ejector mass entrainment ratio. To determine the ejector mass flow rates, one additional mass flow rate has to be known. Therefore, in this approach, the motive nozzle mass flow rate is calculated using the Brennen two-phase nozzle flow correlation [121] based on the determination of the critical flow for the nozzle throat and the speed of sound calculated for the sonic flow inside. The equation will be provided in detail in Chapter 7. The suction nozzle mass flow rate is then retrieved from the mass entrainment ratio equation (Equation 1.1).

5.2.3 Solver settings

The dynamic simulation of the ERS was executed by solving the system of ordinary differential equations generated by the model based on the Modelica language using the explicit Euler algorithm with a fixed time step of 0.1 seconds. This time resolution was selected to adequately capture fast transients and control behavior without a significant increase in computational cost. Initial tests with lower error tolerances led to convergence issues. After iterative refinement, a solver tolerance of 10^{-7} was selected as the optimal value, ensuring numerical stability and convergence in all simulation cases.

To improve computational efficiency and facilitate seamless model initialization, initial values for pressure, temperature, and mass flow were specified for all system components at time t = 0 s. These initial conditions significantly reduced simulation startup times and helped avoid non-physical behavior during early simulation phases. With this configuration, a full 24-hour dynamic simulation of the ERS could be completed in approximately 90 minutes on a standard single-core CPU, offering a practical trade-off between simulation fidelity and computational demand.

5.2.4 Ejector control

The performance of the VGE is strongly influenced by boundary conditions, but it can be effectively optimized through real-time adjustment of the SP, which dynamically adapts the effective throat area of the motive nozzle to match the prevailing operating conditions. In the ejector model used in Dymola, a control algorithm is implemented to dynamically adjust the SP during transient system operation, based on the maximization of the suction

nozzle mass flow rate. This approach is rooted in the physical principle that, for a given set of boundary conditions, the highest mass entrainment ratio corresponds to the highest COP of the system, since it reduces the necessary power input to the system in the pump and heat provided at the generator. By targeting this condition, the system can adaptively track load changes and optimize the overall system performance over time.

The control strategy is executed at every simulation time step by following a search method across a set of sub-models (subROMs), each representing an individual SP performance, by retrieving the predicted suction nozzle mass flow rate. The subROM call function uses the thermodynamic boundary conditions of the ejector motive and suction nozzles, together with the ejector outlet pressure.

Once the complete set of mass flow rate values is evaluated across all spindle positions, the optimum spindle position SP_{opt} is determined by identifying the subROM that brings the maximum mass entrainment ratio for given operating conditions.

$$SP_{opt} = \underset{i \in 0,\ldots,7}{\arg\max} \left(\dot{m}_{SN} = f(SP_i) \right) \tag{5.60}$$

The spindle position that yields the maximum value of suction nozzle mass flow rate is selected as optimal for this time step. If this value exceeds the one from the previous time step, the control logic updates the SP accordingly. This newly selected SP is then passed into the ejector model, which passes the mass flow rates for use in the next time step of the Dymola simulation by calling another subROM for getting the values of mass flow rates.

5.2.5 Simulated conditions

The simulation framework was established to simulate the performance of the R290 ERS under realistic and steady-state conditions of waste heat recovery applications. These environments demand consistent thermal conditions to maintain safe operating temperatures and stable performance of heat-sensitive components like graphics processing units (GPU) and central processing units (CPU). Therefore, the secondary fluid side temperature of the generator, which serves as the thermal driving input to the ejector, was kept constant at the level of 95°C throughout all test cases described in this section.

To represent the cooling space side, the evaporator temperature was fixed at 10°C, in order to mimic the standard supply air temperature for space cooling. A superheat value of 5 K was applied at the evaporator outlet to

ensure single-phase conditions at the ejector suction inlet, providing stable device operation.

These simulation assumptions ensured consistency in thermal load and driving conditions, allowing for a focused evaluation of the ejector system performance under variable ambient environments.

Ambient conditions

To evaluate the performance of the R290 ERS under varying climatic conditions, representative weather data from three distinct European climate zones were selected: Gliwice (humid continental climate), Milano (humid subtropical climate), and Trondheim (subarctic climate), according to the Köppen-Geiger classification [144]. These locations were chosen to provide a broad spectrum of daily ambient temperature profiles typical of the spring/summer period. For each city, a representative day from the year 2024 was selected to reflect periods of high or moderate cooling demand. The corresponding ambient temperature profiles were used as input in the Dymola simulation environment to model the air flow over the condenser unit of the ERS.

Figure 5.4 presents the ambient temperature data for Gliwice (07.07.2024), Milano (07.06.2024), and Trondheim (07.06.2024), plotted with 15-minute averaging intervals. The maximum and minimum ambient temperatures recorded on these days in all locations ranged from 8.5°C in Gliwice to 27.9°C in Milan. A constant ambient relative humidity of 35% was assumed for all cases, and the air volumetric flow rate through the condenser was set to 7 m^3/s using a constant speed cross-flow fan. The temperature profiles were introduced into the simulation as 24-hour data tables with hourly values interpolated using a piecewise linear approximation. This approach ensured a continuous and realistic representation of dynamic ambient conditions throughout the simulation period.

Simulation procedure

The fixed-ejector simulations were performed using fixed-ejector throat diameters of SP1-SP3 for cases of Gliwice and Milano, and the diameters of SP5-SP7 for the case of Trondheim. Their performance was compared with a VGE model with adjustable spindle positioning. From the ejector perspective, the simulations were tested for two motive and suction nozzle pressure levels to assess their impact on overall system performance. The tests aimed for the analysis of the system adaptability to varying operating environments and pressure regimes, enabling a detailed comparison between

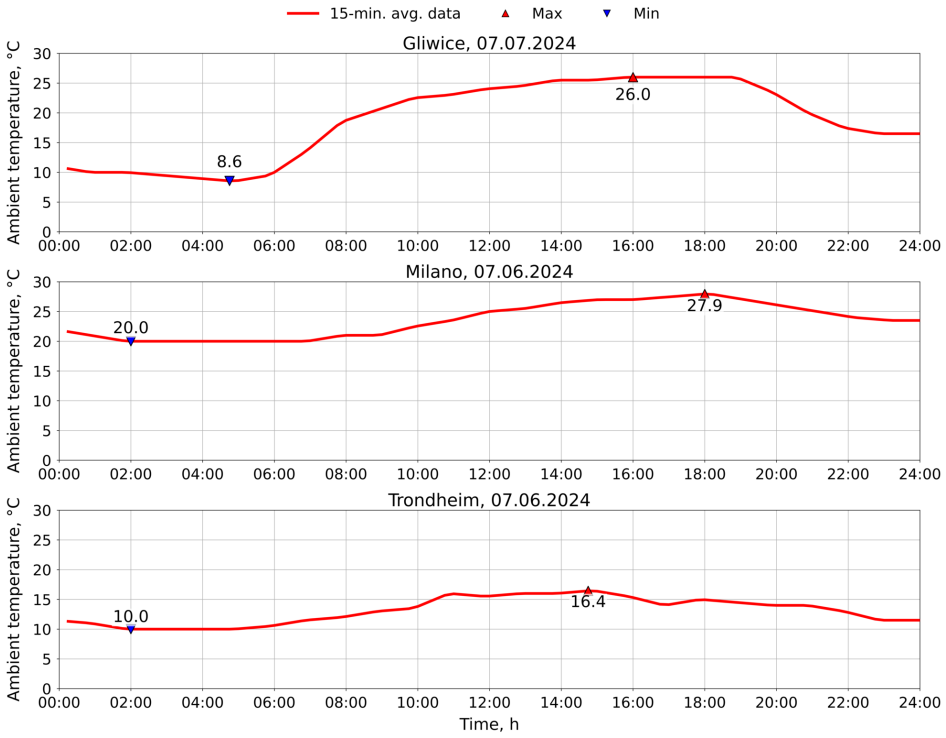

Figure 5.4: *The graphical representation of the temperature data from Gliwice, Milan and Trondheim for three days of 2023 being representatives of the summer and transitional periods seasons.*

fixed and spindle ejectors. The ambient conditions presented by the climate data were introduced into the system in the form of a 24-hour data table with an hourly step, and a linear approximating function between the values with a period of value change equal to 15 min.

5.2.6 Performance parameters

To quantitatively assess the behavior and efficiency of the ERS under dynamic operating conditions, a set of key performance parameters was defined and used consistently throughout the analysis. These indicators allow for assessing both the instantaneous and aggregated system performance and are applicable across different configurations, including both VGE- and FGE-based systems. The primary focus is placed on two core metrics: the cooling capacity resulting from the evaporator operation and the COP. These are further complemented by their respective daily averaged values, which allow a direct comparison of system efficiency over analyzed simulation

periods.

Finally, to quantify the improvement introduced by the VGE system relative to the FGE baseline, a relative difference metric is employed.

The instantaneous cooling capacity fo VGE is defined as the thermal energy extracted by the evaporator and is calculated based on the mass flow rate at the suction nozzle inlet and the specific enthalpy difference across the evaporator:

$$\dot{Q}_{\text{evap}} = \dot{m}_{\text{SN}} \left(h_{\text{evap,out}} - h_{\text{evap,in}} \right) \tag{5.61}$$

The instantaneous power input includes both the hydraulic power consumed by the pump, defined by Equation (5.53) , and the thermal power supplied to the generator:

$$\dot{Q}_{\text{gen}} = \dot{m}_{\text{MN}} \left(h_{\text{gen, out}} - h_{\text{gen,in}} \right) \tag{5.62}$$

The COP is used to assess the overall energy efficiency of the system and is calculated as the ratio of the cooling capacity to the total energy input:

$$\text{COP} = \frac{\dot{Q}_{\text{evap}}}{\dot{P}_{\text{pump}} + \dot{Q}_{\text{gen}}} \tag{5.63}$$

To evaluate the system performance over an entire 24-hour simulation, daily averaged values of both cooling capacity and COP are computed. These are obtained as the arithmetic mean of the instantaneous values across all time steps:

$$\overline{\dot{Q}_{\text{evap}}} = \frac{1}{\text{N}} \sum_{\text{i=1}}^{N} \dot{Q}_{\text{evap,i}} \tag{5.64}$$

$$\overline{\text{COP}} = \frac{1}{\text{N}} \sum_{\text{i=1}}^{\text{N}} \text{COP}_{\text{i}} \tag{5.65}$$

where N is the total number of simulation time steps, and the subscript i denotes the value at the particular time step.

Finally, to directly compare the performance between the VGE and FGE-based configurations, a relative difference metric is used. It was calculated for the selected performance parameters as:

$$\delta Y = \frac{Y_{\text{VGE}} - Y_{\text{FGE}}}{Y_{\text{FGE}}} \cdot 100 \tag{5.66}$$

where Y is an arbitrary performance parameter.

This metric enables a direct quantification of the performance improvement (or reduction) resulting from the implementation of a VGE, based on daily averaged values of the cooling capacity or COP.

5.3 Results and discussion

Figure 5.5 presents the dynamic performance of the R290 ERS over a 24-hour simulation on July 7th, 2024, using ambient temperature data from Gliwice and a constant waste source temperature input of 95°C. This particular day featured the highest ambient temperature amplitude among all the analyzed locations, with outdoor air temperatures fluctuating between approximately 8°C and 26°C. The simulation compares a system operating with VGE to three FGE configurations, i.e., SP1, SP2, and SP3, chosen as they were the only fixed-ejector setups capable of sustaining operation throughout the entire daily ambient temperature profile. Fixed geometries beyond SP3, i.e., SP4 to SP7, could not maintain full-day operation due to limitations under varying load and, therefore, were excluded.

As seen in the figure, the control system of the VGE dynamically adjusts the spindle position in response to changing ambient conditions. The second subplot presents the spindle positions varied from SP7 (most restricted motive nozzle throat) during low ambient temperatures to SP1 (nearly fully open throat) during periods of high thermal demand. This adaptability is the key to maintaining optimal mass flow rate and pressure conditions across the ejector, enabling efficient operation over the full ambient temperature range.

The third subplot shows the results of COP, where the VGE-based system clearly outperforms the FGE-based one, particularly during the cooler early hours of the day. The VGE COP reaches a maximum of 0.64 and a minimum of 0.26, reflecting its ability to adapt to load fluctuations. In contrast, the COP values for fixed ejectors remain relatively flat and are restricted within a narrower range of approximately 0.2 to 0.3, indicating a more rigid performance profile less responsive to environmental changes.

In terms of the generator capacity, the VGE shows a dynamic response with values ranging between 6.6 and 11.2 kW, corresponding to varying spindle position and system demand. For the fixed ejectors, the generator-side heat input remains more stable and falls within the approximate range of 10.0 and 11.5 kW across all three configurations. The lower minimum value observed in the VGE case reflects the system's ability to reduce the necessary generator heat delivered during low-load periods by moving the spindle and decreasing the motive nozzle throat cross-sectional area.

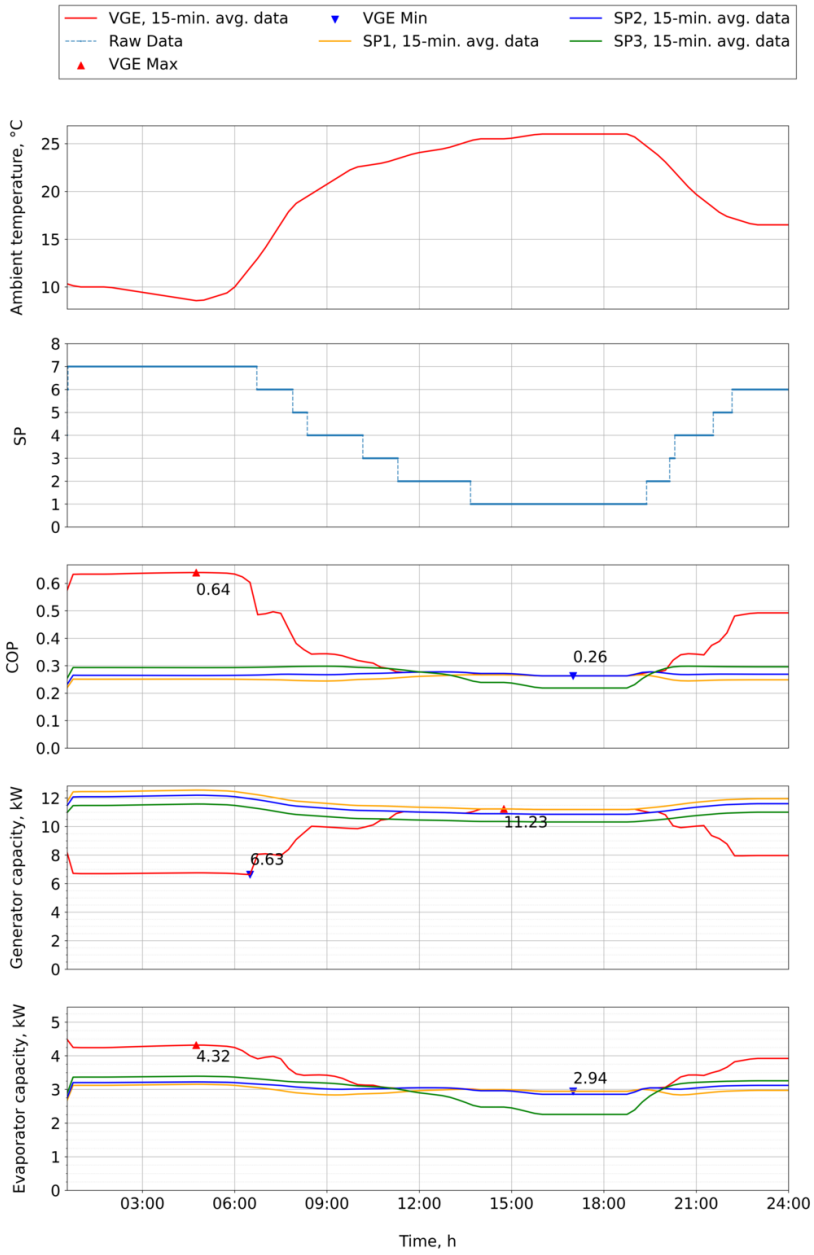

Figure 5.5: *Performance comparison of VGE and fixed geometry ejectors (SP1-SP3) for ambient temperature of Gliwice on July 7th, 2024, using constant waste heat temperature of bearings factory as generator input.*

The evaporator capacity further underscores the superior adaptability of the VGE. The cooling capacity on the evaporator side reaches a maximum of 4.3 kW and a minimum of 2.9 kW for the VGE configuration. In comparison, the fixed ejectors provide slightly lower but steadier evaporator cooling capacity, generally varying between 3.0 and 4.0 kW. The daily averaged results of the COP and cooling capacity for both ejector types for the 24-h simulations using temperature data from Gliwice and waste source temperature from the bearings factory are summarized in Table 5.5.

Table 5.5: *Summarized performance parameters of system using VGE and fixed geometry ejectors (SP1-SP3) for ambient temperature of Gliwice on July 7th, 2024, using waste heat temperature from bearings factory as generator input.*

Case	Daily avg. COP		Daily avg. cooling capacity, kW	
	FGE	VGE	FGE	VGE
VGE	–	0.41	–	3.57
SP1	0.25	–	2.93	–
SP2	0.26	–	3.00	–
SP3	0.27	–	2.94	–

Figure 5.6 presents the results for the R290 ejector-based refrigeration system operating under ambient conditions representative of Milano, with waste heat profile bearings factory. In contrast to the Gliwice case, the ambient temperature profile in Milano exhibits a smaller daily amplitude, ranging from approximately 20 to 28°C, and maintains higher overall temperature levels throughout the 24-hour period. These boundary conditions significantly influence system dynamics, particularly in terms of the control strategy and the ejector adaptability.

At the beginning of the day, the VGE starts its operation at a spindle position of SP4, corresponding to a mid-position throat diameter suitable for higher condenser pressures resulting from elevated ambient temperatures. As the external temperature increases further during the day, the control system incrementally adjusts the spindle to more open positions, reaching SP2 by the end of the afternoon, to accommodate the increased thermal loads necessary for higher condenser saturation temperature and maintain system performance.

The COP, presented in the third subplot, demonstrates a distinct advantage for the VGE in terms of adaptability. The VGE achieves a maximum COP of 0.34 during the early morning hours and a minimum of 0.20 around peak ambient conditions. Again, this dynamic behavior contrasts with the more uniform COP profiles of fixed geometry ejectors (SP1-SP3), which

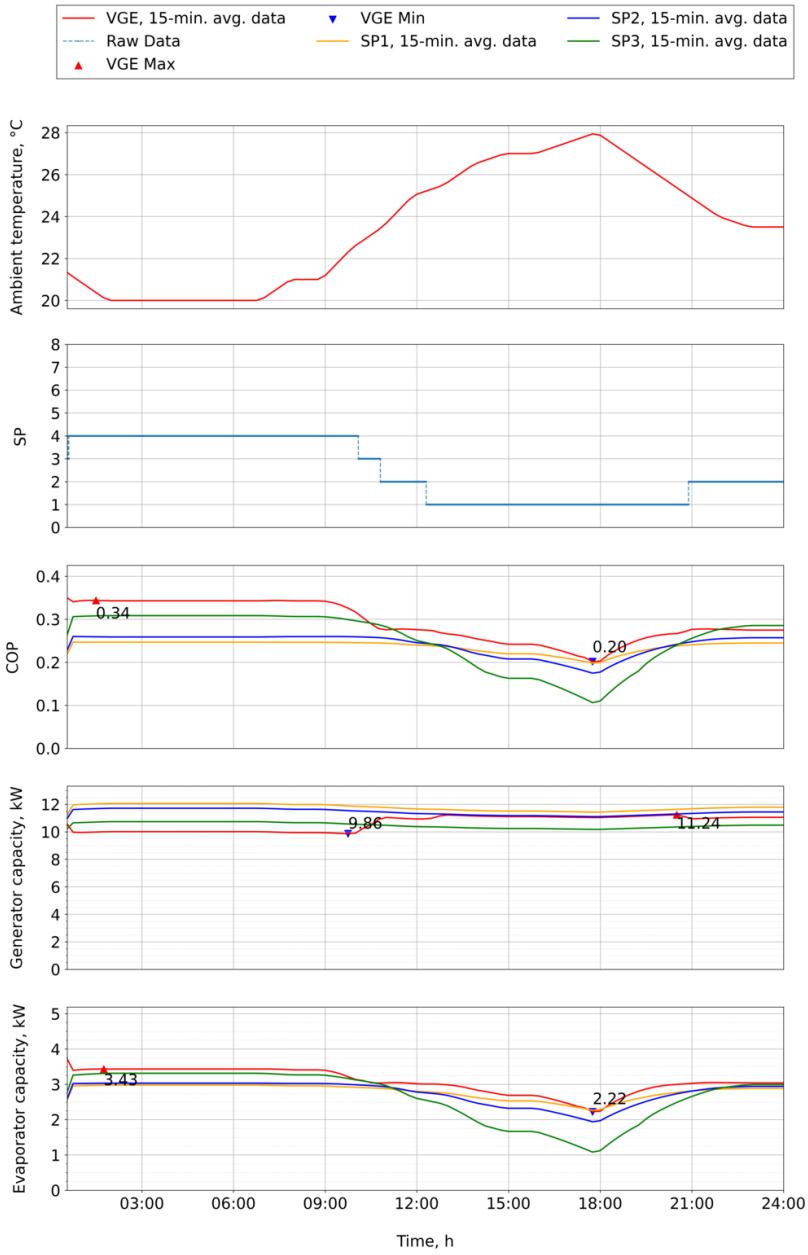

Figure 5.6: *Performance comparison of VGE and fixed geometry ejectors (SP1-SP3) for ambient temperature of Milano on July 7th, 2024, using waste heat temperature from bearings factory as generator input.*

maintain values within a narrower band of approximately 0.22 to 0.28. These results highlight the ability of the VGE to maintain operation closer to optimal thermodynamic conditions, including the case in which the ambient temperature is relatively higher and less variable.

Looking at the generator capacity, the thermal input varies between 9.8 and 11.4 kW, with lower values corresponding to reduced spindle openings during periods of low ambient temperature. In comparison, fixed ejector configurations present more stable characteristics of cooling capacity and remain between 10.5 and 11.4 kW.

The evaporator cooling capacity again reveals the superior performance of the VGE that modulates the cooling output. The system delivers a maximum cooling capacity of 3.4 kW and a minimum of 2.2 kW, whereas fixed ejectors operate within a comparatively narrower range of approximately 2.8 and 3.4 kW. This enhanced flexibility enables the VGE to better match the ejector operation to varying environmental conditions, contributing to more efficient and responsive system operation. The daily averaged results of the COP and cooling capacity for both ejector types for the 24-h simulations using temperature data from Milano and waste source temperature from the bearings factory are summarized in Table 5.5.

Table 5.6: *Summarized performance parameters of system using VGE and fixed geometry ejectors (SP1-SP3) for ambient temperature of Milano on July 7th, 2024, using waste heat temperature from bearings factory as generator input.*

Case	Daily avg. COP		Daily avg. cooling capacity, kW	
	FGE	VGE	FGE	VGE
VGE	–	0.29	–	3.12
SP1	0.23	–	2.75	–
SP2	0.24	–	2.72	–
SP3	0.25	–	2.62	–

Figure 5.7 presents the performance of the R290 ejector-based refrigeration system for the ambient conditions recorded in Trondheim on July 7th, 2024, for the same waste heat input as in the previous two cases. Among all the locations analyzed, Trondheim represents the coldest climate profile, with ambient temperatures varying modestly between approximately 10 and 17°C during the 24-hour simulation. Due to this narrow thermal amplitude and lower overall outdoor temperature, the performance differences between the VGE and FGE are less pronounced compared to the previous cases.

In this case, the VGE operates almost exclusively at spindle position SP7, which is the one with the smallest nozzle throat cross-sectional area,

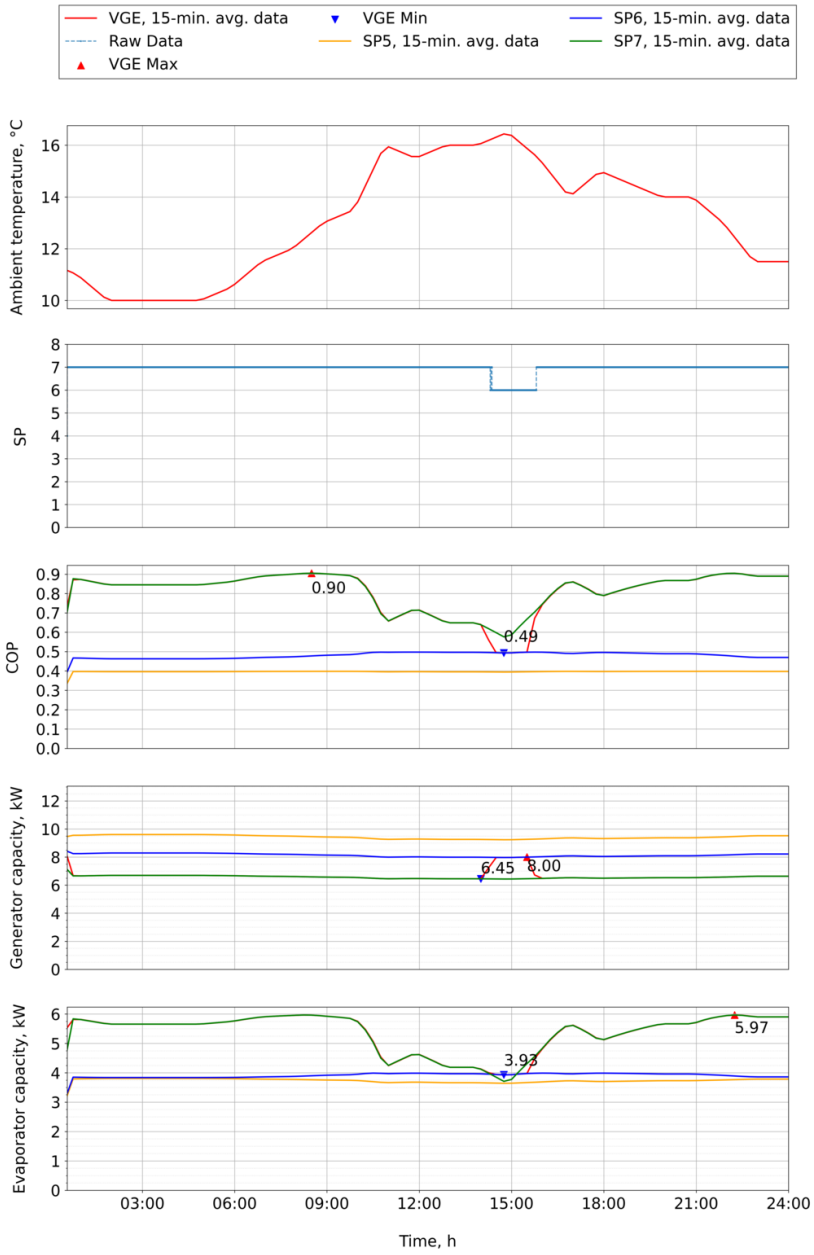

Figure 5.7: *Performance comparison of VGE and fixed geometry ejectors (SP5-SP7) for ambient temperature of Trondheim on July 7th, 2024, using waste heat temperature a bearings factory as generator input.*

consistent with the low condenser pressure requirements under cold ambient conditions. A brief transition to SP6 is visible only during the midday peak in the ambient temperature. However, this adjustment is for a small period of time and only marginally impacts the system performance. Therefore, the performance curves of the VGE and SP7 nearly overlap throughout the day.

The COP results, shown in the third subplot, further confirm this operational similarity. The VGE achieves a maximum COP of 0.90 and a minimum of 0.49, values closely mirrored by the SP7 fixed ejector configuration. The fixed ejectors SP6 and SP5, which are progressively less restrictive, perform slightly below SP7, particularly during the midday period, where the brief change of the VGE to SP6 allows it to maintain a more favorable operating point. However, the overall advantage of the VGE in this scenario is small due to the stability and relatively low value of ambient temperature.

The generator capacity for the VGE varies between 6.5 and 7.9 kW, whereas the fixed ejectors operate within a similar range, approximately 7.9 kW to 8.0 kW, which indicates that at the positions with restricted flow at the motive nozzle and lower condenser pressures, the differences between these positions are negligible.

Similarly, the cooling capacity of the evaporator shows minimal deviation between configurations. The VGE delivers a maximum of 4.0 kW and a minimum of 3.9 kW, while SP7 tracks these values closely throughout the day. The more open fixed ejectors, SP6 and SP5, work with slightly lower performance throughout the period, resulting from a worse suitability of such restricted flow under such low-load conditions. The daily averaged results of the COP and cooling capacity for both ejector types for the 24-h simulations using temperature data from Trondheim and waste source temperature from the bearings factory are summarized in Table 5.5.

Table 5.7: *Summarized performance parameters of system using VGE and fixed geometry ejectors (SP1-SP3) for ambient temperature of Trondheim on July 7th, 2024, using waste heat temperature from bearings factory as generator input.*

Case	Daily avg. COP		Daily avg. cooling capacity, kW	
	FGE	VGE	FGE	VGE
VGE	–	0.80	–	5.37
SP5	0.39	–	3.70	–
SP6	0.47	–	3.84	–
SP7	0.80	–	5.26	–

Figure 5.8 presents a comparative analysis of the daily averaged COP

and cooling capacity differences of VGE-based system operation relative to the FGE-based configurations across all three analyzed locations: Gliwice, Milano, and Trondheim.

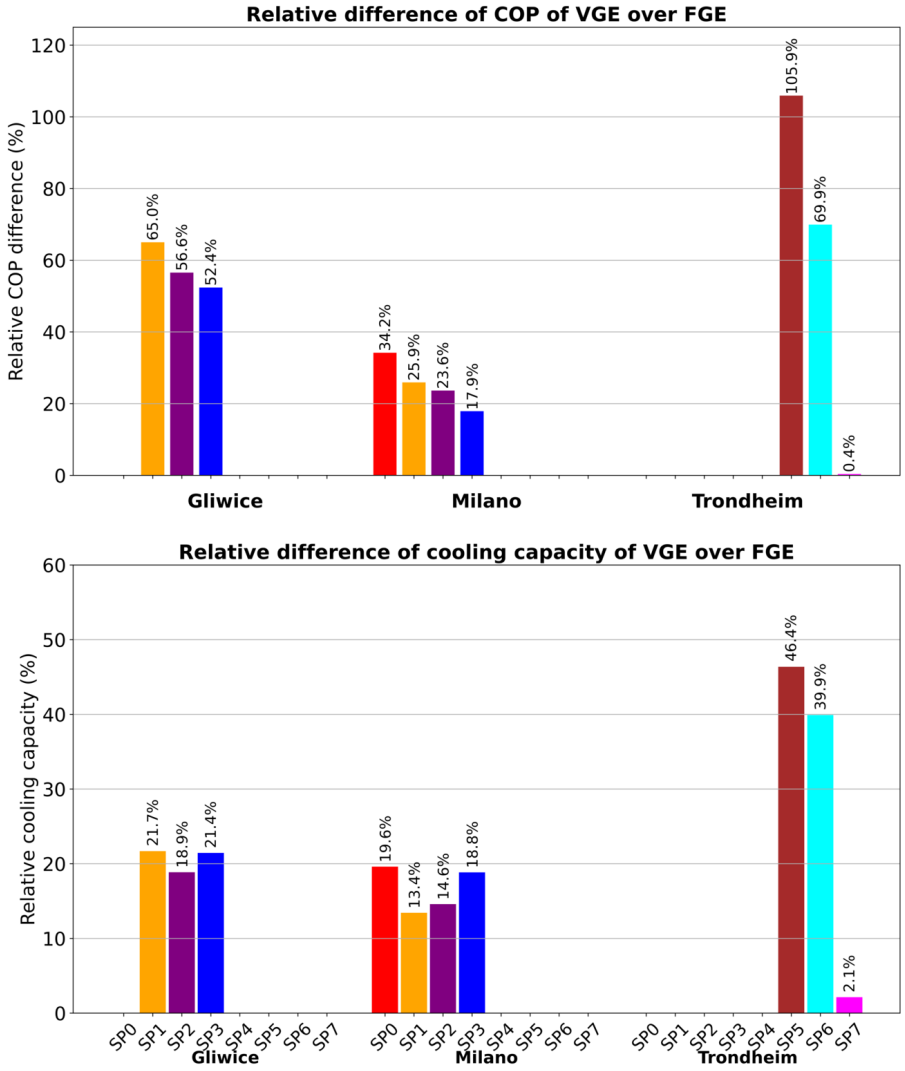

Figure 5.8: *Relative daily average performance differences between VGE and FGE systems for COP (top) and evaporator cooling capacity (bottom) across all studied locations.*

In terms of COP, the VGE consistently outperforms all fixed configurations. The analysis identifies the FGE cases with minimal deviation from VGE, showcasing the best-performing fixed options for specific conditions in each location: SP3 for Gliwice and Milano, and SP7 for Trondheim. In

Gliwice, the VGE shows the most substantial improvement, achieving a 52.4% higher daily average COP relative to SP3, due to the highest variability of the ambient temperature throughout the day. In Milan, which maintains higher and more stable ambient conditions, the improvement is still significant, reaching 17.9% over SP3. Finally, in Trondheim, where the ambient conditions are both relatively cold and stable, the performance gap is marginal, with only a 0.4% COP advantage observed for VGE over SP7, confirming the limited necessity for active modulation in such environments.

When comparing the cooling capacity, the relative advantage of the VGE exhibits a slightly different trend. The FGE configurations showing the smallest difference from the VGE are SP2 for Gliwice, SP2 for Milan, and again SP7 for Trondheim. Compared to the respective optimal FGE cases identified based on the COP, the VGE still delivers a measurable increase in the cooling capacity: it provides a 21.4% improvement over SP3 in Gliwice, 18.8% over SP3 in Milan, and a modest 2.1% increase over SP7 in Trondheim. These findings highlight that although the VGE's efficiency is notably superior in fluctuating conditions, it consistently delivers augmented cooling across diverse climates, albeit less so in stable, low-demand settings.

5.4 Conclusions

The R290 ERS model has been built in Dymola and equipped with the ROM of the R290 VGE. The developed ROM was successfully implemented and validated for use in dynamic analyses, confirming its reliability and computational efficiency for system studies. Comparative analysis in three climate scenarios: Gliwice, Milan, and Trondheim, demonstrates that the VGE-based system offers notable advantages over the one based on FGE, particularly in environments with high daily temperature variability. Across all locations, the VGE achieves daily average COP improvements ranging roughly from 0.4% to over 50%, and cooling capacity increases from about 2% to over 21%, depending on climate conditions.

In both Gliwice, characterized by a high daily temperature amplitude, and Milano, with consistently high ambient temperatures, the VGE outperforms the FGE configurations in terms of COP, and evaporator cooling capacity. By actively modulating the throat area of the motive nozzle in response to changing ambient and source conditions, the VGE maintains operation closer to the critical on-design state, maximizing the advantages brought by the implementation of the ejector to the cycle. Even in the case of Trondheim, where ambient temperatures remain low and relatively stable, the VGE demonstrates its responsiveness by briefly adjusting to a more favorable

geometry during midday peaks. Although performance gains under such stable conditions are less visible, this behavior confirms the suitability of the presented capacity control method using an ejector with a spindle for a wide spectrum of real-world operating conditions.

CHAPTER 6

Dynamic analysis of R290 ejector-based system using industrial low-grade waste heat

6.1 System analysis assumptions

In this stage of the analysis, the R290 ERS model is extended to include time-varying generator operating conditions based on real industrial waste heat data. This enhancement significantly enhances the model's realism, enabling an analysis of the benefits associated with the implementation of the ejector in practical application. The motive nozzle operating conditions, namely the pressure and temperature of the motive flow entering the ejector, are directly influenced by the dynamic waste heat profiles collected from three industrial sites: a mine, a forge, and a bearings factory. These sources introduce short- and long-term thermal fluctuations in the generator inlet, thereby affecting the ejector mass entrainment ratio and imposing a need for continuous spindle control to optimize the ejector performance. Therefore, the analyzed configuration corresponds to an application of air-conditioning system driven by industrial waste heat recovery, highlighting its relevance for energy-efficient cooling solutions in realistic operational conditions.

In contrast, the suction nozzle conditions corresponding to the evaporator outlet are kept constant across all simulations, with a fixed evaporation temperature of 10°C and a superheat value of 3 K. This approach isolates the impact of the temperature variability in the evaporator, allowing for the evaluation of the fluctuations in the input of waste heat on the system dynamics. Similarly to the previous chapter, the condenser, and so the ejector outlet, are subjected to realistic, time-dependent ambient temperature profiles from three different geographical zones, representing various heat rejection environments for the three selected ambient temperature sets already described in Chapter 5.

The simulation approach described in this Chapter results in a wide range of dynamic boundary conditions across the ejector ports: a variable motive nozzle input driven by fluctuating waste heat, a fixed suction nozzle input determined by the stable cooling demand, and a transient diffuser outlet conditions tied to ambient temperature. Such a framework provides a robust basis for assessing the influence of real-world thermal variations on the VGE performance and evaluating the effectiveness of spindle positioning control strategies under dynamic, unsteady-state operation.

6.2 Industrial waste heat characteristics

To assess the performance and control response of the R290 ERS in realistic operating scenarios, source temperature inputs were derived from actual waste heat data from three different industrial sites: mine, forge, and bearings factory. These data sets were supplied by Marani Sp. z o.o. (Zabrze, Poland) [145], a company specializing in converting industrial and natural waste heat into electricity and cooling through novel technologies and offering them also using an outsourcing model. The data capture the thermal characteristics of waste heat streams that are typically available in industrial environments. They were employed to model the thermal driving source on the generator side of the system.

The data were recorded with a time resolution of 1 s and directly introduced into the dynamic simulation environment without any filtering, preserving all the site temperature variations. For visualization purposes, the raw signals were post-processed to generate 15-minute moving average profiles, which, together with the raw data, are presented in Figure 6.1. Although the temperature data sets are within a relatively narrow operational range of 90 to 101°C, they present different variations in thermal dynamics coming from the different industrial sites.

Among the three sources, waste heat temperature coming from the data

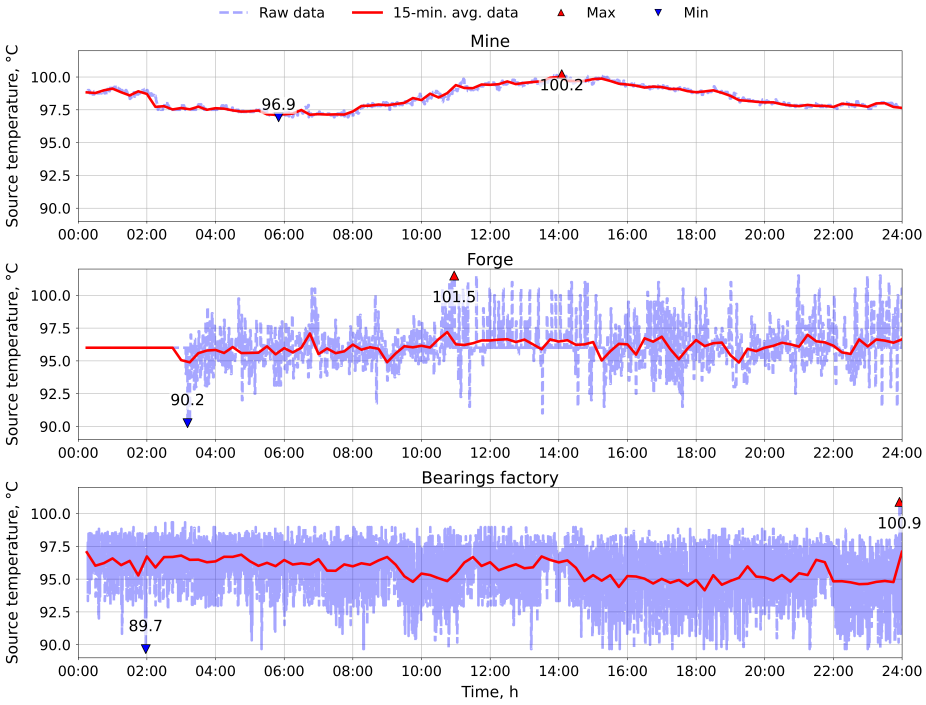

Figure 6.1: *Graphical representation of the waste heat temperature data from a mine, forge, and bearings factory.*

of the mine plant exhibited the most stable temperature behavior, with only moderate variation around its mean value of 98.39°C, with a standard deviation of 0.86°C. The difference between the daily maximum temperature of 100.2°C and the minimum temperature of 96.9°C is only 3.3K, confirming its steady operation and limited thermal fluctuation. In contrast, the forge presents a more dynamic temperature profile, likely influenced by periodic high-temperature industrial processes, with a mean value of 96.1°C with a standard deviation of 1.48°C, and a maximum deviation of 5.83 from the average. The highest temperature reached 101.5°C, while the lowest temperature was equal to 90.2°C, recorded around 3:20 a.m., coinciding with the warm-up phase of the industrial system. The bearings factory demonstrated the largest degree of thermal oscillation, characterized by frequent and sharp short-term deviations in temperature. It exhibited a mean temperature of 95.7°C, a standard deviation of 1.65°C, and a maximum deviation of 6.06°C, with the overall daily temperature difference reaching 11.2 K. This diversity in the source behavior offers valuable insight into the impact of transient heat availability on the ejector performance and control

logic. By applying these unfiltered temperature profiles to the system model, the simulation captures dynamic operating conditions representative of real-world waste heat recovery scenarios. This allows for an in-depth evaluation of the control system ability to respond to fluctuations in generator-side heat input and highlights the need to assess the influence of ejector spindle movement discretization on the overall R290 ERS performance and stability.

6.3 System control method

The control strategy implemented in the present study is based on the SP control method developed and tested in Chapter 5 under fixed source temperature conditions. In the current configuration with variable realistic waste heat data from three industrial sites, an additional layer of complexity is added to the control task. These dynamic temperature inputs require a more adaptive and responsive control mechanism, particularly in terms of regulating the refrigerant superheat and refining spindle actuation behavior.

To address this issue, an analysis of the effect of the superheat values associated with both generator and evaporator on the overall stability and performance of the system was carried out. This parameter play a critical role in controlling the responsiveness and robustness of the analyzed ejector-based system, especially when subjected to real-world transient boundary conditions.

In the simulations presented in Chapter 5 under constant source conditions, a fixed superheat of 5 K was sufficient to ensure vapor quality and prevent two-phase flow from entering the ejector. However, under transient conditions with varying inlet temperatures, maintaining optimal superheat becomes more critical for preserving ejector performance and avoiding issues such as choking or underexpansion in the motive nozzle.

This study evaluates a range of superheat configurations to identify the optimal trade-off between ejector stability and overall system efficiency. An excessive superheat may delay the dynamic response of the system, increasing the inertia of thermal regulation, while insufficient superheat can introduce a risk of two-phase flow entry, leading to unstable operation. By tuning the superheat level under variable source temperature conditions, this analysis aims to determine the most robust and effective operating strategy for ejector refrigeration systems relying on industrial waste heat.

Figure 6.2 presents the transient simulation results for the R290 ERS operating under ambient temperature data from Gliwice and waste heat source conditions from the mine. Six different superheat levels—ranging from 1K to 6K were applied at both the generator and evaporator sides to

observe their influence on the ejector performance and control behavior. The top subplot confirms consistent ambient temperature across all the considered cases. The SP plot reveals distinct control behavior as a function of superheat setting. At lower superheating values (1-3 K), the spindle tends to operate at higher positions, resulting in more restrictive nozzle configurations. In contrast, with increased superheat levels (5-6 K), the SP shifts to lower values, indicating the system compensates the increase of density by opening the ejector throat.

The COP results present that the highest instantaneous value is achieved for the 3K superheat case, peaking at approximately 0.90 during early morning operation. The lowest minimum COP of around 0.21 is observed for the 6K superheat case, which occurred during the temperature peak of ambient conditions. These results indicate that excessively high superheat leads to performance degradation, likely due to decreased enthalpy difference between suction and outlet streams, and potentially overexpanded motive flow. On the other hand, too low superheat settings yields lower COP compared to the 3 K value. The generator capacity profiles show that lower superheat configurations (1-3 K) correspond to higher thermal input, which is a result of higher motive nozzle mass flow rate. Furthermore, the evaporator capacity on the evaporator side also reflects this behavior, with the highest value of evaporator capacity reaching above 5 kW for the 3 K case. This capacity gradually decreases with the increase in superheating values, with the 6 K configuration providing the lowest evaporator capacity below 3.6 kW during the peak ambient temperature.

To better visualize the effect of the superheat level on the overall system performance, Figure 6.3 presents the daily averaged COP and evaporator capacity for each superheat setting. The optimal daily averaged COP of 0.50 is observed for the 3 K superheat, while the worst performance of 0.42 corresponds to the 6 K value. Similarly, the maximum daily averaged evaporator capacity of 3.9 kW is achieved at 3 K, while the lowest, 3.50 kW, is found for 6 K. Notably, the decline in performance with the increasing superheat is more visible in the evaporator capacity than in COP, suggesting that the superheat impact influences more the suction nozzle conditions, and therefore the evaporator capacity, rather than the thermal efficiency alone.

These results confirm that a moderate superheat level of 3 K offers the best trade-off between stability and performance, maximizing the COP and evaporator capacity while maintaining robust ejector operation. Increased superheating levels degrade performance, whereas reduced values may compromise ejector reliability and its stable operation under transient conditions.

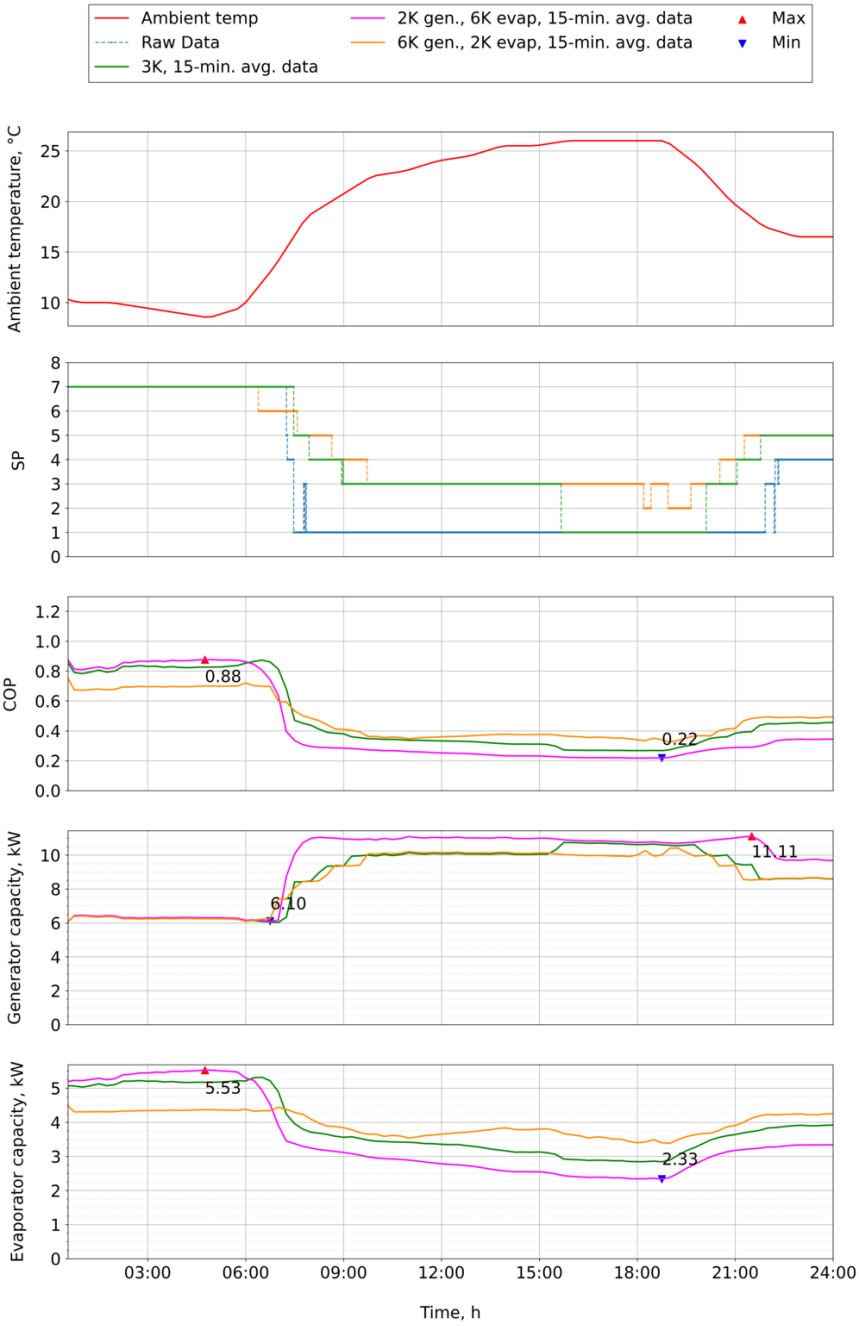

Figure 6.2: *Superheat sensitivity analysis on the ERS results for ambient temperature of Gliwice and waste heat source data from mine.*

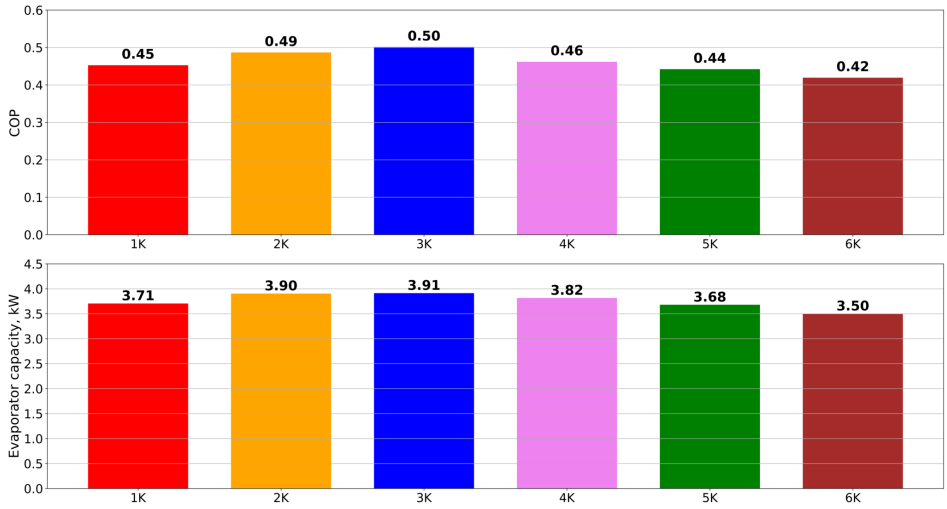

Figure 6.3: *Daily averaged COP and evaporator capacity for different superheating levels in the Ejector Refrigeration System for ambient temperature and source temperature data from mine.*

6.4 Simulated cases

To systematically evaluate the performance and control behavior of the R290 ERS with VGE under realistic conditions, a set of nine distinct simulation scenarios was developed. These cases were designed to combine realistic weather conditions with industrial waste heat source profiles, thereby capturing a wide range of thermal boundary conditions representative of practical applications. The simulated cases are summarized in Table 6.1, where each case is denoted by a capital letter from A to I for ease of reference throughout this chapter. For each location's ambient temperature (Figure 5.4), the simulation was carried out using waste heat data from three different industrial environments presented in the previous section (Figure 6.1). This resulted in a total of nine combinations, each simulating a unique interaction between ambient and source temperature conditions.

Each simulation spanned a full 24-hour cycle, which allowed for the analysis of both short-term dynamic behavior and long-term average performance metrics of evaporator capacity and COP. The naming convention (A-I) will be used throughout the subsequent results and discussion sections to refer to each simulated case.

Table 6.1: *Weather and source temperature data used for simulated cases.*

Case name	Ambient temperature data	Source temperature data
A		Forge
B	07.07.2024, Gliwice	Mine
C		Bearing factory
D		Forge
E	07.06.2024, Milano	Mine
F		Bearing factory
G		Forge
H	07.07.2024, Trondheim	Mine
I		Bearing factory

6.5 Results and discussion

The section presents the results of the numerical simulations performed for the R290 ERS under transient operating conditions, incorporating both variable generator temperature derived from industrial waste heat sources and fluctuating ambient temperatures affecting the condenser and ejector outlet conditions. The purpose of this analysis is to evaluate the system thermodynamic response, cooling performance, and control behavior in realistic boundary scenarios that mimic real-world operation, also focusing on the ejector device and evaluating its performance parameters.

The results are analyzed both locally, with respect to instantaneous values focusing on system stability, efficiency trends, and control response over a 24-hour operating cycle, as well as globally, looking at the 24-hour mean averaged values to evaluate the system operation under various conditions and compare them under operation in different scenarios.

Figure 6.4 presents the dynamic performance of the R290 ERS for the case of Gliwice, evaluated using the waste heat temperature data from a forge. This ambient temperature data is characterized by the highest daily temperature amplitudes among the analyzed cases, with temperatures ranging from approximately 8°C to 25°C. At the same time, the generator temperature exhibits high fluctuations due to the unstable thermal behavior of the forge waste heat, introducing significant variability to the motive nozzle inlet conditions.

Looking at the ejector SP, shown in the third subplot, the graph shows a clear correlation with the trend of ambient temperature. During the early morning hours, when the ambient temperature is at its lowest, the ejector operates at SP1, representing the near-fully open configuration. As the ambient

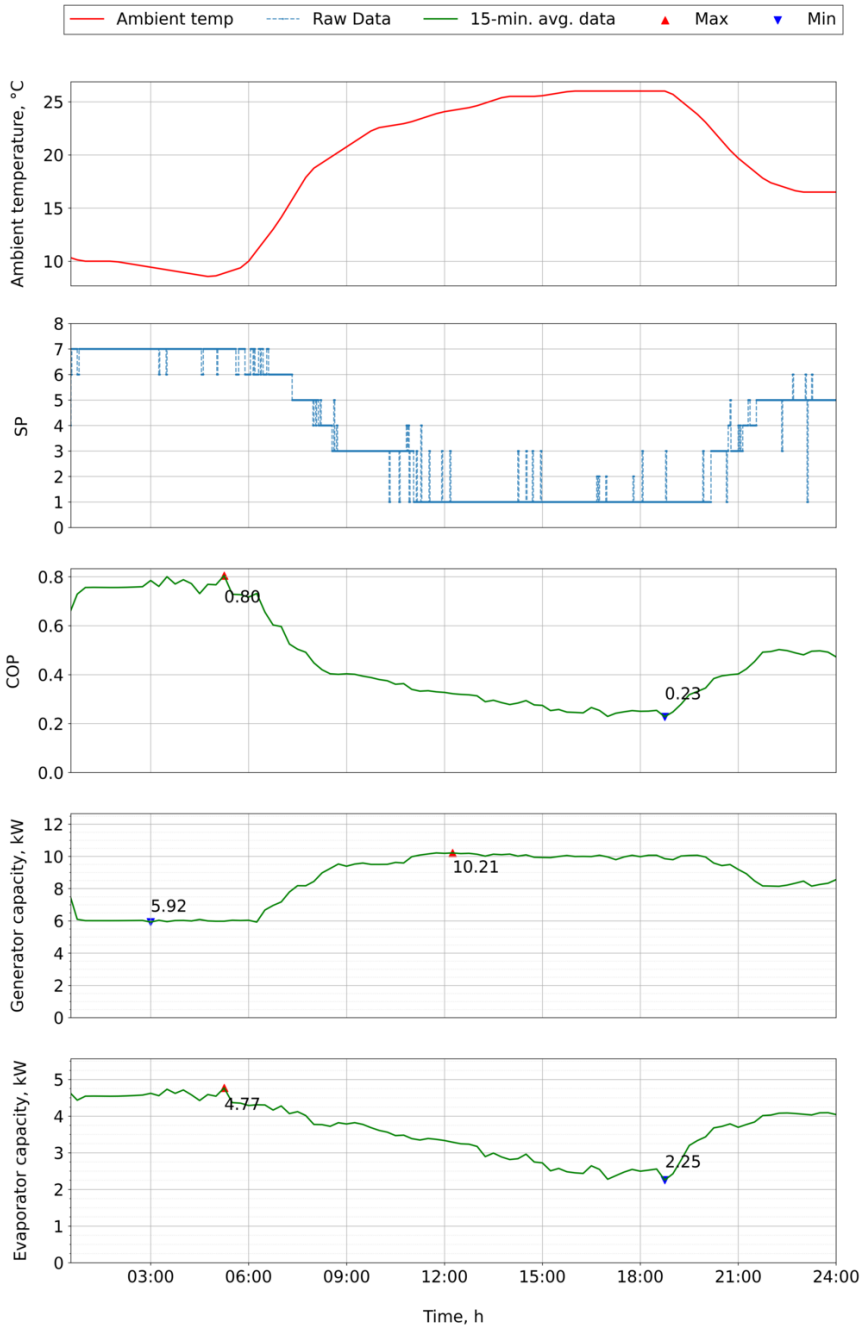

Figure 6.4: *Dynamic simulation results of performance parameters and spindle position (SP) results of the ERS equipped with VGE for Case A*

temperature increases throughout the day, the spindle closes progressively, reaching SP7 at midday, corresponding to the most restrictive nozzle throat. This wide operational range from SP1 to SP7 confirms that for this representative case the VGE adapts dynamically showing its full potential to control the ejector and system capacity by means of spindle. The short-term oscillations in SP are observed, driven by fluctuations in source temperature. These oscillations suggest that further tuning of the control algorithm of the SP responsiveness should be made. In the subsequent chapters, this issue will be addressed by applying a longer averaging period of the source temperature data, in order to mitigate oscillatory behavior.

The COP for this case varies between 0.23 and 0.79 over the course of the day. The highest COP values are recorded during periods of low ambient temperature, while the minimum COP coincides with the peak in ambient temperature, highlighting the strong inverse relationship between the ambient conditions in the condenser and the overall efficiency of the system, characteristic for the refrigeration system. A similar trend is observed in the generator capacity, which ranges from 5.9 to 10.2 kW. The lowest generator demand is observed during the early hours, corresponding to low thermal load and high system efficiency, whereas the maximum occurs when the spindle position is at SP1 and the system requires higher mass flow rate through the motive nozzle to meet increased cooling demand.

Finally, the evaporator capacity of the evaporator ranges from 2.27 to 4.70 kW. The maximum is observed during the early morning, in alignment with both low ambient temperature and higher SPs of the ejector. As the ambient temperature rises, the evaporator capacity gradually decreases, reaching its minimum at the warmest point of the day. While the COP and generator capacity are clearly linked to ambient temperature, the evaporator performance also demonstrates a dependence to the SP curve. This highlights the inherent sensitivity of the ejector performance to variations at the outlet nozzle exposed to the ambient conditions, which often leads to off-design operation. However, the implementation of a VGE and a controllable spindle enables capacity modulation, allowing the system to adapt dynamically and optimize operation by maximizing the SN mass flow rate.

Figure 6.5 presents the ejector operation for case A. The mass entrainment ratio fluctuates between 0.26 and 0.88 during the 24-hour simulation. These values are closely correlated with the SP value, as capacity control strongly influences the mass entrainment capacity. The highest mass entrainment ratio values are observed when the ejector operates in SP7, the most restrictive configuration, where the throat of the motive nozzle is nearly closed, maximizing the mass entrainment ratio. In contrast, the lowest

entrainment occurs in SP1, where the nozzle is almost fully open.

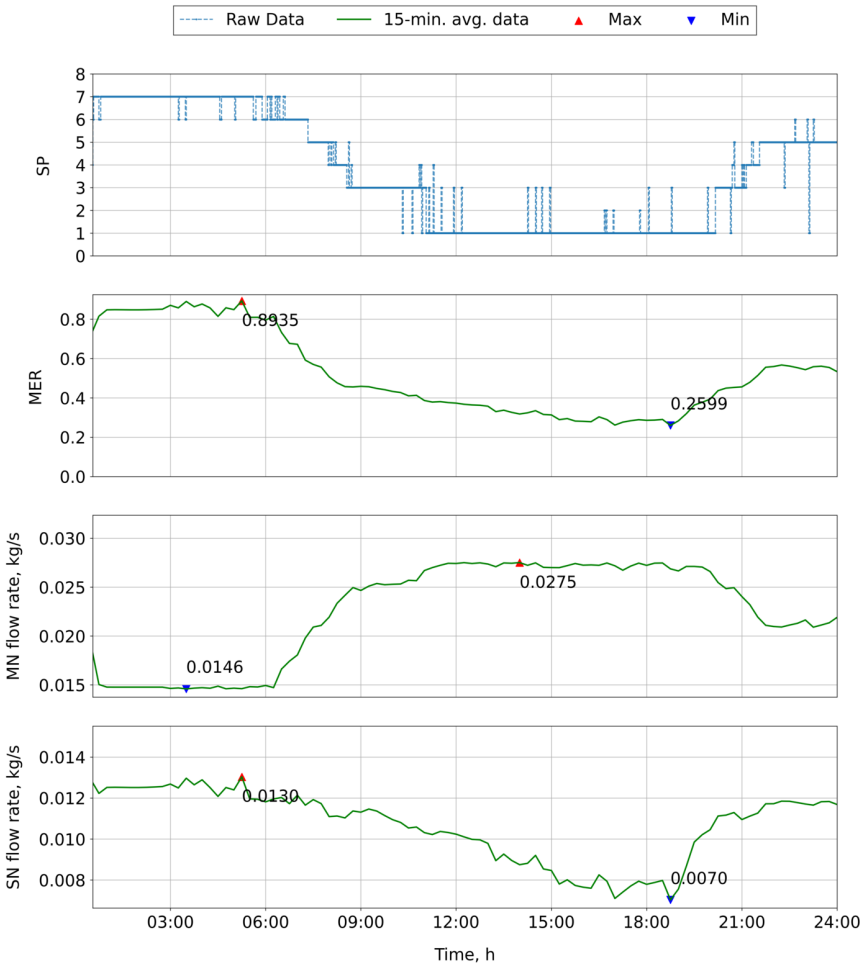

Figure 6.5: *Dynamic simulation results of ejector mass entrainment ratio (MER) and motive and suction nozzle mass flow rates for Case A*

The motive nozzle mass flow rate presents an inverse relationship, following the opposite trend. The motive nozzle flow ranges from a minimum of 0.0145 kg/s at SP7, to a maximum of 0.0275 kg/s at SP1. This outcome is consistent with the expected response of a choked nozzle, where the spindle position directly controls the effective throat area and therefore the critical flow rate through the motive stream.

The suction nozzle mass flow rate varies between 0.0071 and 0.0128 kg/s. Unlike the motive nozzle flow, the suction nozzle mass flow rate does not exhibit a direct one-to-one relationship with a spindle position alone. This is

because suction performance depends on a combination of factors, including ejector geometry, current ambient conditions at the outlet (which affect back pressure), and whether the ejector operates under design-on or design-off conditions. As a result, the suction behavior appears more complex and reflects the combined influence of external boundary conditions and internal geometry modulation.

Figure 6.6 presents the dynamic performance of the ERS for Case B, using ambient temperature data from Gliwice and generator-side input from a mine waste heat source. In contrast to Case A, using the forge waste heat data, the mine data exhibits significantly lower thermal variability, with source temperature fluctuations remaining within a narrow band of approximately ±0.5-1.0 K on an hourly scale. This stability has a direct impact on system operation, particularly with regard to the ejector control behavior.

The SP reflects the reduced variability in the waste heat temperature condition. The SP profile is smooth and gradual, transitioning between SP1 and SP7 throughout the day. Apart from two brief deviations, the control signal does not display the SP oscillations observed in Case A. This indicates a more stable and predictable control response when the source temperature represents a more stable manner.

As for the COP, it ranges from a minimum of 0.29 to a maximum of 0.72. Compared to the forge case presented in Case A, the COP curve appears to be more stable, aligning well with the smoother trends in ambient and source temperatures. The maximum COP again occurs during the early morning when the ambient temperatures are at the lowest and the ejector operates under high-efficiency conditions. As the day progresses and ambient temperatures rise, the COP decreases but remains higher than the values recorded for the forge case, confirming the performance benefits of a stable heat source. Generator capacity varies between 6.2 and 10.5 kW. The trend of capacity follows the expected behavior, with lower values in the early hours of the day and higher values coinciding with increased cooling demand and larger SP openings. The more stable waste heat profile ensures that the generator-side performance remains continuous, avoiding abrupt spikes or dips in the thermal input.

Finally, the evaporator capacity ranges from 3.0 to 4.5 kW. The highest evaporator capacity value is reached during periods of low ambient temperature and optimal ejector operation, while the lowest is recorded during midday when the system faces the highest thermal rejection load. In particular, the capacity of the evaporator maintains a smoother profile than in the previous case, once again benefiting from the steady heat input at the motive

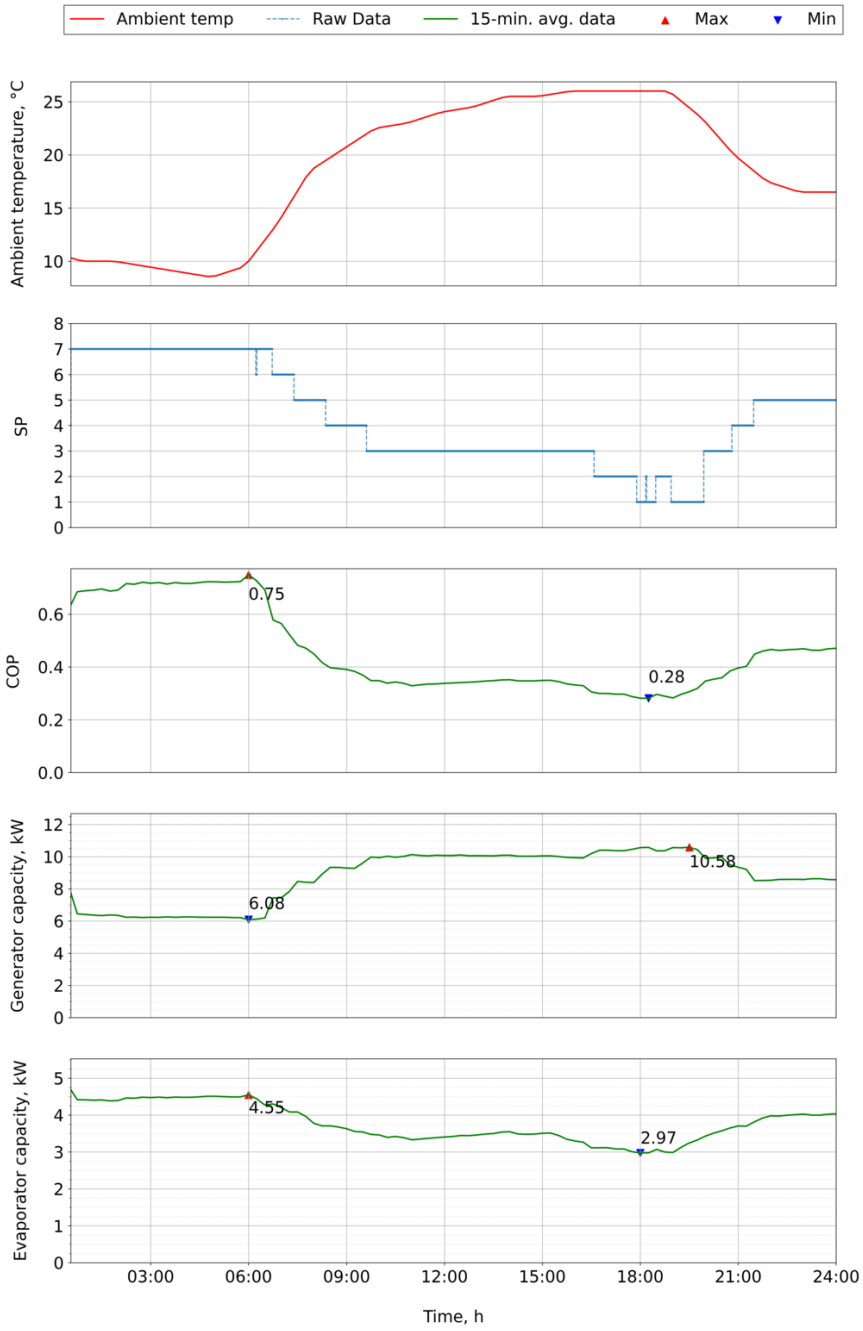

Figure 6.6: *Dynamic simulation results of performance parameters and spindle position (SP) results of the ERS equipped with VGE for Case B.*

nozzle.

In Figure 6.7, the ejector performance for Case B is presented. The mass entrainment ratio ranged from 0.33 to 0.81 over a 24-hour period. The highest entrainment is achieved when the SP is at the most restricted position (SP7), while the lowest mass entrainment ratio corresponds to more open configurations (SP2-SP3) during higher ambient temperature periods. This confirms a consistent inverse correlation between the mass entrainment ratio and spindle position, as tighter nozzle restrictions favor entrainment at lower motive nozzle mass flow rates.

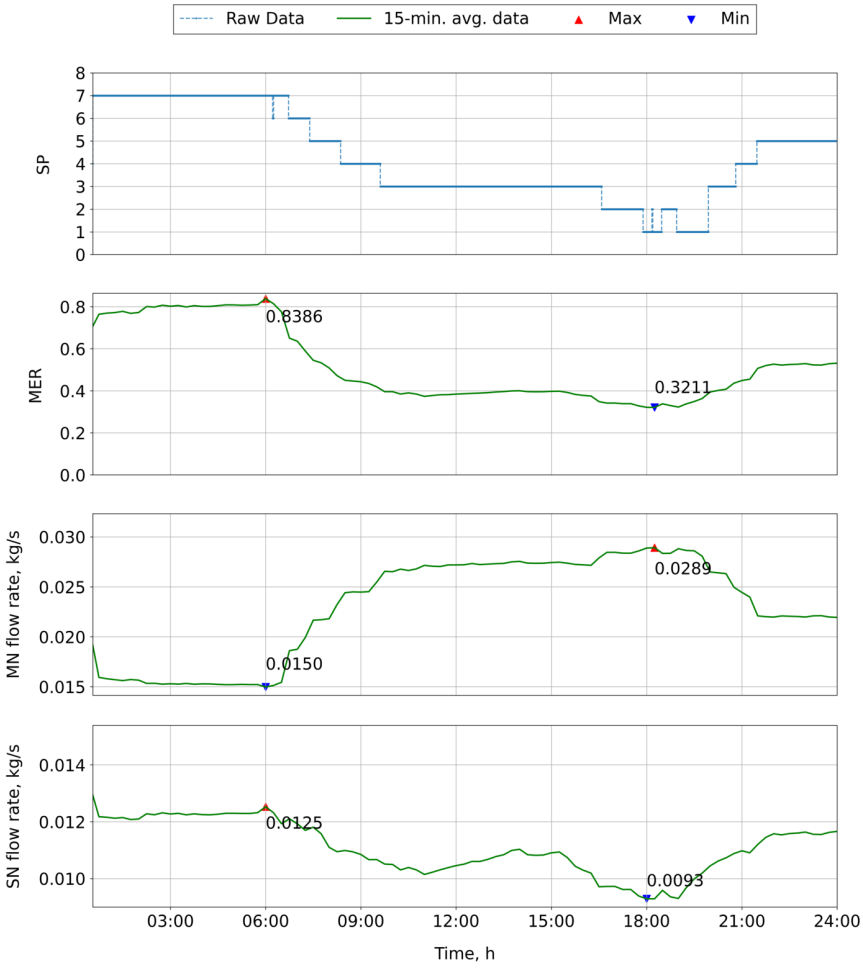

Figure 6.7: *Dynamic simulation results of ejector mass entrainment ratio (MER) and motive and suction nozzle mass flow rates for Case B.*

The motive nozzle mass flow rate shows a trend directly governed by the

SP and the motive nozzle thermodynamic conditions. As the ejector spindle moves toward the maximal opening, the effective throat area increases, allowing higher critical mass flow. Consequently, the motive nozzle mass flow rate rises from a minimum of 0.0152 kg/s at SP7 to a maximum of 0.0286 kg/s when the spindle reaches its most open positions in the middle of the day. These results align with theoretical expectations and confirm that the VGE control algorithm effectively modulates the flow through the motive nozzle in response to changing boundary conditions.

Analysing the suction nozzle mass flow rate, it varies between 0.0094 and 0.0123 kg/s. Although partially dependent on spindle position, this parameter is more complex in nature due to its sensitivity to both the entrainment capacity (linked to SP) and the ejector outlet pressure, influenced by ambient temperature. The suction nozzle mass flow rate is also modulated by the control logic presented in Chapter 3, which dynamically updates the ejector geometry to match system demands. Thus, while a general trend is visible, the suction flow pattern reflects the interaction between the internal geometry and the external thermal conditions, highlighting the importance of the dynamic control for the real-time ejector optimization.

Figure 6.8 presents the dynamic simulation results for Case C, where the R290 ERS is subjected to the ambient temperature profile of Gliwice and a waste heat input from the bearings factory. The source temperature in this case exhibits a moderately variable behavior, ranging from approximately 90 to 98°C. The highest degree of fluctuation occurs during the early morning hours, followed by a more stable thermal profile throughout the rest of the day. These initial instabilities reflect the short-term industrial process variations typical of this type of facility.

The control response of the SP reflects generator variability in this context. In the early hours of the day, the SP plot reveals a series of short-term oscillations caused by the transient changes in the waste heat source temperature. However, as the source conditions stabilize, the control system maintains consistent operation, with only two brief disruptions around 8:15 and again near 21:30. For most of the day-time operation, from approximately 09:00 to 18:40, the system stabilizes at SP1, indicating sustained operation at the fully open ejector geometry due to high thermal demand and elevated ambient temperature levels.

Moving to the next parameter, the COP varies from 0.23 to 0.79 throughout the 24-hour period. The maximum COP is recorded during the early morning when both the ambient and source temperatures are lower. Despite minor fluctuations in SP during this time frame, the COP remains stable, demonstrating the system's resilience to slight control perturbations. A no-

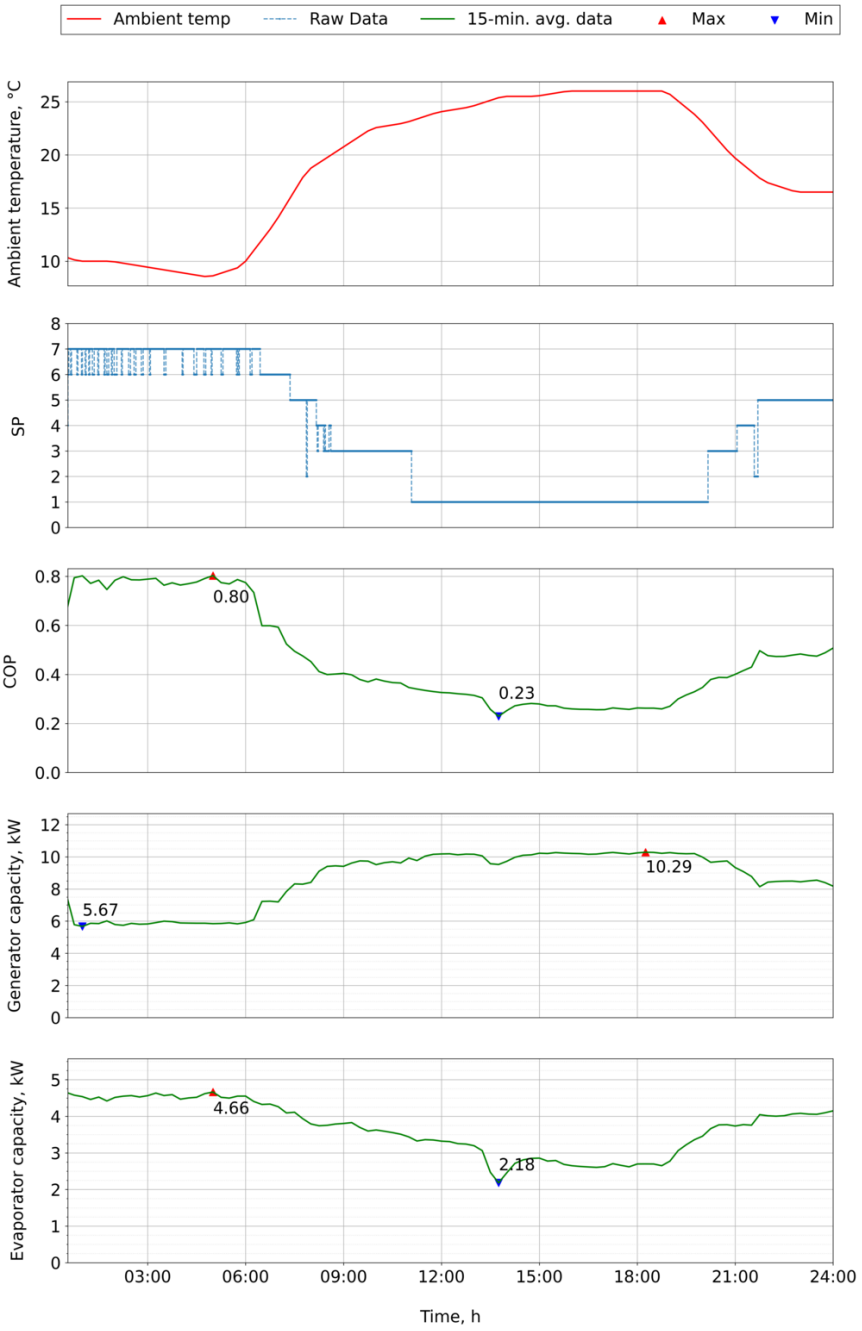

Figure 6.8: *Dynamic simulation results of performance parameters and spindle position (SP) results of the ERS equipped with VGE for Case C.*

table COP drop is observed around 14:00, which corresponds to a short-term decrease in source temperature and a consequent reduction in suction nozzle performance.

The generator capacity ranges between 5.78 and 10.27 kW. The lower values appear during the early morning hours, gradually increasing as the ambient temperature and evaporator capacity increase. The peak generator load coincides with the sustained SP1 period, where the ejector geometry is almost fully open and the system is operating under high-load conditions. Looking at the next parameter, the evaporator capacity of the evaporator in this case varies from a minimum of 2.17 kW to a maximum of 4.60 kW. The highest values are observed during the early morning when the ejector operates under favorable thermodynamic conditions. As ambient temperature increases which results in ejector suction mass flow rate decreased, the evaporator capacity gradually decreases, with the most significant drop occurring around noon, corresponding to the same event that triggered the COP reduction.

Figure 6.9 presents the ejector performance for Case C. Compared to the previous case involving the mine, the ejector performance here shows more irregular behavior due to the higher frequency fluctuations in the temperature profile of the source side, particularly in the early hours of the day. This variability introduces disturbances in the system, reflected in the dynamics of both the mass entrainment ratio and the mass flow rates.

The mass entrainment ratio fluctuates between 0.26 and 0.89 over the 24-hour period. The maximum value occurs during early operation when the ejector geometry is mostly restricted (SP7), resulting in efficient entrainment of the suction stream. The lowest mass entrainment ratio is observed around 14:00, coinciding with a noticeable drop in the temperature of waste heat, which affects the thermodynamic conditions in the motive nozzle and consequently degrades the entrainment performance.

The motive nozzle mass flow rate varies between 0.0139 and 0.0281 kg/s. Its profile reflects both the spindle position and the thermal input to the generator. As the ejector motive nozzle opens, the mass flow rate through this nozzle increases, with the maximum reached during mid-day operation under high ambient load. A sharp disturbance is again seen at approximately 13:45, where the sudden dip in the waste heat source temperature leads to a temporary decline in the motive mass flow.

The suction nozzle mass flow rate ranges between 0.0067 and 0.0126 kg/s. Similarly to the motive nozzle stream, the suction nozzle mass flow rate is highly responsive to both ejector geometry, influenced by the SP value, and external boundary conditions. The most visible reduction in the

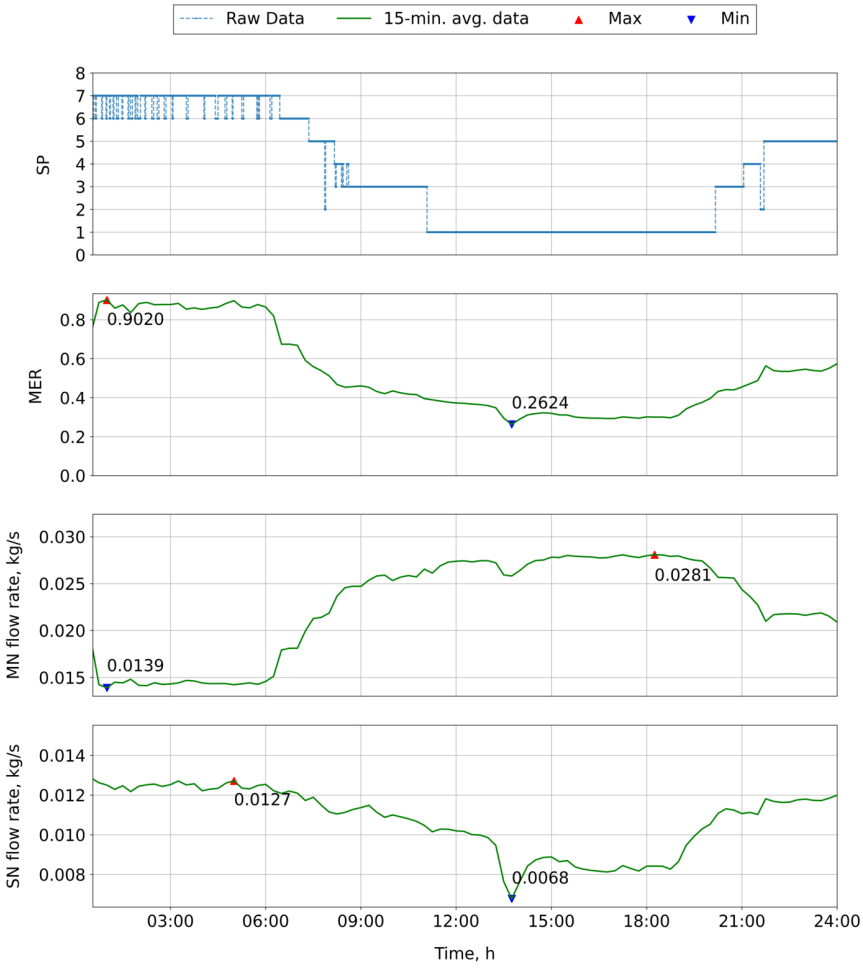

Figure 6.9: *Dynamic simulation results of ejector mass entrainment ratio (MER) and motive and suction nozzle mass flow rates for Case C.*

suction nozzle mass flow rate occurs at the same time as the dip in the mass entrainment ratio and the motive nozzle mass flow rate flow, highlighting the sensitivity of the ejector system to generator instabilities. Outside of this disturbance, the suction nozzle mass flow rate remains relatively steady, with gradual reductions during higher ambient temperatures and partial recovery as external conditions improve toward the evening.

Figure 6.10 presents the simulation results for Case D, where the R290 ERS is exposed to the ambient temperature profile of Milano combined with the generator-side waste heat input from the forge. Compared to Gliwice, the Milano ambient temperature shows a higher baseline with a smaller daily

temperature amplitude, ranging from approximately 20 to 28°C. In contrast, the forge waste heat source exhibits high-frequency oscillations, resulting in a strongly fluctuating generator inlet profile.

The graph of spindle response reflects the instability of the forge data. The plot displays persistent short-term oscillations across the entire 24-hour period, particularly pronounced between 3:15 until midnight. Despite the elevated ambient temperatures, the spindle transitions between SP2 and SP5, indicating continuous adjustments required to respond to transient thermal load and generator-side instability. The oscillatory behavior confirms the control algorithm aims to maintain the stable operation under highly variable source input. Looking at the system COP in this case, it ranges from a minimum of 0.16 to a maximum of 0.40. While the overall efficiency remains comparable to other Milano cases, the fluctuations in source temperature introduce greater variability in the COP curve, with the most significant drop observed between 17:30 and 18:00. This degradation in performance is linked to source-side instabilities propagating through the system. Thermal input of the generator varies from 9.22 to 10.47 kW. This relatively narrow band is consistent with the stable average value of the forge heat source, though the superimposed high-frequency oscillations necessitate continuous ejector modulation. The evaporator capacity ranges from 1.70 to 3.74 kW. As expected, the lowest values occur during the most intense disturbances in the generator-side temperature, while the peak evaporator capacity is reached during periods of the relatively steady operation and low ambient temperature.

In Figure 6.11, the ejector behavior for Case D is presented. The mass entrainment ratio varies between 0.19 and 0.46, closely following the high-frequency spindle position fluctuations. These results highlight the difficulty of maintaining stable entrainment performance when the generator conditions are rapidly changing. Maximum mass flow rate values coincide with more restrictive nozzle configurations (e.g., SP5), while the lowest values correspond to fully open throat positions (SP1-SP2).

The motive nozzle mass flow rate exhibits a dynamic range from 0.0242 to 0.0287 kg/s. Its profile mirrors both the SP variation and the time-varying generator temperature, with frequent local peaks and troughs. The suction mass flow rate similarly fluctuates between 0.0054 and 0.0112 kg/s, with the lowest values appearing during the same time windows as the minimum mass entrainment ratio and motive nozzle flow. This further confirms the interconnected nature of source-side disturbances and the ejector performance degradation.

In Figure 6.12, the dynamic simulation results for Case E are presented,

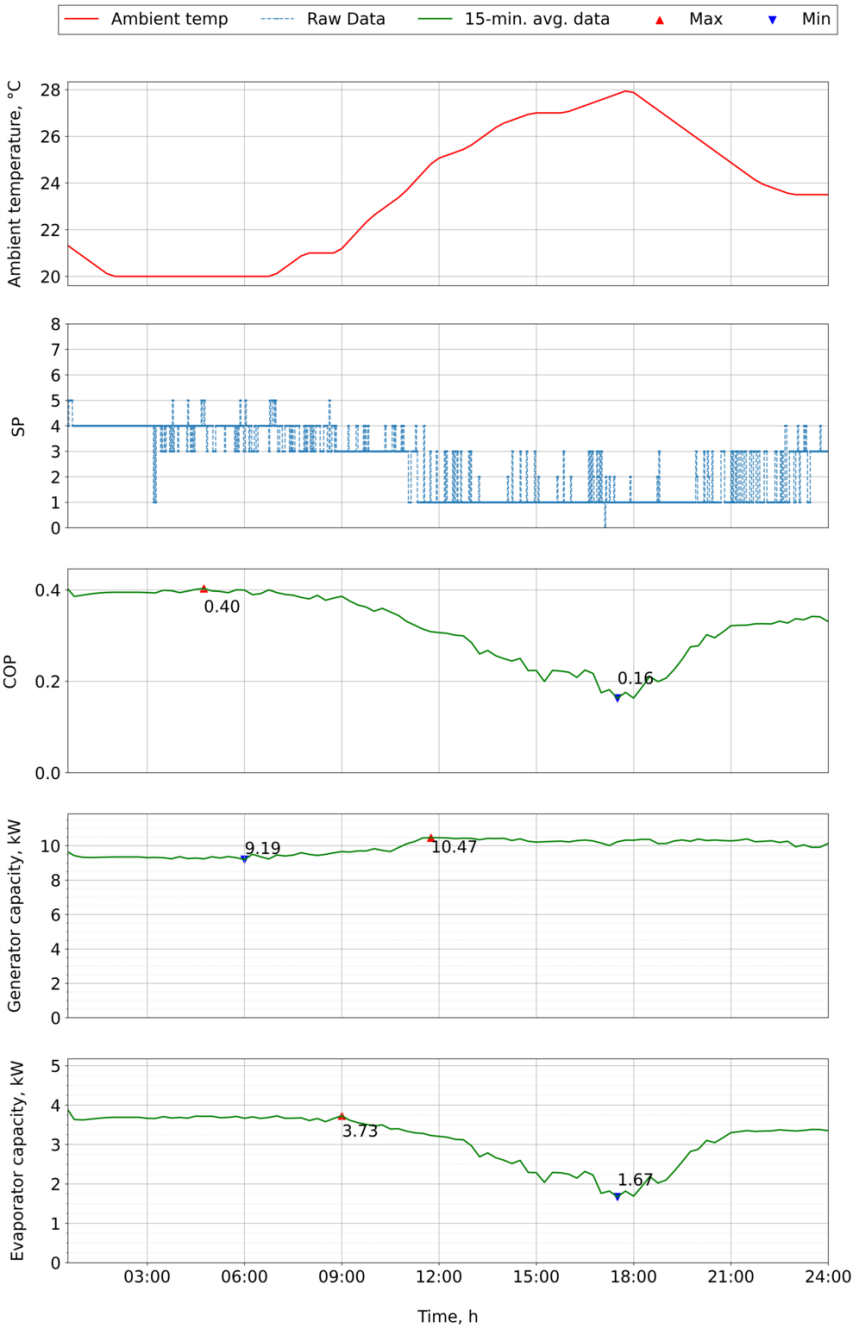

Figure 6.10: *Dynamic simulation results of performance parameters and spindle position (SP) results of the ERS equipped with VGE for Case D.*

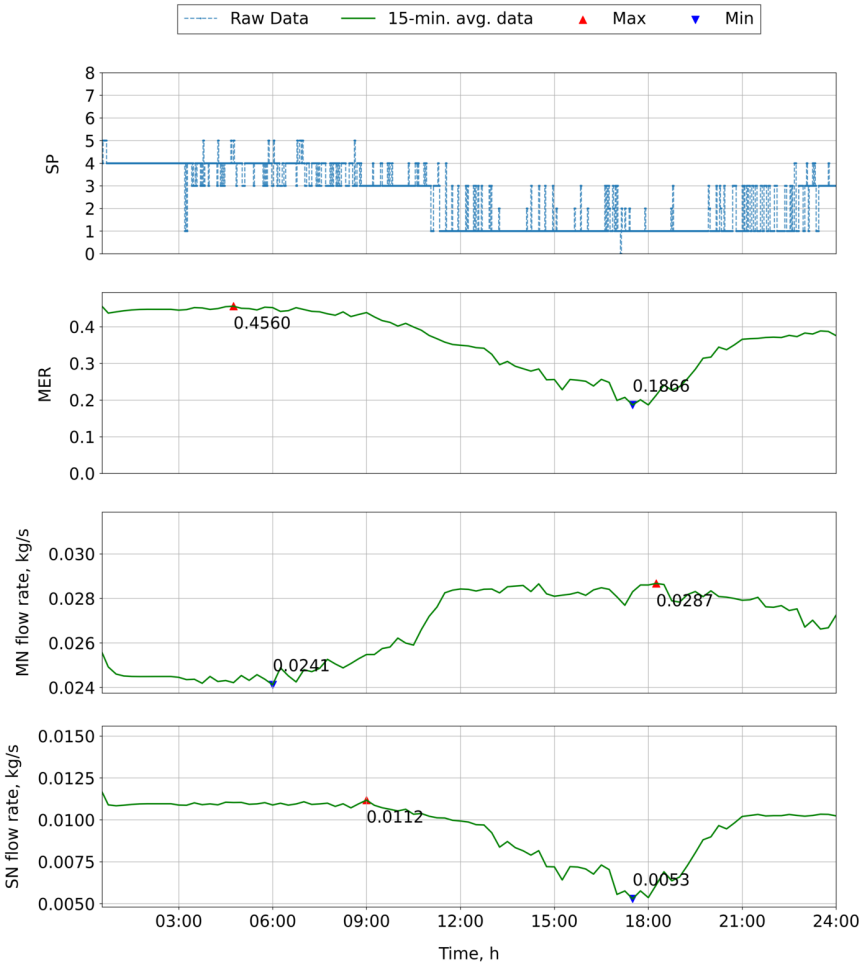

Figure 6.11: *Dynamic simulation results of ejector mass entrainment ratio (MER) and motive and suction nozzle mass flow rates for Case D.*

where the R290 ERS operates under ambient temperature conditions from Milano and uses waste heat input from a mine. The ambient temperature profile retains the high average characteristic of Milano's climate, with values ranging between 20 and 28°C. The mine heat source provides a stable thermal input, with source temperature oscillations confined within a narrow range of 90 and 100°C and minimal high-frequency disturbances. This stability plays a key role in defining the ejector and system behavior.

The SP varies between SP1 and SP5, with smooth transitions and no visible short-term oscillations, except for a few discrete changes at approximately 7:00 and 9:00. This reflects the robustness of the waste heat input

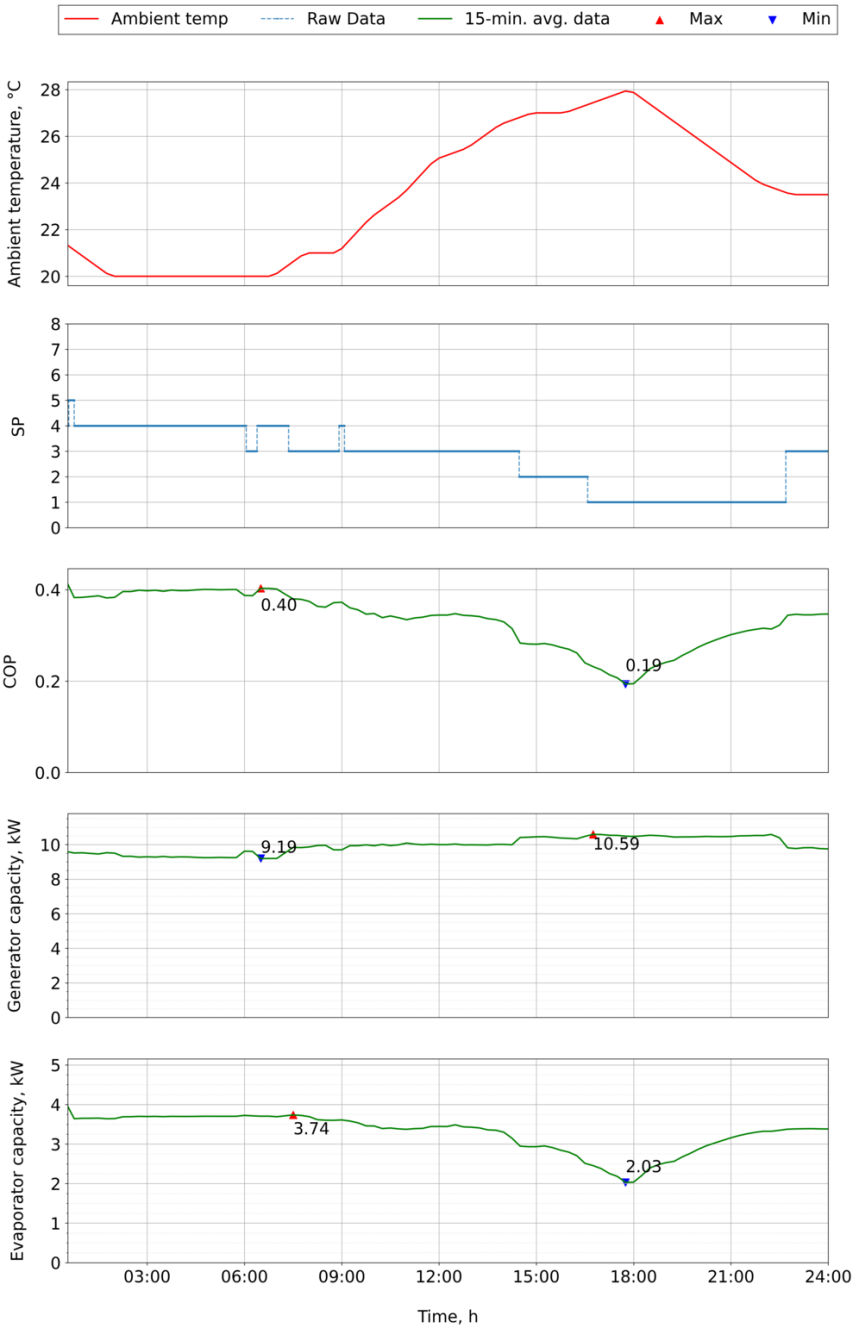

Figure 6.12: *Dynamic simulation results of performance parameters and spindle position (SP) results of the ERS equipped with VGE for Case E.*

from the mine, which enables the control algorithm to operate with minimal corrections. The SP remains at SP2 for the majority of the midday period, indicating sustained operation under high cooling load and ambient temperature. Looking at the COP, it varies between 0.20 and 0.40, with the highest values recorded during the early hours of the day. The smooth and stable COP curve again reflects the favorable impact of steady generator conditions. A slight dip in performance is observed around 17:50, likely linked to the peak in the ambient temperature. However, the system maintains consistent operation throughout the entire period without abrupt performance losses. Generator capacity ranges from 9.19 to 10.59 kW, showing a narrow and stable operational range. The evaporator capacity follows a similar trend, varying between 2.06 and 3.74 kW. These values, while slightly lower than those from more dynamic source inputs, are maintained more consistently throughout the simulation due to the predictable thermal input.

Figure 6.13 illustrates the ejector dynamics for Case E. The mass entrainment ratio ranges from 0.22 to 0.46. This relatively narrow operating range mirrors the behavior observed in the SP curve, with the maximum mass entrainment ratio recorded when the ejector throat is most restricted (SP5), and the lowest mass entrainment ratio values appearing during fully open operation (SP2) at peak ambient load.

The motive nozzle mass flow rate ranges from 0.0241 to 0.0293 kg/s, with the highest values again linked to high thermal demand during the afternoon. The stability of the mine source ensures that these mass flow rates evolve smoothly, without the abrupt variations seen in forge- or bearings-based cases. On the suction nozzle side, the mass flow rate fluctuates between 0.0065 and 0.0111 kg/s. Although partially modulated by the control algorithm, this flow is also shaped by the ambient temperature at the ejector outlet and the dynamic interaction between suction performance and ejector geometry. As in previous cases, the lowest suction nozzle mass flow rate coincides with the minimum mass entrainment ratio and the peak cooling load of the system.

Figure 6.14 illustrates the dynamic performance of the R290 ERS for Case F, where the system operates under Milano ambient conditions with waste heat sourced from the bearings factory. Similar to other Milano cases, the ambient temperature fluctuates within a relatively narrow band (from 20 to 28°C) and peaks around mid-afternoon. In contrast, the generator input from the bearings factory is characterized by pronounced short-term oscillations, especially in the early part of the day. These fluctuations introduce higher-frequency variations in the system response and control behavior.

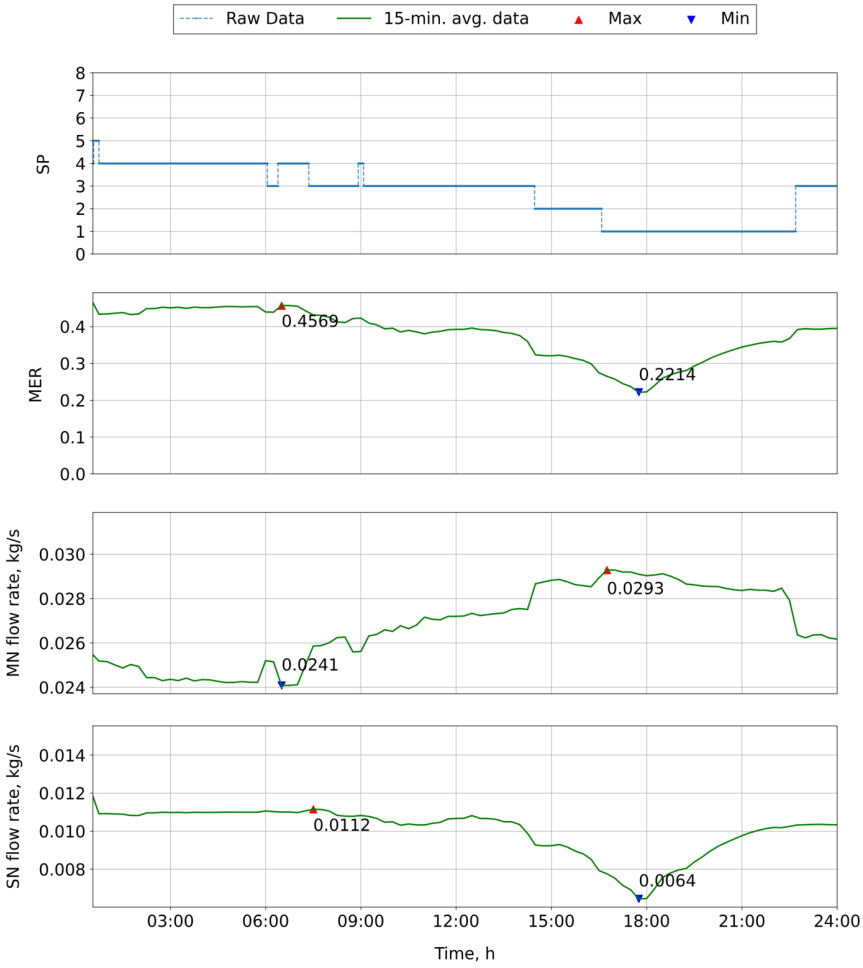

Figure 6.13: *Dynamic simulation results of ejector mass entrainment ratio (MER) and motive and suction nozzle mass flow rates for Case E.*

The ejector SP in this case transitions between SP1 and SP3, with occasional high-frequency oscillations observed from the start untill 6:00 and again after 22:00. For most of the day, i.e., from around 11:00 to 22:00, the system maintains continuous operation at SP1. This stable setting corresponds to high thermal demand, requiring an almost fully open ejector configuration to accommodate increased cooling requirements under persistently high ambient conditions. The COP profile for Case F ranges between 0.11 and 0.41. The lowest performance is recorded around 18:20, coinciding with the peak ambient temperature and a temporary dip in the generator temperature, which degrades motive nozzle conditions and therefore causes

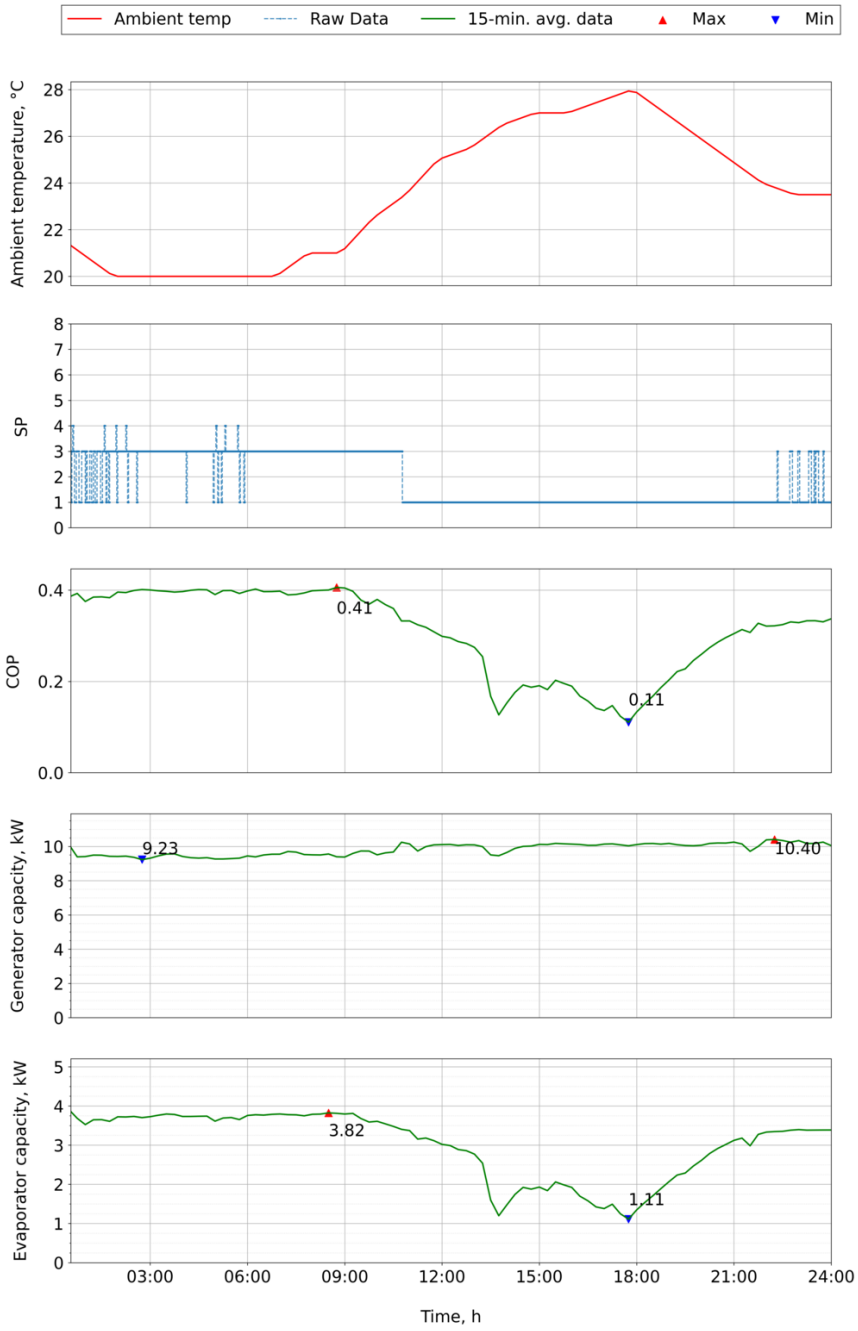

Figure 6.14: *Dynamic simulation results of performance parameters and spindle position (SP) results of the ERS equipped with VGE for Case F.*

the drop of suction nozzle mass flow rates. Despite this performance drop, the COP recovers quickly, reflecting the ability of the control system to adapt to transient disturbances. The heat capacity of the generator varies between 9.25 and 10.40 kW. This narrow operational band reflects the high baseline thermal load imposed by the ambient temperature. The evaporator capacity shows more pronounced variation, ranging from 1.16 to 3.82 kW. The lowest values are again observed at around 18:20, during the temporary system underperformance, while the maximum cooling output corresponds to the early hours of the day under more favorable ejector and ambient conditions.

Figure 6.15 presents the ejector behavior for Case F. The mass entrainment ratio varies from 0.13 to 0.46, with the lowest values observed during the short performance dip mentioned earlier. The highest entrainment is reached when the SP transitions to more restrictive positions (SP3) during early operation.

The motive nozzle mass flow rate ranges between 0.0242 and 0.0280 kg/s. These values are influenced by both SP and the thermodynamic properties of the motive fluid. The flow rate exhibits a gradual increase throughout the day, corresponding to the rising cooling load. As for the suction nozzle mass flow rate, more significant fluctuations are observed, ranging between 0.0037 and 0.0114 kg/s. This metric is the most sensitive to ambient temperature and the transient influence of source-side disturbances, especially evident around 18:30, when both suction and motive nozzle flows experience a noticeable drop, resulting in the observed minimum in the mass entrainment ratio and the system COP.

Figure 6.16 presents the dynamic performance of the ERS under Case G, where the ambient temperature data from Trondheim is combined with the waste heat input from the forge. Among all analyzed locations, Trondheim exhibits the lowest overall ambient temperatures and smallest diurnal variation, with a daily temperature amplitude below 10°C and values remaining within the range between 6 and 16°C. In contrast, the forge waste heat input maintains a highly unstable profile, with substantial short-term temperature oscillations throughout the simulation. This juxtaposition of stable and unstable boundary conditions offers an interesting scenario to assess the adaptability of the VGE work.

The SP profile for this case shows continuous adjustments throughout the day, with the control algorithm modulating the spindle between SP2 and SP7 in response to the short-term disturbances in the source temperature. Despite the relatively stable ambient temperature profile, the ejector control system remains active, reflecting the highly fluctuating character of the generator-side thermal input. The SP oscillations are less frequent than in the Gliwice

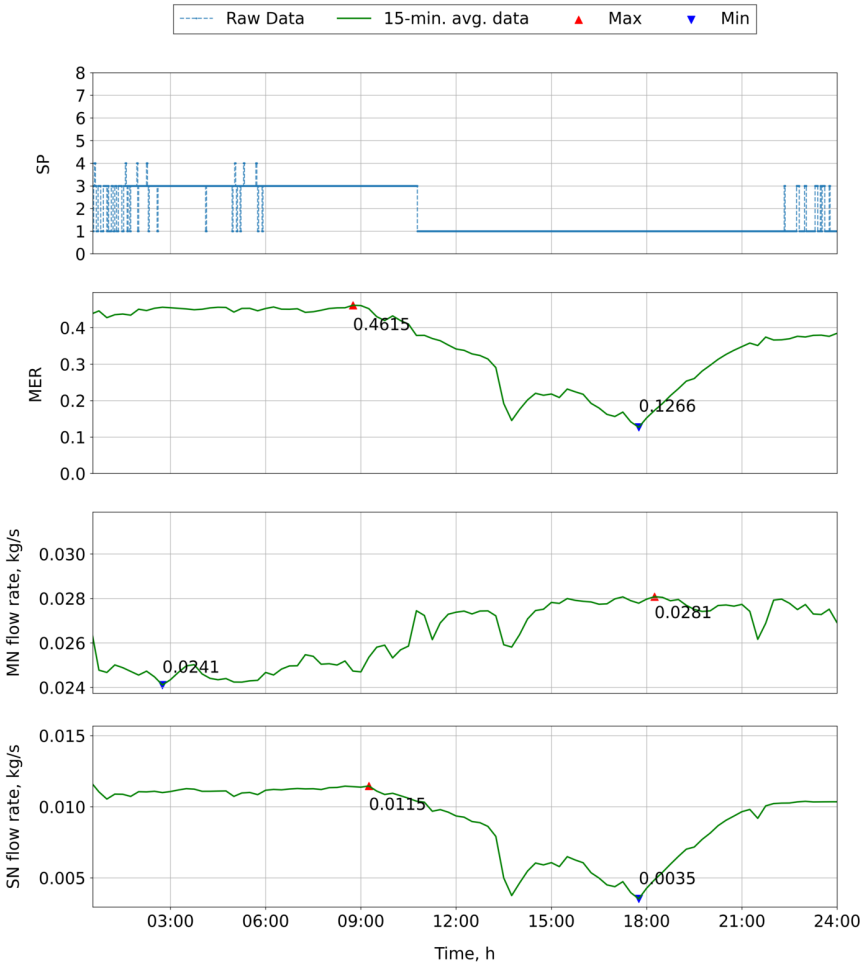

Figure 6.15: *Dynamic simulation results of ejector mass entrainment ratio (MER) and motive and suction nozzle mass flow rates for Case F.*

case with the same source, yet they still appear in several clusters, especially during mid-day periods of increased generator variability. The system COP ranges between 0.48 and 0.75, maintaining relatively high values throughout the entire day. The maximum COP is observed during the early morning hours when the ambient temperatures are lowest and the ejector operates at higher entrainment efficiency. Even during mid-day, the COP remains above 0.5, underscoring the beneficial impact of cooler ambient conditions on the condenser performance and the overall system efficiency. The generator capacity ranges from 6.1 to 8.4 kW, showing a relatively narrow spread compared to other cases. The maximum generator load occurs during early

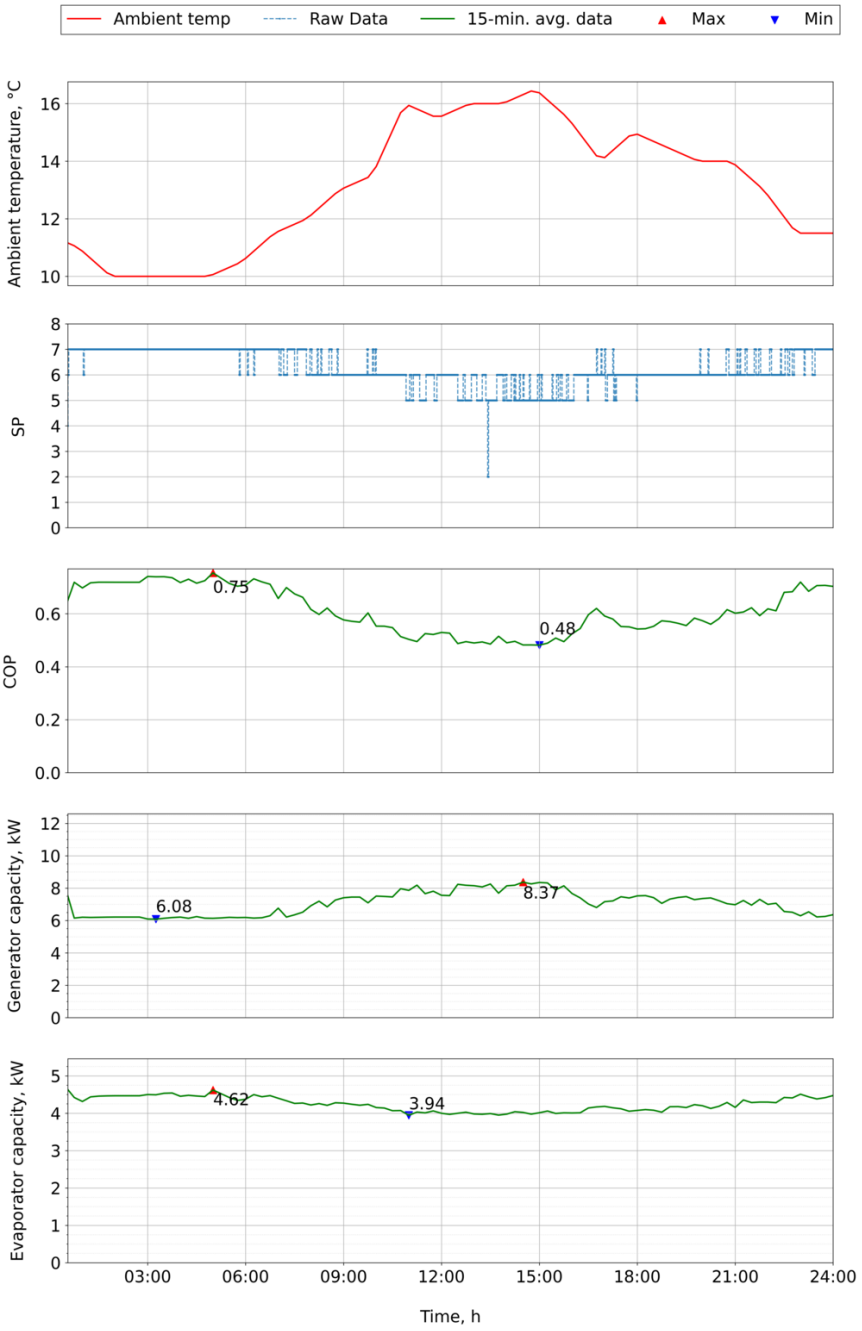

Figure 6.16: *Dynamic simulation results of performance parameters and spindle position (SP) results of the ERS equipped with VGE for Case G.*

afternoon, aligning with periods of increased thermal demand. Due to the cooler ambient temperature profile, the system does not require high motive nozzle mass flow rates, thus limiting the thermal input required at the generator. The evaporator capacity of the evaporator varies between 3.95 and 4.61 kW. These values are higher on average than those observed for the Milano and Gliwice cases, reflecting the favorable ambient temperature conditions in Trondheim. The lower ambient temperatures support the improved ejector entrainment and the reduced back pressure at the outlet, enabling higher and more consistent evaporator performance throughout the simulation period.

Figure 6.17 shows the ejector performance for the same case. The mass entrainment ratio ranges from 0.54 to 0.84 during the simulation. The maximum value is reached in the early morning under high SP configurations (SP7-SP6), when the ejector operates with the most restrictive throat diameter. The minimum mass entrainment ratio occurs during midday, when the spindle position is lower, increasing the effective motive nozzle throat to accommodate higher required flow rates through the motive nozzle. The trend once again confirms the inverse relationship between SP and the mass entrainment ratio.

The motive nozzle mass flow rate fluctuates between 0.0150 and 0.0215 kg/s, with a gradual increase during the day as the spindle opens in response to the system demand. The relatively small amplitude of variation in the motive nozzle flow confirms the stable generator-side flow behavior under lower ambient temperature conditions. No extreme mass flow rate spikes are observed, further validating the stable system behavior. Next, the suction nozzle mass flow rate varies between 0.0114 and 0.0127 kg/s. Compared to other cases, the suction nozzle flow exhibits limited variability, with a gradual profile that mirrors the modest variations in SP and the ambient temperature. The suction nozzle mass flow rate remains consistently high due to the combination of the low outlet back pressure and the steady generator input, resulting in a stable ejector operation and reliable evaporator performance.

Figure 6.18 presents the dynamic simulation results for Case H, where the ERS operates under ambient conditions of Trondheim and the generator-side thermal input from the mine waste heat source. Among all the analyzed cases, this configuration exhibits the most stable behavior, owing to the combination of a relatively narrow ambient temperature range and low-variability source temperature. The ambient air temperature fluctuates modestly between approximately 8 and 17°C, while the mine-derived waste heat data remains highly stable throughout the day.

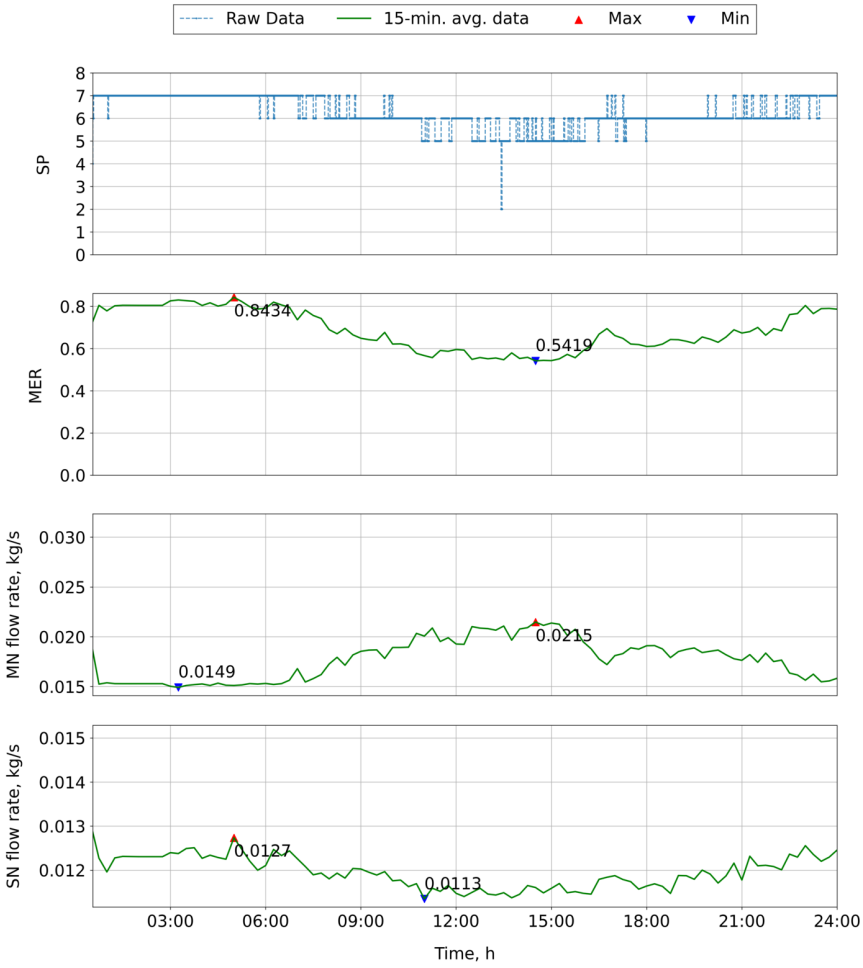

Figure 6.17: *Dynamic simulation results of ejector mass entrainment ratio (MER) and motive and suction nozzle mass flow rates for Case G.*

The SP curve, shown in the third subplot, confirms this stability, with the ejector operating predominantly at SP6. A brief transient shift to SP7 occurs early in the day, but aside from this, the control system maintains a steady spindle position, reflecting the absence of sharp variations in either generator or ambient boundary conditions. The graph of COP follows a smooth trajectory ranging from 0.52 to 0.74. These values are among the highest observed across all scenarios, further highlighting the benefit of reduced external variability on overall system efficiency. The peak COP is attained during the early morning hours under optimal thermal lift conditions, while the minimum is recorded at midday when ambient temperature and

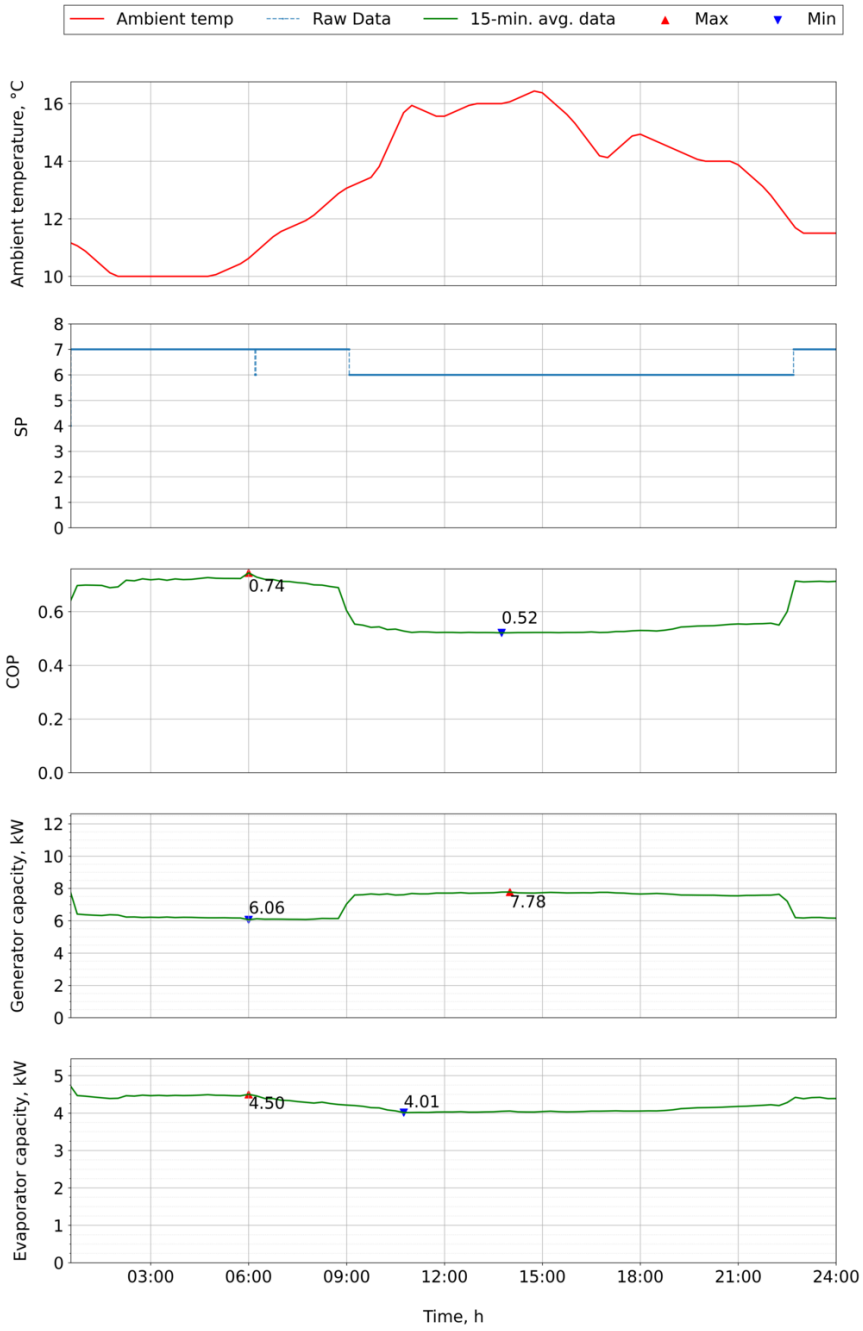

Figure 6.18: *Dynamic simulation results of performance parameters and spindle position (SP) results of the ERS equipped with VGE for Case H.*

condenser back pressure are highest. However, the relative change is modest, and no sudden efficiency losses are observed throughout the simulation. The generator-side thermal input varies between 6.08 and 7.77 kW. The flow remains consistent, and its evolution over time corresponds to the gradual increase in thermal demand as the day progresses. The limited spread in values indicates a more balanced system operation, aided by the predictability of the mine heat source. On the evaporator side, the evaporator capacity ranges from 4.01 to 4.51 kW. Compared to other cases, this is the most stable cooling performance recorded, with minimal deviation from the mean value. The early morning and late evening hours yield slightly higher cooling output, while midday values are marginally reduced due to increased condenser temperature. Still, the differences remain small, and the evaporator maintains near-constant operation throughout the day.

Figure 6.19 presents the ejector dynamics for the same scenario. The mass entrainment ratio varies within a relatively narrow band between 0.59 and 0.83. The peak value is observed during the early morning, corresponding to the SP7 operation and favorable thermodynamic conditions. As the spindle transitions to SP6, the mass entrainment ratio slightly decreases but maintains a high value throughout the day. This confirms the system ability to sustain efficient entrainment even with minimal geometric modulation.

The motive nozzle mass flow rate fluctuates between 0.0150 and 0.0199 kg/s. This range is narrower compared to more variable cases, and the shape of the curve aligns with spindle transitions and thermal load progression. The suction nozzle mass flow rate, ranging from 0.0115 to 0.0125 kg/s, exhibits a similarly smooth trend. The suction flow is maintained at a high level due to the combined effect of favorable ambient temperature and effective entrainment from the motive stream. These results confirm that under stable conditions, the VGE system is capable of maintaining consistent and high-performance operation with minimal actuator involvement, making it particularly suited for sites with predictable waste heat availability.

Figure 6.20 presents the results for Case I, where the ERS operates under the ambient temperature conditions of Trondheim and the waste heat data from the bearings factory. This configuration represents a combination of low ambient variability and a highly dynamic source temperature profile, characterized by frequent short-term fluctuations.

The ambient temperature ranges from 8 to 17°C, exhibiting modest variability typical for the Trondheim location. In contrast, the waste heat source from the bearings factory presents high-frequency oscillations, with temperature swings of up to 3-4 K within short-time intervals. This unstable thermal input affects the generator-side conditions and introduces a challenge

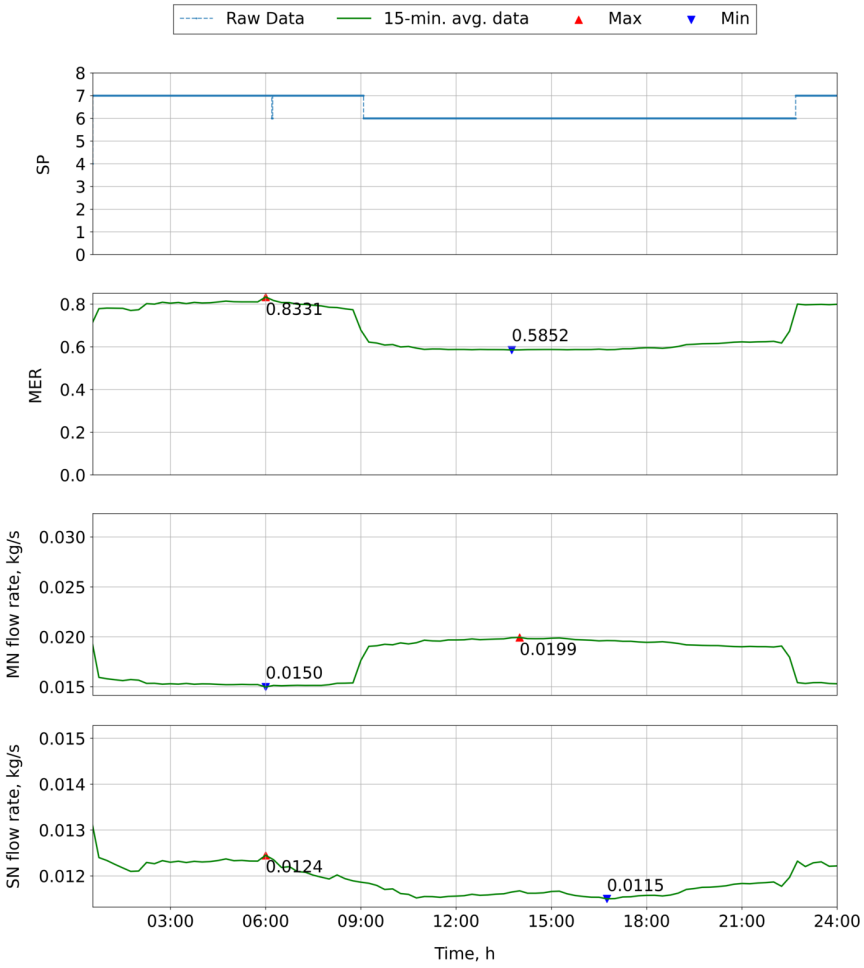

Figure 6.19: *Dynamic simulation results of ejector mass entrainment ratio (MER) and motive and suction nozzle mass flow rates for Case H.*

for the SP control system.

Looking at the plot of the spindle position, it reveals multiple short-term adjustments throughout the day, particularly during the morning and afternoon, as the system reacts to rapid source temperature changes. The ejector transitions primarily between SP6 and SP7, with high-frequency fluctuations especially prominent in the early and late parts of the day. This behavior suggests that the system attempts to stabilize entrainment despite the unstable motive inlet conditions, leveraging the VGE capacity for rapid response. The COP in this case varies from 0.51 to 0.73. Despite the source-side instability, the system maintains relatively high efficiency.

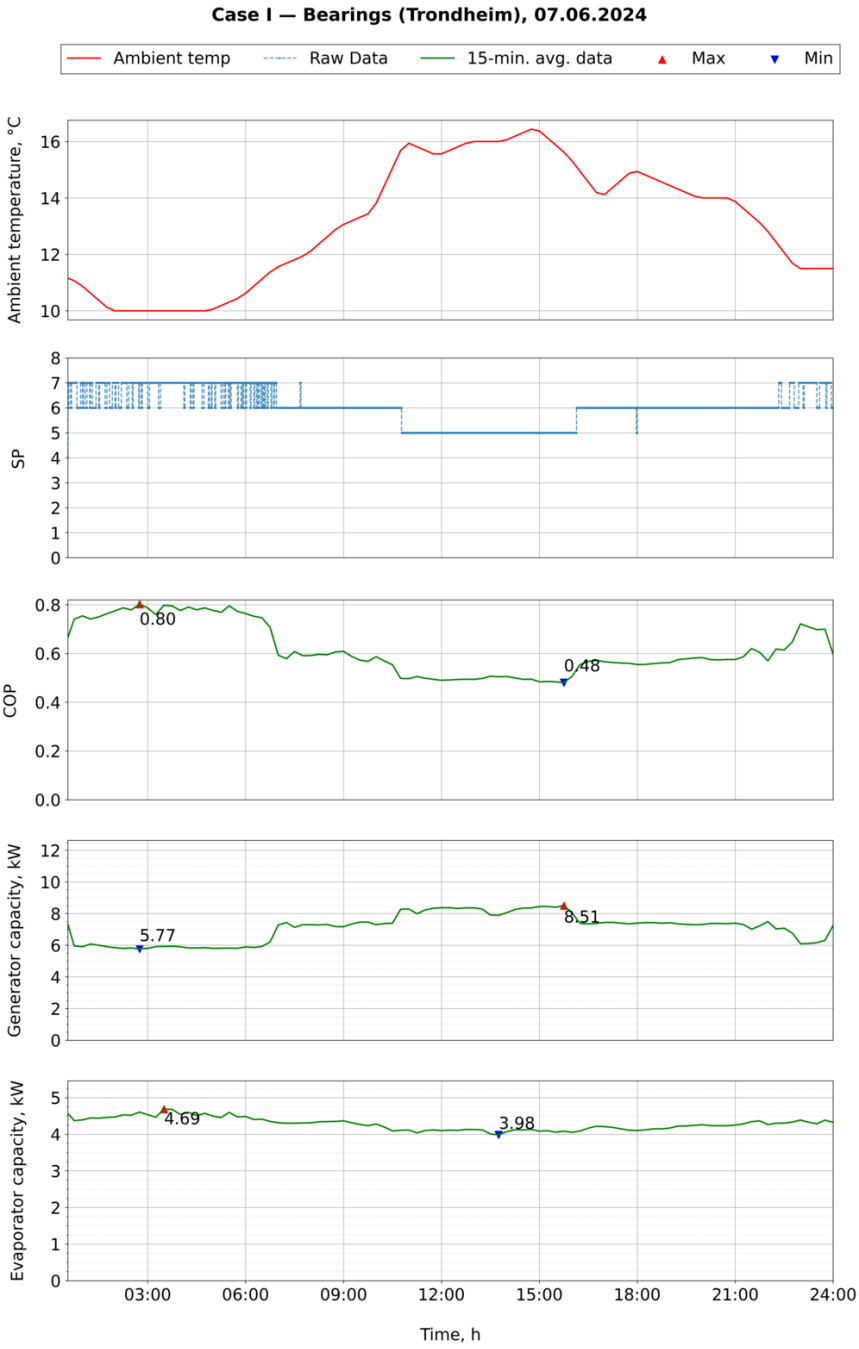

Figure 6.20: *Dynamic simulation results of performance parameters and spindle position (SP) results of the ERS equipped with VGE for Case I.*

The maximum COP is achieved during the early morning hours, as in the previous cases, while the minimum corresponds to a temporary drop in suction nozzle performance around midday. The overall profile remains relatively smooth, suggesting that the VGE mitigates the impact of source fluctuations on energy efficiency. Generator heat input ranges from 6.03 to 7.83 kW. The influence of source temperature oscillations is partially visible in this signal, particularly during the early morning and late evening, where sudden changes in the waste heat availability trigger corresponding adjustments in the motive nozzle flow. However, the heat capacity remains within a constrained band, indicating the resilience of the system to these transient disturbances.

As for the evaporator capacity of the evaporator, it fluctuates between 3.99 and 4.51 kW. The lower values align with periods of source-side instability, especially when the suction mass flow rate is briefly reduced. Still, the system recovers quickly, and the evaporator performance stabilizes during midday operation. The narrow spread of values again confirms the effectiveness of the VGE control in adapting to rapid changes and ensuring continuous thermal output.

Figure 6.21 presents the ejector performance under these conditions. The mass entrainment ratio ranges from 0.55 to 0.82, with the maximum recorded during early operation at SP7. The ratio drops temporarily around midday in response to the source-side temperature dips and associated changes in the flow balance between motive and suction nozzles.

The motive nozzle mass flow rate varies between 0.0150 and 0.0215 kg/s, showing a mild increasing trend during the day, in line with increasing thermal load and progressive opening of the spindle. Fluctuations in motive flow reflect the direct influence of generator temperature variability on choked flow at the motive nozzle. The suction nozzle mass flow rate remains within the range of 0.0113 to 0.0127 kg/s. While the suction flow pattern is overall stable, several transient dips are visible, particularly in the early and late parts of the day. These correspond to disturbances in the generator profile and confirm the importance of maintaining stable source conditions for optimal entrainment. Nevertheless, the active control system of the VGE successfully regulates the suction nozzle flow and ensures reliable operation even in a challenging thermal context.

The results summarized in Table 6.2 provide a comparative assessment of the daily averaged performance metrics of the R290 ERS system equipped with VGE across all the considered climatic zones and distinct waste heat sources in this analysis. The evaluation of daily averaged COP, evaporator capacity, and generator capacity demonstrates distinct patterns associated

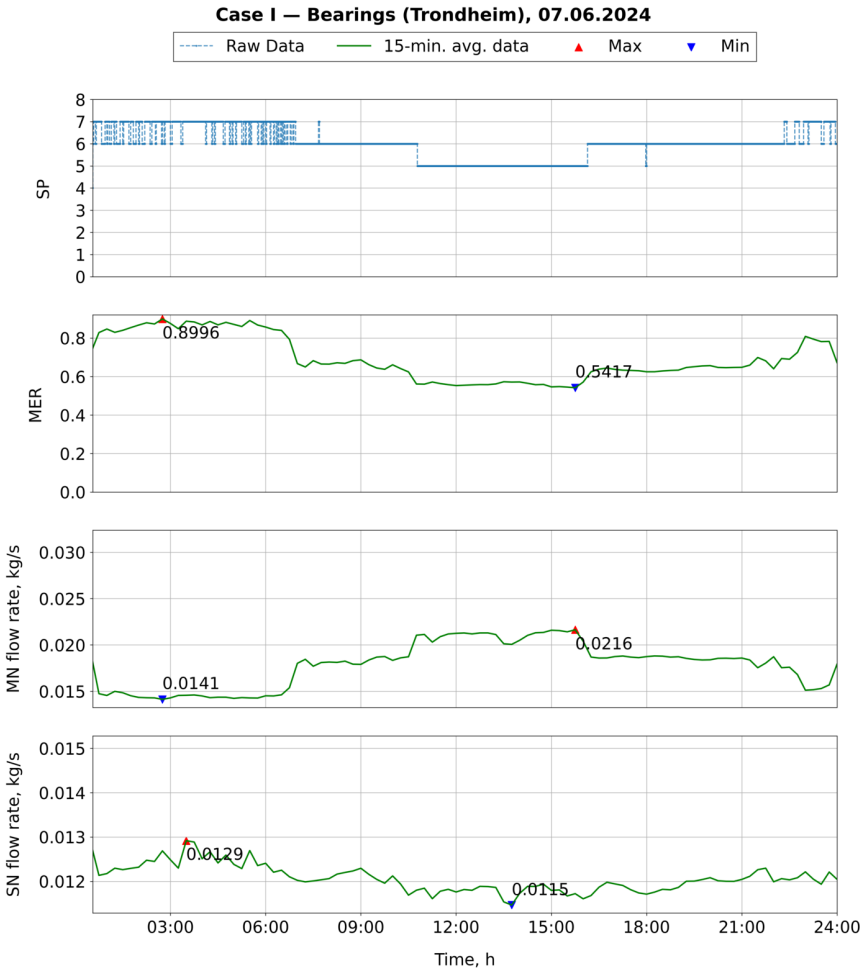

Figure 6.21: *Dynamic simulation results of ejector mass entrainment ratio (MER) and motive and suction nozzle mass flow rates for Case I.*

with ambient temperature, source stability, and system adaptability.

Starting with cases using temperature data from Gliwice, so intermediate scenario. Despite the significant daily ambient temperature variation, the system performed relatively well, with the COP values around 0.46. This outcome is particularly notable given the three different waste heat sources with varying degrees of thermal stability. Case C, using the moderately fluctuating bearings source, achieved the highest COP and the lowest generator heat load, suggesting that the control system was able to effectively manage short-term variability in the generator input when ambient conditions were favorable. The daily average cooling power in Gliwice remained stable

Table 6.2: *Daily averaged results of evaporator capacity and COP parameters of the ERS equipped with VGE analyzed for varying ambient and waste source temperature conditions.*

Location	Case	Daily avg. COP	Daily avg. evaporator capacity, kW	Daily avg. generator capacity, kW
Gliwice	A	0.46	3.68	8.62
	B	0.46	3.82	8.78
	C	0.47	3.71	8.65
Milano	D	0.32	3.18	9.94
	E	0.34	3.33	9.98
	F	0.31	3.05	9.86
Trondheim	G	0.61	4.27	7.14
	H	0.61	4.25	7.14
	I	0.61	4.31	7.21

across all cases ranging from 3.7 kW to 3.8 kW and indicating reliable system operation even under challenging and highly dynamic boundary conditions. In contrast, the performance in Milano (Cases D-F) was notably lower, with COP values ranging from 0.31 to 0.34, presenting higher influence of the variable heat source temperature used, when compared with the cases of Gliwice. This COP reduction arises from the higher average ambient temperature in this location, which increases the condensation pressure and negatively impacts ejector entrainment and system efficiency. Additionally, the generator heat load remained high around 10 kW, while the evaporator capacity was the lowest among all locations (3.1-3.3 kW). Case F, using the bearings waste heat source, resulted in the lowest COP and evaporator capacity, reflecting the dual impact of unfavorable ambient conditions and highly variable generator temperature input. On the other hand, Case E, using the stable mine source temperature, achieved the highest COP in Milano, reinforcing the benefit of a predictable thermal input.

Finally, in the Trondheim cases (G-I) the system consistently achieved the highest daily average COP of 0.61 across all source configurations. This outcome is primarily attributed to the lowest ambient temperatures among the tested cases, which reduced the ejector back pressure and enhanced the device performance. Furthermore, it achieved the generator capacity ranging from 7.1 kW to 7.2 kW, while delivering the highest average evaporator capacity of up to 4.3 kW in Case I. These values confirm that at cooler climates the variability of generator conditions is of lower importance, and the ERS benefits from an optimal ambient temperature operating window

for ERS.

In summary, the tabulated results reinforce the conclusion that system efficiency is highly sensitive to both ambient temperature and source stability. The ERS operation in cooler climates presented higher COP and reduced generator heat input, while stable waste heat sources enhance overall control effectiveness and energy performance for all the cases.

6.6 Conclusions

The analysis of all the simulated cases revealed the significant influence of both ambient and generator-side thermal conditions on the performance and control behavior of the R290 ERS equipped with VGE. The flexibility of the VGE through dynamic spindle control demonstrated a clear advantage across the considered range of environmental scenarios.

In the scenarios involving relatively stable waste heat source temperature (case of the mine) consistently led to the improved system stability, smoother control response, as well as higher mean daily values of COP and evaporator capacity. These conditions minimized the need for frequent spindle adjustments and allowed the system to operate closer to its optimal thermodynamic conditions. This effect was particularly evident in Cases B, E, and H, in which the system benefited from reduced the generator variability, despite varying ambient conditions coming from historical data for Gliwice, Milano, and Trondheim. In contrast, configurations utilizing unstable waste heat inputs, so these coming from the forge or the bearings factory, presented a necessity for quicker response of the spindle control, indicated by high SP variability, which caused local reductions in both COP and evaporator capacity. This behavior was notably visible in Cases A, D, F, and I, where the ejector system had to rapidly adapt to source-side fluctuations. Although the VGE managed to maintain system functionality and relatively stable performance, its efficiency was reduced due to the frequent ejector off-design operation and the resulting impact on the mass entrainment ratio, which locally decreased.

The ambient temperature conditions significantly influence the system performance. Cooler climates, such as the one presented by representative of Trondheim, provided a favorable condenser environment with lower ambient temperature, which resulted in improved overall system efficiency, reduced generator thermal load, and more consistent COP performance. This was observed in Cases G, H, and I, underscoring the benefits of deploying ERS systems in thermally favorable climates. For the cases of Milano and Gliwice, the system performance dropped in terms of COP and evaporator

capacity, but the VGE was able to adapt the ERS operation to these less favorable conditions and provided the stable system operation.

In summary, the results confirm the effectiveness of implementation of the VGE to ERS under a wide range of dynamic conditions. The combination of a relatively stable thermal input in the generator and moderate ambient conditions presents optimal performance with the minimal SP control intervention. However, even under thermally unstable or highly transient conditions, the VGE demonstrates resilient system behavior through its capability to modulate the motive nozzle geometry parameters in the real time. These findings highlight that the VGE presents a viable solution for flexible, efficient, and stable operation in modern refrigeration systems subjected to variable thermal environments, potentially replacing conventional single fixed-type ejector systems, that would be installed in order to cover the same operational range. This can be achieved not only through the standalone application of VGE but also via hybrid configurations combining fixed-type ejectors with VGE or through the use of multiejector modules.

CHAPTER 7

Evaluation of other natural refrigerants and their blends in an ejector-based refrigeration system

One of the most important issues for the development and adoption of environmentally friendly and efficient ejector-based refrigeration systems is a selection of appropriate working fluids, which must comply with current environmental requirements and demonstrate attractive performance. In this context, apart from natural refrigerants playing the most important role in the sustainable refrigeration, refrigerant blends offer additional opportunities to tailor the thermodynamic behavior of refrigeration systems, capable of achieving better performance characteristics than those utilizing pure single-component fluids. Thanks to the dimensionless mass entrainment ratio output of the ULF-VGE ROM, developed in this thesis and presented in Chapter 4, and the model derivation from validated CFD numerical models, it is possible to analyze the VGE performance for different refrigerants without carrying out a full redesign of the ejector geometry. Such an approach brings a substantial reduction in the computational effort and accelerates the flexibility of ejector applications for various fluids and their blends.

In this chapter, the analysis devoted to the assessment of the potential

application of the R290 VGE to ERS utilizing other refrigerants will be divided into three parts. First, a screening procedure to identify refrigerants and their blends whose thermophysical properties, specifically the two input pressure ratios for the ULF-VGE ROM at a representative ERS operating point, fall into the operational envelope defined for the R290 VGE. This ensures that only thermodynamically similar fluids are selected for the operation with the optimized R290 VGE geometry. Second, a mathematical model for calculating the motive nozzle mass flow rate required for the implementation with the ULF-VGE ROM is described and implemented in the ERS simulations within Dymola. Finally, the performance of the optimized R290 VGE geometry is assessed for various fluids and their blends. For the simulations, a single case of variable ambient temperature for Gliwice has been selected due to its highly variable daily temperature variation and a temperature range that covers the entire range of evaluated SP. For the variable waste-heat temperature profile, the data from the forge was selected as a mid-variability candidate, as the effect of its influence on the system COP and cooling capacity has been identified as low. This provides direct insights into how flexible the controllable ejector optimized for a single hydrocarbon refrigerant can be when applied to alternative refrigerants.

7.1 Refrigerants screening for the optimized R290 VGE geometry

Based on the literature, different blends of hydrocarbons can bring different outcomes when applied into the typical vapor-compression refrigeration cycles. For example, mixtures with butane or pentane allow for increasing the energy efficiency due to their thermodynamic characteristics [146]. The authors stated that the mixtures of R290 with lower boiling point components or synthetic fluids such as DME can improve the system COP by shifting the operating pressures to more favorable regions for the vapor-compression systems. Caramaschi et al. [147] demonstrated that hydrocarbon-based natural refrigerants mixtures can yield higher COPs than pure hydrocarbons under low-charge heat pump operation, while still maintaining acceptable volumetric capacities. Calleja-Anta et al. [148] reported that DME as a pure refrigerant can outperform R290 in the vapor-compression systems, showing COP increases of up to 30% over the system with R290. Moreover, the authors stated that DME-rich natural mixtures like DME/R744 or DME/R1270 are the best mixtures for applications with low hydrocarbon charge limits. These results indicate that, while DME and its mixtures show

strong potential, R290 is still a reliable baseline refrigerant for advancing sustainable refrigeration. Targeted use of other natural refrigerant mixtures may further improve cycle efficiency or cooling capacity, depending on the design priorities. In addition, the potential of these mixtures for thermally-driven cycles requires additional study, since their performance has not yet been systematically tested.

In the context of the ERS equipped with already optimized VGE geometry for R290, being aware of the high variability in ejector geometries that were designed for different fluids, it can be expected that only refrigerants with similar thermodynamic characteristics can be successfully used with the R290 VGE, achieving comparable performance with minimal required operation adjustments. Therefore, mixtures of R290 with other hydrocarbons will be analyzed. Additionally, the non-natural ether candidate of DME will be considered for this analysis due to its repeatedly demonstrated performance improvements in the conventional vapor-compression cycles, especially in the transcritical binary R744-DME cycle [11, 15, 148, 149] as a pure refrigerant or mixture component. Therefore, a systematic screening of natural refrigerants and selected blends is necessary to identify refrigerants that show the best alignment with the operating envelope defined for the R290-based VGE.

7.1.1 Properties of selected refrigerants and their blends

The representation of selected hydrocarbons refrigerants on the pressure-specific enthalpy diagram in Figure 7.1 allows for grouping the fluids' saturation curves that are similar to each other, indicating the fluid pairs like in the case of R290/R1270, or R601 and R601a, having similar shapes of the saturation curves and operating in similar pressure ranges.

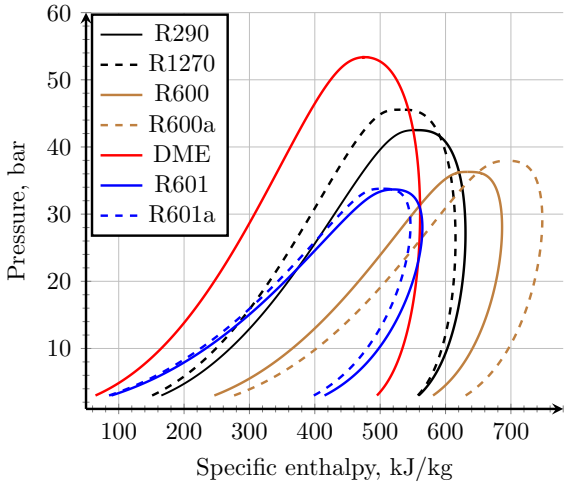

Figure 7.1: *Saturation curves of selected natural refrigerants and DME presented on the pressure - specific enthalpy diagram.*

On the other hand, looking at the values of critical temperature of those fluids presented in Table 7.1, all the alternative refrigerants except R1270 will need to operate in far subcritical conditions when compared to R290 utilizing the waste heat temperature data, analyzed in this thesis, in the range of 90-100°C, aiming also at completely different values of the ejector motive nozzle and diffuser outlet pressure levels. However, the observed thermodynamic similarities provide a compact rationale for transposing the R290-optimized VGE operating map to other refrigerant and their blends.

Table 7.1: *Critical conditions of selected refrigerants. Adapted and modified from [41].*

Refrigerant	Critical temperature, °C	Critical pressure, bar
R290	96.7	42.5
R1270	91.1	45.6
R600	151.9	38.0
R600a	134.7	36.3
RE170 (DME)	127.2	53.4
R601	195.6	33.7
R601a	187.2	33.7

Taking a closer look at the thermophysical properties of R290 and

R1270, they are characterized by similar critical conditions, namely the $T_{crit} = 96.7°C$, and $p_{crit} = 42.5$ bar for R290 and $T_{crit} = 91.1°C$ and $p_{crit} = 45.6$ bar for R1270. Their saturation domes overlap to a large extent, with comparable dome widths and so the latent heat values, indicating that the ERS operating pressure levels should be similar for their subcritical cycles. Moving to butanes, the R600 and R600a exhibit markedly higher critical temperatures and lower critical pressures, namely the R600 having $T_{crit} = 151.9°C$, $p_{crit} = 38.0$ bar, and R600a with $T_{crit} = 134.7°C$, $p_{crit} = 36.3$ bar. Their saturation domes shift to the right and widen relative to R290 and R1270. This trend signals a larger latent heat potential over the temperature range of interest, and lower operating pressures for the same condensation/evaporation levels, indicating that they may feature better cooling capacity but at a cost of lower ejector performance and a different choking regime at different pressure ratios. The critical points of pentanes such as R601 and R601a are characterized by the lowest pressure levels, but having the extremely high temperature values, being $T_{crit} = 195.6°C$ and $p_{crit} = 33.7$ bar for R601, and $T_{crit} = 187.2°C$, $p_{crit} = 33.7$ bar for R601a. Lastly, the artificial DME, frequently proposed as a drop-in alternative to R290 in conventional vapor-compression systems, has a relatively high critical pressure and temperature when compared with the hydrocarbons ($T_{crit} = 127.2°C$, $p_{crit} = 53.4$ bar), which can be also observed in its saturation dome being the largest in terms of both the pressure range and the span of specific enthalpy.

The representation of the same fluids on the temperature-specific entropy diagram is presented in Figure 7.2 highlights additional thermodynamic features.

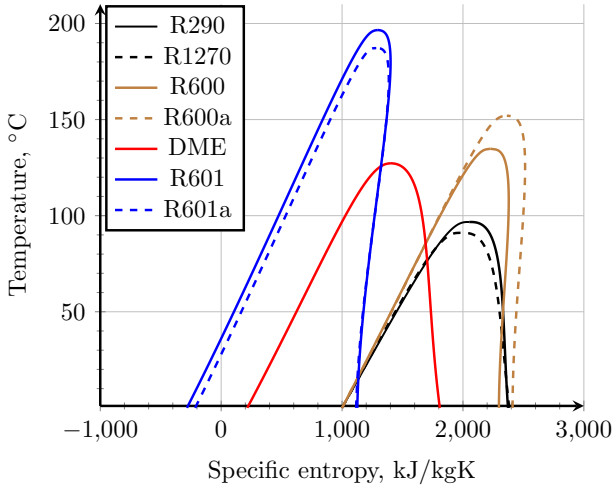

Figure 7.2: *Saturation curves of selected natural refrigerants and DME presented on the pressure-specific enthalpy diagram.*

Starting with the saturation domes of the R290 and R1270, they are again closely aligned, with narrow dome widths and comparable specific entropy spans, confirming their nearly identical cycle characteristics. The butanes (R600 and R600a) present slightly wider two-phase domes, when compared to the R290. Their critical point temperature is visibly higher, which implies larger refrigerating effect potential, but at relatively lower working pressures. The pentanes (R601 and R601a) exhibit the widest specific entropy ranges at the low temperatures, but with overall very slim dome shapes, emphasizing their high vaporization enthalpy and suitability for very low-pressure cycles and a smaller potential for high temperature applications. In contrast, DME shows a distinctive dome with both a larger entropy span and an elevated critical temperature compared to R290, confirming its broader operating envelope and higher flexibility. Overall, the T-s representation reinforces the grouping trends seen in the p-h diagrams while underlining differences in entropy change of the phase transitions, which is crucial for the cycle irreversibilities and ejector choking behavior.

The selection of refrigerants for this study was based on the operational limits of the ULF-VGE ROM, which was built based on the same set of numerical input data as for the R290 VGE ROM. To ensure the compatibility of other refrigerants and their mixtures with the ULF-VGE ROM limits, the representative operating point was selected for the VGE operation in the ERS, corresponding to the saturation pressure levels of 85°C at the motive

nozzle, 5°C at the suction nozzle, and 20°C at the ejector outlet. For this point, the pressure ratios for the ULF-VGE ROM from Equations 4.35 and 4.36, representing the ratios of the pressure of the motive nozzle to the diffuser outlet and the diffuser outlet to the suction nozzle of the ejector, were calculated.

To identify suitable alternative refrigerants for the VGE, the mixtures of natural refrigerants listed in the ASHRAE refrigerants database [150] were selected for screening. Each candidate was evaluated at the same operating point, and the corresponding pressure ratios for ULF-VGE ROM were calculated. A tolerance range of $\pm 10\%$ relative to the reference values of the R290 was established as the admissibility criterion, ensuring that only refrigerants with comparable thermodynamic behavior could be directly implemented within the ULF-VGE ROM framework. The results of this screening process are summarized in Table 7.2, where the refrigerants that meet the selection criteria are highlighted in bold text.

Among the pure refrigerants, only R1270 satisfied the defined pressure ratio limits, as its values closely matched those of R290 at the selected operating point. In addition, three ASHRAE-listed binary mixtures of R290 with R1270, namely R436A, R436B, and R436C, were identified as suitable candidates. These blends, containing 90%, 95%, and 75% of R1270, respectively, exhibit thermodynamic properties sufficiently close to R290 and remain within the $\pm 10\%$ range.

As far as the mixtures with other hydrocarbons are concerned, the analysis showed that blends containing larger fractions of R600a or R600 highly exceeded the allowable limits. Nevertheless, R436C, a mixture of 95% R290 and 5% R600a, remained within the limits and was therefore selected for the analysis. Additionally, the ternary mixture R443A, composed of 40% R290, 5% R600a, and 55% R1270, was selected due to its compliance with the pressure ratio constraints. Finally, looking at the mixture of DME, the binary mixture R511A composed of 95% R290 and 5% DME was identified as the only suitable, while other compositions exhibited excessive deviations from the reference R290 values. Hence, the highlighted set of refrigerants forms a consistent and representative basis for subsequent performance assessment of the ejector refrigeration system.

7.2 Implementation of the Reduced Order Model of Variable Geometry Ejector for other refrigerants simulations

In the analysis devoted to alternative natural refrigerants application in the ERS equipped with VGE, the ULF-VGE ROM providing the mass

Table 7.2: *Screening of the refrigerants with properties similar to the R290 and the R290 blends with the comparison of the pressure ratio and temperature parameters for a representative operating point of the ERS operation.*

ASHRAE number	**Refrigerant (mass composition**	P_{MN},	P_{SN},	P_{OUT},	Π_S	Π_M
		85°C	5°C	20°C	-	-
290	R290	34.36	5.51	8.36	1.518	4.108
E170	DME	24.66	3.17	5.10	1.609	4.839
1270	**R1270**	**40.79**	**6.76**	**10.17**	**1.504**	**4.010**
600	R600	11.26	1.24	2.08	1.671	5.422
600a	R600a	14.87	1.87	3.02	1.619	4.921
601	R601	4.17	0.31	0.57	1.851	7.372
601a	R601a	5.15	0.43	0.77	1.796	6.723
436A	56% R290 & 44% R600a	22.27	2.99	4.75	1.589	4.688
436B	52% R290 & 48% R600a	21.54	2.87	4.57	1.593	4.715
436C	**95% R290 & 5% R600a**	**34.36**	**5.02**	**7.70**	**1.532**	**4.465**
433A	**10% R290 & 90% R1270**	**40.35**	**6.68**	**10.05**	**1.505**	**4.016**
433B	**5% R290 & 95% R1270**	**40.58**	**6.72**	**10.11**	**1.504**	**4.013**
433C	**25% R290 & 75% R1270**	**39.58**	**6.52**	**9.83**	**1.506**	**4.029**
443A	**40% R290 & 5% R600a 55% R1270**	**35.71**	**5.53**	**8.46**	**1.530**	**4.223**
511A	**95% R290 & 5% DME**	**34.54**	**5.52**	**8.39**	**1.519**	**4.119**
441A	54.8% R290 & 6% R600a 36.1% R600 & 3.1% DME	19.68	2.37	3.86	1.634	5.093

entrainment ratio as a single output variable was used. However, for a consistent evaluation of the ejector performance, the complete set of mass and energy balance equations (Equations (5.58) and (5.59)) requires the definition of the mass flow rate to satisfy the set of equations. Therefore, a

Dymola built-in motive nozzle model was used for the ejector component, which, combined with the mass entrainment ratio output from the ULF-VGE ROM, enabled the definition of both mass flow rates entering the ejector. The model relies on the two-phase critical flow correlation proposed by Brennen [121], in which the mass flux at the motive nozzle throat is determined from the sonic flow condition using the local speed of sound. This approach provides a framework for estimating the critical flow conditions that may be used in both single and two-phase regions and hence completes the system of equations required for the ejector model.

The calculation of the motive nozzle mass flow rate follows the aforementioned Brennen formulation, which explicitly accounts for the liquid compressibility and thermodynamic interactions between the vapor and liquid phases. To determine the state of the flow, the following equation for the gas volume fraction of the two-phase flow was used:

$$\frac{\Theta}{1-\Theta} = \left[\frac{\Theta_{\text{MN}}}{1-\Theta_{\text{MN}}} + \frac{\kappa}{\kappa+1}\frac{p_{\text{MN}}}{\rho_{\text{L}} c_{\text{ss,L}}^2}\right]\left(\frac{p_{\text{MN}}}{p}\right)^{\frac{1}{\kappa}} - \frac{\kappa}{\kappa+1}\frac{p_{\text{MN}}}{\rho_{\text{L}} c_{\text{ss,L}}^2}\frac{p}{p_{\text{MN}}} \tag{7.1}$$

where Θ is the local gas volume fraction, κ is the polytropic exponent, c_{ss} is the speed of sound.

The local velocity in a nozzle can be evaluated through the application of momentum and energy conservation equations:

$$v^2 = \frac{2p_{\text{MN}}}{\rho_{\text{L}}}\left[1 - \frac{p}{p_{\text{MN}}} + \frac{\kappa}{2(\kappa+1)}\frac{p_{\text{MN}}}{\rho_{\text{L}} c_{\text{L}}^2}\left(\frac{p^2}{p_{\text{MN}}^2} - 1\right)\right] + \Phi \tag{7.2}$$

where the additional term Φ depends on the polytropic exponent κ. For $\kappa \neq 1$, it is given by:

$$\Phi = \frac{\kappa}{\kappa-1}\left\{\frac{\Theta_{\text{MN}}}{1-\Theta_{\text{MN}}} + \frac{\kappa}{\kappa+1}\frac{p_{\text{MN}}}{\rho_{\text{L}} c_{\text{L}}^2}\right\}\frac{p_{\text{MN}}}{\rho_{\text{L}} c_{\text{L}}^2}\left\{1 - \left(\frac{p}{p_{\text{MN}}}\right)^{\frac{\kappa-1}{\kappa}}\right\} \tag{7.3}$$

while for $\kappa = 1$, it reduces to:

$$\Phi = \left\{\frac{\Theta_{\text{MN}}}{1-\Theta_{\text{MN}}} + \frac{1}{2}\frac{p_{\text{MN}}}{\rho_{\text{L}} c_{\text{L}}^2}\right\}\ln\left(\frac{p_{\text{MN}}}{p}\right) \tag{7.4}$$

The throat pressure p_* is then obtained by equating the local velocity evaluated at $p = p_*$ using Equation (7.2), to the mixture sonic velocity computed from Equation 7.5 and substituting p with p_*.

$$c_{ss}^2 = \frac{\frac{p}{\rho_\text{L}}\left(1 + \frac{\Theta}{1-\Theta}\right)^2}{\frac{1}{\kappa}\frac{\Theta}{1-\Theta} + \frac{p}{\rho_\text{L} c_\text{L}^2}}. \tag{7.5}$$

where the subscript $*$ denotes the conditions at the motive nozzle throat.

This pressure condition defines the choking point, resulting in the critical throat pressure ratio p_*/p_MN and the associated gas volume fraction at the nozzle throat Θ_*, computed utilizing Equation 7.1.

Once the throat conditions are established, the critical mass flow rate for the nozzle can be determined using the following equation:

$$\frac{\dot{m}_{MN}}{A_*(\rho_\text{MN} p_\text{MN})^{1/2}} = \frac{(1-\Theta_*)c_{ss,*}}{\left[\frac{p_\text{MN}(1-\Theta_\text{MN})}{\rho_\text{L}}\right]^{1/2}} \tag{7.6}$$

Finally, the suction nozzle mass flow rate can be calculated from the mass entrainment ratio **??** obtained as an output from an ULF-VGE ROM, and the critical mass flow rate of the motive nozzle using the following equation:

$$\dot{m}_{SN} = \phi \cdot \dot{m}_{MN} \tag{7.7}$$

The implementation of the motive nozzle model for VGE is executed in the Dymola software by integrating the motive nozzle model with a data table that contains throat diameters corresponding to specific SP values previously defined in Section 2.3. The SP logic dynamically selects the effective throat diameter based on the SP determined by the spindle control logic and transfers this value as an input to the motive nozzle equations in the following time step. In this way, the ROM framework ensures that the motive nozzle throat geometry for the mathematical nozzle model and the suction nozzle mass flow rate coming out from the ULF-VGE ROM remain consistent within the system configuration.

7.3 Verification of Universal Low-temperature Fluids Reduced Order Model

First, the comparative analysis of the R290 VGE performance using two different ROM approaches presented in Chapter 4, namely the VGE ROM and the novel approach ULF-VGE ROM, are presented in Figure 7.3. The performance is evaluated by plotting the mass entrainment ratio as a function

of the ejector outlet pressure. The analysis is conducted for eight distinct spindle positions (from SP0 to SP7) under constant motive and suction nozzle operating conditions, which for the VGE ROM were previously presented in Figure 4.13.

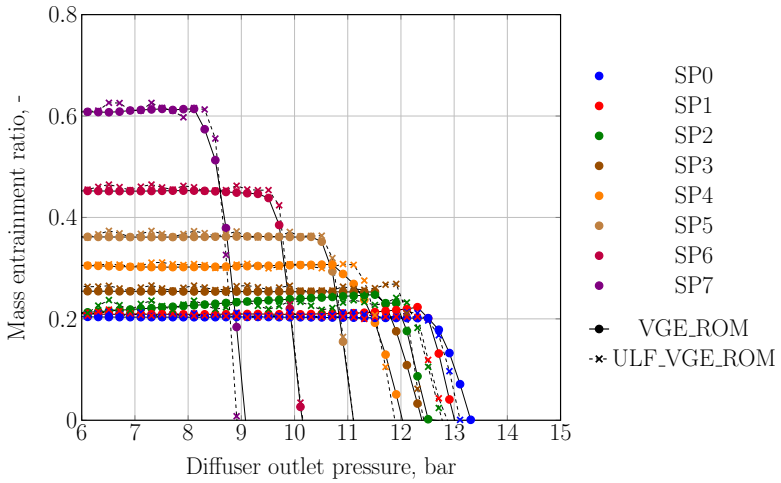

Figure 7.3: *Ejector performance curves of the R290 VGE comparing the baseline VGE ROM and the ULF-VGE ROM for SP0-SP7 at $T_{MN,sat}$ = 94°C, $T_{SN,sat}$ = 5°C, and varying pressure at the diffuser outlet.*

The ejector performance curves for both models exhibit typical operational characteristics with a clear distinction between the on- and off-design modes. It demonstrates a strong correlation between the two models, with the data from both models overlapping, indicating that the ULF-VGE ROM accurately approximates the performance of the baseline VGE ROM, with very small differences in their characteristics. One of them can be observed as the slight increase of the value of the ejector critical pressure, which for the ULF-VGE ROM is slightly higher for all the analyzed SP except SP0 and SP1. The highest difference of the critical pressure value of around 0.2 bar can be observed for SP3, SP4, and SP7, for which the mass entranment ratio is around 3-5% higher for the ULF-VGE ROM in the vicinity of critical point, when compared with VGE ROM. For the other cases of SP0, SP1, SP2, and SP6, the difference of value of critical pressure is below 0.1 bar, which corresponds to the mass entrainment ratio relative errors below 2%. Furthermore, the on-design part of the ULF-VGE ROM lines is not perfectly straight, but rather a slightly wavy set of points, which may indicate a reduction in accuracy resulting from a change in the input parameters used from pressure and enthalpy in the VGE ROM to the pressure ratio and

temperature in the ULF-VGE ROM formulation. However, this alignment validates the ULF-VGE ROM's approach of using two pressure ratios and temperatures, which was designed to enhance its applicability to various fluids and their blends.

For the spindle position with the most restricted throat, SP7, the ejector achieves its maximum mass entrainment ratio of approximately 0.6. The critical pressure for this configuration is approximately 9 bar. As the spindle position increases (from SP7 towards SP0), both the maximum mass entrainment ratio and the ejector critical pressure generally decrease. For instance, at SP0 and SP1, the ejector achieves a mass entrainment ratio of around 0.2, with a critical pressure of approximately 10.5 bar. The consistent performance observed between the two models confirms the ULF-VGE ROM's reliability and its potential for broader application.

Next, the results of the ULF-VGE ROM analysis for a R1270 fluid using the same fixed motive and suction nozzle temperatures and varying ejector outlet pressure are presented in Figure 7.4.

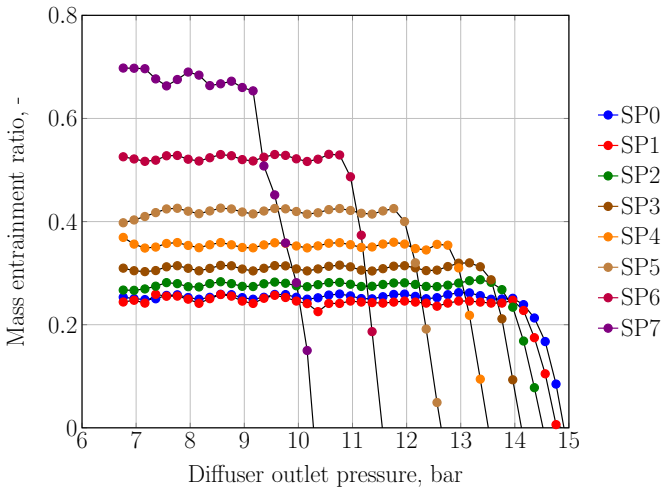

Figure 7.4: *Ejector performance curves of the ULF-VGE ROM using R1270 for SP0-SP7 at $T_{MN,sat}$ = 94°C, $T_{SN,sat}$ = 5°C, and varying pressure at the diffuser outlet.*

The ejector performance curves for R1270 exhibit the same characteristic behavior of operation, but with higher values of mass entrainment ratio than for the case of R290 presented in Figure 7.3. For the most restricted throat at the SP7, the ejector achieves the highest mass entrainment ratio, which is approximately 0.7. The critical pressure for this configuration is observed at around 9.2 bar. For SP0, SP1, and SP2, the maximum mass entrainment ratio is around 0.25, with critical pressures of approximately 12.5 bar, 13 bar,

and 14 bar, respectively. When using R1270 as the working fluid, the ULF-VGE ROM exhibits more pronounced wavy behavior in its performance curves, particularly for the most restricted spindle positions: SP6 and SP7. Despite this, the model still maintains the characteristic on- and off-design modes of operation, making it suitable for dynamic analysis of the ERS in Dymola. However, these more significant fluctuations in the predicted mass entrainment ratio suggest that higher mass flow rate oscillations may occur during the dynamic simulations of 24-h operation using realistic data due to inherent instabilities.

The final analysis of the ejector performance curves presents the performance of the ejector using a R290/DME blend with the ratio of 90%/10%, respectively. The corresponding performance curves are presented in Figure 7.5.

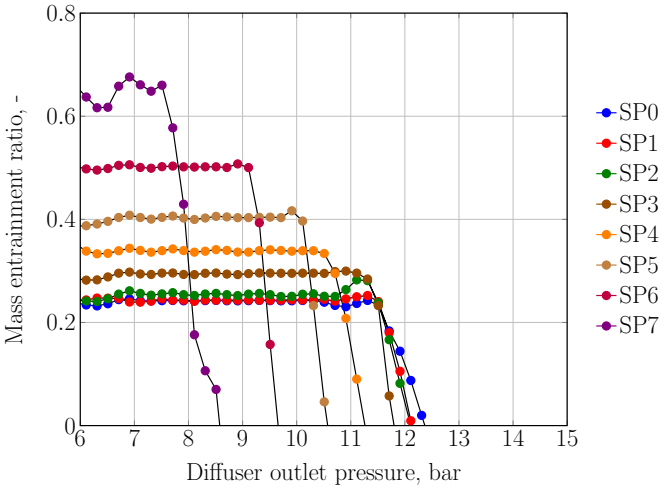

Figure 7.5: *Ejector performance curves of the ULF-VGE ROM using a 90% R290 and 10% DME blend for SP0-SP7 at $T_{MN,sat}$ = 94°C, $T_{SN,sat}$ = 5°C, and varying pressure at the diffuser outlet.*

The performance curves for the R290/DME blend exhibit a similar wavy behavior, with even more pronounced instabilities for the most restricted spindle position of SP7. This increased instability is attributed to the significant differences in the pressure ratio and temperature characteristics of DME compared to pure R290, indicating that at the last SP at which the ejector is entraining the secondary flow, the ejector is particularly prone to instabilities. Despite this, the model successfully maintains the characteristic on- and off-design modes of operation, but the more significant fluctuations in the predicted mass entrainment ratio suggest that higher mass flow rate

oscillations may be expected during real-world operation due to potential instabilities. For the most restricted spindle position of SP7, the ejector achieves a maximum mass entrainment ratio of approximately 0.65, with a critical pressure of around 8 bar. At SP6, the maximum mass entrainment ratio drops to approximately 0.5, and the ejector critical pressure is around 9 bar. At the least restricted positions, such as SP0 and SP1, the mass entrainment ratio is approximately 0.25, with a critical pressure of about 11 bar.

This analysis highlights the complexity of modeling an ejector and using a single geometry for a variety of fluids, due to the supersonic flow dynamics inside that are highly sensitive to the fluid, and it can drastically affect its performance. As a consequence, the VGE analyzed in this thesis, designed to be used with R290, is able to effectively handle also the other refrigerants with very similar characteristics or their blends with a small percentage of additives. Moreover, the instability of the mass entrainment ratio observed at SP7 indicates that, when the R290-optimized VGE is applied to other fluids, its operation should be restricted to narrower conditions (e.g., from SP0 to SP6) to ensure stable performance.

7.4 Application of Universal Low-temperature Fluids Reduced Order Model for other refrigerants

In the next step, the numerical analysis of refrigerant mixtures applied to VGE-based ERS was performed to assess their performance characteristics, with emphasis on the COP and cooling capacity. The system was simulated using an ambient temperature and waste heat profile from a single Case B from the Table 6.1 presented in the previous chapter (Chapter 6). A comparative analysis of the performance of pure R290 with three different R290-based mixtures, and pure R1270 is illustrated in Figure 7.6.

The daily averaged performance metrics provide a clear comparative analysis. Starting with the daily averaged COP, the results indicate that the mixtures of 5% R290/95% R1270 and 25% R290/75% R1270 demonstrate superior performance with a COP of 0.54 and 0.53, respectively. These values are approximately 10% higher than the 0.49 value obtained for the ERS system running with pure R290. The 40% R290/55% R1270/5% R600a mixture also performed better than pure R290, with a COP of 0.47, but was outperformed by the other two mixtures. As far as the daily averaged cooling capacity is concerned, similarly to the COP results, the 5% R290/95% R1270 and 25% R290/75% R1270 mixtures exhibit a higher cooling capacity of 4.57 kW and 4.43 kW, respectively, when compared to 3.80 kW of pure

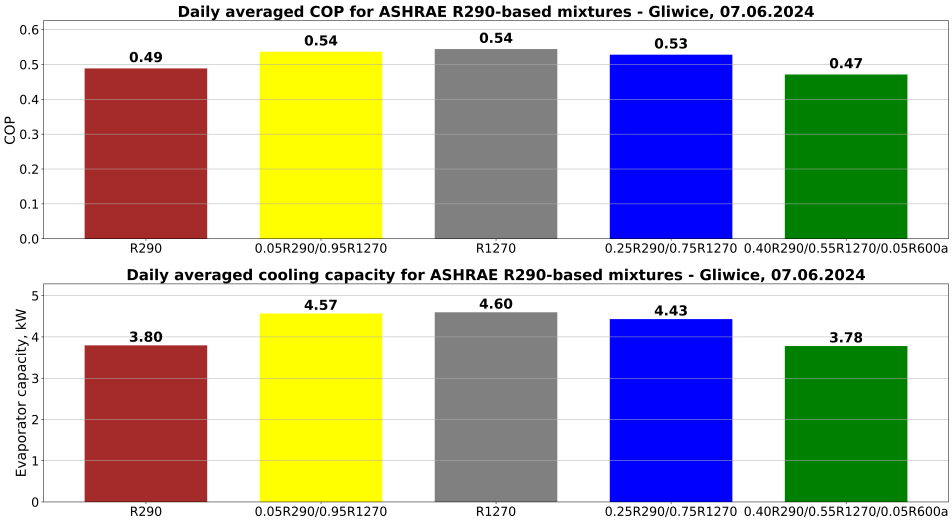

Figure 7.6: *Daily averaged values of the COP and the evaporator capacity for various R290-based blends and R1270 refrigerants operating in ERS equipped with VGE and using ambient temperature data from Gliwice.*

R290. This results in an improvement of 20% and 17%, respectively. The 40% R290/55% R1270/5% R600a mixture had both the cooling capacity and COP slightly worse when compared to R290, so its performance was worse than the one presented by other mixtures simulations. These findings confirm that the R290 VGE used in ERS can be successfully used with pure R1270 or its blends with R290, which generally enhances the thermodynamic performance related to the R290-based system.

The daily averaged performance of a ERS system utilizing various concentration R290/R1270 refrigerant blends is presented in Figure 7.7. The objective was to evaluate how the blends ratio of these two refrigerants influences the key ERS performance metrics. The study aimed to identify, whether a particular blend composition yielded superior performance compared to the pure components or other mixtures.

The analysis of the daily averaged COP indicates a systematic improvement as the R1270 mass fraction increases within the mixture. For pure R290, the COP reached the lowest value of 0.49, whereas pure R1270 delivered the highest, at 0.54. The progression, however, is not uniform across all compositions. Up to the 70% R290/ 30% R1270 mixture, the increase in COP remains relatively modest, suggesting only incremental efficiency gains in this composition range. Beyond this point, the improvement becomes more pronounced, highlighting that higher proportions of R1270

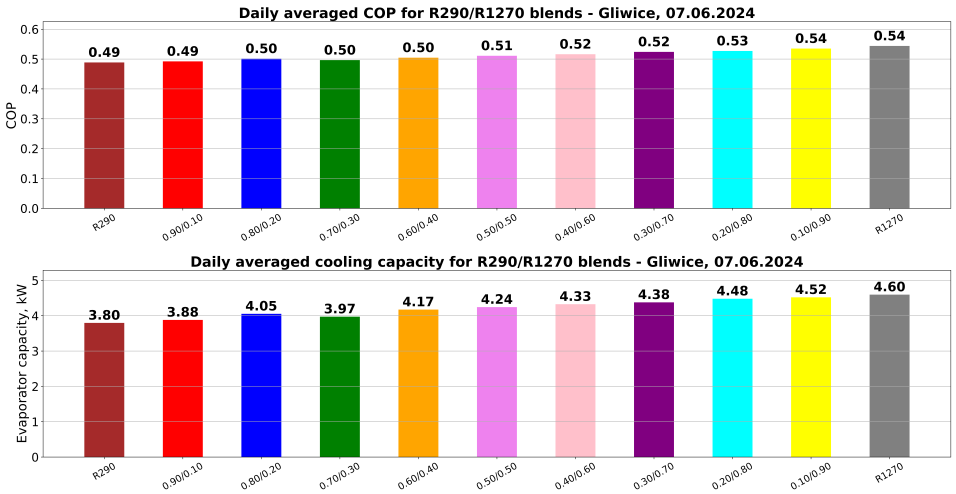

Figure 7.7: *Daily averaged values of the COP and evaporator capacity for various R290/R1270 refrigerant mixtures operating in ERS equipped with VGE and using ambient temperature data from Gliwice.*

have a stronger influence on the overall thermodynamic performance of the system. This behavior underlines the advantageous role of R1270 in enhancing energy efficiency, particularly when it constitutes a dominant fraction of the working fluid.

A similar tendency is observed for the daily averaged evaporator capacity, where a consistent increase accompanies the rising content of R1270. The lowest value of 3.80 kW was recorded for pure R290, while the highest, 4.60 kW, was measured for pure R1270. For most intermediate compositions, the variation follows a fairly regular upward trend, with one notable deviation at the 70% R290/ 30% R1270 mixture. At this point, the measured capacity slightly departs from the otherwise progressive increase, which could reflect experimental uncertainties or minor non-linear interactions between the refrigerants at this concentration. Overall, the results demonstrate that R1270 is more effective than R290 in facilitating heat absorption in the evaporator, thereby improving the cooling capacity of the system under the investigated operating conditions.

The evaluation of the daily averaged COP for the R290/DME mixtures presented in Figure 7.8 shows a gradual decline as the proportion of DME in the blend increases.

For pure R290, the COP was 0.49, and this value remained almost unchanged for the first four mixture compositions to 60% R290/ 40% DME. The lowest performance, with a COP of 0.46, was observed for the 50%

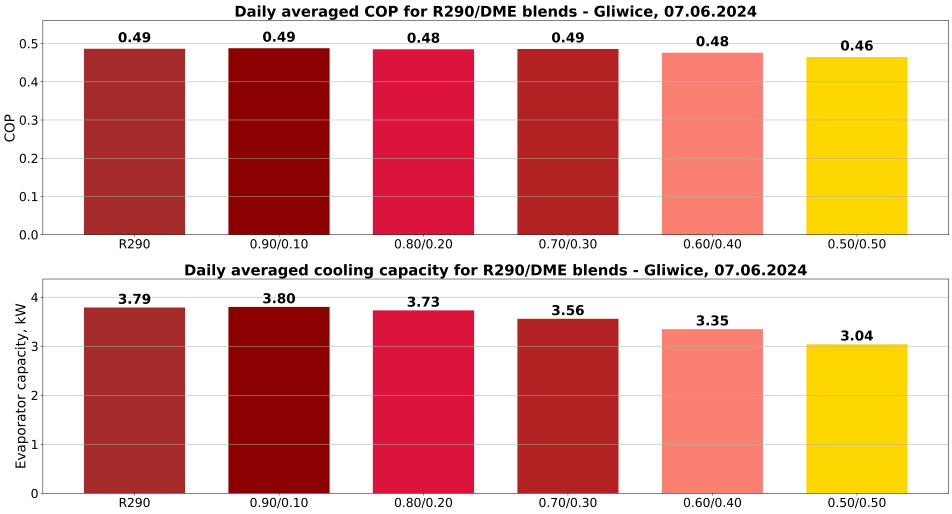

Figure 7.8: *Daily averaged values of the COP and evaporator capacity for various R290/DME refrigerant mixtures operating in ERS equipped with VGE and using ambient temperature data from Gliwice.*

R290/ 50% DME composition. These results suggest that, unlike in the case of R290/R1270 blends, the incorporation of DME does not provide a thermodynamic advantage. Instead, the COP remains nearly constant for small additions of DME and then starts to decrease at higher concentrations. This behavior indicates that DME has a detrimental effect on the overall energy efficiency of the ERS equipped with VGE when present in significant proportions.

A similar downward trend is observed in the daily averaged evaporator capacity. For pure R290, the capacity reached 3.79 kW, and a nearly identical value of 3.80 kW was measured for the 90% R290/ 10% DME mixture, indicating negligible impact at low DME content. However, as the DME fraction increases further, a progressive reduction is observed: 3.73 kW for the 80% R290/ 20% DME mixture, 3.56 kW for 70% R290/ 30% DME , 3.35 kW for 60% R290/ 40% DME, and a minimum of 3.04 kW for the 50% R290/ 50% DME mixture. This steady decline demonstrates that DME weakens the cooling capacity of the working fluid mixture, with the effect becoming more pronounced as its proportion increases. Collectively, the results indicate that R290 alone provides both the highest COP and cooling capacity, while the addition of DME systematically reduces system performance.

When compared with the R290/R1270 blends, where R1270 enhanced

both COP and evaporator capacity, it becomes clear that R1270 acts as a performance-improving additive, whereas DME behaves oppositely by diminishing system efficiency and cooling performance. This contrasting behavior highlights the crucial influence of refrigerant selection on the thermodynamic performance of the VGE, and thus on the ERS.

7.5 Conclusions

The ULF-VGE reduced-order formulation, coupled with a compact motive-nozzle model, enabled the alternative fluids simulations without ejector geometry re-design by maintaining the ejector behavior through the dimensionless mass entrainment ratio output of the ULF-VGE ROM. A systematic screening at a representative ERS operating point indicated the refrigerant candidates whose pressure-ratio pairs was within $\pm 10\%$ of the R290 reference values, selecting only the R1270 among pure fluids and a set of R290-based mixtures, i.e. 433A/B/C, 436C, 443A, and 511A. The ULF-VGE ROM and VGE ROM verification for R290 showed a close agreement between the baseline and generalized models, with small offsets in the critical pressure at SP3 and SP7 and mild disturbances in the reproduction of the on-design part of the ejector efficiency curve. The analysis of the ULF-VGE ROM performance for other fluids with thermophysical properties similar to R290 confirmed its potential to evaluate its applicability for dynamic ERS studies for alternative refrigerants.

Performance assessments highlighted the dependence of system performance on evaluated fluids under identical boundary conditions. Relative to R290, the blends with R1270 present an increase of COP and cooling capacity of the ERS related to the R290 system. The pure R1270 showed the best COP and cooling capacity improvements of 10% and 20% consecutively, when related to pure R290.

In contrast, the mixture of R290 and DME presented opposite behavior, showing a decrease of performance with the increase of DME percentage in the mixture, up to -6% for COP and -20% for cooling capacity for the 50/50 ratio. Similarly, the fluid 444A, being a mixture of 40% R290, 5% R600a, and 55% R1270 also presented a slight drop in performance relative to the R290 system for both the COP and cooling capacity, indicating that even a small amount of the R600a with different thermodynamic characteristics is unfavorable for the designed R290 VGE.

In conclusion, the above findings show that the R290-optimized VGE ensures applicability to the R1270 and R1270/R290 blends showing even better ERS performance than the system utilizing pure R290, whereas blends

of R290 with refrigerants of much different thermodynamic characteristics than R290, i.e. with DME, butane, and pentane, presented slight or even no improvement when related to ERS running with R290, which undermine the benefit of VGE application for those fluids.

CHAPTER 8

Conclusions and future plans

This PhD thesis present an in-depth numerical study of the ERS equipped with VGE, driven by ultra-low-grade waste heat and operating with the natural refrigerant R290. The study comprises the experimental campaign focusing on assessment of the R290 spindle ejector, the development of CFD-backed ROMs enabling fast and accurate dynamic simulation, assess the ERS performance under varying ambient and waste heat temperatures, and analyze the potential for application of the R290 VGE for alternative natural refrigerants and their blends.

A VGE with a controllable spindle designed by Besagni and Cristiani [29] was manufactured to modulate the motive nozzle effective throat area and provide the ejector capacity control to maximize its performance for variable operating conditions using a single ejector. The device was equipped with a micrometer knob allowing for repeatable spindle positioning over the analyzed SP range and integrated into the R290 test rig. The experimental campaign confirmed a successful ejector entrainment control by means of the spindle. Increasing the ejector SP (decreasing effective throat area) systematically increased the mass entrainment ratio. However, due to the test being carried out for the motive nozzle pressure conditions lower than those for which the ejector was originally designed, the empirically deter-

mined control line was non-linear, in contrast to the linear curve reported in literature [29, 101]. The static pressure results indicated the shock trains and pressure recovery varying between the SPs, confirming that the data provides a valuable insights of the supersonic flow inside the ejector and can be a basis for further calibration of the CFD model.

Two CFD-based ROMs of the R290 VGE were developed using the POD-RBF technique to enable fast and accurate reproduction of the ejector behavior, allowing its implementation to the dynamic system simulations of ERS. The baseline VGE ROM formulation using pressure and specific enthalpy for both inlet nozzles together with the outlet pressure returns two values of motive and suction mass flow rates for a given operating point. Additionally, a generalized ULF-VGE ROM was developed using the pressure ratios and inlet temperatures as inputs in order to return the VGE characteristic expressed in the mass entrainment ratio. By combining this generalized model with a mathematical nozzle, it allows for its application to alternative refrigerants of similar thermodynamic characteristics. Hence, it creates a potential for extension of R290 VGE modeling for other studies similar to R290 fluids studies without the necessity of remodeling the geometry. Moreover, owing to its general formulation with the mass entrainment ratio as the output and its coupling with a separate nozzle model, the ULF-VGE ROM can be applied to simulate the R290 VGE ERS at different cooling capacities by scaling the ejector throat. This scaling changes the motive nozzle mass flow rate, which influences the cooling capacity being directly linked to the suction nozzle mass flow rate derived from the ROM mass entrainment ratio.

A calibration study established the CFD map resolution required to eliminate the interpolation error. The ROM verification showed a close agreement to CFD results, with relative errors below 1% with a proper reproduction of the critical-point and the on- an off-design transition. Both ROMs were implemented in Dymola as external functions, providing very fast evaluations suitable for dynamic ERS simulations, while preserving the physics of ejector operation.

A dynamic R290 ERS model equipped with the ROM of VGE was built in the Dymola software. Under time-varying ambient temperature data from Gliwice, Milano, and Trondheim, the VGE presented higher COP and cooling capacity when compared with the same system utilizing FGE, as a consequence of the ability of VGE to maintain the ejector operation in the on-design for the simulations with temperature data representing three different climatic zones. The sensitivity analysis indicated the superheat of 4 K as an optimal value for both evaporator and generator, showing the

necessity of proper selection for the maximization of system performance. The VGE-based ERS indicated the improvement for the daily-averaged operation between 0.4% to 52.4% for the COP, and between 2.1 to 13% for the evaporator cooling capacity, when compared with the system utilizing the best-suited FGE.

The VGE-based system benefits from the high daily variability of temperature in hot climates, in which the spindle control provides continuous ejector operation in the on-design mode despite the variability of the outlet pressure. When temperatures are low and stable, the benefits of the introduction of VGE are substantially smaller. Nevertheless, small SP changes for the highest midday temperatures confirm the responsiveness of the control logic and allow to maintain high efficiency across the full range of tested operating conditions in the ambient temperature between 8.6 to 27.9°C.

The realistic waste heat temperature data profiles provided by Marani Sp. z o.o. company were used to evaluate the real potential of ERS application for ultra-low waste heat recovery. The temperature profiles from the forge, mine, and bearings factory were used for simulations of ERS operation in different climatic zones. When the waste-heat source was relatively stable, the ERS exhibited smoother control and higher COP and cooling capacity owing to reduced spindle movements and operation closer to thermodynamic optima. In contrast, the unstable source profiles required rapid SP modulation, which resulted in local reductions in the mass entrainment ratio visible as transient drops in the COP and cooling capacity. In summary, the combination of a stable generator input with moderate ambient conditions yields the best performance with minimal control effort. The VGE maintained functional stability thanks to rapid SP adaptation, demonstrating the ability to cope with disturbances coming from the variability of waste heat and ambient temperature, and can replace the standard FGE-based systems.

The ULF-VGE ROM enabled ERS simulations for alternative natural refrigerants and selected blends, allowing the R290 VGE to be used without requiring a redesign of the ejector geometry. The R1270 with the thermophysical properties close to R290 retained similar ejector behavior in the analysis of mass entrainment ratio at fixed inlet nozzle conditions and under varying ejector outlet pressure conditions. On the other hand, the R290 blends with other refrigerants exhibited mild oscillations of the on-design curves, indicating potential ejector suction mass flow rate instabilities. Hence, the performance drop for applications in systems operating at different pressure and temperature levels, when operating with R290-based refrigerant blends with fluids of different thermodynamic characteristics.

The VGE operating in the ERS using pure R1270 presented an increase

in evaporator capacity by 21% and a COP improvement of 10% for the single case analyzed, demonstrating that the R290-optimized VGE can also be successfully applied in ERS for waste heat utilization with R1270 as refrigerant.

The combined outcomes confirmed that a single VGE can effectively replace multiple FGEs to expand the ejector operating envelope, maintaining its operation near the on-design conditions, providing the optimal performance of the ERS. The proposed control system of SP can operate with the waste heat temperature at different level of variability

For the work continuation, starting with the ways of improvement of the VGE modeling, the hybrid ROM solution combining the high-resolution CFD maps with targeted experimental data could benefit the prediction accuracy around the on/off-design transition and bring the modeling one step closer to reality. Additionally, decreasing the spindle step size for the ROM inputs or developing a method for continuous control of the spindle position could improve the efficiency of the system providing a quick and continuous ejector response to the varying system operating conditions.

As for the future plans for the application of the R290 VGE for alternative refrigerants, based on the results of this thesis it seems that using current operational envelope allows for the R290 VGE ROM usage only with the refrigerants with very similar characteristics, therefore an extension of the ULF-VGE ROM operational envelope should be performed to cover much wider range of pressure ratios for this particular ejector geometry. Another approach could be to use a tool for a quick ejector geometry evaluation for other refrigerants and develop a way on how to better transform the ULF-VGE for the other fluids.

As for the system level, a possible improvement could be a combination of the FGE-based multiejector modules with a VGE providing smooth and fast modulation, which can be especially beneficial for the industrial sites with distinct thermal dynamics, in which the combination of two types of ejectors could provide a stable cooling capacity decoupled from the variable heat source. From a techno-economic perspective, further enhancement of the proposed ERS concept may be achieved by its integration with the state-of-the-art heat exchangers for the waste heat utilization to reduce temperature differences and exergy losses in the generator loop, thereby increasing the overall system COP. In parallel, incorporation of the state-of-the-art cold energy storage technology would help decoupling cooling demand from the waste-heat availability, mitigating peak-load operation and reducing off-design operation of the ejector. The combined effect of these measures is expected to yield superior system efficiency and stability,

directly improving key economic indicators, like specific investment cost or payback time, which always remain the crucial incentive from an investor's point of view.

Bibliography

[1] United Nations Environment; Programme and Ozone Secretariat. Handbook for the Montreal Protocol on Substances that Deplete the Ozone Layer, 1987.

[2] UN Environment Ozone Secretariat. Briefing note on Ratification of the Kigali Amendment, 2017.

[3] Giorgio Besagni, Riccardo Mereu, and Fabio Inzoli. Ejector refrigeration: A comprehensive review. *Renewable and Sustainable Energy Reviews*, pages 373–407, 9 2015.

[4] European Parliament and Council of the European Union. Regulation (EU) No 517/2014 of the European Parliament and of the Council of 16 april 2014 on fluorinated greenhouse gases and repealing Regulation (EC) No 842/2006 text with EEA relevance, 2014.

[5] European Parliament and Council of the European Union. Commission Implementing Decision (EU) 2023/2432 of 26 October 2023 determining, pursuant to Regulation (EU) No 517/2014 of the European Parliament and of the Council on fluorinated greenhouse gases, reference values for the period 1 January 2024 to 31 December 2024 for each producer or importer which has lawfully placed hydrofluorocarbons on the market in the Union from 1 January 2015, as reported under that Regulation (notified under document C(2023) 7800), 2023.

[6] Silvia Minetto, Francesco Fabris, Sergio Marinetti, and Antonio Rossetti. A review on present and forthcoming opportunities with natural working fluids in transport refrigeration. *International Journal of Refrigeration*, 152:343–355, 4 2023.

[7] Paride Gullo, Armin Hafner, and Krzysztof Banasiak. Transcritical R744 refrigeration systems for supermarket applications: Current status and future perspectives. *International Journal of Refrigeration*, 93:269–310, 7 2018.

[8] Xiaolei Yuan, Yumin Liang, Xinyi Hu, Yizhe Xu, Yongbao Chene, and Risto Kosonen. Waste heat recoveries in data centers: A review. *Renewable and Sustainable Energy Reviews*, 188:113777, 10 2023.

[9] Jerzy Gagan, Kamil Śmierciew, Michał Łukaszuk, Dariusz Butrymowicz, Andrzej Pawluczuk, Mikołaj Mastrowski, Marek Bergander, and Artur Cebula. Experimental assessment of the first industrial implementation of ejector refrigeration system operating with R1233zd(E) driven by ultra-low temperature heat source. *International Journal of Refrigeration*, 154:138–150, 7 2023.

[10] Paride Gullo, Brian Elmegaard, and Giovanni Cortella. Advanced exergy analysis of a R744 booster refrigeration system with parallel compression. *Energy*, 107:562–571, 2016.

[11] Manel Martínez-Ángeles, Emanuelle Sicco, Gabriele Toffoletti, Laura Nebot-Andrés, Daniel Sánchez, Rodrigo Cabello, Giovanni Cortella, and Ramón Llopis. Evaluation of CO_2-doped blends in single-stage with IHX and parallel compression refrigeration architectures. *International Journal of Refrigeration*, 151:50–62, 2023.

[12] Nyoman I. Suamir and Saavas A. Tassou. Performance evaluation of integrated trigeneration and CO_2 refrigeration systems. *Applied Thermal Engineering*, 50(2):1487–1495, 2013.

[13] Ehsan Gholamian, Pedram Hanafizadeh, and Pouria Ahmadi. Advanced exergy analysis of a carbon dioxide ammonia cascade refrigeration system. *Applied Thermal Engineering*, 137:689–699, 2018.

[14] Walid I. Mazyan, Ali Ahmadi, Hussain Ahmed, and Mina Hoorfar. Increasing the COP of a refrigeration cycle in natural gas liquefaction process using refrigerant blends of propane-NH_3, propane-SO_2 and propane-CO_2. *Heliyon*, 6(8):e04750, 2020.

[15] Daniel Sánchez, F. Vidan-Falomir, Laura Nebot-Andrés, Rodrigo Llopis, and Ramón Cabello. Alternative blends of CO_2 for transcritical refrigeration systems. experimental approach and energy analysis. *Energy Conversion and Management*, 279:116690, 2023.

[16] Pongsid Srikhirin, Satha Aphornratana, and Supachart Chungpaibulpatana. A review of absorption refrigeration technologies. *Renewable and Sustainable Energy Reviews*, 5(4):343–372, 2001.

[17] Rasoul Nikbakhti, Xiaolin Wang, Ahmed Kadhim Hussein, and Aghil Iranmanesh. Absorption cooling systems - Review of various techniques for energy performance enhancement. *Alexandria Engineering Journal*, 59(2):707 – 738, 2020.

[18] Raoudha Garma, Nizzar Ben-Ezzine, and Ahmed Bellagi. Experimental and numerical investigation on diffusion-absorption refrigeration system using low GWP refrigerant R600, C_9H_20 and helium. *International Journal of Thermofluids*, 27:101246, 2025.

[19] Anman Liang, Sheng Yang, Yi Ding, and Siqi Ma. Triple effect absorption refrigeration systems for the deep recovery of low grade waste heat. *Applied Thermal Engineering*, 250:123500, 2024.

[20] Liufeng Su, Qixiang Yan, Wencheng He, Junnan Ren, Xiaolong Liao, and Chuan Zhang. An innovative absorption refrigeration system for cooling high geothermal tunnels: Theoretical analysis and on-site testing. *Tunnelling and Underground Space Technology*, 162:106627, 2025.

[21] Amir Sharafian, Seyyed Mahdi Nemati Mehr, Poovanna Cheppudira Thimmaiah, Wendell Huttema, and Majid Bahrami. Effects of adsorbent mass and number of adsorber beds on the performance of a waste heat-driven adsorption cooling system for vehicle air conditioning applications. *Energy*, 112:481–493, 2016.

[22] M. Verde, L. Cortés, Jose M. Corberán, Alessio Sapienza, Salvatore Vasta, and G. Restuccia. Modelling of an adsorption system driven by engine waste heat for truck cabin A/C. performance estimation for a standard driving cycle. *Applied Thermal Engineering*, 30(13):1511–1522, 2010.

[23] Shanshan Cai, Zhipeng Hua, Min Dai, Song Li, Xiaobing Luo, and Zhengkai Tu. Performance analysis of adsorption refrigeration using a composite adsorbent with improved heat and mass transfer. *International Journal of Heat and Mass Transfer*, 216:124523, 2023.

[24] Jing Xu, Meng Huang, Zhiliang Liu, Quanwen Pan, Ruzhu Wang, and Tianshu Ge. Performance evaluation of a high-efficient hybrid adsorption refrigeration system for ultralow-grade heat utilization. *Energy*, 288:129870, 2024.

[25] Ahmed Askalany, Ehab S. Ali, and Ramy H. Mohammed. A novel cycle for adsorption desalination system with two stages-ejector for higher water production and efficiency. *Desalination*, 496:114753, 2020.

[26] Mohamed G. Gado, Shinichi Ookawara, Sameh Nada, and Hamdy Hassan. Renewable energy-based cascade adsorption-compression refrigeration system: Energy, exergy, exergoeconomic and enviroeconomic perspectives. *Energy*, 253:124127, 2022.

[27] Raul Roman and Jorge I. Hernandez. Performance of ejector cooling systems using low ecological impact refrigerants. *International Journal of Refrigeration*, 34(7):1707–1716, 2011.

[28] Giorgio Besagni, Nicolò Cristiani, Lorenzo Croci, Gaël Raymond Guédon, and Fabio Inzoli. Multi-scale evaluation of ejector performances: The influence of refrigerants and ejector design. *Applied Thermal Engineering*, 186:116502, 2021.

[29] Giorgio Besagni and Nicolò Cristiani. Multi-scale evaluation of an R290 variable geometry ejector. *Applied Thermal Engineering*, 188:116612, 2021.

[30] Ian W. Eames, Ali E. Ablwaifa, and Volodymyr Petrenko. Results of an experimental study of an advanced jet-pump refrigerator operating with R245fa. *Applied Thermal Engineering*, 27(17):2833–2840, 2007.

[31] Nawel Khaldi, Safa Sdiri, and Mariem Lazaar. Thermodynamic analysis and optimization of an ejector refrigeration system for sustainable cooling applications. *International Journal of Refrigeration*, 174:372–387, 2025.

[32] Jerzy Gagan, Kamil Śmierciew, Andrzej Pawluczuk, Michał Łukaszuk, Adam Dudar, and Dariusz Butrymowicz. The first experimental tests of novel bivalent hybrid ejector-compressor refrigeration system. *Energy*, 317:134646, 2025.

[33] Bartosz Gil and Jacek Kasperski. Performance Analysis of a Solar-powered Ejector Air-conditioning Cycle with Heavier Hydrocarbons as Refrigerants. *Energy Procedia*, 57:2619–2628, 2014.

[34] İbrahim Üçgül. Thermo-economic analysis of ejector cooling system. *YEKARUM e-DERGİ, Süleyman Demirel University*, 5(2):1–9, 2020.

[35] Tailan Yin, Qichao Yang, Jiawei Jiang, Zeye Zheng, Yuanyang Zhao, Guangbin Liu, and Liansheng Li. Energy, exergy, and economic analysis of a novel solar-assisted ejector subcooling co2 transcritical refrigeration systemt. *Solar Energy*, 284:113080, 2024.

[36] Liben Jiang, Zhaolin Gu, Xiao Feng, and Yun Li. Study of new absorption-ejector hybrid refrigeration system. In *International Refrigeration and Air Conditioning Conference at Purdue*. Purdue University, 2002.

[37] Liben Jiang, Zhaolin Gu, Xiao Feng, and Yun Li. Thermo-economical analysis between new absorption-ejector hybrid refrigeration system and small double-effect absorption system. *Applied Thermal Engineering*, 22(9):1027–1036, 2002.

[38] Finnian Freeling, David Behringer, Felix Heydel, Marco Scheurer, Thomas A. Ternes, and Karsten Nödler. Trifluoroacetate in precipitation: Deriving a benchmark data set. *Environmental Science & Technology*, 54(18):11210–11219, 2020.

[39] Bukola O. Bolaji and Zhongjie Huan. Ozone depletion and global warming: Case for the use of natural refrigerant - a review. *Renewable and Sustainable Energy Reviews*, 18:49–54, 2013.

[40] James M. Calm. The next generation of refrigerants - historical review, considerations, and outlook. *International Journal of Refrigeration*, 31(7):1123–1133, 2008.

[41] J. Koh and Zulkifli Zakaria. Hydrocarbons as refrigerants—a review. *ASEAN Journal on Science and Technology for Development*, 34:35, 08 2017.

[42] Naeem Abas, Ali Raza Kalair, Nasrullah Khan, Aun Haider, Zahid Saleem, and Muhammad Shoaib Saleem. Natural and synthetic refrigerants, global warming: A review. *Renewable and Sustainable Energy Reviews*, 90:557–569, 2018.

[43] Riley B. Barta, Eckhard A. Groll, and Davide Ziviani. Review of stationary and transport CO_2 refrigeration and air conditioning technologies. *Applied Thermal Engineering*, 185:116422, 12 2021.

[44] Osama A. A. Ibrahim, Saif A. Kadhim, Karrar A. Hammoodi, Farhan L. Rashid, and Ali H. Askar. Review of hydrocarbon refrigerants as drop-in alternatives to high-GWP refrigerants in VCR systems: The case of R290. *Cleaner Engineering and Technology*, 10 2024.

[45] Zheng Hu, Zilong Deng, Wei Gao, and Yongping Chen. Experimental study of the absorption refrigeration using ocean thermal energy and its under-lying prospects. *Renewable Energy*, 213:47–62, 2023.

[46] Han Yuan, Ji Zhang, Xiankun Huang, and Ning Mei. Experimental investigation on binary ammonia-water and ternary ammonia-water-lithium bromide mixture-based absorption refrigeration systems for fishing ships. *Energy Conversion and Management*, 166:13–22, 2018.

[47] Zheng Hu, Yueru Wan, Chengbin Zhang, and Yongping Chen. Compression-assisted absorption refrigeration using ocean thermal energy. *Renewable Energy*, 186:755–768, 2022.

[48] Ding Lu, Wei Jiang, Zijian Liu, Xixi Guan, Zhiliang Zhang, Yin Bai, Xiaobo Zhang, Jiansong Qin, and Maoqiong Gong. Study on the ammonia-water two-stage evaporation absorption refrigeration system for the cooling process with temperature-distributed heat load. *International Journal of Refrigeration*, 151:125–135, 2023.

[49] Carlos Amaris, Konstantinos M. Tsamos, and Savvas A Tassou. Analysis of an R744 typical booster configuration, an R744 parallel-compressor booster configuration and an R717/R744 cascade refrigeration system for retail food applications. part 1: Thermodynamic analysis. *Energy Procedia*, 161:259–267, 2019.

[50] Muqing Chen, Qichao Yang, Benlin Shi, Xiaonan Chen, Weikai Chi, Guangbin Liu, Yuanyang Zhao, and Liansheng Li. Performance comparison of ultra-low temperature cascade refrigeration cycles using R717/R170, R717/R41 and R717/R1150 to replace R404A/R23. *Thermal Science and Engineering Progress*, 44:102048, 2023.

[51] Muhammad N. Jaafar, Masli I. Rosli, Darman Nordin, and Junaidah Buhari. Systematic literature review on the risk assessment of ammonia refrigeration systems in the food industry. *Journal of Loss Prevention in the Process Industries*, 96:105629, 2025.

[52] Hailing Fu, Shuo Huang, Yuan Li, Jiasen Cheng, Yang Guo, Kang Wang, and Ranran Sun. The research and application of technology and core components in commercial refrigeration and freezing systems:a review. *Journal of Stored Products Research*, 108:102400, 2024.

[53] Stefan Elbel and Neal Lawrence. Review of recent developments in advanced ejector technology. *International Journal of Refrigeration*, 62:1–18, 11 2016.

[54] Jianyong Chen, Sad Jarall, Hans Havtunn, and Björn Palm. A review on versatile ejector applications in refrigeration systems. *Renewable and Sustainable Energy Reviews*, pages 67–90, 5 2015.

[55] Björn Palm. Hydrocarbons as refrigerants in small heat pump and refrigeration systems - A review. *International Journal of Refrigeration*, 31(4):552–563, 2008.

[56] Ayan Sengupta, Paride Gullo, Vahid Khorshidi, and Mani Sankar Dasgupta. Waste heat utilization: Energy and economic benefits from multi-ejector chiller sub-cooling R744 supermarket refrigeration systems. *Energy*, 312:133657, 2024.

[57] Orelien T. Boupda, Frederic Lontsi, Thomas Djiako, and Roger Ekani. Development and exergo-energetic analysis of an energy-efficient solar-assisted transcritical CO_2 refrigeration system with two-phase ejector. *Energy Conversion and Management: X*, 25:100854, 2025.

[58] Miguel Ávila Gutiérrez, Bernardo P. Pérez, Francisco Sánchez de la Flor, and José Manuel Salmerón Lissén. Semi-empirical performance assessment of a transcritical CO_2 system combined with a heat-driven ejector refrigeration system (ERS) using hydrocarbons as a subcooling solution for low-temperature refrigeration applications. *Energy Conversion and Management*, 341:120068, 2025.

[59] International Institute of Refrigeration (IIR). Impact of standards on hydrocarbon refrigerants in europe. Technical report, IIR, 2018.

[60] Zhao Yang, Biao Feng, Haiyun Ma, Lei Zhang, Chenjun Duan, Bing Liu, Yong Zhang, Siyi Chen, and Zongyu Yang. Analysis of lower GWP and flammable alternative refrigerants. *International Journal of Refrigeration*, pages 12–22, 1 2021.

[61] Daniel Colbourne, Kwok O. Suen, TTingxun X. Li, Ivan Vince, and Asbjorn L. Vonsild. General framework for revising class A3 refrigerant charge limits - a discussion. *International Journal of Refrigeration*, 117:209–217, 2020.

[62] Lingeng Zou, Ye Liu, and Jianlin Yu. Recent advances on performance enhancement of propane heat pump for heating applications. *Energy*, 314, 12 2025.

[63] Stella Maia Rocha de Carvalho, Luiz Henrique Parolin Massuchetto, Raiza Barcelos Corrêa do Nascimento, Hugo Valença de Araújo, and José Vicente Hallak d'Angelo. Optimization of a vapor injection refrigeration cycle using hydrocarbon mixed refrigerants. *International Journal of Refrigeration*, 98:109–119, 2019.

[64] Y.S. Lee and C.C. Su. Experimental studies of isobutane (R600a) as the refrigerant in domestic refrigeration system. *Applied Thermal Engineering*, 22(5):507–519, 2002.

[65] Khalid Joudi and Qusay Al-amir. Experimental assessment of residential split type air-conditioning systems using alternative refrigerants to r-22 at high ambient temperatures. *Energy Conversion and Management*, 86:496–506, 12 2018.

[66] Md Walid Faruque, Mahdi Hafiz Nabil, Mohammed Raihan Uddin, M. Monjurul Ehsan, and Sayedus Salehin. Thermodynamic assessment of a triple cascade refrigeration system utilizing hydrocarbon refrigerants for ultra-low temperature applications. *Energy Conversion and Management: X*, 14:100207, 2022.

[67] Bartosz Gil, Amaury Fievez, and Bartosz Zajaczkowski. Pool boiling heat transfer coefficient of dimethyl ether and its azeotropic ternary mixtures. *International Journal of Heat and Mass Transfer*, 171:121063, 2021.

[68] Daniel Calleja-Anta, Manel Martínez-Añgles, and Rodrigo Llopis. RE170 (Dimethyl Ether) and ternary mixtures (R744/RE170/R600) as alternatives to R290 for refrigeration and heat pump applications. *International Journal of Refrigeration*, 5 2025.

[69] Michał Sobieraj. Development of novel wet sublimation cascade refrigeration system with binary mixtures of R744/R32 and R744/R290. *Applied Thermal Engineering*, 196, 7 2021.

[70] Yaxiang Hou, Weidong Wu, Huaichen Wang, and Haoxiang Zhou. Experimental study on the transcritical cycle performance of a closed-loop heat pump drying system based on R744/R290/R32 ternary refrigerant. *International Communications in Heat and Mass Transfer*, 159:108255, 2024.

[71] Clemens Forman, Ibrahim Kolawole Muritala, Robert Pardemann, and Bernd Meyer. Estimating the global waste heat potential. *Renewable and Sustainable Energy Reviews*, 57:1568–1579, 2016.

[72] Hussam Jouhara, Navid Khordehgah, Sulaiman Almahmoud, Bertrand Delpech, Amisha Chauhan, and Savvas A. Tassou. Waste heat recovery technologies and applications. *Thermal Science and Engineering Progress*, 6:268–289, 2018.

[73] Michael Papapetrou, George Kosmadakis, Andrea Cipollina, Umberto La Commare, and Giorgio Micale. Industrial waste heat: Estimation of the technically available resource in the eu per industrial sector, temperature level and country. *Applied Thermal Engineering*, 138:207–216, 2018.

[74] Mauro Luberti, Robert Gowans, Patrick Finn, and Giulio Santori. An estimate of the ultralow waste heat available in the european union. *Energy*, 238:121967, 2022.

[75] Alexander S. Rattner and Srinivas Garimella. Energy harvesting, reuse and upgrade to reduce primary energy usage in the USA. *Energy*, 36(10):6172–6183, 2011.

[76] Intergovernmental Panel on Climate Change (IPCC). *Summary for Policymakers*, pages 1–30. Cambridge University Press, 2014.

[77] Lizhi Zhang. Design and testing of an automobile waste heat adsorption cooling system. *Applied Thermal Engineering*, 20(1):103–114, 2000.

[78] Vikas H. Chaudhari and Avinash D. Desai. Experimental study of single bed prototype adsorption refrigeration unit using waste heat energy. *Materials Today: Proceedings*, 49:1799–1803, 2022.

[79] Peyman Gholamali Zadeh and Jae Dong Chung. Exploring adsorption refrigeration for automobile air-conditioning: A comprehensive review. *Applied Thermal Engineering*, 241:122390, 2024.

[80] Marco S. Fernandes, Gonçalo J. V.N. Brites, José J. Costa, Adélio R. Gaspar, and Vítor A.F. Costa. Review and future trends of solar adsorption refrigeration systems. *Renewable and Sustainable Energy Reviews*, 39:102–123, 2014.

[81] Congqi Huang, Shuangquan Shao, Ningbo Wang, Yanhua Guo, and Wei Wu. Performance analysis of compression-assisted absorption refrigeration-heating system for waste heat recovery of liquid-cooling data center. *Energy*, 305:132325, 2024.

[82] Stefan Elbel. Historical and present developments of ejector refrigeration systems with emphasis on transcritical carbon dioxide air-conditioning applications. *International Journal of Refrigeration*, 34(7):1545–1561, 2011.

[83] Jakub Bodys, Jacek Smolka, Michał Palacz, Michał Haida, Krzysztof Banasiak, and Andrzej J. Nowak. Experimental and numerical study on the R744 ejector with a suction nozzle bypass. *Applied Thermal Engineering*, 194:117015, 5 2021.

[84] Jianyong Chen, Yunhai Li, Weixiong Chen, Xianglong Luo, Ying Chen, Zhi Yang, and Ian W. Eames. Investigation of the ejector nozzle in refrigeration system. *Energy*, 157:571–587, 2018.

[85] Paride Gullo, Martin Ryhl Kærn, Michał Haida, Jacek Smolka, and Stefan Elbel. A review on current status of capacity control techniques for two-phase ejectors. *International Journal of Refrigeration*, 119:64–79, 2020.

[86] Rafał Fingas, Michał Haida, Jacek Smolka, Lorenzo Croci, Jakub Body, Michał Palacz, and Giorgio Besagni. Experimental analysis of the R290 variable geometry ejector with a spindle. *Applied Thermal Engineering*, 10 2025.

[87] Mikołaj Mastrowski, Jacek Smolka, Dariusz Butrymowicz, Łukasz Antczak, Jerzy Gagan, and Kamil Śmierciewd. Experimental validation of the theoretical ejector model in a low-grade waste heat refrigeration system using R1233zdE as a working fluid. *Applied Thermal Engineering*, 236:121716, 10 2024.

[88] Jacek Smolka, Zbigniew Bulinski, Adam Fic, Andrzej J. Nowak, Krzysztof Banasiak, and Armin Hafner. A computational model of a transcritical R744 ejector based on a homogeneous real fluid approach. *Applied Mathematical Modelling*, 37(3):1208–1224, 2013.

[89] Michał Palacz, Michał Haida, Jacek Smolka, Andrzej J. Nowak, Krzysztof Banasiak, and Armin Hafner. HEM and HRM accuracy comparison for the simulation of CO_2 expansion in two-phase ejectors for supermarket refrigeration systems. *Applied Thermal Engineering*, 115:160–169, 2017.

[90] Armin Hafner, Sven Forsterling, and Krzysztof Banasiak. Multi-ejector concept for R744 supermarket refrigeration. *International Journal of Refrigeration*, 43:1–13, 2014.

[91] Krzysztof Banasiak, Armin Hafner, Ekaterini E. Kriezi, Kenneth B. Madsen, Michael Birkelund, Kristian Fredslund, and Rickard Olsson. Development and performance mapping of a multi-ejector expansion work recovery pack for R744 vapour compression units. *International Journal of Refrigeration*, 57:265–276, 2015.

[92] Michał Haida, Krzysztof Banasiak, Jacek Smolka, Armin Hafner, and Trygve M. Eikevik. Experimental analysis of the R744 vapour compression rack equipped with the multi-ejector expansion work recovery module. *International Journal of Refrigeration*, 64:93–107, 2016.

[93] Jing Ge, Hongjie Chen, Jun Li, and Yang Jin. Experimental comparison of critical performance for variable geometry ejectors with different mixer structures. *Chemical Engineering Journal*, 478:147487, 2023.

[94] Xiangjie Chen, Mark Worall, Siddig Omer, Yuehong Su, and Saffa Riffat. Theoretical studies of a hybrid ejector CO_2 compression cooling system for vehicles and preliminary experimental investigations of an ejector cycle. *Applied Energy*, 102:931–942, 2013.

[95] Stefan Elbel and Pega Hrnjak. Experimental validation of a prototype ejector designed to reduce throttling losses encountered in transcritical R744 system operation. *International Journal of Refrigeration*, 31:411–422, 2008.

[96] Jishnu Chandran R., Senthil Kumar Arumugam, Sreeja Sadasivan, Bibin John, and P. Rajesh Kanna. Effect of spindle position on the performance and two-phase characteristics of controllable ejector for transcritical CO_2 refrigeration system. *The Journal of Supercritical Fluids*, 205:106125, 2024.

[97] Jingwei Zhu and Stefan Elbel. Experimental investigation of a novel expansion device control mechanism: Vortex control of initially subcooled flashing R134a flow expanded through convergent-divergent nozzles. *International Journal of Refrigeration*, 85:167–183, 2018.

[98] Jingwei Zhu and Stefan Elbel. Experimental investigation into the influence of vortex control on transcritical R744 ejector and cycle performance. *Applied Thermal Engineering*, 164:114418, 2020.

[99] Paride Gullo, Michael Birkelund, Ekaterini E. Kriezi, and Martin Ryhl Kærn. Novel flow modulation method for R744 two-phase ejectors - proof of concept, optimization and first experimental results. *Energy Conversion and Management*, 237:114082, 2021.

[100] Paride Gullo, Michael Birkelund, Ekaterini E. Kriezi, and Martin Ryhl Kærn. Comprehensive experimental performance study on a small-capacity transcritical R744 vapour-compression refrigeration unit equipped with an innovative ejector. *International Journal of Refrigeration*, 152:192–203, 2023.

[101] Jacek Smolka, Michał Palacz, Jakub Bodys, Krzysztof Banasiak, Adam Fic, Zbigniew Bulinski, Andrzej J. Nowak, and Armin Hafner. Performance comparison of fixed- and controllable-geometry ejectors in a CO_2 refrigeration system. *International Journal of Refrigeration*, 65:172–182, 2016.

[102] Ligeng Li, Hua Tian, Kai Liu, Yibo Wu, Xuan Wang, Xingyu Liang, and Gequn Shu. Optimum pressure control with three controllable ejectors of a CO_2 multi-ejector refrigeration system. *International Journal of Refrigeration*, 157:172–185, 2024.

[103] Szabolcs Varga, Armando C. Oliveira, and Bogdan Diaconu. Numerical assessment of steam ejector efficiencies using CFD. *International Journal of Refrigeration*, 32:1203–1211, 2009.

[104] Paulo R. Pereira, Szabolcs Varga, João Soares, Armando C. Oliveira, António M. Lopes, Fernando G. de Almeida, and João F. Carneiro. Experimental results with a variable geometry ejector using R600a as working fluid. *International Journal of Refrigeration*, 46:77–85, 2014.

[105] Vu Van Nguyen, Szabolcs Varga, Joao Soares, Vaclav Dvorak, and Armando C. Oliveira. Applying a variable geometry ejector in a solar ejector refrigeration system. *International Journal of Refrigeration*, 113:187–195, 2020.

[106] Giorgio Besagni, Nicolò Cristiani, Lorenzo Croci, Gaël Raymond Guédon, and Fabio Inzoli. Computational fluid-dynamics modelling of supersonic ejectors: Screening of modelling approaches, comprehensive validation and assessment of ejector component efficiencies. *Applied Thermal Engineering*, 186:116431, 2021.

[107] John T. Munday and David F. Bagster. A new ejector theory applied to steam jet refrigeration. *Industrial & Engineering Chemistry Process Design and Development*, 16(4):442–449, 1977.

[108] Barry N. Taylor and Chris E. Kuyatt. Guidelines for evaluating and expressing the uncertainty of nist measurement results. *Technology*, 1994.

[109] The MathWorks Inc. Matlab version 9.10.0.1613233 (r2021a), 2021.

[110] Michał Haida, Jacek Smolka, Armin Hafner, Ziemowit Ostrowski, Michał Palacz, Andrzej J. Nowak, and Krzysztof Banasiak. System model derivation of the CO_2 two-phase ejector based on the CFD-based reduced-order model. *Energy*, 144:941–956, 2018.

[111] Michał Haida, Jacek Smolka, Armin Hafner, Ziemowit Ostrowski, Michał Palacz, Kenneth B. Madsen, Sven Försterling, Andrzej J. Nowak, and Krzysztof Banasiak. Performance mapping of the R744 ejectors for refrigeration and air conditioning supermarket application: A hybrid reduced-order model. *Energy*, 153:933–948, 2018.

[112] Michał Palacz, Jacek Smolka, Adam Fic, Zbigniew Bulinski, Andrzej J. Nowak, Krzysztof Banasiak, and Armin Hafner. Application range of the HEM approach for CO_2 expansion inside two-phase ejectors for supermarket refrigeration systems. *International Journal of Refrigeration*, 59:251–258, 2015.

[113] Haida, Michał, Jacek Smołka, Michał Palacz, J. Bodys, Andrzej Józef Nowak, Zbigniew Buliński, A. Fic, K. Banasiak, and A. Hafner. Numerical investigation of an R744 liquid ejector for supermarket refrigeration systems. *Thermal Science*, 20, 2016.

[114] Michał Palacz, Michał Haida, Jacek Smolka, Marcin Plis, Andrzej J. Nowak, and Krzysztof Banasiak. A gas ejector for CO_2 supercritical cycles. *Energy*, 163:1207–1216, 2018.

[115] Michał Haida, Rafał Fingas, Wojciech Szwajnoch, Jacek Smolka, Michał Palacz, Jakub Bodys, and Andrzej J. Nowak. An object-oriented R744 two-phase ejector reduced-order model for dynamic simulations. *Energies*, 12(7):1282, 2019.

[116] Knut Emil Ringstad, Yosr Allouche, Paride Gullo, Åsmund Ervik, Krzysztof Banasiak, and Armin Hafner. A detailed review on co2 two-phase ejector flow modeling. *Thermal Science and Engineering Progress*, 20:100647, 2020.

[117] Stanislau Stasheuski, Karri Keskinen, David P. Schmidt, Ville Vuorinen, Jari Hyvönen, and Ossi Kaario. Impact of modelling assumptions in cavitating flow of simplified injector. *International Journal of Multiphase Flow*, 177:104847, 2024.

[118] Jose Sierra-Pallares, Javier García del Valle, Pedro García Carrascal, and Francisco Castro Ruiz. A computational study about the types of entropy generation in three different R134a ejector mixing chambers. *International Journal of Refrigeration*, 63:199–213, 2016.

[119] Michał Palacz, Michał Haida, Jacek Smolka, Andrzej J. Nowak, Krzysztof Banasiak, and Armin Hafner. HEM and HRM accuracy comparison for the simulation of CO_2 expansion in two-phase ejectors for supermarket refrigeration systems. *Applied Thermal Engineering*, pages 160–169, 2017.

[120] Ziemowit Ostrowski, Ryszard A. Białecki, and Alan J. Kassab. Solving inverse heat conduction problems using trained POD-RBF network inverse method. *Inverse Problems in Science and Engineering*, 16(1), 2008.

[121] Christopher E. Brennen. *Fundamentals of Multiphase Flows*. Cambridge University Press, Cambridge, 2005.

[122] Modelica Association. *Modelica® - A Unified Object-Oriented Language for Systems Modeling, Language Specification Version 3.6*. Modelica Association, 2023.

[123] TLK Thermo. TIL Library. `https://www.tlk-thermo.com/index.php/en/services/simulation`. Accessed: 2024-11-05.

[124] Dassault Systems. DYMOLA Systems Engineering. `https://www.3ds.com/products-services/catia/products/dymola`.

[125] Stefanie Blust, Pierre A.C. Barroca, Yosr Allouche, and Armin Hafner. A numerical study of the r744 primary cooling system for atlas and cms lhc detectors. *International Journal of Refrigeration*, 165:145–155, 2024.

[126] Hagar Elarga, Håkon Selvnes, Alexis Sevault, and Armin Hafner. Numerical investigation of a co2 cooling system connected to spawn-of-energy-plus thermal zones. *Applied Thermal Engineering*, 222:119908, 2023.

[127] Luca Contiero, Krzysztof Banasiak, Bart Verlaat, Armin Hafner, Sven Försterling, and Yosr Allouche. Thermal design of an ejector-supported cycle using krypton for cooling of particle detector accelerators. *International Journal of Refrigeration*, 178:160–169, 2025.

[128] Mahmood Mastani Joybari, Håkon Selvnes, Erling Vingelsgård, Alexis Sevault, and Armin Hafner. Parametric study of low-temperature thermal energy storage using carbon dioxide as the phase change material in pillow plate heat exchangers. *Applied Thermal Engineering*, 221:119796, 2023.

[129] Holger Martin. *N6 Pressure Drop and Heat Transfer in Plate Heat Exchangers*, pages 1515–1522. Springer Berlin Heidelberg, Berlin, Heidelberg, 2010.

[130] Giovanni A. Longo and Andrea Gasparella. Refrigerant R134a vaporisation heat transfer and pressure drop inside a small brazed plate heat exchanger. *International Journal of Refrigeration*, 30(5):821–830, 2007.

[131] B. Thonon, R. Vidil, and C. Marvillet. Recent research and developments in plate heat exchangers. *Journal of Enhanced Heat Transfer*, 2(1-2):149 – 155, 1995.

[132] Giovanni Longo, Giulia Righetti, and Claudio Zilio. A new computational procedure for refrigerant condensation inside herringbone-type brazed plate heat exchangers. *International Journal of Heat and Mass Transfer*, 82:530–536, 04 2015.

[133] Eastman. Therminol 59 Heat Transfer Fluid. `https://www.eastman.com/en/products/brands/therminol`. Accessed: 2025-10-28.

[134] Ehsanolah Assareh, Siamak Hoseinzadeh, Neha Agarwal, Mostafa Delpisheh, Ali Dezhdar, Masoud Feyzi, Qiliang Wang, Davide Astiaso Garcia, Ehsan Gholamian, Mehdi Hosseinzadeh,

Maryam Ghodrat, and Moonyong Lee. A transient simulation for a novel solar-geothermal cogeneration system with a selection of heat transfer fluids using thermodynamics analysis and ann intelligent (ai) modeling. *Applied Thermal Engineering*, 231:120698, 2023.

[135] Humphrey Adun, Michael Adedeji, Jeffrey Dankwa Ampah, Olusola Bamisile, Dilber Uzun Ozsahin, and Yihua Hu. Novel heat transfer fluid for maximum recovery of heat of compression: A steady state analysis on improving the performance of liquid air energy storage. *Journal of the Taiwan Institute of Chemical Engineers*, 152:105176, 2023.

[136] Volker Gnielinski. New equations for heat and mass transfer in turbulent pipe and channel flow. *International chemical engineering*, 16(2):359–367, 1976.

[137] Frederick William Dittus. Heat transfer in automobile radiators of the tubular type. *Univ. of California Pub., Eng.*, 2(13):443–461, 1930.

[138] Dieter Steiner. *Wärmeübergang beim Strömungsverdampfen von Reinstoffen und von Mischungen*. Habilitation, Universität Karlsruhe, 1996.

[139] Mirza M. Shah. A general correlation for heat transfer during film condensation inside pipes. *International Journal of Heat and Mass Transfer*, 22:547–556, 1979.

[140] Siegfried Haaf. *Wärmeübertragung in Luftkühlern*, pages 435–491. Springer Berlin Heidelberg, Berlin, Heidelberg, 1988.

[141] Th.E. Schmidt. Heat transfer calculations for extended surfaces. *Refrigeration Engineering*, 57:351–357, 1949.

[142] Pengtao Wang, Ahmad Abu-Heiba, Ramy H. Mohammed, Jeremy Spitzenberger, Stephen Kowalski, Hongbin Ma, and Kashif Nawaz. Thermodynamic analysis of a two-stage binary-fluid ejector heat pump water heater. *Thermal Science and Engineering Progress*, 44(1), 2023.

[143] Xiaolin Zhang, Shuai Deng, Li Zhao, Wen Su, and Weicong Xu. Performance analysis on a power and ejector-refrigeration system and the involved ejector. *Frontiers in Energy Research*, Volume 7 - 2019, 2019.

[144] Hylke E. Beck, Tim R. McVicar, Noemi Vergopolan, Alexis Berg, Nicholas J. Lutsko, Ambroise Dufour, Zhenzhong Zeng, Xin Jiang, Albert I. J. M. van Dijk, and Diego G. Miralles. High-resolution (1 km) Köppen-Geiger maps for 1901-2099 based on constrained CMIP6 projections. *Scientific Data*, 10(1), October 2023.

[145] Marani Sp. z o.o. `https://www.marani.pl/firma/misja-wizja-wartosci/`, 2025.

[146] Zhihao Zhang, Tingsen Chen, Liubao Shi, Guogeng He, Jialiang Hua, Xingmin Wang, Ruikang Li, and Hanyue Zhang. Flow boiling heat transfer characteristics of the new hydrocarbon blend R487A in a horizontal tube: an experimental study. *Applied Thermal Engineering*, 279:128097, 2025.

[147] Matteo Caramaschi, Jonas Kjær Jensen, Stefano Poppi, Kasper Korsholm Østergaard, Torben Schmidt Ommen, Martin Ryhl Kærn, Hatef Madani, and Brian Elmegaard. Natural refrigerant mixtures in low-charge heat pumps: An analysis of the potential for performance enhancements. *International Journal of Refrigeration*, 165:70–83, 2024.

[148] Daniel Calleja-Anta, Manel Martínez-Ángeles, and Rodrigo Llopis. RE170 (dimethyl ether) and ternary mixtures (R744/RE170/R600) as alternatives to R290 for refrigeration and heat pump applications. *International Journal of Refrigeration*, 176:120–133, 2025.

[149] Daniel Calleja-Anta, Daniel Sánchez, Laura Nebot-Andrés, Ramón Cabello, and Rodrigo Llopis. Alternative mixtures to R600a. theoretical assessment and experimental energy evaluation of binary mixtures in a commercial cooler. *International Journal of Refrigeration*, 152:83–92, 2023.

[150] ANSI/ASHRAE. Designation and safety classification of refrigerants. ANSI/ASHRAE Standard 34-2022, 2022.